CRITICALITY AND DIVERSITY IN A BACTERIAL SENSORY NETWORK

VRIJE UNIVERSITEIT

CRITICALITY AND DIVERSITY IN A BACTERIAL SENSORY NETWORK

ACADEMISCH PROEFSCHRIFT

ter verkrijging van de graad Doctor of Philosophy aan
de Vrije Universiteit Amsterdam,
op gezag van de rector magnificus
prof.dr. J.J.G. Geurts,
volgens besluit van de decaan
van de Faculteit der Bètawetenschappen
in het openbaar te verdedigen
op vrijdag 6 juni 2025 om 9.45 uur
in de universiteit

door

Fotios Avgidis

geboren te Cholargos, Griekenland

promotor:	prof.dr. T.S. Shimizu
copromotor:	prof.dr. T. Emonet
promotiecommissie:	prof.dr. P.R. ten Wolde prof.dr. A. Briegel prof.dr. V. Sourjik prof.dr. K.M. Taute prof.dr. F.J. Bruggeman

The work described in this thesis was performed at AMOLF, Science Park 104, 1098XG, Amsterdam, The Netherlands.

Cover design: Alexandra Tsoukala
DOI: https://doi.org/10.5463/thesis.1219

An electronic version of this thesis can be obtained from `www.amolf.nl` and `www.ub.vu.nl`. Printed copies can be obtained by request via `library@amolf.nl`

What is true for E. coli is true for the elephant.

Jacques Monod

CONTENTS

1 Introduction **1**
1.1 *Escherichia coli* and its motility . . . 2
1.2 Chemotaxis of *E. coli* . . . 2
1.3 Criticality . . . 4
1.4 Phenotypic diversity . . . 5

2 Spontaneous switching in a protein signaling array reveals near-critical cooperativity **7**
2.1 Introduction . . . 8
2.2 Results . . . 8
2.2.1 Single-cell FRET reveals two-state switching fluctuations in the absence of sensory stimulation . . . 8
2.2.2 Temporal statistics of switching events are well described by an Ising model . 13
2.2.3 Switching statistics reveal near-critical allosteric cooperativity of chemosensory arrays . . . 21
2.2.4 Switching statistics reveal fundamental flipping timescale of chemosensory arrays . . . 25
2.2.5 Near-critical cooperativity allows for large response amplitudes without compromising response speed . . . 25
2.3 Discussion . . . 32
2.4 Methods . . . 32
2.4.1 Cell culture and growth media . . . 32
2.4.2 FRET microscopy . . . 33
2.4.3 FRET analysis . . . 34
2.4.4 Cluster intensity analysis . . . 34
2.4.5 Switching analysis . . . 35
2.4.6 Numerical simulations of the conformational spread model . . . 35
2.4.7 Determination of the correlation length . . . 37
2.5 Supplementary Text . . . 37
2.5.1 Changing activity bias by genetic modification . . . 37
2.5.2 The Ising model in the thermodynamic limit can not explain spontaneous switching . . . 37
2.5.3 Finite-size Ising models exhibit two-state switching near criticality . . . 38
2.5.4 Scaling of the critical energy . . . 38
2.5.5 Scaling of the residence and transition times . . . 39
2.5.6 Scaling analysis of the experimental data . . . 39
2.5.7 Scaling of the fundamental frequency ω_0 . . . 40
2.5.8 Field dependence of two-state switching in finite lattices . . . 40
2.5.9 Array size estimation from residence time distributions . . . 42
2.5.10 The effect of chemoreceptor mixing within chemosensory arrays . . . 43

3 Growth-dependent sensory bet-hedging enhances navigation **49**
3.1 Introduction . . . 50

3.2 Results . . . 51
3.2.1 Single-cell FRET reveals substantial diversity in ligand sensitivity across an isogenic population of cells. . . . 51
3.2.2 Sensitivity distributions shift as a function of cell density in rich media, but not in minimal media . . . 51
3.2.3 Tar/Tsr ratio distribution shift as a function of cell density in rich media, but not in minimal media . . . 52
3.2.4 Diversity in the Tar/Tsr ratio is sufficient to quantitatively predict chemosensory diversity . . . 54
3.2.5 Chemosensory diversity boosts collective navigation in co- ntrasting environments via phenotypic filtering . . . 60
3.2.6 Growth environment, and not growth time, dictates the Tar/Tsr ratio distribution . . . 61
3.2.7 Regulation of chemoreceptor expression as a function of growth rate . . . 61
3.2.8 Leveraging gene-expression noise as a sensory bet-hedging mechanism . . . 63
3.3 Discussion . . . 67
3.4 Methods . . . 67
3.4.1 Strains and plasmids. . . . 67
3.4.2 Growth conditions. . . . 69
3.4.3 Single-cell FRET microscopy . . . 71
3.4.4 FRET image analysis . . . 72
3.4.5 MWC Model . . . 73
3.4.6 Colony expansion rate quantification . . . 74
3.4.7 Chemoreceptor copy number quantification. . . . 74
3.4.8 Chemoreceptor image analysis . . . 75
3.4.9 Fabrication of microfluidic chemostats . . . 75
3.4.10 Supernatant experiments . . . 76
3.4.11 Image analysis of microfluidic chemostat experiments . . . 77
3.4.12 Fabrication of microfluidic devices for swimming competition experiments . 78
3.4.13 Swimming competition experiments . . . 78
3.4.14 Chemoreceptor copy number quantification on swim plates . . . 79
3.4.15 Fabrication of microfluidic devices for single cell swim tracking . . . 79
3.4.16 Swim tracking experiments . . . 79
3.4.17 Growth rate measurements. . . . 81
3.4.18 Growth rate and cell volume quantification . . . 83

4 Dynamics of sensory diversity within and across generations 85
4.1 Introduction . . . 86
4.2 Results . . . 87
4.2.1 Sensitivity to ligand is on average robust against cell-cycle phase variation . . 87
4.2.2 Pre-stimulus activity of the chemotaxis pathway is on average robust against cell-cycle phase variation . . . 88
4.2.3 Ratio of the two major chemoreceptors, Tar/Tsr, is constant as a function of cell-cycle phase . . . 89
4.2.4 Slow relaxation of the Tar/Tsr ratio upon growth environment shift demonstrates the existence of an epigenetic environmental memory . . . 92
4.2.5 Non-genetic inheritance of sensory preference. . . . 92
4.3 Discussion . . . 96
4.4 Methods . . . 101
4.4.1 Strains and plasmids. . . . 101

4.4.2 Growth conditions. . . . 101
4.4.3 Microfluidic chemostat design and fabrication 101
4.4.4 FRET and receptor ratio measurements in growing cells 102
4.4.5 FRET and receptor ratio image analysis 103
4.4.6 Fluorophore maturation correction 104

5 Non-genetic adaptation by collective migration **107**
5.1 Introduction 108
5.2 Results 108
5.2.1 Collective migration tunes the population's distribution of swimming phenotypes 108
5.2.2 Tuning of swimming phenotype distributions is non-genetic and occurs without changes in CheYZ expression 110
5.2.3 Tuning of swimming phenotype distributions adapts the population to the physical environment 111
5.2.4 Adapted TB distribution rapidly relaxes back to batch distribution 113
5.2.5 Collective migration tunes the population's distribution of sensing phenotypes to adapt to the chemical environment 113
5.3 Discussion 119
5.4 Methods 129
5.4.1 Strains, media, and growth conditions. . . . 129
5.4.2 Growth rates measurements 130
5.4.3 Formation of propagating waves and expansion speed measurements using swim plate and capillary tube assays 130
5.4.4 Microfluidic device preparation. . . . 131
5.4.5 Tracking single cells and tumble detection 131
5.4.6 Measuring the time scales of relaxation of TB distribution to the standing batch distribution 131
5.4.7 Protein expression measurements in swim plates 131
5.4.8 Single-cell protein copy number quantification using fluorescent microscopy 132
5.4.9 Fluorescent image analysis for protein copy number quantification 132
5.4.10 Reproducibility and statistical analysis 132

6 Summary **135**

Bibliography **137**

List of PhD Publications **155**

Acknowledgments **157**

1

INTRODUCTION

A single silicon atom cannot perform any computation. However, when many silicon atoms are assembled in the right way, they can form a computer. Similarly, one neuron alone is not conscious, but many neurons together can form a brain, nature's most complex computer. If higher-order assemblies are merely the sum of their parts, an intriguing question arises: since a cell is just a collection of molecules moving chaotically and occasionally colliding, what gives it life? Owing to Friedrich Wöhler's urea synthesis experiments, we know that no "vital force" exists [1]. The answer to the basis of life instead, lies in structure. A few molecules can assemble to form the essential components of a cell: DNA, RNA, and proteins. The interactions among these structures impart life to the cell. This realization opens up numerous new questions: How do these complex structures function? How did they evolve? Is there an underlying design principle? Are they optimally designed?

This thesis aims to understand how function arises from simple components, with two specific objectives. First, we explore how a sensory network comprising just a few protein species exploits near-critical dynamics — the behavior of a system poised in a narrow regime between order and chaos. Second, we aim to understand how the same simple network gives rise to diverse behaviors among individuals, how this diversity changes during an organism's lifetime, and how individuals exploit this diversity to adapt to different environments. To answer these questions, we utilize arguably the best characterized sensory system throughout biology: the chemotaxis network of the enteric bacterium *Escherichia coli*. The chemotaxis network, the "brain" of the bacterium, allows it to navigate its environment, moving toward favorable conditions and avoiding stressful ones.

Both criticality and diversity are observed widely across biology, but their mechanistic origins and functional consequences remain challenging to study in a rigorous experimental setting. We chose to study them in the *E. coli* chemotaxis network because the system itself is very simple. It comprises only about a dozen protein species and is largely decoupled from gene expression and metabolism. Most importantly, however, we have a very good mechanistic understanding of this system, precise genetic control, and a vast array of experimental tools to study it. These characteristics make *E. coli* chemotaxis an ideal vehicle for studying fundamental questions about criticality and diversity.

Our approach includes a wide range of experiments across various scales. We use Förster Resonance Energy Transfer (FRET) microscopy to measure signaling dynamics in living cells, genetic engineering and fluorescence microscopy to assess protein expression, and physiology experiments to study bacterial growth. We also assess their chemotactic performance at the behavior level, by tracking how individual bacteria swim, and following how millions of bacteria collectively migrate

as population waves. We combine these experiments with theoretical analysis to understand how only a dozen or so protein species implement a control network that gives rise to such complex behaviors of bacterial cells.

1.1 *Escherichia coli* AND ITS MOTILITY

It would be an omission not to properly introduce the model organism used to derive all the experimental conclusions of this thesis. *Escherichia coli* is one of the most thoroughly studied model organisms, extensively characterized genetically, biochemically, and behaviorally. In fact, it was one of the first organisms to have its entire genome sequenced [2]. Due to its rapid growth rate—*E. coli* can divide every 20 minutes under ideal conditions—and ease of culture in the lab, *E. coli* has played a crucial role in the development of molecular biology and biotechnology, as well as experimental studies of evolution.

E. coli's natural environment is the small intestine of mammals, but it is also frequently found in the large intestine, soil, and water. Since it reproduces asexually, all *E. coli* cells have a single parent cell. Notably, most common laboratory *E. coli* strains descend from a cell obtained from an anonymous patient in Palo Alto, California, in the 1920s [3].

As *E. coli* reproduces asexually, the DNA molecules of all descendants of a single parent cell are identical apart from the occasional random mutation. *E. coli* has a single circular chromosome that consists of a double-stranded chain of DNA. When cut and untangled, this chromosome has a length that is about a thousand times longer than its cell body [4].

E. coli is only about 1 femtoliter in volume, with 70% of its total weight being water, similar to humans. The remaining 30% is composed of proteins (15%), RNA (6%; mostly ribosomal RNA), and only 1% of the cell weight is DNA [5]. Unlike humans, however, *E. coli* does not experience significant inertia; instead, viscous forces dominate its movement [6]. This is because the Reynolds number of an *E. coli* cell swimming in water is only about $5\text{x}10^{-5}$, whereas an average human swimming in the same environment would have a Reynolds number of about $2\text{x}10^{6}$ [5] [6]. For *E. coli* flagella to generate thrust, they need to utilize viscous drag. Even under these conditions, *E. coli* can swim about 20 body lengths per second [4]. Another important consequence of life at low Reynolds numbers is the significance of diffusion. The movement of metabolites toward an *E. coli* cell and the removal of metabolic byproducts away from the cell are entirely controlled by diffusion, with local stirring caused by cell movement being irrelevant [6].

1.2 CHEMOTAXIS OF *E. coli*

A major advance in our understanding of *E. coli* physiology came in the 1960s, when Julius Adler identified *E. coli* mutants that couldn't metabolize certain sugars and amino acids but still swam towards their sources [7] [8]. This observation proved that metabolism and sensing can be decoupled in *E. coli*. The ability of *E. coli* to move toward beneficial or away from harmful stimuli in its environment, a process termed chemotaxis, was, however, mechanistically understood only a decade later by Howard Berg. Berg built a microscope using analog electronics that could track single *E. coli* cells [9]. Using this tracking microscope, Berg and collaborators studied the trajectories of individual bacteria and found that they resemble a random walk consisting of straight segments ("runs") interrupted by short intervals of random motion in place, which causes the cell to re-orient itself ("tumbles") [10]. When an *E. coli* cell ascends an attractant gradient, the duration of the runs becomes longer, biasing their random walk (figure 1.1a).

This run-and-tumble motion in *E. coli* is powered by multiple rotating flagella. Each flagellum is driven by a single motor, and runs and tumbles correspond to counterclockwise (CCW) and clockwise (CW) motor rotation, respectively. The rotation of the motor is determined by the chemotaxis pathway of *E. coli*, a signaling network based entirely on protein-protein interactions (Figure 1.1b).

This network allows the cell to detect chemical and physical signals through membrane-embedded protein arrays composed of five different types of chemoreceptors. The two primary receptors, Tar (which mainly senses the amino acid aspartate) and Tsr (which mainly senses the amino acid serine), make up 90% of the total chemoreceptor population when *E. coli* cells are grown in rich media. The other three chemoreceptors—Tap (sensing dipeptides), Trg (sensing sugars), and Aer (sensing oxygen)—are present at substantially lower copy numbers [11].

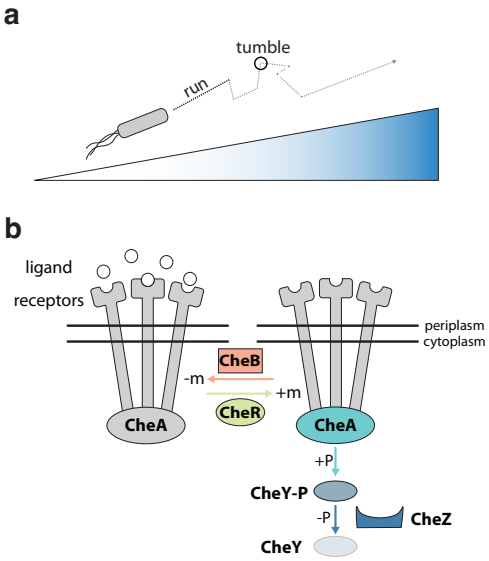

Figure 1.1: Chemotaxis in *Escherichia coli*. (a) *E. coli* movement alternates between run and tumble motions. When ascending an attractant gradient, the chemotaxis network suppresses tumbling, thereby increasing the duration of the run phase. (b) The chemotaxis network of *E. coli*. The kinase CheA phosphorylates the response regulator CheY, producing CheY-P in the absence of ligand binding to the receptors. CheY-P binds to the flagellar motor, reducing its tumbling bias. CheZ dephosphorylates CheY. The adaptation enzymes CheR and CheB methylate and demethylate the receptors, respectively; methylation decreases receptor sensitivity, while demethylation increases it.

When active, a kinase called CheA phosphorylates the response regulator CheY, producing CheY-P. Binding of attractant molecules to chemoreceptors reduces the activity of CheA, leading to a decrease in the intracellular level of CheY-P. CheY-P interacts with the flagellar motor, reducing the fraction of time it rotates CW (i.e., the motor's CW bias), and hence also the fraction of time the cell spends tumbling (i.e., the cell's tumble bias). Consequently, attractant binding increases the duration of the bacterium's runs [12]. Another enzyme, CheZ, catalyzes the removal of the phosphate groups from CheY-P, effectively undoing the action of CheA. The chemotaxis network also contains the scaffolding protein CheW, which structurally links the transmembrane receptors with cytosolic CheA to form the membrane-lining signaling arrays. Finally, there are two adaptation enzymes, CheR and CheB, which change the methylation level of the receptors. Specifically, CheR methylates inactive chemoreceptors, while CheB demethylates active chemoreceptors. Methylation decreases the receptor sensitivity, while demethylation enhances it, allowing the cell to adapt to constant background levels of chemoeffectors [11].

1

1.3 CRITICALITY

Let us now switch gears and talk about physics. Critical phenomena in physics refer to the behavior of systems at or near a critical point, on the boundary between different phases of matter. A classic example of a critical point is the liquid-vapor critical point, where a liquid and its vapor can coexist. At this critical point, small changes in conditions—such as temperature or pressure, in the case of the liquid-vapor critical point—can lead to drastic changes in the system's behavior as it transitions from one phase to another (e.g., from liquid to vapor) [13].

At critical points, systems exhibit characteristic properties that are remarkably independent of system-specific details (and hence often referred to as "universal" properties). One example is critical slowing down, where the system's response to perturbations becomes extremely slow. Criticality is also characterized by extreme sensitivity to perturbations as well as enormous spontaneous fluctuations, both indicating a high degree of cooperativity among the system's components. How such fluctuations can produce nontrivial effects was demonstrated over 150 years ago, when Thomas Andrews noticed the "critical opalescence" of fluids [14], which arises from the large density fluctuations near the liquid-vapor critical point. He reported that water turns opaque or "milky" near its critical temperature and pressure, and changing the temperature of water by just a few degrees restores its normal, transparent appearance.

Phase transitions are often categorized into first- and second-order transitions, with the main difference being continuity [13]. First-order transitions, such as the boiling of water to steam discussed above, are discontinuous. During this phase transition, there is a sudden change in system properties, such as its density. The order parameter in first-order transitions, a measure of the degree of order in the system, typically changes discontinuously at the transition point. In the case of the liquid-gas transition, the order parameter is the difference in densities between the gas and liquid phases. In contrast, second-order transitions are characterized by continuous changes in the order parameter, though thermodynamic responses near the critical point often exhibit power-law divergences. An example of a second-order transition is the transition from a paramagnetic to a ferromagnetic state in a magnet. Its magnetization gradually increases from zero as the temperature decreases below the critical temperature. The order parameter in second-order transitions changes smoothly, and while its derivative may not always diverge, susceptibilities and related thermodynamic quantities often do. For the ferromagnetic critical point, the order parameter is the magnetic moment.

But how is all this relevant to biology? The concept of criticality provides a unified physical framework to understand how assemblies of simple components give rise to complex behavior. In physical systems, these simple components are water molecules, in the case of the liquid-gas critical point and magnetic spins in the case of the ferromagnetic critical point. In biological systems, these components can range from proteins to cellular membranes, and from whole cells, such as bacteria and neurons, to even whole animals [15]. In fact, critical phenomena have been postulated in antibodies [16], plasma membrane vesicles [17], bacterial communities [18], and even the human brain [19] and flocks of birds [20]. In **Chapter 2** of this thesis, using a combination of single-cell FRET experiments and computer simulations of a two-dimensional conformational spread (Ising) model, we show how the chemoreceptor array of *E. coli*, an assembly of thousands of molecules, is poised at criticality.

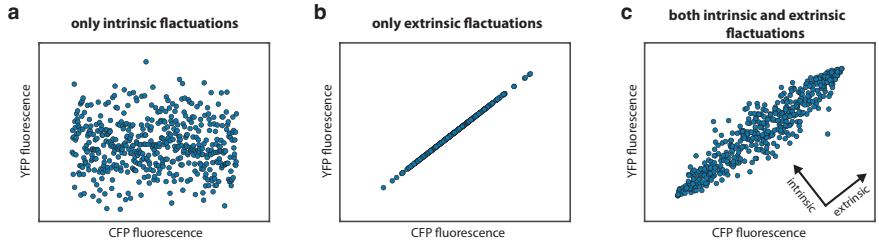

Figure 1.2: Intrinsic and extrinsic noise in stochastic gene expression. (a) Expected cell-to-cell variability when gene expression noise is exclusively intrinsic. Intrinsic fluctuations arise from the inherent stochasticity of transcription and translation. As these sources of variability are random, they affect the copies of the YFP and CFP genes independently, resulting in uncorrelated YFP and CFP levels. (b) Extrinsic fluctuations are due to factors that influence both YFP and CFP genes, such as variations in the copy numbers of RNA polymerases and ribosomes or cell cycle-related effects. These fluctuations produce correlated levels of YFP and CFP expression. (c) Expected cell-to-cell variability when gene expression noise is both intrinsic and extrinsic. This distribution closely resembles the experimental data obtained in [21]. The presence of correlated noise with a significant off-diagonal component indicates that gene expression in bacteria is influenced by both intrinsic and extrinsic fluctuations. Image based on [22], based on data from [21].

1.4 PHENOTYPIC DIVERSITY

Bacteria, due to their clonal reproduction, form isogenic populations of cells. However, even when grown in the same environment, genetically identical bacteria can exhibit strikingly different phenotypes. This individuality originates from stochastic gene expression. The enzymes responsible for transcribing DNA into mRNA (RNA polymerases) and translating mRNA into proteins (ribosomes) are present in finite copy numbers. Additionally, the biochemical reactions they catalyze are inherently stochastic. Since DNA is usually present in single or very few copies in bacteria, this stochasticity does not average out [22]. Consequently, the number of proteins can fluctuate significantly between bacteria with the same DNA.

The observation that gene expression fluctuates markedly between isogenic cells dates back to the 1950s when a pioneering study by Novick and Weiner showed that the production of the enzyme beta-galactosidase in individual *E. coli* cells was highly variable [23]. However, it took almost 50 years until Elowitz and colleagues explored the causes of stochastic gene expression in detail [21] (Figure 1.2). They introduced two copies of the same lac promoter—the activity of which Novick and Weiner were studying indirectly—into two loci nearly equidistant from the origin of replication of the *E. coli* chromosome, each driving the expression of a different fluorophore gene. The two fluorophores, YFP and CFP, have almost identical DNA sequences but significantly different spectral characteristics. Using this system, they measured the expression of each fluorophore using fluorescence microscopy and distinguished between extrinsic fluctuations (those affecting the expression of both gene copies equally, such as polymerase and ribosome copy numbers and cell cycle phase) and intrinsic fluctuations (those affecting each gene copy separately due to the randomness inherent to transcription and translation). They found that cells exhibited significant amounts of both extrinsic and intrinsic gene expression noise.

Phenotypic diversity due to gene expression noise is not necessarily a nuisance, however. In fact, it has become clear that, in some cases, bacteria can benefit from phenotypic diversity. This diversity allows bacteria to establish a subpopulation of cells that are not adapted to the present environment but are prepared for potential future environments. This diversification, often termed "bet-hedging," enables bacterial cells to rapidly adapt to various environments. An alternative survival strategy would involve cells sensing their environment and responding accordingly by reg-

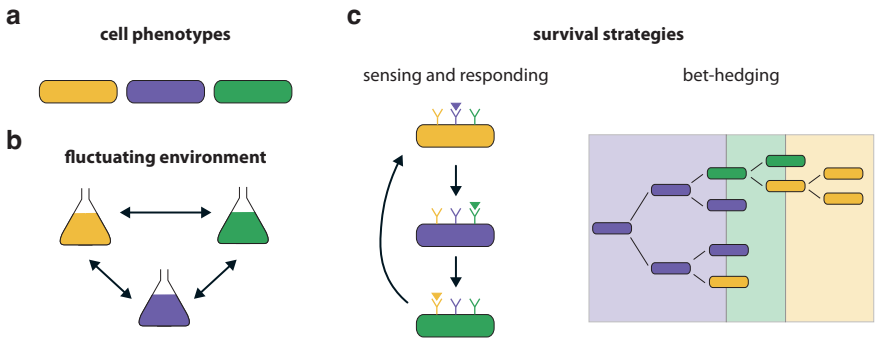

Figure 1.3: Contrasting survival strategies. (a) Clonal bacterial populations can exhibit diverse phenotypes, with each color representing a different phenotype. (b) The external environment of a bacterial population can change rapidly. Here, each color represents a different environment. The optimal phenotype for surviving in each environment has a color matching the environment color. (c) Two contrasting survival strategies. (Left) Cells employ a "sensing and responding" mechanism, where they detect their current environment through dedicated sensory pathways and express the necessary proteins to survive. (Right) Cells employ a "bet-hedging" strategy, where they assume diverse phenotypes due to gene expression noise, some of which are by chance already optimized for future environments. These cells can then repopulate the new environment. Bet-hedging does not require dedicated sensory pathways. Image based on [25].

ulating gene expression [24] [25] (Figure 1.3). However, such a “sensing and responding” approach would be slower than bet-hedging since it requires changes in gene expression and the evolution of unique signal transduction pathways for each potential environment. These factors render sensing and responding impractical for fast-changing or rare and unpredictable environments.

Bacteria have been shown to employ bet-hedging strategies in various contexts. A medically relevant example is bet-hedging used by bacteria to evade antibiotics. Heterogeneity in the growth rate of *E. coli* creates subpopulations of cells that grow much slower than average [26]. These “persisters,” linked to fluctuations in the expression of a single gene, are more resilient to antibiotic stress than normally growing cells. When the antibiotic treatment ends, these persisters can resume growth and repopulate the environment. However, the relevance of phenotypic diversity extends beyond survival under stress. It also, for example, plays a crucial role in ecological interactions. In microbial communities, diverse phenotypes can lead to niche differentiation, where different phenotypes exploit distinct ecological niches, reducing direct competition and promoting coexistence [27] [28]. More recently, it was shown that bacteria also perform sensory bet-hedging, to increase their chance of detecting new sources of ligand and therefore increase their overall chance of survival [29] [30] [31].

Chapters 3 to 5 of this thesis focus on different aspects of phenotypic diversity. In **Chapter 3**, we characterize the diversity of sensory phenotypes of *E. coli* cells grown in different environments and identify the molecular origins of this diversity. Furthermore, we show that diversity in the sensing phenotypes of bacteria can be beneficial for navigating environments where populations benefit from readiness to multiple possible sensory cues. In **Chapter 4**, we examine the effects of the cell-cycle phase on sensory diversity and study how phenotypes are inherited from mother to daughter cells, and how sensory diversity relaxes when the environment shifts. Finally, in **Chapter 5**, we demonstrate that bacteria migrating collectively can leverage the inherent diversity in tumble bias and chemoreceptor expression to rapidly and flexibly adapt their phenotypic composition to different environmental conditions.

2

SPONTANEOUS SWITCHING IN A PROTEIN SIGNALING ARRAY REVEALS NEAR-CRITICAL COOPERATIVITY

Dynamic properties of allosteric complexes are crucial for cellular information processing. However, direct observations of allosteric switches have been limited to compact molecular assemblies. In this Chapter, we report in vivo FRET measurements of spontaneous discrete-level fluctuations in the activity of an entire Escherichia coli chemosensory array — an extensive membrane-associated assembly comprising thousands of molecules. Finite-size scaling analysis of the temporal statistics by a two-dimensional conformational spread model revealed nearest-neighbor coupling strengths within 3% of the Ising second-order phase transition, indicating that chemosensory arrays are poised at criticality. Our analysis yields estimates for the intrinsic timescale of conformational changes (~ 10 ms) of allosteric units, illuminates the role of cooperativity in generating biologically relevant signal noise, and identifies near-critical tuning as a design principle for balancing the inherent tradeoff between response amplitude and response speed in higher-order signaling assemblies.

2.1 INTRODUCTION

Large protein assemblies at the heart of many cell signaling processes exhibit varying degrees of structural and dynamical order, from liquid-like granules [32, 33] to solid-like arrays [34–36]. Recent experiments are revealing how phase transitions leading to the formation of liquid-like assemblies — first-order transitions analogous to the condensation of gas into liquid — are used by cells to implement various information-processing tasks, such as signal initiation and confinement [37], kinetic proofreading [38], and noise control [39]. Theory also predicts that a different phase transition can occur within solid-like assemblies — a second-order transition analogous to the ordering of magnetic spins in a ferromagnet at low temperatures, arising from conformational interactions between protein subunits [40]. However, requirements for second-order phase transitions are more stringent than those for first-order transitions — they occur only at a special point in phase space, a critical point. It remains unclear if such second-order transitions occur in signaling assemblies and if so, how they constrain or contribute to the functional design of protein assemblies.

Recent structural studies are revealing an increasing number of solid-like signaling assemblies with a high degree of spatial order, where subunit proteins are arrayed in a regular pattern. The repertoire of such crystal-like assemblies reported to date is diverse in both form and function, and includes one-dimensional filament-like assemblies found in cellular homeostasis and inflammation signaling [41, 42], protein rings that mediate control of cell motility and apoptosis [43, 44], as well as two-dimensional arrays involved in chemosensing, neuromuscular control, and innate immune responses [45–48]. Yet, despite exciting advances in resolving the ultrastructure of these large assemblies, mechanistic design principles of their signaling function remain challenging to address experimentally. By contrast to compact oligomeric signaling complexes of fixed size, these extensive structures tend to assemble through open-ended polymerization and/or multivalent interactions, making them inherently variable in both size and composition [35]. The resulting polydispersity and stoichiometric diversity tend to mask their true signaling dynamics, as well as their size- and composition-dependence, both *in vivo* and *in vitro*. An ideal functional assay would therefore interrogate assembly-level dynamics *in singulo* — at the level of an individual assembly — but experimental realization has remained elusive.

2.2 RESULTS

2.2.1 SINGLE-CELL FRET REVEALS TWO-STATE SWITCHING FLUCTUATIONS IN THE ABSENCE OF SENSORY STIMULATION

Here we report *in vivo* FRET experiments that resolve this challenge for the chemosensory array of *Escherichia coli*, a canonical two-dimensional signaling assembly lining the cytoplasmic membrane, which allows motile bacteria to navigate chemical environments with exquisite sensitivity [28, 49, 50]. This higher-order assembly comprises thousands of receptor, kinase, and scaffolding molecules arranged in a well-defined lattice structure [51–53] and thus serves as a paradigm for signaling in two-dimensional protein assemblies. The *in vivo* signaling activity of chemosensory arrays are determined by the combined effects of sensory inputs to chemoreceptors and adaptation feedback via reversible covalent modifications (methylation/demethylation) of specific chemoreceptor residues. The array's activity output can be read out by an intermolecular FRET system [49] that reports on CheA kinase activity, the signaling output of arrays, by labeling two downstream proteins: the response regulator CheY, which receives phosphoryl groups from CheA, and its phosphatase CheZ, resulting in a signal that is proportional to kinase activity [49] (Fig. 2.1a). Our strategy leverages recent advances in extending this *in vivo* FRET technique to the single-cell level [54, 55], to achieve functional measurements of individual arrays within live cells. Imaging studies have revealed that the partitioning of chemoreceptors and associated proteins into arrays

is highly variable across cells, even within isogenic populations, with some cells possessing many small arrays while others have only one or a few large arrays [56, 57]. Thus, by searching for cells in which signaling is dominated by a single large array, we aimed to achieve *in singulo* measurements of functional array output.

To identify cells whose chemoreceptor population is concentrated into a single large array, we focused on fluctuations in kinase output that are observable by FRET at the single-cell level. Motile behavior of individual *E. coli* cells are known to be highly variable over time [58–60], and numerous studies have implicated a role for the adaptation enzymes CheR and CheB in generating this variability through stochasticity in their enzymatic activity [58, 61–63]. Recent single-cell FRET measurements confirmed strong temporal fluctuations of intracellular signaling activity [54, 55], but surprisingly, the largest temporal fluctuations were found in cells deleted for both CheR and CheB, and expressing only a single chemoreceptor species (out of five in wildtype *E. coli*). Strikingly, a subset of these cells demonstrated switch-like fluctuations between fully active and inactive states while the input ligand stimulus was held constant [54]. Two-level switching in whole-cell kinase activity is surprising because it implies synchronous switching of very large molecular populations — *E. coli* chemoreceptors and their associated kinases are expressed at a level of $\sim 10^3 - 10^4$ copies per cell [64]. A possible explanation is that these giant fluctuations are the result of intrinsic fluctuations within the chemosensory array. However, it is also possible that other factors, such as spurious fluctuations in the applied ligand signal, are driving synchronous switching of a larger number of otherwise independent signaling arrays.

We therefore began by testing whether two-level fluctuations occur in the absence of any external ligand stimulus. The aspartate receptor Tar in the absence of CheR and CheB has a steady-state activity bias $\langle a \rangle$ (defined as the activity relative to its maximum level) close to unity, and does not switch unless this bias is shifted down by chemoeffector ligands [54]. However, there are known genetic modifications of chemoreceptors that mimic the effects of methylation/demethylation by CheR/CheB, and can modify the chemoreceptor activity bias while maintaining otherwise normal signaling function [65]. To rule out possible ligand fluctuations as the driver of switching, we therefore tuned down the activity bias by expressing Tar in the QEEE covalent modification state by a single-residue replacement at one of four adaptation-modification residues (from QEQE in wildtype Tar), which yields an intermediate activity bias without the addition of chemoeffectors (see Supplementary Text, Fig. 2.2f) [65]. This allowed us to measure temporal fluctuations by single-cell FRET recordings in thousands of individual cells (Figs. 2.1b and 2.2a). In 204 of 1414 cells obtained from 19 FRET experiments, we observed switching between a high and low activity state (> 65% of transitions showing activity level changes of > 0.7). Spontaneous switching in the absence of exogenous ligands was not specific to Tar receptors, as we observed similar switching behavior (two-state switching in 548/4446 cells, across 44 experiments) in analogous experiments with Tsr-I214K, a single-residue replacement mutant of the serine receptor Tsr within its 'control cable' region [66] with a down-shifted activity bias similar to that of Tar [QEEE] (Figs. 2.1b, 2.2b, and 2.2f).

Spontaneous two-state switching is a hallmark of allosteric signaling complexes such as ion channels [67], but their observation requires measurements at the level of individual complexes; ensemble-averaged experiments can not resolve the switching dynamics because the timing of switching events is uncorrelated and thus switching dynamics are averaged out. To confirm whether the observed two-level switches indeed represent the behavior of single chemosensory arrays, we performed single-cell FRET experiments using an adapted protocol with reduced FRET-pair expression. The reduced cytoplasmic level of fluorescence in these experiments allowed detection of chemosensory arrays as intensity peaks of CheZ-YFP fluorescence, due to the well-established phenomenon [68, 69] of CheZ clustering at chemosensory arrays (Figs. 2.1c and 2.3), and the number of stable switching states could be determined through FRET experiments on the same

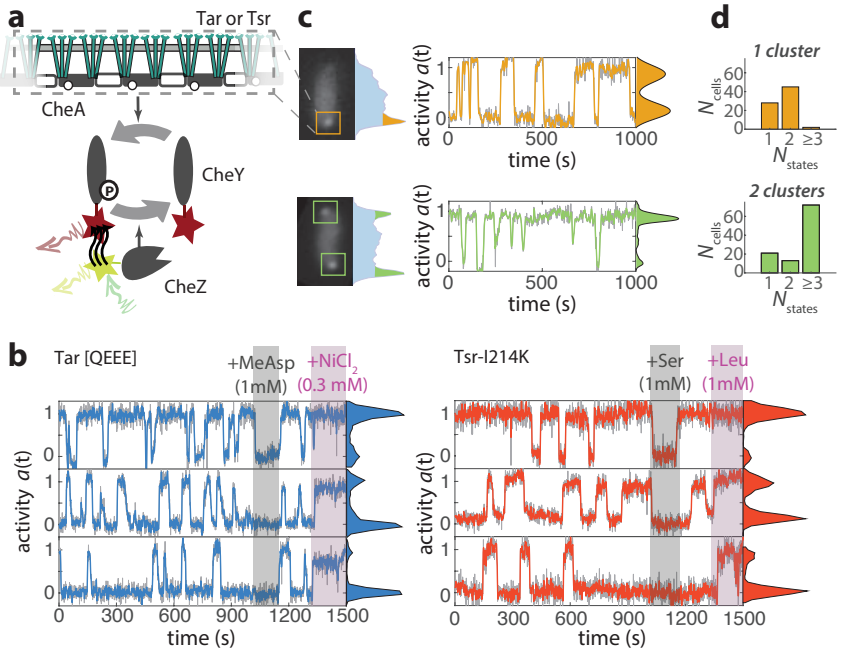

Figure 2.1: *In singulo* measurements of chemosensory array dynamics reveal two-state switching fluctuations in the absence of sensory stimulation. **(a)** Illustration of single-cell FRET assay to measure kinase activity [54] with schematic side-view of a membrane-associated chemosensory array (dashed box) of chemoreceptors (either Tar or Tsr). The kinase within the chemosensory array phosphorylates CheY (CheY-P), while CheZ dephosphorylates CheY. The FRET signal (black arrows) between fluorescently labeled CheZ and CheY, measured from the emitted fluorescent intensities (red and yellow arrows) is proportional to the activity of the chemosensory array. **(b)** Activity time series from single-cell FRET experiments that reveal two-state switching, of representative cells without adaptation enzymes expressing only the chemoreceptor Tar [QEEE] (left, blue) or the chemoreceptor Tsr-I214K (right, red). Cells are exposed to measurement buffer (MotM) for most of the experiment. To obtain the minimum and maximum FRET levels, cells are exposed to an attractant stimulus (Tar: 1 mM α−methylaspartate (MeAsp); Tsr: 1 mM L-serine (Ser)) and a repellent stimulus (Tar: 0.3 mM $NiCl_2$; Tsr: 1 mM L-leucine (Leu)). These levels were then used to normalize the activity time series of each cell between zero and unity. Example time series other than two state are shown in Fig. 2.2. **(c)** Chemosensory cluster organisation from CheZ localization (left) and corresponding activity time series (right, raw in gray, 6 s averaged– in color) and histograms (on right margin) of activity determined by FRET, for a representative cell expressing only chemoreceptor Tsr-I214K, with a single visible cluster exhibiting two-state switching (gold) and a representative cell with two visible clusters exhibiting multi-state switching (green). Additional time series and cluster organisation are shown in Fig. 2.3. **(d)** Histograms of the number of states in switching cells, for cells with one visible cluster (top, gold) and for cells with two visible clusters (green, bottom).

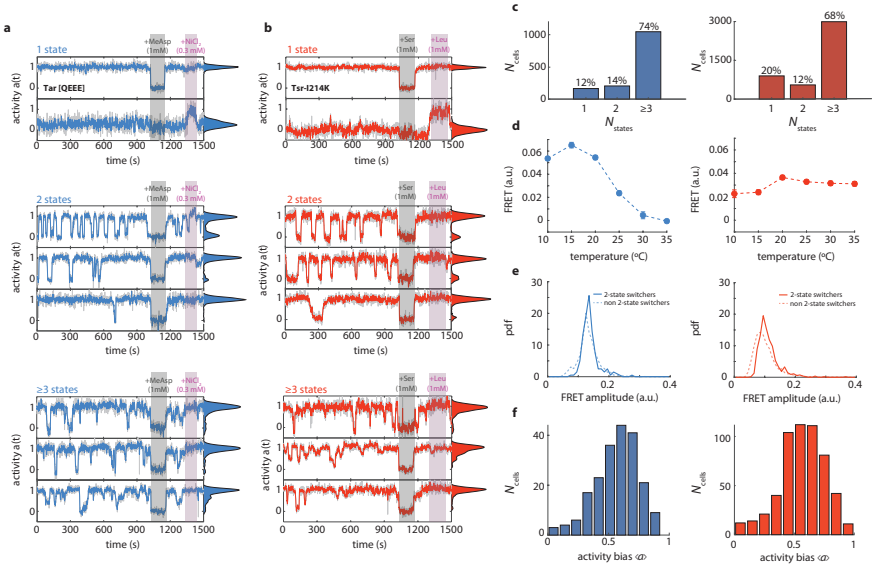

Figure 2.2: Classification of fluctuation phenotypes and temperature dependence in cells expressing chemoreceptors Tar or Tsr. **(a)** Activity time series of eight representative individual cells expressing only the chemoreceptor Tar [QEEE] without adaptation enzymes (pVS120/TSS1964). Temporal fluctuations during flow of measurement buffer are recorded prior to stimulation by saturating pulses of attractant (1 mM $\alpha-$methylaspartate; MeAsp) (gray) and repellent (0.3 mM $NiCl_2$) (pink). Cells with one, two, and three or more stable states are shown. On each raw time series (gray), a 3 s moving average filter was applied and the resulted time series are superimposed (blue), shown together with associated activity histograms of the filtered time series. **(b)** As in (a), but with cells expressing only Tsr-I214K in the same background (pPA114/TSS1964), and stimulated with an attractant stimulus of 1 mM L-Serine (Ser) and a repellent stimulus of 1 mM Leucine (Leu). **(c)** Histogram of number of states of total 1414 Tar [QEEE] cells (left, blue) and 4446 Tsr-I214K cells (right, red). **(d)** Temperature dependence of the steady-state FRET signal (population averaged) for cells expressing only Tar [QEEE] (left, blue) or Tsr-I214K (right, red). **(e)** Histograms of maximum FRET amplitude of 1414 cells expressing Tar [QEEE] (left, blue) and 4446 cells expressing Tsr-I214K (right, red). Cells exhibiting two-state switching behavior (solid lines) have approximately equal or higher maximum FRET signals (and hence kinase activity) compared to the rest of the cells (dashed lines), ruling out that switching cells have an anomalously low expression of chemoreceptor array components. **(f)** Histogram of activity bias $\langle a \rangle$ of cells exhibiting two-state switching behavior, for Tar [QEEE] (left, blue) and Tsr-I214K (right, red). Activity bias $\langle a \rangle$ is defined as the sum of all residence time intervals for active (up) state ($a \approx 1$) divided by the sum of all residence time intervals.

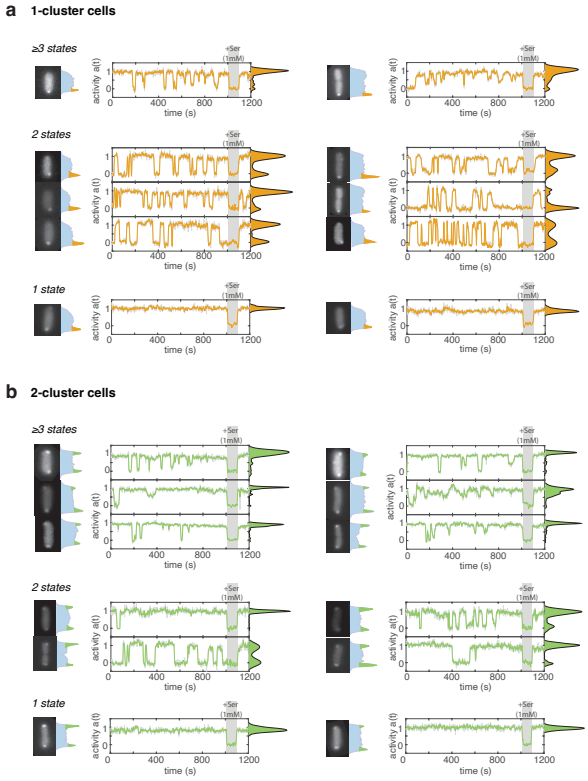

Figure 2.3: Further examples of fluctuation phenotypes of cells exhibiting one or two large CheZ-YFP clusters in experiments of Fig. 2.1c with reduced FRET-pair expression. **(a)** FRET time series of cells exhibiting one large Tsr-I214K receptor cluster and no adaptation enzymes (pPA114/TSS1964), shown alongside YFP-channel fluorescence images and intensity profile along the long axis of the cell. Cells demonstrating one, two, and three or more stable states are shown. In these experiments FRET pair expression was induced at lower levels than standard conditions (which are optimized for FRET photon budget), in order to decrease cytoplasmic levels of CheZ-YFP fluorescence and therefore allow detection of large chemosensory arrays through detection of CheZ-YFP clusters. Cells are exposed to measurement buffer and then to an attractant stimulus of 1 mM L-Serine (gray). On each raw time series (gray), a 6 s moving average filter was applied and the resulted time series are superimposed (orange), shown together with marginal histograms of the filtered activity time series. **(b)** As in (a), but for cells exhibiting two large Tsr-I214K receptor clusters. For histograms of classified fluctuation phenotypes, for both one-cluster and two-cluster cells, see Fig. 2.1.

individual cell (Fig. 2.1c). We found that cells that exhibited only a single detectable cluster predominantly demonstrated only one or two stable activity states, whereas cells with two clusters typically demonstrated three or more states (Figs. 2.1d and 2.3). These results support the idea that two-level FRET switching fluctuations reflect stochastic switching in the signaling state of a single dominant array.

We performed further tests to discriminate whether two-state switching is driven by intrinsic or extrinsic fluctuations. First, we ruled out that switching fluctuations are driven by ligands secreted by the cells themselves by tests on single-residue replacement mutants of the ligand binding pocket (residue 69) of both Tar [QEEE] and Tsr-I214K known to abolish ligand binding in both receptor types [70, 71]. Cells expressing these mutated receptors showed no response to their cognate ligands, as expected, but still exhibited switching behavior (Fig. 2.4). Array switching dynamics were unaffected by exogenously added pyruvate, a metabolic intermediate known to exhibit large temporal fluctuations in *E. coli* [72] (Fig. 2.5a), indicating that metabolic fluctuations are not the cause of the chemosensory array switching. Finally, cells expressing Tsr-F396Y, a single-residue replacement mutant defective in response cooperativity, demonstrated no switching behavior (Fig. 2.5b-d), indicating that the switching phenotype is linked to cooperativity within the array. Taken together, these observations suggest that two-state switching reflects a generic property of chemosensory arrays that is not specific to a single chemoreceptor species, and that it arises not from extrinsic fluctuations of ligand inputs or metabolism, but rather from intrinsic fluctuations that drive cooperative switching of thousands of molecules within a single large chemosensory array.

To consider the physical mechanism underlying this long-range cooperativity, we further dissected the temporal statistics of switching fluctuations (Fig. 2.6a) by extracting the time interval between switching events, hereafter called the residence time Δt_{up} and Δt_{down} for time spent in the up ($a \approx 1$) and down ($a \approx 0$) state, respectively, as well as the duration of the activity transient upon switching, hereafter called the transition time τ_+ and τ_- for upward and downward switches, respectively (Fig 2a, S4). We first interpreted these data as a barrier-crossing stochastic process in which the up and down states correspond to wells within an energy landscape (Fig. 2.6b), the shape of which could be approximated from the observed activity time series histograms with the free energy difference ΔG (in units of the thermal energy $k_B T$) between the up and down states determined by the activity bias $\langle a \rangle$ as $\Delta G = \ln[(1-\langle a \rangle)/\langle a \rangle]$. Consistent with this picture, we found that for both Tar [QEEE] and Tsr-I214K arrays, the residence time intervals between switching events (which occurred at a stable average frequency throughout the course of experiments; Fig. 2.7) were exponentially distributed across the full range of $\langle a \rangle$ (Fig. 2.6c), and the average residence time of each cell $\langle \Delta t_{\text{up/down}} \rangle$ as a function of ΔG was found to obey an Arrhenius-type exponential scaling $\langle \Delta t_{\text{up/down}} \rangle (\Delta G) = \tau_r e^{-\gamma_{\text{up/down}} \Delta G}$ (Fig. 2.6d), where τ_r is a characteristic residence timescale independent of the cell's activity bias and $\gamma_{\text{up/down}}$ are fitting constants. Thus, at the level of residence-time statistics, both Tar and Tsr arrays behave like a Brownian particle diffusing in a double-well potential along a "reaction coordinate" corresponding to the array's activity a [73]. From the crossings of the Arrhenius fit lines in Fig. 2.6d, we determined τ_r for both receptor species: $\tau_r^{\text{Tar}} = 47.0 \pm 1$ s and $\tau_r^{\text{Tsr}} = 65.5 \pm 1$ s.

2.2.2 TEMPORAL STATISTICS OF SWITCHING EVENTS ARE WELL DESCRIBED BY AN ISING MODEL

To investigate whether and how the observed temporal statistics could be explained by allosteric subunit interactions, we turned to theory. We used an Ising-type conformational spread model of allostery [74–76], which assumes that subunit conformations are coupled through nearest-neighbor interactions. The strength of these interactions is parameterized by a coupling energy J (promoting order) whose magnitude relative to $k_B T$ (promoting disorder) determines a finite spatial range (*i.e.*

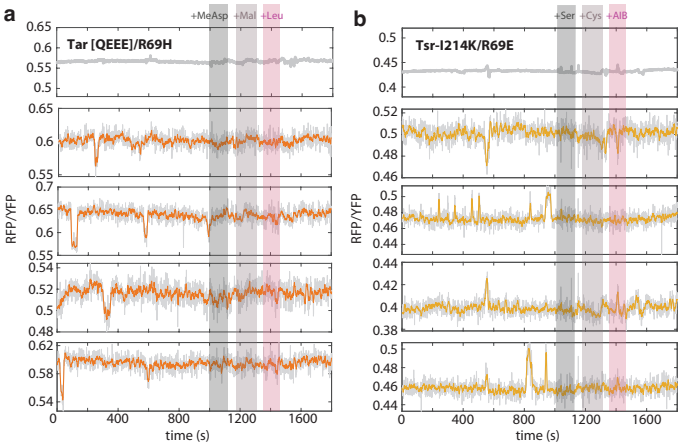

Figure 2.4: Switching behavior does not stem from ligand sensing. **(a)** FRET response from cells expressing only the receptor Tar [QEEE]/R69H, a double mutant receptor with impaired ligand binding sites, exposed to buffer or different chemoeffectors (shaded regions). The following saturating doses of chemoattractants were tested: MeAsp: 1 mM α−methylaspartate; Mal: 1 mM Maltose; Leu: 1 mM Leucine. Measurement at 25°C. Due to the absence of ligand binding, the minimum and maximum FRET levels (determined by adding attractant and repellent, respectively) cannot be extracted and thus FRET time series are shown in (non-normalized) raw RFP/YFP intensity units. Shown are the population-averaged response (top) and 4 example single-cell time series (red). On each raw single time series (gray), a 7 s moving average filter was applied and the resulting time series are superimposed (red). **(b)** FRET response from cells expressing only the receptor Tsr-I214K/R69E, a double mutant receptor with impaired ligand binding sites, exposed to buffer or different chemoeffectors (shaded regions). The following saturating doses of chemoattractants were tested: Ser: 1 mM L-Serine; Cys: 10 mM Cysteine; AIB: 10 mM α-aminoisobutyric acid. Measurement at 35°C. Shown are the population-averaged time series (top) with 4 example single-cell time series (yellow). On each raw time series (gray), a 7 s moving average filter was applied and the resulting time series are superimposed (yellow).

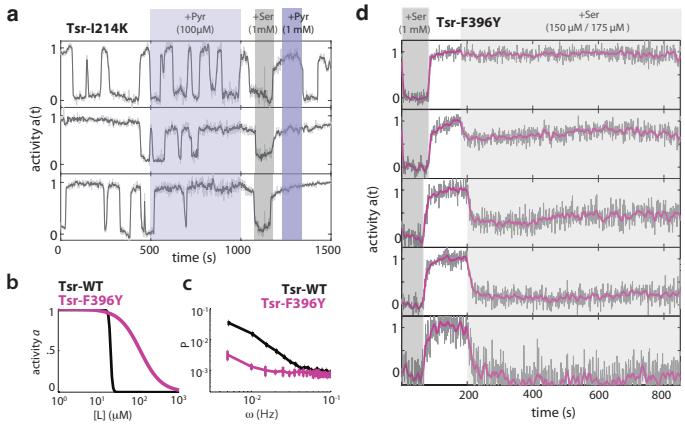

Figure 2.5: Switching behavior does not stem from metabolic fluctuations, but rather arises from cooperativity within the array. **(a)** Switching in the presence of pyruvate. Intracellular pyruvate levels have recently been shown to exhibit large fluctuations in *E.coli* [72]. Suppressing those fluctuations in cells expressing only the receptor Tsr-I214K by adding 100 M pyruvate (pink shaded region) did not interrupt switching; thus establishing that switching does not stem from such metabolic fluctuations. Pyruvate is not a chemoeffector, as evident by the absence of response to an 1 mM pyruvate stimulus (dark pink shaded region). **(b)** Hill curves illustrating the difference in cooperativity of the dose–response curves between wildtype Tsr (black) and Tsr-F396Y (purple) . The dose–response parameters are the average single-cell fit values obtained from single-cell FRET experiments on both genotypes in cells lacking other chemoreceptors and the adaptation enzymes (pPA114/TSS1964). **(c)** Power spectral density (PSD) estimates for temporal signal fluctuations from cells expressing wildtype Tsr and Tsr-F396Y . Shown are the average of the single-cell PSD estimates from a single experiment, error bars represent standard error of the mean (s.e.m.). **(d)** Example single-cell time series for a FRET experiment with cells expressing only Tsr-F396Y. At the start of the experiment, a saturating concentration ($[L]$ = 1mM, dark grey) is applied for a short time. After flushing buffer ($[L]$ = 0, white), an intermediate concentration ($[L]$ = 150–175 μM, light grey) is sustained for ~ 10 minutes. 5 representative single-cell time series, each normalized to its activity level before adding the first stimulus are shown. The top two curves are taken from an experiment (34 cells) responding to 150 μM, bottom three curves from a second experiment (49 cells) responding to 175 μM. To the unfiltered data (gray) a 10 s moving average filter is applied and superimposed (purple).

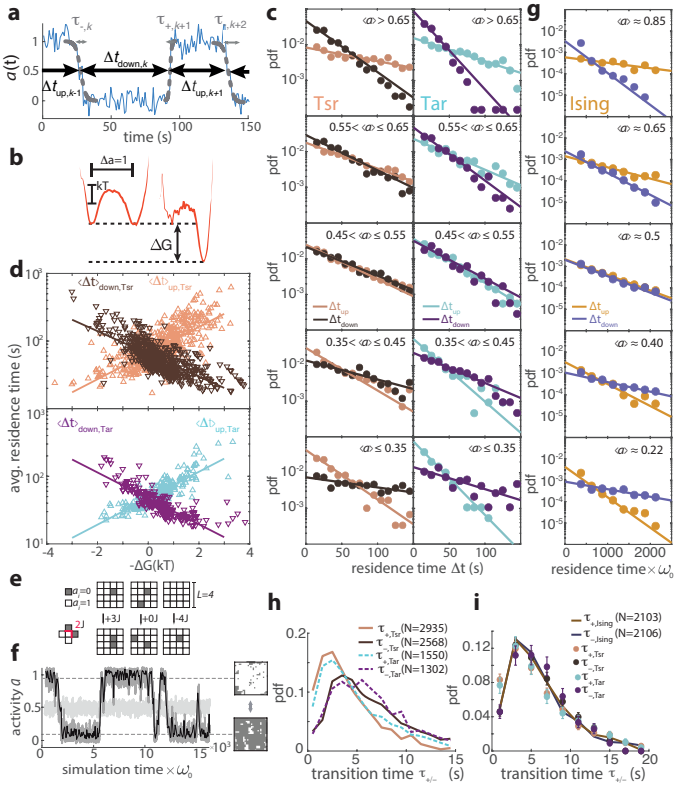

Figure 2.6: Temporal statistics of switching events are well described by an Ising-type conformational spread model. **(a)** Definitions of residence times $\Delta t_{\mathrm{up/down}}$ and transition times $\tau_{+/-}$, determined routinely for each switching event (see Materials and Methods). **(b)** Coarse-grained energy landscape along the array-activity coordinate a (estimated as the negative logarithm of the activity histogram) based on selected time series with $\langle a\rangle \approx 0.5$ (15 cells, left) and $\langle a\rangle \approx 0.9$ (12 cells, right) from cells expressing Tsr-I214K. **(c)** Histogram of residence times from experiments. Residence times for Tsr-I214K (left) and Tar [QEEE] (right), with each event sorted by activity bias of the corresponding cell (colors as in panel (d)). In each panel, data (points) are shown together with fits to single exponential functions (solid lines). Fit parameters and number of data points are shown in Tables 2.2 and 2.4. pdf: probability density function. **(d)** Mean residence times per cell as a function of the energy bias ΔG between the high and low activity state for all cells expressing Tsr-I214K (top) and Tar [QEEE] (bottom). Fit parameters and number of data points are shown in Table 2.6. **(e)** Conformational spread model of chemosensory array activity with size $L \times L$, in which each individual unit can switch between activity states of 1 (white) or 0 (dark). A difference in neighboring spins is associated with an energy cost of J, shown for three different transitions on a lattice with size $L = 4$ in the absence of external field ($H = 0$). **(f)** Example activity time series obtained by simulating dynamics on a strongly coupled ($L = 26$, $J = 0.4625\ k_{\mathrm{B}}T$, dark gray) and weakly coupled lattice ($L = 20$, $J = 0.2375\ k_{\mathrm{B}}T$, light gray). The strongly coupled lattice exhibits stochastic switches between two activity levels (dashed lines), with representative simulated array states for each activity level (right). The simulated time series was downsampled to approximate the experimental acquisition frequency (solid black line). **(g)** As in panel (c), but histograms of residence times from simulated time series with $L = 12$ and $J = 0.5\ k_{\mathrm{B}}T$, sorted by the activity bias generated by an applied external field H. Fit parameters and number of data points are shown in Table 2.9. **(h)** Histograms of switching events for Tsr-I214K (solid lines) and Tar [QEEE] (dashed lines). **(i)** Transition times from simulated two-state time series ($N = 12$, $J = 0.5\ k_{\mathrm{B}}T$, varying H). To approximate the experimental signal-to-noise ratio, gaussian white noise was added to the simulated time series (see Fig. 2.10). Experimental (points) and simulated (solid lines) histograms are scaled horizontally to have mean transition time of cells expressing Tsr, for comparison.

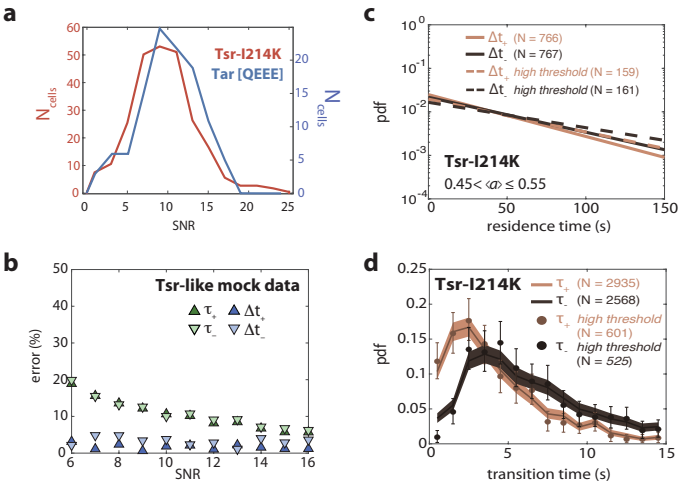

Figure 2.7: Effect of signal-to-noise ratio on switching statistics. **(a)** Signal-to-noise ratio (SNR) for two-state switching cells calculated as the maximum FRET response divided by the standard deviation of fluctuations in the FRET signal during attractant response. **(b)** Relative uncertainties for transition times τ and residence times Δt, based on analyzing mock two state time series with added Gaussian white noise. The simulated time series are based on the average transition and residence times measured for Tsr-I214K. **(c)** Dependence of extracted residence times on threshold choice. Solid lines: single exponential fit to residence times for Tsr-I214K for cells with $a \approx 0.5$. The selection parameter for two-state switching cells throughout this Chapter is that more than 65% of the cell's transitions exhibit activity level changes exceeding 70% of the full-scale amplitude. Increasing both thresholds to 80% only has a marginal effect on the fitted distribution (dashed lines). Increased thresholds yield the following average residence times: $\Delta t_{\mathrm{up}} = 62.40 \pm 3.73$ s (mean ± s.e.m.) and $\Delta t_{\mathrm{down}} = 63.26 \pm 3.36$ s. For comparison, regular thresholds yield: $\Delta t_{\mathrm{up}} = 60.37 \pm 1.84$ s and $\Delta t_{\mathrm{down}} = 59.61 \pm 1.68$ s. **(d)** Dependence of extracted transition times on threshold choice. Increased thresholds yield the following average transition times: $\tau_+ = 4.10 \pm 0.12$ s and $\tau_- = 6.07 \pm 0.15$ s. For comparison, regular thresholds yield: $\tau_+ = 4.29 \pm 0.06$ s and $\tau_- = 6.07 \pm 0.07$ s.

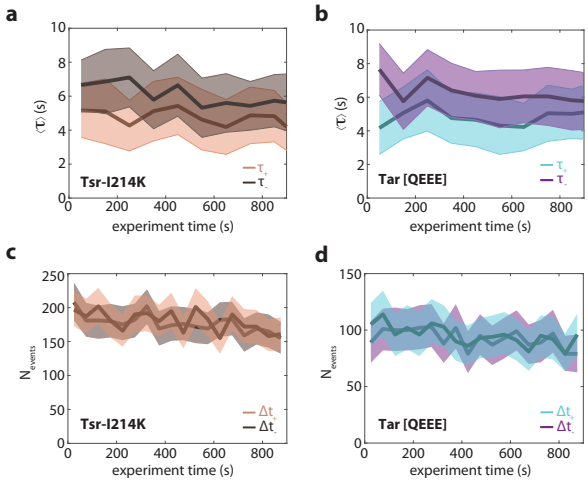

Figure 2.8: Effect of experimental parameters on switching statistics. **(a)** Mean upwards (orange) and downwards (brown) transition times for switching events plotted as a function of their incidence time, for cells expressing Tsr-I214K. Error bars represent standard deviation. Mean transition times are stable throughout the duration of each experiment. **(b)** Mean upwards (turqoise) and downwards (purple) transition times for switching events plotted as a function of their incidence time, for cells expressing Tar[QEEE]. **(c)** Number of upwards (orange) and downwards (brown) switching events with respect to their incidence time, for cells expressing Tsr-I214K. Shaded areas represent 95% confidence intervals obtained through bootstrap resampling. The frequency of transitions is constant throughout the duration of each experiment. **(d)** Number of upwards (turquoise) and downwards (purple) switching events with respect to their incidence time, for cells expressing Tar[QEEE].

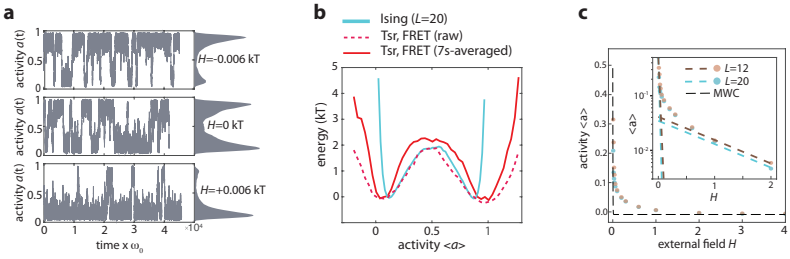

Figure 2.9: Influence of external biasing field H on conformational-spread (Ising) model. **(a)** Example time series and histograms from simulations of the conformational spread model with $L = 20$, coupling energy J = 0.475 $k_B T$, and external field as indicated. **(b)** Energy landscape based on 8 simulation runs as shown in panel (a) with $H = 0$, calculated as $-\log$ of the histogram (cyan line). For comparison, the energy landscape based on the experimental FRET time series on Tsr-I214K is superimposed, both for the raw time series (red dashed line) as well as data processed with a 7 s moving average filter (red solid line; see Fig. 2.6b). **(c)** Array activity $\langle a \rangle$ as a function of a biasing field H, for two different Ising lattices (blue: $L = 20$, $J = 0.4875$ and brown: $L = 12$, $J = 0.50$). The response was determined by measuring the mean activity after applying a field H to 192 independent runs of randomly initialized lattices with $a(t = 0) \approx 0.5$. Also shown is the field dependence of a Monod-Wyman-Changeux (MWC) lattice of $L = 20$, the strongly coupled limit of the conformational spread model. Inset: $\langle a \rangle$ on a logarithmic activity axis. The dashed lines (brown: $L = 12$, cyan: $L = 20$) indicate the activity scaling based on the slope $d \log \langle a \rangle / dH$ around $\langle a \rangle = 0.5$ and the expected scaling for a single lattice unit for large H: $d \log \langle a \rangle / dH = -1$. See section 2.2.7 in the Supplementary Text for a detailed explanation regarding the scaling parameters.

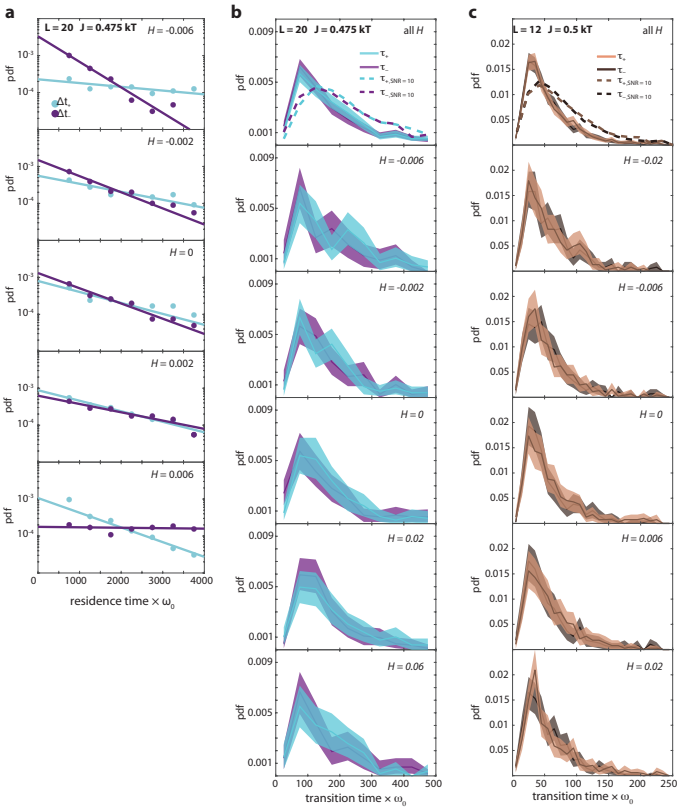

Figure 2.10: Transition time distributions obtained from numerical simulations using a conformational spread model. **(a)** Residence time events from Ising simulations with a lattice size L of 20 by 20 spins with a coupling energy of J = 0.475 $k_B T$, together with exponential fits to the data (dashed lines). Each event is sorted by the bias H of the external field. See Fig. 2.6g for residence time distributions with a lattice size L of 12 by 12 spins and coupling energy of J = 0.5 $k_B T$. **(b)** Histograms of transition time events from Ising simulations with a lattice size L of 20 by 20 spins and coupling energy of J = 0.475 $k_B T$. Each event is sorted by the bias H of the external field. Shaded areas represent 95% confidence intervals obtained through bootstrap resampling. N represents the number of transition events. **(c)** As in (b), but from Ising simulations with a lattice size L of 12 by 12 spins and a coupling energy of J = 0.5 $k_B T$. Similar to the experiments, the average transition times do not depend on the activity bias (here caused by an external field). The Ising lattice sizes and coupling energies were chosen in both cases to recapitulate the ratio of the residence over transition times determined experimentally for Tsr.

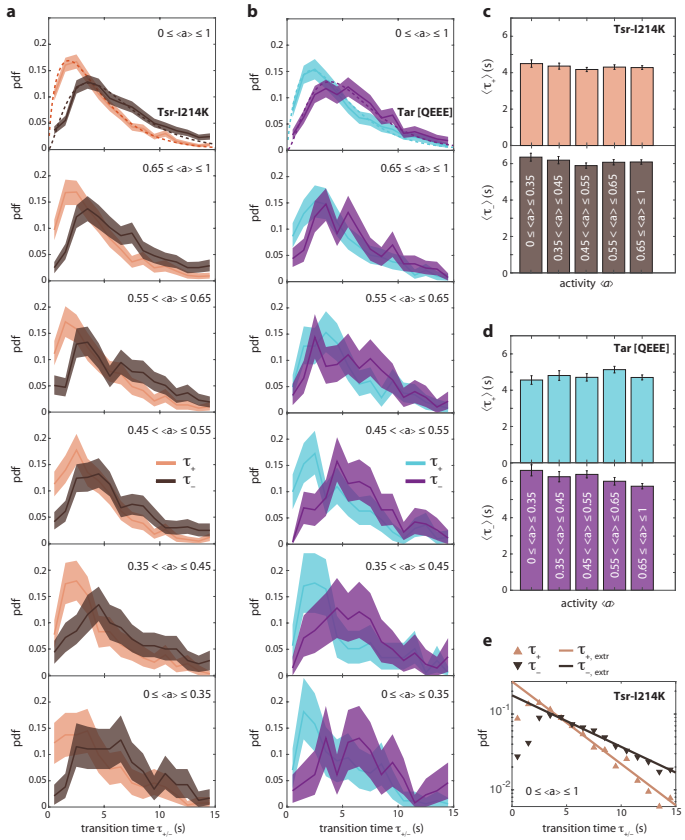

Figure 2.11: Experimental transition times do not depend on cellular activity bias, and are robust against possible undersampling bias. **(a)** Histograms of transition time events across 549 cells expressing Tsr-I214K with each event sorted by the activity bias of the corresponding cell. Shaded areas represent 95% confidence intervals obtained through bootstrap resampling. Dashed lines: gamma distribution fits with the following parameters: upwards transition: $\alpha = 1.72$ and $\beta = 2.5$; downwards transition: $\alpha = 2.45$ and $\beta = 2.48$. **(b)** As in (a), but with 204 cells expressing Tar [QEEE]. Gamma distribution fit parameters: upwards transition: $\alpha = 1.87$ and $\beta = 2.57$; downwards transition: $\alpha = 2.74$ and $\beta = 2.2$. **(c)** Histograms of mean transition time per activity bias for cells expressing Tsr-I214K; (top) mean upwards transition time, (bottom) mean downwards transition time. Error bars represent standard error of the mean. Mean upwards and downwards transition times are independent of the activity bias. **(d)** As in (c), but for cells expressing Tar [QEEE]. **(e)** Analysis of possible undersampling bias due to finite acquisition rate (1 s^{-1}). Extrapolation of the transition time distributions for cells expressing Tsr-I214K for the extreme case where the true shape of the distribution follows an exponential distribution instead of a gamma distribution. Exponential fits yield the following extrapolated transition times: $\tau_+ = 3.72$s and $\tau_- = 5.67$ s, which fall within 15 percent of the measured values of $\tau_+ = 4.29$ s and $\tau_- = 6.07$ s.

a correlation length) over which action at one site can affect distant sites. By varying J, therefore, the model can represent allosteric systems along a continuous scale of conformational disorder, including that of the more widely used Monod-Wyman-Changeux (MWC) model (which is recovered upon taking the fully ordered limit $J \to \infty$). Importantly for signaling function, two-dimensional Ising models are known to exhibit a second-order phase transition as a function of J, with a spontaneous ordering of subunit conformations above a critical coupling energy J^*. Although, to date, strong experimental support for conformational spread models has been obtained in one-dimensional protein rings [77, 78], Ising models exhibit a critical point only in two or higher dimensions, and the implications of the Ising second-order transition in two-dimensional protein assemblies remain untested experimentally.

We performed kinetic Monte Carlo simulations on an $L \times L$ lattice of allosteric units with free boundary conditions, each of which can flip between two conformational states, active ($a = 1$) or inactive ($a = 0$) (Fig. 2.6e and Materials and Methods). The flipping rate of the unit at site i was modified from a fundamental flipping frequency ω_0 by the influence of its nearest neighbors ($j \in 1, \ldots, N_j$, where N_j is the number of nearest neighbors) through the coupling energy J (in units of $k_B T$) as $\omega = \omega_0 e^{-J(2a_i - 1)\sum_j (2a_j - 1)}$, corresponding to an Ising model in which each active-inactive bond on the lattice contributes an energy penalty of J (see Materials and Methods). At low coupling strength ($J \ll J^*$), each unit switches independently and the total activity of the array demonstrates only small fluctuations about its mean value at $\langle a \rangle = 1/2$ (Fig. 2.6e). However, as the coupling energy is increased toward its critical value J^*, the correlation length approaches the finite size of the array, generating a double well potential and the arrays exhibit switching events between fully active and fully inactive states (Figs. 2.3f and 2.9a,b). We analyzed the temporal activity statistics of a simulated array with parameters within this two-state switching regime ($J = 0.5\ k_B T$, $L = 12$), with various values of a weak biasing field H_b that modifies the flipping rate by a factor $e^{H_b(a-1/2)}$ (see Materials and Methods; for the field dependence of the switching phenotype, see Fig. 2.9c and Supplementary Text), to approximate the diverse FRET activity biases observed across individual cells in the population (Fig. 2.2f). Simulated residence time distributions (Figs. 2.6g and 2.9c) were in excellent agreement with their experimental counterparts (Fig. 2.6c), recapitulating at each activity bias their characteristic exponential shape.

By contrast, the measured transition time distributions had peaked profiles for both Tar and Tsr arrays (Fig. 2.6h). The average downward transition time $\langle \tau_- \rangle$ and the average upward transition time $\langle \tau_+ \rangle$ were similar between Tar and Tsr arrays, with $\langle \tau_- \rangle$ slightly greater than $\langle \tau_+ \rangle$ in both cases ($\langle \tau_+^{\mathrm{Tsr}} \rangle = 4.29 \pm 0.06$ s, $\langle \tau_-^{\mathrm{Tsr}} \rangle = 6.07 \pm 0.07$ s, $\langle \tau_+^{\mathrm{Tar}} \rangle = 4.79 \pm 0.08$ s and $\langle \tau_-^{\mathrm{Tar}} \rangle = 6.06 \pm 0.09$ s; mean ± s.e.m.). Remarkably, however, when normalized by these mean values, all measured time distributions collapsed onto a common profile that, in turn, was in excellent agreement with its simulated counterparts (Fig. 2.6i). Furthermore, both measured and simulated transition-time statistics demonstrated no dependency on the activity bias (Fig. 2.10b,c and 2.11). Collectively, the high degree of quantitative agreement between these measured and simulated temporal statistics suggest that an Ising-type conformational spread model with a near-critical coupling strength ($J \approx J^*$) provides an excellent approximation to chemoreceptor array dynamics.

2.2.3 SWITCHING STATISTICS REVEAL NEAR-CRITICAL ALLOSTERIC COOPERATIVITY OF CHEMOSENSORY ARRAYS

We sought to quantify the degree to which both Tar and Tsr arrays are close to criticality. The behavior of Ising-type models near criticality depends strongly on the system size L, a phenomenon known as finite-size scaling [79]. We identified as a key experimental observable the ratio $\langle \Delta t \rangle / \langle \tau \rangle$ between the residence and transition timescales (see Supplementary Text). Simulations at various values of J indeed revealed a strong dependence of $\langle \Delta t \rangle / \langle \tau \rangle$ on L (Fig. 2.12a), with all results

collapsing onto a single curve defined by the finite-size scaling relation $\frac{\Delta t}{\tau} \sim L^{(z-b)} \exp(c_0 \epsilon L)$, where z, b, c_0 are scaling constants and $\epsilon = \left|J - J^*\right| / J^*$ is a "reduced temperature" providing a dimensionless measure of the (energetic) distance to criticality [80, 81] (see Supplementary Text and Fig. 2.13 for determination of the scaling constants). Because different combinations of J and L can yield the same value of ϵL, this scaling does not allow unique determination of J from the measured $\langle \Delta t \rangle / \langle \tau \rangle$ (Figs. 2.12a and 2.14). However, finite-size scaling theory predicts that the critical coupling energy J^*, separating the highly ordered (polarized) and disordered (non-polarized) regimes, also depends on the system size L [82, 83]. Consistent with this prediction, a phase diagram on the J-L plane constructed from simulations showed that the boundary between polarized (Fig. 2.12b, gray region) and non-polarized (Fig. 2.12b, blue region) dynamics coincided well with the theoretically predicted scaling (Fig. 2.12b, gold curve) $J_L^* \approx J_\infty^* (1 - bL^{-1})^{-1}$, where $J_\infty^* \approx 0.44\ k_B T$ is the critical coupling energy in the thermodynamic limit ($L \to \infty$) and b is a boundary condition-dependent constant ($b = 1.25$ for free boundary conditions; see Supplementary Text). Interestingly, we found that iso-lines corresponding to L-J combinations of constant $\langle \Delta t \rangle / \langle \tau \rangle$ (Fig. 32.12b, beaded curves) were nearly parallel with the profile of J_L^*. Dividing out J_L^* from the iso-lines corresponding to the measured $\langle \Delta t \rangle / \langle \tau \rangle$ values of Tar ($\langle \Delta t \rangle / \langle \tau \rangle \approx 8$; blue in Fig. 2.12b) and Tsr ($\langle \Delta t \rangle / \langle \tau \rangle \approx 12$; red in Fig. 2.12b) revealed remarkable confinement of the coupling energy for both Tar and Tsr to within ±3% of J_L^* across a broad range in L (Fig. 2.12b, Inset). Thus, despite uncertainty in the array size L, finite-size scaling analysis of the observed temporal statistics strongly suggests that both Tar and Tsr arrays are poised very close to the Ising critical point.

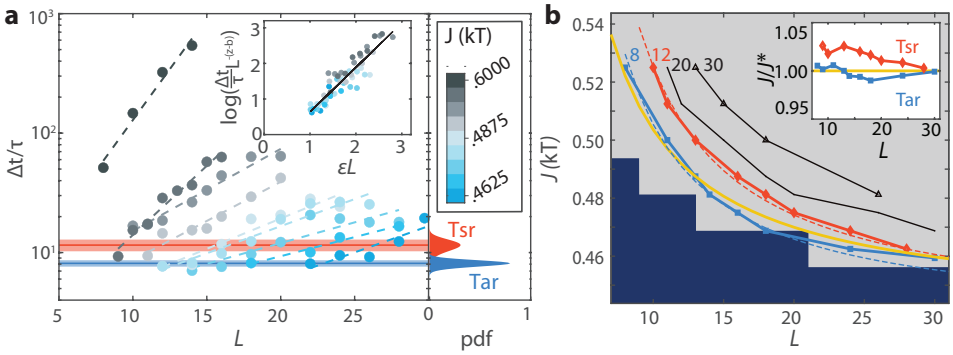

Figure 2.12: Finite-size scaling analysis of switching statistics reveals near-critical allosteric cooperativity of chemosensory arrays. **(a)** (left) Switching timescale ratio $\langle \Delta t \rangle / \langle \tau \rangle$ for various values of the coupling energy J (blue to black) as a function of lattice size L (circles), with exponential fits (dashed lines). Inset shows data collapse for the near-critical region ($J < 0.6\ k_B T$), upon rescaling by factors $\epsilon = \left|J - J^*\right| / J^*$ and $L^{-(z-b)}$ according to finite-size scaling theory (see Fig. 2.18 for determination of scaling parameters). (right margin) Estimated distribution (see Fig. 2.19) of the switching timescale ratio $\langle \Delta t \rangle / \langle \tau \rangle$ across cells, for Tsr-I214K (red) or Tar [QEEE] (blue). **(b)** Phase-diagram of switching behavior as in the L–J plane. Parameter value pairs generated polarized (gray region) and non-polarized (dark blue region) fluctuations as estimated from the peak-valley ratio of the time series histograms. Iso-lines of similar switching timescale ratios, as indicated, were constructed from the simulations (beaded colored and black curves). Theoretical finite-size scaling predictions for the critical coupling energy J_L^* [83] (gold curve) and the switching time ratios (dashed lines, see Table 2.11 for fit parameters) are superimposed. Inset: Switching timescale ratio iso-lines for Tar (blue) and Tsr (red), normalized by the finite size scaling of the critical coupling energy J^* reveals values within 3% of the critical energy.

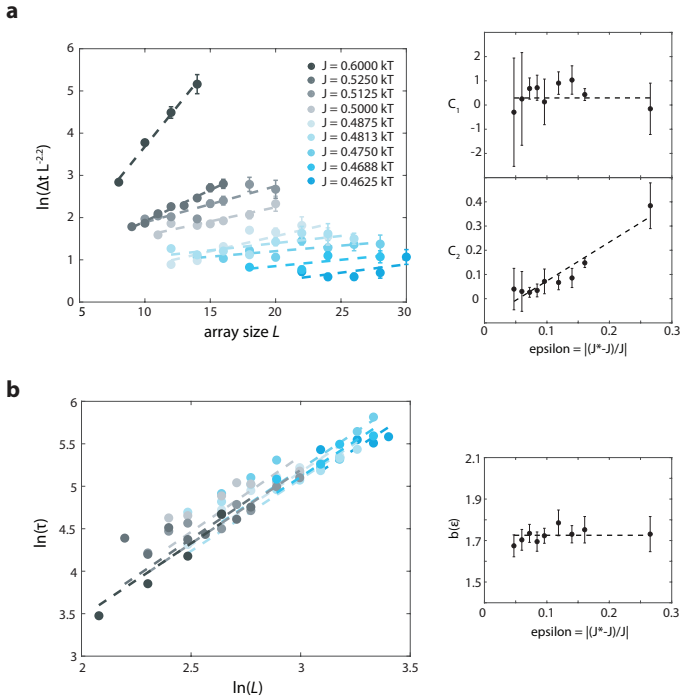

Figure 2.13: Mean residence and transition times as a function of lattice size obtained from numerical simulations of the conformational spread (Ising) model. **(a)** (Left) mean residence times as a function of array size L, scaled according to equation S6. Dashed lines are fits of a function of the form $c_1 + c_2 L$ to the data and colors indicate different coupling energies (the same color scheme is used throughout the figure). Error bars represent standard error of the mean. (Right) scaling of the fitting parameters c_1 and c_2 as a function of the energy level ϵ. **(b)** (Left) Logarithm of mean transition times as a function of the logarithm of the array size L. Dashed lines are fits of the linear form $\ln(\tau) = b(\epsilon)\ln(L)$; (right) Fitted values of $b(\epsilon)$ demonstrated nearly no dependence on ϵ, and hence in our scaling analysis we treated the exponent b as fixed parameter that is independent of ϵ.

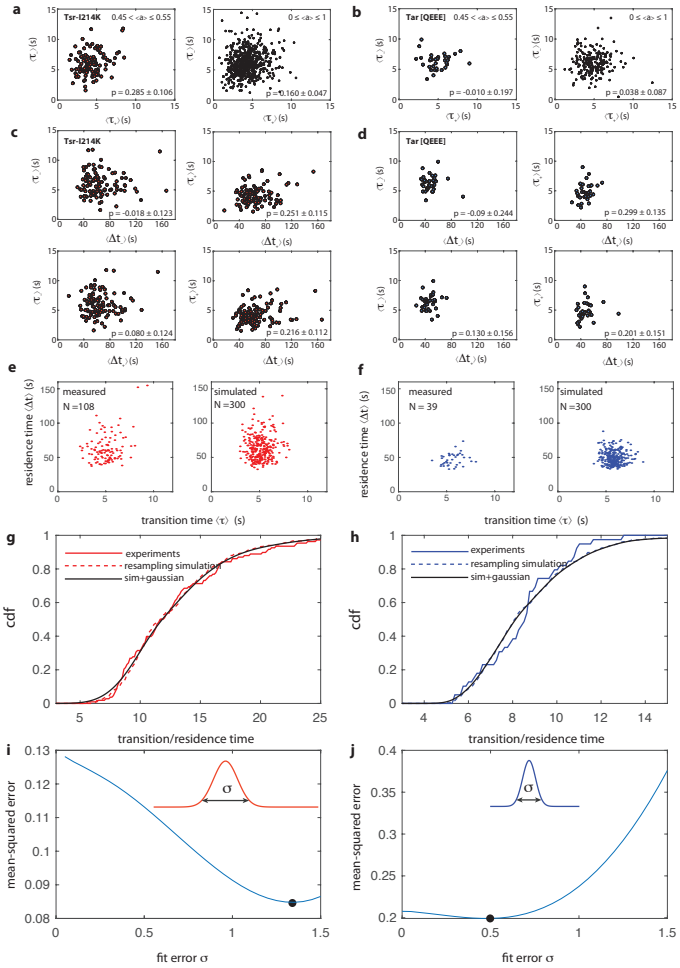

Figure 2.14: Apparent correlations among switching timescale parameters and convolution-based estimation of true variation in residence/transition time ratio. **(a)** Correlations between upwards and downwards transition times for cells expressing Tsr-I214K (red points). Error margins in Pearson correlation coefficients are 95% confidence intervals obtained through bootstrap resampling. **(b)** as in (a) but for cells expressing Tar [QEEE] (blue points). **(c)** Correlations between transition and residence times for cells that have an intermediate activity bias and express Tsr-I214K (red points). Error margins in Pearson correlation coefficients are 95% confidence intervals obtained through bootstrap resampling. Only small strength of association is observed between these switching parameters. **(d)** as in (c) but for cells expressing Tar [QEEE] (blue points). **(e)** Measured transition time vs residence time for (Left) 108 cells expressing Tsr-I214K from FRET experiments, with activity $0.45 \leq \langle a \rangle \leq 0.55$, and (Right) for 300 simulated cells. For each simulated cell, residence times and transition times were drawn respectively from an exponential and gamma distribution with parameters extracted from the experiments (Figs. 2.6 and 2.11), where the sum of residence times was limited to the experimental duration (1000 s). The variation in the simulation represents the sampling error that is observed without variation in parameters between cells. **(f)** As in (e) but for cells expressing Tar [QEEE]. **(g)** The cumulative density function (cdf) for the distribution of transition/residence time ratio per cell in experiments (solid red line) and in the simulated data (dashed line). The simulated cdf (sampling noise) was convolved with a Gaussian pdf (cell–cell variation in ratio) with variance σ^2, representing true cell–cell variation in timescale ratio, and superimposed on the curve (black line, $\sigma = 1.3$.) **(h)** As in (b) but then for cells expressing Tar [QEEE] ($\sigma = 0.5$). **(i)** Mean squared error (mse) between the convolved cdf (resampling cdf $*$ gaussian pdf) and the experimental cdf, as a function of the standard deviation σ. The value of σ that minimizes the mse represents the cell–cell variation in timescale ratio that best describes the experimentally observed variation. **(j)** As in (i) but for cells expressing Tar [QEEE].

2.2.4 SWITCHING STATISTICS REVEAL FUNDAMENTAL FLIPPING TIMESCALE OF CHEMOSENSORY ARRAYS

Finite-size scaling analysis also allowed us to estimate from the observed residence and transition times the fundamental flipping timescale $1/\omega_0$ of allosteric units as a function of L (see Supplementary Text), and this dependence was very similar for both Tar and Tsr (Fig. 2.15). Although our FRET measurements do not provide a direct estimate of L, we can motivate approximate upper and lower bounds based on structural and biochemical findings in the literature. Cryo-EM studies have revealed the detailed ultrastructure of bacterial chemosensory arrays [52, 53, 84], revealing an extended regular arrangement (Fig. 2.15) of 'core units', the smallest complex of array components that has shown kinase activity *in vitro* [85] and *in vivo* [86], consisting of one CheA kinase dimer, two CheW scaffolding protein monomers and two trimers of chemoreceptor dimers. Expression data under defined growth conditions [64] suggest an approximate number of 1000 core units per cell, close in number to a lattice of size $L \times L = 30 \times 30$, which we take as an approximate upper bound. However, it is also possible that the fundamental unit of cooperativity is an even larger complex than the core units. For example, taking instead the repeating unit cell of the array structure's p6 symmetry group (Fig. 2.15) as the allosteric unit leads to ≈ 300 repeating units per cell, or approximately $L \times L = 17 \times 17$, which we take as an approximate lower bound. With these approximate limits, our scaling analysis yields a flipping timescale of individual allosteric units in the range $1/\omega_0 \approx$ 15-35 ms (Fig. 2.15). The importance of protein structural dynamics for function is increasingly recognized [87], but estimates of the transition timescales are usually obtained via *in vitro* measurements [88–90] or molecular dynamics simulations [91], and span an enormously wide range (from picoseconds to milliseconds). Our *in vivo* estimate for the chemoreceptor array allosteric unit lies near the upper extreme of that range, perhaps reflecting the large size of allosteric units (even the core unit, the smaller of the two limits considered here, contains 16 protein monomers).

2.2.5 NEAR-CRITICAL COOPERATIVITY ALLOWS FOR LARGE RESPONSE AMPLITUDES WITHOUT COMPROMISING RESPONSE SPEED

Why are chemosensory arrays poised so close to criticality? Previous theoretical studies have shown that signal amplification due to coupling within Ising-type conformational spread models comes at the cost of prolonged response times [92, 93]. Avoiding excessive response slow down is crucial because control of chemotactic behavior depends on making temporal comparisons during run-and-tumble navigation [94–96]. To address the influence of receptor coupling on response times to external stimuli, we simulated the dynamic response of arrays with $L = 20$ after an applied step stimulus (implemented within the model by an external ligand field H_L that modifies the flipping rate by a factor $e^{H_L(1-2a)}$; see Materials and Methods) favoring the inactive conformation to mimic the effect of attractant chemoeffector stimulation, and repeatedly (N=4–10) measured the response time as well as the response amplitude for various combinations of J and H_L (Fig. 2.16a). For every stimulus size H_L, increasing the coupling strength J led to a decrease in the response speed (defined as the inverse of response time) but an increase in response amplitude, indicating a tradeoff (Figs. 2.16a and 2.16c). The profile of these H_L-isolines are interesting when viewed as a Pareto front [97] for navigating the tradeoff, having a convex shape with a knee above which response speed drops off sharply. Remarkably, the critical coupling energy ($J = J^*$; Fig. 2.16b, gold curve) traverses this knee at every stimulus size, indicating that near-critical cooperativity allows balancing of these two response objectives, allowing for large response amplitudes without drastically compromising response speed.

However despite this balancing, these simulation results suggest that for weaker stimuli ($H <$ 0.2 in Fig. 2.16b), response speeds of near-critical arrays can still drop well below the typical *E. coli* tumble frequency of ~1 s^{-1} (Fig. 2.16b, dashed line) — too slow to effectively bias the

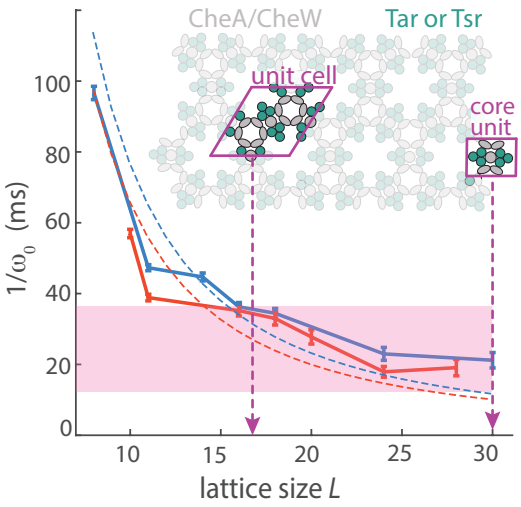

Figure 2.15: Estimation of the intrinsic fluctuation timescale of allosteric units. Fundamental transition timescale $1/\omega_0$ of allosteric units, plotted as a function of the assumed array size, L, for Tar (blue) or Tsr (red) arrays, based on simulations calibrated by experimentally observed residence- and transition-times (solid lines), shown together with the expected dependence based on finite-sized scaling theory (dashed blue and red lines; see Supplementary Text). Two possible fundamental units of cooperativity in the bacterial chemosensory array are highlighted within a schematic top view of chemosensory arrays: 'core unit' consisting of a CheA kinase dimer, two CheW monomers, and two trimers of chemoreceptor dimers (purple rectangle) and the repeating unit cell of the array, consisting of one full core unit and four half core units (purple parallelogram). Each chemosensory array contains approximately 1000 core units or 300 repeating unit cells, leading to lower and upper limits of array size (purple lines). Using these as lower and upper limits yield a timescale range $1/\omega_0 \approx$15–35 ms (shaded area).

cells' random walk. We tested this prediction experimentally by ligand stimulation of Tsr arrays with a sub-saturating dose of the chemoeffector serine. Adaptation-deficient cells expressing Tsr as the sole chemoreceptor exhibited response time courses remarkably similar to those of near-critical array simulations (Fig. 2.16a, Inset) — a long yet variable delay (~30 s on average) followed by an abrupt, switch-like decay to zero (Fig. 2.17) — thereby confirming critical slowing of response. This is surprising because wildtype cells are known to respond much faster, on a timescale of order ~100 ms [98, 99], and suggests they possess some additional mechanism to prevent otherwise deleterious slowing of response. The salient genotypic difference is that wildtype possess both an intact adaptation system and a more diverse chemoreceptor population (potentially mixing all five chemoreceptor species within arrays). Of these two differences, mixing of chemoreceptor species within chemosensory arrays is known to attenuate cooperativity [100] and hence might alleviate wildtype chemoreceptor arrays of deleterious slowing. However, while FRET experiments on adaptation-deficient cells expressing the wildtype chemoreceptor complement indicated that receptor mixing does partly remedy slowdown, response times for subsaturating stimuli still substantially exceeded the run/tumble timescale (by up to ~13 fold, depending on conditions) (Fig. 2.17, Supplementary Text), suggesting a key role for adaptation feedback in further mitigating critical slowing.

How is it possible that the adaptation system, which provides negative feedback through covalent modification of chemoreceptors on a ~ 10 s timescale, can accelerate the ligand-induced array response prior to adaptation? The covalent modifications throughout the array amount to a source of spatial disorder [101], which can limit the extent (correlation length) of cooperative interactions within the array [75, 102]. To test the impact of such feedback-induced disorder on array response dynamics, we modified our simulations to include adaptation feedback (Fig. 2.16c), implemented as a stochastic modulation of a local field on each allosteric unit that counteracts the activity of that unit (Methods). These simulations with feedback-induced disorder also demonstrate a speed-amplitude trade-off (Fig. 2.16d), but the response slowdown at high values of J leads to a decrease in response amplitude due to the loss of timescale separation between the initial response and subsequent adaptation. Importantly, the disorder-induced reduction in the extent of cooperativity (Fig. 2.18a) strongly attenuates response slowdown and near-critical ($J \approx J^*$) coupling (Fig. 2.16d, gold curve) achieves response speeds faster than the typical tumble frequency (Fig. 2.16d, dashed line) for all stimulus magnitudes while maintaining substantial signal amplification.

We therefore conclude that in wildtype cells, the combined effects of receptor-species mixing and sensory adaptation mitigate critical slowing down that could otherwise be deleterious, and also transform the binary switching behavior of near-critical arrays into continuous fluctuations (Fig. 2.18b-e). It has been shown that *E. coli* can exploit such signal fluctuations to enhance its exploratory propensity in the absence of environmental signals by driving a Lévy- rather than a Brownian-type random walk [58–60, 103]. Chemosensory array activity in wildtype cells exhibited large noise amplitudes of up to $\eta = 0.95$ (Fig. 2.18f). These fluctuation amplitudes exceed by more than two fold previous theoretical predictions of models that did not account for near-critical cooperativity of arrays [58, 61–63, 65]. Thus, in addition to balancing the speed-amplitude tradeoff, near-critical cooperativity affects environmental exploration of wildtype *E. coli* cells by augmenting steady-state signal noise that promotes exploratory behavior.

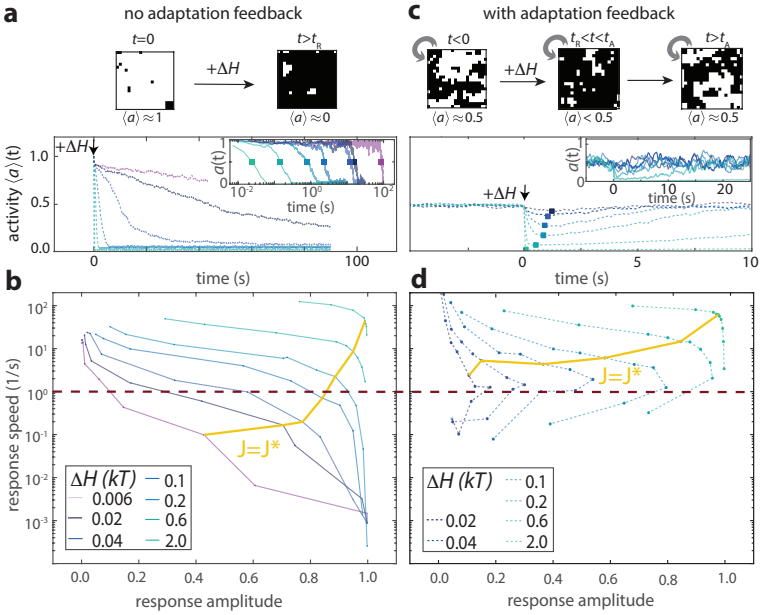

Figure 2.16: Consequences of near-critical cooperativity in chemosensory arrays with and without adaptation feedback. **(a)** (top) Without adaptation feedback, near-critical cooperativity extends the range of cooperativity across the entire array, leading to all-or-none response. Shown are example states (binary squares) of an array initialized in the all-active ($\langle a\rangle \approx 1$) state at time $t = 0$ when a positive external field ($\Delta H > 0$, mimicking chemoattractant addition) was applied, and at a later time $t > t_R$ exceeding the response time t_R of the array. (bottom) Simulated response time series (dashed curves) of activity bias $\langle a\rangle(t)$, computed by averaging 48 stochastic trajectories of a 20x20 array without adaptation feedback and $J = 0.52$, for various values of added external field ΔH (see panel **(b)** for color code), initialized at $\langle a\rangle \approx 1$ and assuming $1/\omega_0 = 30$ ms (from Fig. 2.15). Inset: Example single-array stochastic trajectories (solid curves), which invariably demonstrate all-or-none switch-like response. Colored rectangles illustrate the definition of the response time t_R as the average time of crossing half-maximal activity, $a = 0.5$ (colored rectangle). The response amplitude is defined as $1 - \langle a\rangle(J, \Delta H)/0.5$. **(b)** Speed-amplitude trade-off in array responses without adaptation feedback. For each stimulus size ΔH (see legend for color code), a thin curve indicates the dependence of response amplitude and speed on the coupling energy J. Thick gold curve is the critical iso-line tracing out points on each thin curve corresponding to $J = J^*$. Horizontal dashed line represents the speed required to respond within a typical run time (1 s) of *E. coli* [104], corresponding to an approximate lower bound for effective run-tumble chemotaxis. **(c)** (top) Adaptation feedback injects spatial disorder within the array that limits the extent of cooperativity and stabilizes intermediate activity states. Shown are example array states (binary squares) in the presence of adaptation feedback (indicated by gray arrows), before stimulus ($t < 0$), just after response ($t_R < t < t_A$) and following sensory adaptation ($t > t_A$), each with corresponding activity bias $\langle a\rangle$. (bottom) Simulated response time series (dashed curves) of activity bias $\langle a\rangle(t)$, computed by averaging 96 stochastic trajectories of a 20x20 array with adaptation feedback and $J = 0.52$, for various values of added external field ΔH (see panel (d) for color code), initialized at $\langle a\rangle \approx 0.5$ and assuming $1/\omega_0 = 30$ ms (from Fig. 2.15). The response time and amplitude are determined from an exponential fit to the averaged activity time series (colored rectangles). Inset: Example single-array stochastic trajectories (solid curves), smoothed with a 7 s moving average filter to aid visual inspection. **(d)** As in panel (b), but for speed-amplitude trade-off in array responses with adaptation feedback. Note that response slowdown is mitigated compared to non-adapting arrays, and speed of near-critical arrays (thick gold curve) remains above the lower-bound response speed set by the run-and-tumble behavior timescale (horizontal dashed line) across all stimulus sizes.

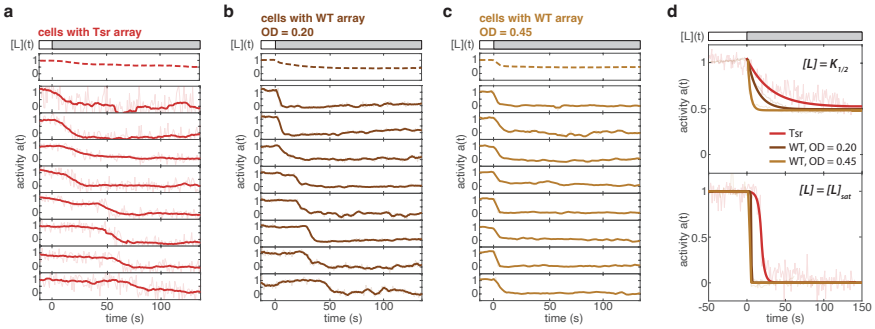

Figure 2.17: Experimental observation of critical slowing down of sub-saturatligand response, and its attenuation by mixing of receptor species. **(a)** (Top) Stimulation protocol. Cells are exposed to measurement buffer (white) and at t = 0, a sub-saturating L-Serine stimulus corresponding to their $K_{1/2}$ is applied. (Top panel) Population-averaged time series of 41 adaptation-deficient cells expressing WT Tsr as their sole chemoreceptor (pPA114/TSS1964), responding to an L-Serine stimulus of 20 M (dashed line, time series is low-pass filtered with a time window of 20 s). (Bottom panels) Single-cell time series of 8 representative cells (light red) superimposed with a low-pass filtered time series with a time window of 20 s (dark red). **(b)** Same as in (a), but for adaptation-deficient cells expressing all 5 chemoreceptor species (TSS58) and harvested at low optical density (OD = 0.20), where their receptor clusters are primarily comprised of Tsr. Cells are stimulated with a sub-saturating L-Serine stimulus of 35 M. Population-averaged time series (dashed line, time series is low-pass filtered with a time window of 5 s) is comprised of 78 cells and single-cell time series are superimposed with a low-pass filtered time series with a time window of 5 s. **(c)** Same as in (a), but for cells harvested at an intermediate optical density (OD = 0.45) where their receptor clusters are primarily comprised of Tar. Cells are stimulated with a sub-saturating L-Serine stimulus of 50 M. Population-averaged time series (dashed line, time series is low-pass filtered with a time window of 5 s) is comprised of 81 cells and single-cell time series are superimposed with a low-pass filtered time series with a time window of 5 s. **(d)** (Top) Exponential fits to the population-averaged responses to their respective $K_{1/2}$ concentrations of L-Serine. Fits yield response times of: 30.29 s (Tsr), 13.14 s (WT, OD = 0.20), and 3.4 s (WT, OD = 0.45). (Bottom) Sigmoidal fits to the population averaged responses to saturating stimuli. Stimuli are 10 mM L-Serine for cells expressing WT Tsr and 1 mM L-Serine for cells expressing all chemoreceptor species. Fits yield response times of: 6.82 s (Tsr), 0.61 s (WT, OD = 0.20), and 0.21 s (WT, OD = 0.45). The ligand exchange profile of the flowcell was measured using a fluorescent dye, and a sigmodial fit to the data yielded an exchange time of 4.27 s.

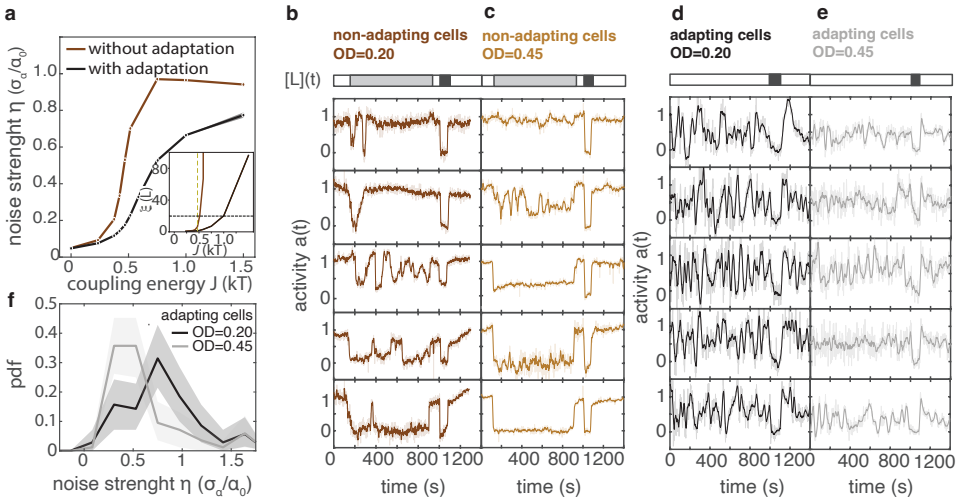

Figure 2.18: Steady-state noise is enhanced by near-critical cooperativity and attenuated by both adaptation feedback and receptor species mixing. **(a)** Noise strength η in the Ising model as a function of the coupling energy J. The average value of η is depicted, obtained by measuring the standard deviation in array activity from simulation runs with $L = 20$, for both with (192 runs) and without (48 runs) adaptation. For each value of J, adaptation feedback decreases the noise strength. Inset: correlation length ξ as a function of coupling energy J, computed as the average value of ξ across 48 independent array states for each value of J. The correlation length ξ increases with J, thereby increasing the noise strength. However, as the correlation length ξ of the lattice size increases, the fluctuations become fully binary resulting in the saturation of the noise strength η at a noise plateau. **(b)** (Top) Stimulus protocol for L-serine concentration. At the start of the experiment, cells are exposed to buffer (white) and at t = 100 s a sub-saturating stimulus corresponding to their $K_{1/2}$ is sustained (35 M L-Serine; gray). Towards the end of the experiment, cells are exposed to saturating stimulus for normalization (1 mM L-Serine; dark gray). (Bottom) Representative activity time series of adaptation-deficient cells expressing all 5 chemoreceptor species (TSS58), harvested at low optical density (OD = 0.20) where their receptor clusters are primarily comprised of Tsr (light brown) superimposed with a low-pass filtered time series with a time window of 5 s (dark brown). **(c)** Same as in (a), but for cells harvested at an intermediate optical density (OD = 0.45) where their receptor clusters are primarily comprised of Tar. Cells are stimulated with a sub-saturating L-Serine stimulus of 50 M and a saturating stimulus of 1 mM. **(d)** (Top) Stimulus protocol for ligand concentration. Cells are exposed to buffer (white) and towards the end of the experiment, a pulse of saturating stimulus is delivered (1 mM L-Serine and 1 mM MeAsp; dark gray). (Bottom) Representative activity time series of adapting cells expressing all 5 chemoreceptor species (VS115), harvested at low optical density (OD = 0.20) where their receptor clusters are primarily comprised of Tsr. **(e)** Same as in (c), but for cells harvested at an intermediate optical density (OD = 0.45) where their receptor clusters are primarily comprised of Tar. **(f)** Histograms of noise strength of adapting cells expressing all 5 chemoreceptor species harvested at OD = 0.20 (76 cells; black) and OD = 0.45 (87 cells; gray). Fluctuation amplitudes are extracted by calculating the standard deviation of a low-pass filtered time series over a 10 s window divided by the mean FRET level of a single cell. Shaded areas represent 95% confidence intervals obtained through bootstrap resampling.

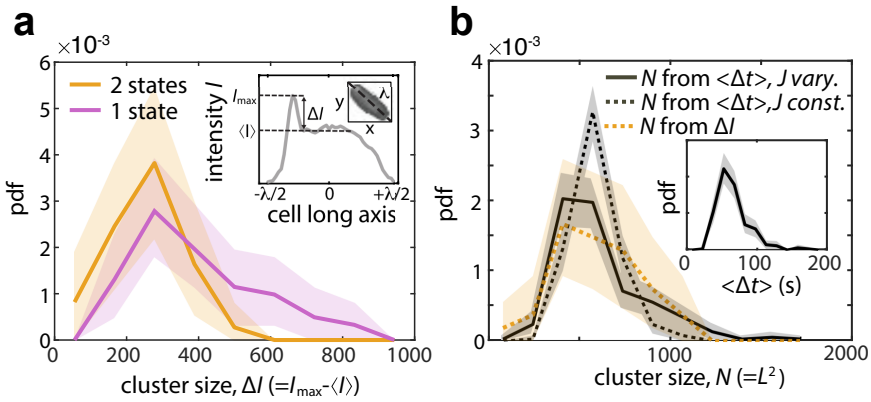

Figure 2.19: Comparison of cell-to-cell variability in measured cluster size and array size inferred from switching statistics. **(a)** Distribution of chemosensory cluster size, determined by CheZ-YFP fluorescence intensity, in 33 cells exhibiting a single Tsr-I214K cluster and demonstrating two-state switching ("2-states", solid yellow curve) and 55 cells exhibiting a single Tsr-I214K cluster but demonstrating no switching ("1-state", solid purple curve). Consistent with the experiments presented in Fig. 2.1c,d and Fig. 2.3, clusters were rendered detectable by lowering FRET plasmid induction below that in our standard FRET protocol to decrease cytoplasmic fluorescence and thereby allow visualization of CheZ-YFP localization. Consistent with expectations from the finite-size Ising model (in which switching events become increasingly rare for larger array sizes L at a given coupling energy J), the average cluster size of cells exhibiting no switching (mean ± s.e.m. = 388 ± 23) is significantly larger than the average cluster size of cells exhibiting two-state switching (mean ± s.e.m. = 250 ± 17). A two-sample Kolmogorov-Smirnov test indicates that these two distributions are statistically significantly distinct, with $p = 0.0041$. Inset illustrates the method used for determining the cluster size. Cluster size is defined as the difference ΔI between the maximum CheZ-YFP intensity $I_{\max}$ along the long axis of each cell of length λ and its average intensity $\langle I \rangle$; see Section 2.4.4 for details. **(b)** Distribution of the array size inferred from cell-to-cell variation in two-state switching temporal statistics, compared against the measured cluster-size distribution of two-state switching cells of panel **a** (dashed yellow curve). Inferred array sizes were calculated in two ways (see Supplementary Text Section 2.5.8). First, by using the finite-size scaling relation (Eqn. S15) to transform the distribution of the average two-state switching residence times $\langle \Delta t \rangle$ per cell (inset), assuming J co-varies with L such that the timescale ratio remains constant, as in Fig. 2.12b (solid curve: mean ± s.d. = 608 ± 251). Second, as in the first method but assuming J remains constant at $J = 0.426\ k_B T$, close to J^*_∞. (dashed dark curve: mean ± s.d. = 593 ± 130). The inset shows the average two-state switching residence times $\langle \Delta t \rangle$ of 116 cells expressing Tsr-I214K and with a near-zero activity bias (corresponding to data points falling within the range $-0.25 k_B T \leq -\Delta G \leq 0.25 k_B T$ in Fig. 2.6d, upper panel). To enable proportional comparison, the cluster intensity is linearly scaled to match the average of the means of the two distributions of $N = L^2$. Shaded areas in all plots represent 97.5% confidence intervals obtained through bootstrap resampling.

2.3 DISCUSSION

A compelling open question is how *E. coli* chemoreceptor arrays achieve the observed near-critical cooperativity. The strength of conformational interactions in canonical allosteric oligomers such as hemoglobin are usually assumed to be determined by their tertiary structure, which is in turn encoded by their amino acid sequence. On the one hand, it is possible that the conformational coupling strength J is similarly "hard-coded" at the level of protein structures within bacterial chemoreceptor arrays, which would imply tuning through natural selection over evolutionary timescales. On the other hand, J (and/or L) might be physiologically regulated. In principle, these two possibilities could be distinguishable by the temporal statistics of switching, but current limits on achievable *in vivo* single-cell FRET experiment duration preclude resolution through this approach (Fig. 2.19 and Supplementary Text). A more promising approach for future single-cell FRET studies would involve directly testing potential regulatory mechanisms, such as modulation of the expression level of scaffolding protein CheW, which has recently been shown to affect both the array composition and apparent response cooperativity at the population level [105]. An increasing number of biological systems involving many components, from protein sequences [106] to cellular membranes [107], as well as communication between cells [18, 108] and even whole organisms [109, 110], have been reported to self-organize into narrow zones of phase space close to a critical point, on the boundary between order and disorder [111]. Our finding that bacterial chemoreceptor arrays are poised close to the Ising critical point reveals near-critical cooperativity as a design principle for balancing competing response objectives in large allosteric signaling assemblies. While we have here shown that nearly all features of switching temporal statistics can be explained within the framework of the canonical equilibrium Ising model, it has not escaped our attention that the single feature not captured by our equilibrium Ising modeling, namely asymmetry in the transition times for the up- and down-directions of activity switching (Fig. 2.6h), suggests a breaking of time-reversal symmetry — a hallmark of nonequilibrium dynamics. Interestingly, our finite-size scaling estimate (Fig. 2.15) of the fundamental allosteric transition timescale ω_0^{-1} ($\approx$ 15-35 ms) is close to the timescale of CheA autophosphorylation [112], which operates out of equilibrium by hydrolyzing ATP. It is therefore plausible that in chemosensory arrays, the dynamics of allosteric cooperativity are driven by an underlying nonequilibrium process involving CheA. Indeed, recent theoretical studies [113, 114] indicate that the switching statistics observed in our experiments point to near-critical allosteric cooperativity also when the Ising framework is generalized to include CheA-driven nonequilibrium effects. Given the many spatially extended arrays being discovered across cell biology [35, 36, 47, 48] as well as their anticipated role in synthetic biology [115], we envisage that our approach of exploiting *in vivo* fluctuation signatures of such assemblies to understand their function could find use across a wide range of systems.

2.4 METHODS

2.4.1 CELL CULTURE AND GROWTH MEDIA

All spontaneous switching experiments were performed with TSS1964 [54], a receptorless non-adapting derivative of *E. coli* K-12 RP437 (HCB33) expressing adhesive FliC flagellar elements that immobilizes them on glass surfaces. Chemoreceptor mutants were expressed and induced as listed in Table 2.1. CheZ-YFP and CheY-mRFP were expressed in tandem from pSJAB106 [54] using 50 μM IPTG for Tar [QEEE] and Tsr-F396Y, and 100 μM IPTG for Tsr-I214K. For experiments were CheZ localization was used to visualise chemoreceptor clusters, IPTG induction was lowered to 15 μM for Tsr-I214K. For experiments, cells were grown in Tryptone Broth ('TB':10 g/L bacto-tryptone, 5g/L NaCl) at 33.5 $^\circ$C with shaking, from a saturated overnight culture in TB, with 100 μg/mL ampicillin and 34 μg/ml chloramphenicol in both cultures and appropriate inducers in the day culture. Unless otherwise specified, cells were harvested at optical density 0.46 - 0.47, then washed once with and

thereafter placed in motility media ('MotM': 10 mM KPO_4, 0.1 mM EDTA, 1 μM L-methionine, 10 mM lactic acid, pH 7.0). Because of auxotrophic limitation of *E. coli* RP437, growth and protein expression are arrested in MotM [116]. Cells were incubated at room temperature for 1.5 hours, before imaging, to allow for fluorescent protein maturation.

Table 2.1: Plasmids used in this study to express various chemoreceptor alleles.

Product	Vector	Induction	Resistance	Source
Tar [QEEE]	pLC113	2.0 μM NaSal	Cam	[100]
Tar [QEEE]/R69H	pLC113	2.0 μM NaSal	Cam	This Study
Tsr-WT	pPA114	0.6 μM NaSal	Cam	[117]
Tsr-I214K	pPA114	0.6 μM NaSal	Cam	[66]
Tsr-I214K/R69E	pPA114	0.6 μM NaSal	Cam	This Study
Tsr-F396Y	pPA114	0.6 μM NaSal	Cam	[118]

2.4.2 FRET MICROSCOPY

Single-cell FRET microscopy was performed as reported previously [54]. For each experiment, cells were immobilized on a glass coverslip were placed in a flow cell under continuous flow (400 μL/min) established by a syringe pump (Harvard Apparatus PHD 2000, USA). The sample was illuminated every second with an LED system (CoolLED pE-2, UK) through a 40x 1.30 NA oil objective (Nikon, JP) for 17 ms using an upright microscope (Nikon FN1, JP). Epifluorescent light was sent through an optical splitting device (Cairn Research OptoSplit II, UK) in combination with a 580 nm dichroic mirror (Semrock, USA) and two emission band-pass filters (527/42 nm and 641/75 nm; Semrock, USA) to project the emitted donor and acceptor channels in parallel on the sensor of an EM-CCD camera (Princeton Instruments proEM 512, USA), set with a multiplication gain of 100.

The flow cell temperature was controlled through a custom-built stage heater, based on a water-cooled thermoelectric Peltier element controlled through a PID controller (T = 18 °C for Tsr-I214K, T = 25 °C for Tar [QEEE]). The activity bias depended on temperature [119], therefore we controlled the temperature to keep the average activity bias close to 1/2, at which we found the number of switchers to be maximum (Fig. 2.2d). The buffer solution temperature was controlled through a heat bath with heating and cooling capacity (Grant Instruments LT ecocool 100, UK). Experiments involving WT Tsr, Tsr-F396Y, or mixed receptor clusters were performed at room temperature.

In experiments where the receptor clusters were imaged in conjunction with FRET microscopy, an inverted microscope (Nikon Eclipse Ti-E, JP), equipped with a 100x 1.45 NA oil objective (Nikon, JP), was utilized. For FRET microscopy, the sample was illuminated every 2 seconds with an LED system (CoolLED pE-4000, UK) for 20 ms. Epifluorescent light was directed into a 2-camera image splitter (Cairn Research TwinCam, UK) equipped with a 580 nm dichroic mirror (Semrock, USA) and two emission filters (520 nm and 593 nm; Semrock, USA), leading to two identical sCMOS cameras (Hamamatsu ORCA-Flash4.0 V2, JP), where the emitted donor and acceptor channels were projected separately. To enhance their signal-to-noise ratio, FRET images were binned by a factor of 4x4 pixels. In order to visualize large chemoreceptor clusters resulting from CheZ-YFP localization near the chemoreceptors, the sample was imaged once at the beginning and end of each experiment for 200 ms using the same optical path as in FRET microscopy. CheZ-YFP images were not binned to preserve all spatial information. Receptor cluster imaging experiments were performed at room temperature.

2.4.3 FRET ANALYSIS

Analysis of the fluorescent timeseries were performed essentially as reported previously [54]. After drift correction using rigid stack registration [120] in ImageJ, Images were segmented using the Mahotas python library [54, 121] to obtain single-cell donor ($D(t)$) and acceptor ($A(t)$) fluorescence intensity time series. Afterwards, intensity time series were corrected for bleaching by dividing out an exponential decay. The FRET time series were calculated from the ratio of acceptor and donor emissions $R(t) = A(t)/D(t)$ as [49, 54]:

$$\mathrm{FRET}(t) = \frac{R(t) - R_0}{R(t) + \alpha} \tag{2.1}$$

where the R_0 is the ratio during a large and saturating attractant stimulus (e.g. the ratio in the absence of any FRET [49]) and $\alpha = 0.3$ is a constant depending on FRET measurement setup and the specific FRET donor-acceptor pair used [54].

This intermolecular FRET signal [49] measures the concentration of the CheY-CheZ complex [Yp-Z] formed during dephosphorylation, which is limited by the rate of kinase autophosphorylation [49]. Hence, the FRET signal is proportional to kinase activity [119]:

$$\mathrm{FRET} \propto [\text{Yp-Z}] = a\frac{k_A}{k_Z}[\text{CheA}] \approx a\frac{k_A}{k_Z}[\text{CheA}]_\mathrm{T} \tag{2.2}$$

where [CheA] is the concentration of kinases and a the activity per kinase.

To compute kinase activity, each ratiometric FRET time series was normalized to the maximum FRET level measured by a saturating repellent stimulus: $a(t) = \mathrm{FRET(t)}/\mathrm{FRET}_{max}$

We ruled out that two-state switching cells have an anomalously low expression of chemoreceptor array components, by confirming that the maximum amplitude of the CheY-CheZ FRET signal, proportional to the amount of receptor-kinase complex (Eqn. 2.2), was comparable between switching and non-switching cells (Fig. 2.2e).

2.4.4 CLUSTER INTENSITY ANALYSIS

The CheY phosphatase, CheZ, is recruited to chemoreceptor arrays by binding to the short form of CheA, $\mathrm{CheA_S}$. Because this binding affinity is high, resulting in a long exchange time ($\equiv$ 10 mins), comparable to that of CheA within arrays [122], and insensitive to array activity [123], the CheZ-YFP fluorescence intensity can be used as a proxy for receptor cluster size. In a typical FRET experiment, the CheY-RFP/CheZ-YFP FRET pair is overexpressed to increase the FRET signal-to-noise ratio, causing background fluorescence to obscure the fluorescent foci corresponding to receptor clusters. However, once the induction of the FRET plasmid is lowered sufficiently, fluorescent foci become visible via traditional widefield microscopy (Fig. 2.3) in the expanse of FRET signal-to-noise ratio. To extract the cluster size, the sample was screened for cells with one large fluorescent focus. Since receptor clusters are typically localized at the poles of the cells, the YFP fluorescent intensity I along the long axis of each cell (Fig. 2.19a, inset) was extracted. To account for non-localized, cytoplasmic CheZ-YFP, the average background intensity was calculated as follows:

$$< I >= \int_{-\infty}^{\infty}\int_{-l/2}^{+l/2} I(x,y)\,dx\,dy \tag{2.3}$$

And then, the cluster size is defined as:

$$\Delta I = I_{max} - < I > \tag{2.4}$$

Where $I_{\max}$ is the maximum of the fluorescent intensity along the long axis of the cell I .

2.4.5 SWITCHING ANALYSIS

Switching events were analyzed automatically using a custom-made Matlab script (Mathworks, USA). For each cell, attractant and repellent responses were detected automatically based on the timing and duration of the stimulus delivery. Next, the ratiometric FRET time series of each cell, after correcting for photobleaching, was normalized between one and zero based on the repellent and attractant response amplitude, respectively. The FRET signal was then low-pass filtered using a 3-s moving average filter, and switching events were detected as peaks in the derivative of the filtered signal. With each switching event, an amplitude (change in kinase activity), residence time (time until next event), and transition time (duration of the switch based on a fit of the form $1-e^{-1}$) are associated. The switching behavior of each cell was classified according to the amplitude and number of the switching events per cell. A two-state switching cell is defined as a cell with at least 65% of its transitions showing activity level changes of at least 0.7 or 70% of total kinase activity – increasing these thresholds to respectively 65% and 0.8 has only marginal effect on the switching statistics (Fig. 2.7c,d). For each two-state switching cell, the bleaching correction is refined by another correction step using only the activity in either the $a = 0$ state, for cells with bias < 0.5, or $a = 1$ state, for cells with bias > 0.5. The time series is then re-normalized using the maximum activity level of the histograms during the two-state switching, and the amplitude, transition time, and residence time associated with each switching event are extracted again. To verify that the automated switching analysis extracts events reliably, we generated mock time series that recapitulated the switching phenotype of Tsr-I214K and added Gaussian white noise to approximate the experimental signal-to-noise ratio. By comparing the transition and residence times of the mock time series to the times extracted by our automated analysis, we find that the relative uncertainty is minimal, even for low signal-to-noise ratios (fig. 2.7b).

2.4.6 NUMERICAL SIMULATIONS OF THE CONFORMATIONAL SPREAD MODEL

Conformational spread was modeled by a two-dimensional Ising model on an $L \times L$ lattice with free boundary conditions. Each lattice site represents an allosteric unit, whose conformational state was represented in the main text by an activity variable $a_i \in \{0,1\}$. For the discussion here, we make the mapping $\sigma = 1-2a$ and discuss the model in terms of the 'spin variable' σ which takes one of two values, $\sigma = 1$ for active, and $\sigma = -1$ for inactive. The activity of the unit at site i is influenced by its N_j nearest neighbours through the coupling energy J a biasing field H_b and a ligand field H_L, giving a Hamiltonian (total energy) $\mathscr{H}$ for this lattice (in units of $k_B T$):

$$\mathscr{H} = -J \sum_{\langle ij \rangle} \sigma_i \sigma_j + (H_b/2 + H_L/2) \sum_i \sigma_i \tag{2.5}$$

where $\langle ij \rangle$ indicates that the summation is over all nearest neighbour pairs in the lattice. The biasing and ligand fields H_b and H_L were set to zero for most of our simulations, except where specified otherwise in the text. The probability of finding the lattice in a given configuration is then proportional to $e^{-\mathscr{H}}$ and the ratio of probabilities $p_i(\sigma_i)$ and $p_i(-\sigma_i)$ for the i-th site to be in state σ_i as opposed to $-\sigma_i$ is

$$\frac{p_i(\sigma_i)}{p_i(-\sigma_i)} = e^{-\Delta\mathscr{H}} \tag{2.6}$$

where $\Delta\mathscr{H} \equiv \mathscr{H}(\sigma_i) - \mathscr{H}(-\sigma_i)$ is the change in the Hamiltonian upon flipping σ_i. We set the rate $\omega(\sigma_i \to -\sigma_i)$ for the unit at site i to flip from a state σ_i to the opposite state $-\sigma_i$ as

$$\omega(\sigma_i \to -\sigma_i) = \omega_0 \exp\left[-J\sigma_i \sum_j^{N_j} \sigma_j + (H_b/2 + H_L/2)\sigma_i\right] \tag{2.7}$$

where ω_0 is the fundamental flipping frequency of a single lattice unit and N_j is the number of nearest neighbors, so as to satisfy (together with Eqs. 2.5 and 2.6) the detailed balancing condition,

$$\frac{p_i(\sigma_i)}{p_i(-\sigma_i)} = \frac{\omega(-\sigma_i \to \sigma_i)}{\omega(\sigma_i \to -\sigma_i)}. \tag{2.8}$$

We note that the fundamental frequency ω_0 corresponds to the rate of conformational transitions in an individual allosteric unit. Because this rate is unknown for the bacterial chemosensory array, in our simulations we set this parameter to unity, implying that the simulated temporal statistics are expressed in units of the fundamental timescale $1/\omega_0$.

The rates as defined in Eq. 2.7 were used in a kinetic Monte Carlo scheme (essentially as in [124], but modified to have free boundary conditions; see below) which uses in every iteration one random number to draw the time until the next flip, and another to determine which site flips. The lattice was an $L \times L$ lattice with free boundary conditions, such that the number of nearest neighbors N_j at each lattice site was

$$N_j = \begin{cases} 2 & \text{at corners,} \\ 3 & \text{at edges,} \\ 4 & \text{otherwise.} \end{cases} \tag{2.9}$$

To calculate the activity a of the lattice at each time point, we map the spin variable $\sigma_i \in \{-1, +1\}$ at each site to an activity variable $a_i \in \{0, 1\}$ as $a_i = (\sigma_i + 1)/2$ and take its mean across the lattice,

$$a = \frac{1}{L^2} \sum_i a_i. \tag{2.10}$$

To simulate adaptation feedback, a bias field is defined where each lattice unit has a specific bias field $H_{b,i}$ that represents the effect of receptor methylation according to [65]:

$$H_{b,i} = \alpha(m_i - m_o) \tag{2.11}$$

where $0 < m_i < M$ is the methylation level of site i with maximum value M, and $\alpha = 1 k_B T$ is the energy per methylation site [65]. We chose $M = 64$, corresponding to approximately 8 receptor dimers per Ising lattice unit and 8 methylation sites per dimer [125]. The methylation offset m_0 is set to $M/8$ [65]. All units with $a_i = 1$ (and $m_i < M$) experience demethylation at rate k_B and all units with a_i=0 (and $m_i > 0$) are methylated with rate k_R. This activity-dependent (de)methylation activity results in robust perfect adaptation to a steady-state activity level of $a_0 = k_R/(k_B + k_R)$. We defined these rates in terms of the fundamental frequency ω_0 according to $k_B = k_R = n_R/L^2 * V_R/\omega_0 = 0.0015\omega_0$, where $n_R = 200$ is the approximate number of adaptation proteins per cell [64], and $V_R = 1/10$s is the maximum rate of the methylation reaction [126], reflecting that the adaptation enzymes work at saturation [127]. Arrays were simulated for sufficient time to reach steady state ($a_0 \approx 0.5$) before the application of an external field H_L (representing chemoattractant ligand stimulation) was used to probe the array responses.

Simulations were implemented with Python (code will be made available online) and single simulation runs for extended times were performed on regular desktop computers. Parallel computations were performed on the LISA cluster of the SURFsara national computing facility (Amsterdam). For the parallel runs, each parameter set was given a unique seed for random number generation. The resulting time series were sampled at regular intervals, and subsequently downsampled to approximate the acquisition frequency of experiments (1Hz) relative to the array-level switching frequency ($\sim 10^{-2}$ Hz). Simulated activity time series were then further processed in the same way as experimental data to extract the temporal statistics of switching.

2.4.7 DETERMINATION OF THE CORRELATION LENGTH

The correlation length $\xi(J)$ was determined from exponential fits to the correlation function of Ising arrays [128]:

$$c(r) = \overline{\sigma_i \sigma_j} = e^{\frac{-r}{\xi(J)}} \tag{2.12}$$

where $\overline{\sigma_i \sigma_j}$ is the spin product averaged over all pairs with equal distance $r = |i - j|$. For each unit i, j, pairs are sampled horizontally and vertically (e.g. keeping either i or j constant, ignoring diagonal values). For each J, the correlation length $\xi(J)$ is computed as the average correlation length of 48 independent array states.

2.5 SUPPLEMENTARY TEXT

2.5.1 CHANGING ACTIVITY BIAS BY GENETIC MODIFICATION

The activity of the chemoreceptors in bacteria is determined by fast ligand binding and slow changes in the activity bias level through modifications of the chemoreceptors by a pair of adaptation enzymes [125]. Upon attractant binding, the activity decreases, but activity-dependent modification of the chemoreceptors provides effective negative feedback that restores the activity to its prestimulus level. This way, the wild-type chemosensory array faithfully returns to a steady-state activity bias of, on average, 0.3, but with variation between cells presumably due to expression level variation of the adaptation enzymes [54]. In the absence of the adaptation enzymes, both chemoreceptors Tar and Tsr when natively expressed, have an activity bias close to 1 [49]. Switching between the active and inactive array state is only observed if the activity bias has intermediate values and maximizes at 0.5. In our previous study on fluctuations in chemosensory activity [54], we used small amounts of chemoattractant to bring the activity bias to intermediate values to observe switching behavior. Here, we wanted to observe fluctuations in the absence of chemoeffectors and adaptation enzymes and therefore change the activity bias in a ligand-independent way.

The adaptation enzymes (CheR and CheB in *E. coli*) change the energy bias of the chemoreceptors by sequentially methylating and demethylating of 4 conserved glutamate residues on chemoreceptor Tar and 5 in Tsr [65, 100, 129]), where (CheR-mediated) methylation increases the activity bias and demethylation (by CheB) decreases it. Previous studies identified genetic modifications of those sites that mimic methylation, and can modify the chemoreceptor activity bias without changing other chemoreceptor properties such as signal amplification. For both chemoreceptors the effect of methylation can be mimicked by exchanging a glutamate (E) for glutamine (Q). The fully unmethylated state (EEEE(E)) has an activity bias close to 0. For Tar, its QEEE modification state has an intermediate activity bias and shows fluctuations in the absence of chemoeffectors [55], and is used throughout this work.

In the case of Tsr, the QEEEE modification state has a bias close to 1 [129] and therefore we pursued alternative modifications that could produce an intermediate activity bias. Of the many available mutations in Tsr receptors, the I214K mutation in the 'control cable' region of Tsr was a promising candidate [66]. In population-averaged FRET experiments, it showed an intermediate activity bias and similar dose–response curve parameters to L-Serine as Tar [QEEE] to MeAsp. Therefore, we investigated the behavior of cells expressing only Tsr-I214K with single-cell FRET and observed similar switching behavior as in the case of Tar [QEEE].

2.5.2 THE ISING MODEL IN THE THERMODYNAMIC LIMIT CAN NOT EXPLAIN SPONTANEOUS SWITCHING

The two-dimensional Ising model [130, 131] is known to demonstrate a second-order phase transition as a function of the ratio J/k_BT where J is the coupling energy, T is the temperature, and k_B is Boltzmann's constant. Increasing J across a critical value J^* at fixed T (or equivalently, decreasing

T below a critical value T^* at fixed J) leads to an abrupt ordering of the lattice for J above (or T below) this critical point, with the lattice becoming polarized with all spins in either the up or down states. For a two-dimensional lattice in the thermodynamic limit (where the lattice size $L \to \infty$), an exact solution of the model was obtained by Onsager [132], giving the precise critical value $J^*/k_B T = \ln(1+\sqrt{(2)})/2 = 0.440686\ldots$ (and equivalently $k_B T^*/J = 2.26918\ldots$). Near this critical point, various thermodynamic observables (such as the correlation length ξ and the correlation time τ_c) are known to diverge as power laws characterized by critical exponents as a function of the "reduced temperature",

$$\epsilon \equiv \left|T - T^*\right|/T^* = \left|J^* - J\right|/J, \tag{2.13}$$

which provides a dimensionless measure of the distance from the critical point [133]. For example, the critical exponent ν (= 1 for 2-D lattices) defines how the correlation length diverges, $\xi \sim \epsilon^{-\nu}$, and another exponent z (≈ 2.2 for 2-D lattices [81]) in turn defines the scaling of the correlation time $\tau_c \sim \xi^z = \epsilon^{-\nu z}$, as the critical point is approached ($\epsilon \to 0$). The divergence of the correlation time at the critical point implies that above J^* (or equivalently below T^*), the system becomes frozen in one of the two polarized states. Thus, the Ising model in the thermodynamic limit is unable to explain the switching fluctuations we have observed in chemoreceptor arrays.

2.5.3 FINITE-SIZE ISING MODELS EXHIBIT TWO-STATE SWITCHING NEAR CRITICALITY

By contrast to the behavior in the thermodynamic limit discussed above, in Ising lattices of finite size, the correlation length ξ can not grow beyond the lattice size L, and the scaling of various observables near criticality becomes a function of the system size L, a phenomenon known as finite-size scaling [79, 134]. For example, the singularity in the correlation time scaling $\tau_c \sim \xi^z = \epsilon^{-\nu z}$ at the critical point ($\epsilon = 0$) is lost due to the cutoff of ξ at L and instead becomes $\tau_c \sim L^z$. Thus, fluctuations in near-critical 2-D Ising lattices of finite size demonstrate all-or-none switching between polarized states (intuitively, because $\xi \sim L$) that become increasingly slow as the lattice size grows (intuitively, because $\tau_c \sim L^z$) — an example of the phenomenon of "critical slowing down" observed across a broad range of dynamical systems near criticality. The excellent agreement between the temporal statistics of our experimental data with those of simulated Ising lattices (Fig. 2.6) suggested that both Tar and Tsr chemoreceptor arrays are well described as finite-size Ising systems close to criticality.

To quantitatively estimate the degree to which chemosensory arrays are close to criticality, we applied finite-size scaling to further analyze our experimental and simulated temporal statistics, as described below. The basic idea is to use the observed degree of near-critical slowing to estimate the distance to criticality, and (with appropriate calibrations) also obtain an estimate for the fundamental conformational timescale $1/\omega_0$ of allosteric units.

2.5.4 SCALING OF THE CRITICAL ENERGY

An important result of finite-size scaling theory is that the position of the critical point (*i.e.* the value of J^*, or equivalently, T^*) itself becomes a function of the system size L [134]. As noted above, the well-known Onsager exact solution for the infinite two-dimensional Ising lattice [132] gives the critical coupling energy J^* (in units of $k_B T$) explicitly as

$$J^*_\infty = \frac{1}{2}\ln\left(1+\sqrt{2}\right) \approx 0.44. \tag{2.14}$$

For finite lattices there is no exact analytical solution, but both analytical [82] and numerical [83] approaches to finite-size scaling theory have established that the critical coupling energy J^* (or equivalently the critical temperature T^*) dependence on the system size L. The dependence J^*_L of

the critical coupling energy with system size is well approximated as [82, 83],

$$J_L^* \approx \frac{J_\infty^*}{1 - cL^{-1}}, \tag{2.15}$$

where c is constant whose value and sign depend on the boundary conditions. For periodic boundary conditions, c is negative ($c_{p.b.c.} = -0.36$) and hence J_L^* approaches J_∞^* from below as $L \to \infty$. By contrast, c is positive for free boundary conditions ($c_{f.b.c.} = +1.25$) and in this case J_L^* approaches J_∞^* from above as $L \to \infty$. Given that chemoreceptor arrays cover only a finite area of the plasma membrane, they have open ends. In our simulations, therefore, only free boundary conditions are considered, meaning that $J_L^* > J_\infty^*$ for all values of L.

2.5.5 SCALING OF THE RESIDENCE AND TRANSITION TIMES

As noted above, for coupling energies close to the critical energy ($J \approx J^*$), the spatial correlation length of activity states approaches the lattice size L, leading to polarized all-or-none fluctuations. Thus, within this regime, the activity time series is well approximated as a random telegraph process [135], and hence the residence timescale Δt (i.e. time between switching events) is expected to be proportional to the correlation time τ_c (because $\tau_c = (\langle \Delta t_{\text{up}} \rangle^{-1} + \langle \Delta t_{\text{down}} \rangle^{-1})^{-1}$ for a random telegraph process). Numerical studies have found that a good approximation for the scaling of τ_c in finite lattices in the near-critical region, $\tau_c \sim L^z \exp[c_0 \epsilon L]$, with $\epsilon = \left|(J_\infty^* - J)/J\right|$ and the "dynamical critical exponent" $z = 2.2 \pm 0.1$ [80, 81]. We confirmed that the residence times extracted from our simulations at various combinations of ϵ and L were well-fit by a scaling of the same form,

$$\Delta t = c_t L^z \exp[c_0 \epsilon L] \tag{2.16}$$

with $z = 2.2$ (Fig. 2.13a), and these fits yielded for the remaining scaling constants $c_0 = 1.6 \pm 0.5$ and $c_t = 1.4 \pm 0.5$.

For the transition time τ (the duration of the activity transient upon switching), we found that our data were well-described (Fig. 2.13b) by a power-law,

$$\tau = c_\tau L^b \tag{2.17}$$

with $c_\tau = 1$ and $b = 1.725$.

2.5.6 SCALING ANALYSIS OF THE EXPERIMENTAL DATA

While the finite-size scaling relations obtained above provide an excellent approximation to the simulated data, they can not be directly applied to the experimentally observed timescales because the simulations yield timescales in units of the fundamental flipping timescale $1/\omega_0$, which remains unknown for the chemosensory array. That is, Δt_{sim} and τ_{sim} from simulations are related to Δt_{exp} and τ_{exp} from experiments as, respectively,

$$\begin{aligned} \Delta t_{\text{sim}} &= \Delta t_{\text{exp}} \omega_0, \\ &\text{and} \\ \tau_{\text{sim}} &= \tau_{\text{exp}} \omega_0. \end{aligned} \tag{2.18}$$

We therefore identify as a key experimental observable the dimensionless timescale ratio $\Delta t/\tau$, which removes the dependence on the unknown constant ω_0. Using Eqs. 2.16 and 2.17, we obtain a scaling for the timescale ratio $\Delta t/\tau$,

$$\frac{\Delta t}{\tau} = \frac{c_t}{c_\tau} L^{(z-b)} \exp(c_0 \epsilon L). \tag{2.19}$$

This scaling provides a one-to-one relationship between the timescale ratio $\Delta t/\tau$ and the product ϵL, as evidenced by the collapse of simulated data at various combinations of ϵ and L onto a single curve (Fig. 2.12a Inset). However, because the size L is not precisely known for the chemoreceptor array, we can not uniquely determine ϵ.

We therefore chose to assess the distance from criticality by comparing iso-lines in the J-L plane, corresponding to parameter combinations that yield a given value of the timescale ratio $r_{\text{iso}} \equiv \Delta t/\tau$, with J_L^*, with the finite-size scaling of the critical coupling energy given by Eq. 2.15. The iso-lines determined from simulations (Fig. 2.12b) were fit well by an expression obtained by solving Eq. 2.19 for ϵ,

$$\epsilon = \frac{\log[r_{\text{iso}}/c_R] + (b-z)\log L}{c_0 L}. \tag{2.20}$$

where we have defined $c_R \equiv c_t/c_\tau$. For the scaling shown in Fig. 2.12e (dashed curves), we fitted Eq. 2.20 to the data corresponding to the iso-line for Tar (r_{iso}=8.5) and Tsr (r_{iso}=11.5), where each of the parameters (Table S11) was constrained to the obtained scaling value +/- one standard deviation.

2.5.7 SCALING OF THE FUNDAMENTAL FREQUENCY ω_0

As noted above, the 'timescales' determined from the simulations are a dimensionless quantity Δt_{sim}, expressed relative to the fundamental flipping timescale $1/\omega_0$ of individual lattice units. Thus, $\Delta t_{\text{sim}}$is related to experimentally observed timescale Δt_{exp} as $\Delta t_{\text{sim}} = \Delta t_{\text{exp}}\omega_0$. Given the finite-size scaling relations obtained above, one could therefore estimate ω_0 as a function of L by comparing the timescales extracted from experiments and numerical simulations. To obtain such a scaling relation for ω_0, we use the fact that along the iso-lines for $\Delta t/\tau$, Δt scales in the same way as τ. Thus plugging the iso-line scaling of ϵ (Eq. 2.20) into the residence time scaling (Eq. 2.16) yields for the simulated residence time,

$$\Delta t_{\text{sim}} = c_t L^z \exp\left[\log(c_\tau r_{\text{iso}}/c_t) + (b-z)\log L\right] = c_\tau r_{\text{iso}} L^b, \tag{2.21}$$

which indeed scales as the transition time ($\sim L^b$), and using this we obtain the scaling relation for ω_0 (as defined in Eq. 2.7) as a function of the lattice size L and experimental residence timescale Δt_{exp}:

$$\omega_0 = \Delta t_{\text{sim}}/\Delta t_{\text{exp}} = c_\tau r_{\text{iso}} \frac{L^b}{\Delta t_{\text{exp}}}. \tag{2.22}$$

2.5.8 FIELD DEPENDENCE OF TWO-STATE SWITCHING IN FINITE LATTICES

While we have shown that temporal statistics compatible with the experimentally observed two-state switching behavior can be generated by a near-critical Ising model with J close to J^*, proximity to the Ising critical point depends also on the biasing field H, which must vanish ($H \to 0$) at the critical point. It is therefore of interest to ask what ranges of H are compatible with two-state switching. Switching fluctuations are large collective excitations involving nearly all $N = L^2$ lattice units, and due to the fluctuation-dissipation relation [136],

$$\langle\sigma^2\rangle - \langle\sigma\rangle^2 = k_B T \chi / L^2 \tag{2.23}$$

where $\chi \equiv \partial|\langle\sigma\rangle|/\partial H$ is the field-dependent susceptibility, their likelihood can be assessed by the field-dependence of the activity bias $\langle a\rangle = (\langle\sigma\rangle + 1)/2$ of Ising lattices. Intuitively, switching is most likely where the activity variance $\langle a^2\rangle - \langle a\rangle^2$ ($= (\langle\sigma^2\rangle - \langle\sigma\rangle^2)/4$) is greatest, which through Eqn. 2.23 is also where the susceptibility χ (and equivalently the absolute logarithmic activity derivative $|\partial \log\langle a\rangle/\partial H|$) is largest.

A biasing field H (in units of k_BT) modifies the flipping rate of a single spin $\omega(\sigma_i \to -\sigma_i)$ by a multiplicative factor $\exp(H\sigma_i/2)$ (Eqn. 2.7). Thus, a positive field ($H > 0$) pushes the bias towards the limiting value $\langle\sigma\rangle \to -1$ (equivalently $\langle a\rangle \to 0$), but there will always be a finite amplitude of fluctuations such that $\langle\sigma\rangle > -1$ (equivalently $\langle a\rangle > 0$).

For strong fields ($H \gg J$), fluctuations in activity will be dominated by single spin flips, and hence the activity bias will approach that expected for an arbitrary spin σ_i in the lattice,

$$\langle a\rangle \to \left\langle \frac{p(\sigma_i)}{p(\sigma_i)+p(-\sigma_i)} \right\rangle = \left\langle \frac{1}{1+e^{\Delta\mathscr{H}}} \right\rangle \tag{2.24}$$

where the averages are taken over all spins $\{\sigma_i\}$ and $\Delta\mathscr{H} \equiv \mathscr{H}(\sigma_i) - \mathscr{H}(-\sigma_i)$ is the change in the Hamiltonian (Eqn. 2.5) upon flipping σ_i. Given that the $\Delta\mathscr{H} \approx H$ for strong fields, the activity bias reduces to

$$\langle a\rangle \approx \frac{1}{1+e^{H}}, \text{ for } H \gg J \tag{2.25}$$

which decays with derivative $\partial\log\langle a\rangle/\partial H = \chi/2\langle a\rangle \approx -1$ characteristic of this single spin-flip dominated regime.

In the limit of weak coupling ($J \to 0$), Eqn. 2.25 becomes an exact identity valid for all values of H, and the derivative $\partial\log\langle a\rangle/\partial H \to -1/2$ as $H \to 0$.

Conversely, in the limit of strong coupling ($J \to \infty$), the system approaches the MWC limit [137–139], for which the activity bias becomes instead

$$\langle a\rangle = \frac{1}{1+e^{NH}} \tag{2.26}$$

with $N = L^2$ is the system size, and valid at all finite values of H. The corresponding derivatives $\partial\log\langle a\rangle/\partial H \approx -N$ for strong fields ($e^{NH} \gg 1$) and $\partial\log\langle a\rangle/\partial H \to -N/2$ for weak fields ($H \to 0$), respectively.

Near criticality where $J \approx J^*$, and $0 < H/J \ll 1$ the activity bias in the thermodynamic limit ($L \to \infty$) is known to scale as a power law [140],

$$\langle a\rangle = \frac{1}{2}(1 - H^{1/\delta}) \tag{2.27}$$

with $\delta = 15$ for two-dimensional lattices, which gives a steep field dependence $\partial\log\langle a\rangle/\partial H \approx -\delta^{-1}H^{(1/\delta-1)}$ that diverges as $H \to 0$.

In finite-size Ising lattices, this singularity is rounded to give a finite size-dependent maximal steepness at $H = 0$ that scales as a power law in L,

$$|\partial\log\langle a\rangle/\partial H|_{H=0} = |\partial\log\langle a\rangle/\partial H|_{\max} = \chi_{\max} \sim L^x \tag{2.28}$$

with an exponent x in the range $1.75 \le x \le 2.0$ depending on J/J^* [136]. Thus, the steepness at zero field grows as $\sim L^x$ with system size, and the range ΔH of the field exhibiting this steep dependence narrows as $\sim L^{-x}$.

Despite the steep dependence at small $|H|$ ($< \Delta H$), it has been shown that in finite Ising lattices (with periodic boundary conditions) near criticality this steepness decays sharply as H increases beyond ΔH. As a result, the response curve of $\langle a\rangle$ vs H in develops a substantial tail that contrasts starkly to that in the strongly coupled MWC limit [76]. Our simulations (on finite lattices with free boundary conditions, $L = 20$, $J = 0.475k_BT \approx J^*(L)$, Fig. 2.9c) also show a similar trend: a steep dependence of $\langle a\rangle$ on H for $H < 0.03$ that then deviates strongly to develop a substantial tail before crossing over eventually to the expected scaling for the single-spin dominated regime $\partial\log\langle a\rangle/\partial H \to -1$ at $H \approx 0.3$ (Fig. 2.9c, Inset). Thus, there exists a substantial range in H beyond the steep region ΔH (≈ 0.03 for $L = 20$ and $J \approx J^*(L)$) exhibiting collective excitations. While we

expect switching to be most prominently observed within the steep region $|H| < \Delta H$, they can also occur within this intermediate regime ($0.03 < H < 0.3$) of mildly attenuated collective excitations, albeit with reduced frequency.

Nevertheless, taking as a conservative estimate the width ΔH of the steep region as the range of switching behavior for the $L = 20$ lattice, an exponent of $x = 2$ for the finite-size scaling of the switching range, i.e. $\Delta H \sim L^{-2}$, our estimated size range L = 17-30 for chemosensory arrays our experiments (see Main Text) implies that the biasing field is no greater than $|H| < \Delta H \approx 0.01\text{-}0.04 k_B T$ in cells demonstrating two-state switching. Combined with the fact that two-state switching requires a value of J near its critical value ($J \approx J^* \approx 0.44 k_B T$), this suggests that the strength of any biasing field in these cells is at most 3-10% of the coupling energy.

Note that for *E. coli* chemoreptor arrays the activity bias in the absence of ligand is known to depend on temperature [119], and in our experiments we have deliberately set the temperature T to a value that gives the largest fraction of two-state switcher cells. Thus, the population-average value μ_H of the biasing field H is set through this procedure to be very close to zero. We also observed (Fig. 2.1c) that approximately two thirds of cells with a single large cluster demonstrated two-state switching, whereas most of the remaining third or so showed no switching. If we interpret the non-switcher cells as having an effective biasing field outside of the two-state switching regime discussed above (*i.e.* $|H| > \Delta H$) and further assume for simplicity a normal distribution $N(\mu_H, \sigma_H^2)$ of H across the population, the above considerations suggest an average $\mu_H \approx 0$ and standard deviation $\sigma_H \approx 0.01\text{-}0.04 k_B T$ (given that for a normal distribution approximately two thirds of the population lies within $\mu_H \pm \sigma_H$).

Finally, we note that this rather narrow range of variation in H across cells does not preclude larger variations at the molecular scale within each cell. Given that H in our Ising Hamiltonian (Eqn. 2.5) is applied identically across all alosteric units, it can be considered a mean-field approximation for values of H that could in reality vary with some amplitude across the $N = L^2 \sim 10^3$ allosteric units. From this perspective, the above estimate for the cell-to-cell variation in H could be compatible with variation at the level of allosteric units as large as $\sigma_H \times \sqrt{N} \sim 0.5 k_B T$.

2.5.9 ARRAY SIZE ESTIMATION FROM RESIDENCE TIME DISTRIBUTIONS

It has been shown that chemosensory array sizes vary strongly between cells [57, 141]. Because CheZ is known to localize to the arrays (Fig. 2.1b), in our FRET experiments with reduced FRET pair expression, the arrays are visible as fluorescece intensity peaks above the cytoplasmic CheZ-YFP background (clusters). We can integrate fluoresce intensity over the cluster area to obain a 'cluster size' measure that serves as a proxy for the true array size (Fig. 2.19a and Section 2.4.4). These experiments revealed that the average cluster size in cells exhibiting only a single detectable cluster was smaller for cells exhibiting two-state switching than for cells exhibiting no switching (one-state) (p = 0.004, two-sample KS test), consistent with the expectation that switching events become increasingly rare with increasing array size L (at a given J).

It is also possible to estimate the array size L using the temporal statistics we measured by FRET and the Ising finite-size scaling theory. This can be done in two ways, depending on different assumptions that can be made about J under cell-to-cell variations in L. One possibility is that J remains constant under variations in L. In this case, L can calculated by plugging in the measured residence timescale $\langle \Delta t \rangle$ of each cell scaled by ω_0 into Eq. (2.16) and solving for L. Another possibility is that J varies together with L in such a way that the timescale ratio r_{iso} (= 11.5 for Tsr) remains constant. In this case, a relationship between L and Δt can be found by solving Eq. (2.21) for:

$$L = \left(\frac{\omega_0 \Delta t}{c_\tau r_{\mathrm{iso}}} \right)^{1/b} \tag{2.29}$$

In Fig. 2.19b, these two estimation methods (constant J and varying J) were used to convert

transform the $\langle \Delta t \rangle$-distribution from FRET experiments into the distribution of array size. Parameters were the same as those used in Fig. 2.12 (and listed in Table 2.15) ($z = 2.1$, $b = 1.75$, $c_0 = 1.18$) and those obtained in Sections 2.5.3 and 2.5.4 ($c = 1.25$, $c_t = 1.4$, $c_\tau = 1$). For ω_0, we chose a value in the center of the range given in Fig. 2.15 ($1/\omega_0 = 21$ ms). Data for the $\langle \Delta t \rangle$-distribution were the same as those shown in Fig. 2.6d for Tsr-I214K, restricted to the activity-bias range $-0.25 \leq \Delta G / k_B T \leq 0.25$.

Fig. 2.19b compares the distribution of cluster intensities for those cells exhiting only one cluster but exhibiting two state switching, to the distribution of arary size estimated from two-state swtiching statistics. The shapes of the distributions for each finite-size scaling estimation method (constant J and varying J) and from CheZ-YFP cluster intensity are indistiguishable within experimental error (Fig. 2.19b).

2.5.10 THE EFFECT OF CHEMORECEPTOR MIXING WITHIN CHEMOSENSORY ARRAYS

The receptor population within chemosensory arrays typically comprise multiple chemoreceptor species, allowing cells to integrate distinct signals, but at the cost of reduced cooperativity[100]. *E. coli* possesses five chemoreceptor genes (*tar, tsr, tap, trg, aer*), but they are not all expressed in equal amounts. The two 'major' chemoreceptors (*tsr* and *tar*) are expressed at higher levels compared to the other three 'minor' chemoreceptors [125]. The expressed chemoreceptor population of wildtype *E. coli* cells is known to vary across growth phases of cultured cells, with Tsr dominating the population early on (at low opitcal density, OD), and an increased Tar/Tsr ratio at later phases (at high OD) of batch-culture growth [142, 143]. This change in the expressed chemoreceptor population makes the chemosensory response cooperativity dependent on the growth phase at which cells are harvested [54]. Therefore, harvesting cells at different ODs allows tests of wildtype array properties at different degrees of chemoreceptor mixing.

We first measured the effect of receptor mixing on response timescales. Adaptation-deficient cells with a wildtype complement of chemoreceptors harvested at OD=0.20 demonstrated substantial response delays (≈ 13 s) to sub-saturating stimuli (Fig. 2.17b,d). By contrast, when cells of the same genotype were harvested at OD=0.45, the response delay was reduced to ≈ 3 s (Fig. 2.17c,d), that is, an order of magnitude increase in response speed relative to the pure Tsr arrays (Fig. 2.17a). The response to saturating stimuli in adaptation deficient cells was faster than the response to subsaturating stimuli for each genotype (Fig. 2.17d), but were still much slower than the typical run/tumble timescale (~ 1 s) in the case of Tsr-only arrays (≈ 7 s). Evidently, homogeneous arrays exhibit the strongest response slowdown, but even when all chemoreceptor genes are present, the array's response can be very slow, depending on chemoreceptor ratios. without some mechanism to mitigate this response slowdown, chemotactic performance would be severely impaired.

Effects of varying array composition were also evident in the fluctuation phenotype of cells. Adaptation deficient cells with the wildtype complement of chemoereceptor ges harvesetd at OD=0.2 exhibited discrete-level switching fluctuations in the absence of stimulation (Fig. 2.18b), indicating that the degree of receptor mixing within arrays is low at this early phase of growth. By contrast, cells of the same genotype harvested at OD=0.45 demonstrated fluctuations of reduced amplitude (Fig. 2.18c), consistent with reduced cooperativity due to a greater degree of chemoreceptor mixing. Thus, although chemoreceptor diversity in the array can contribute to mitigating critical slowdown, that diversity is physiologically modulated and is evidently insufficient to fully mitigate slowdown across the full range of physiological conditions. These observations suggest that *E. coli* cells must rely on a different mechanism to ensure that response seeds remain fast enough for effective chemotaxis under varying physiological conditions.

Table 2.2: Mean residence times and number of events extracted from cells expressing Tsr-I214K.

Bias	$\langle \Delta t_{\mathbf{up}} \rangle$ **(s)**	**± std**	$\langle \Delta t_{\mathbf{down}} \rangle$ **(s)**	**± std**	$N_{\mathbf{up}}$	$N_{\mathbf{down}}$
$0.65 < \alpha \leq 1$	116.2 ± 3.27	± 101.8	38.6 ± 0.79	± 26.2	967	1091
$0.55 < \alpha \leq 0.65$	72.4 ± 2.31	± 61.2	48.0 ± 1.20	± 32.6	703	733
$0.45 < \alpha \leq 0.55$	60.4 ± 1.84	± 50.9	59.6 ± 1.68	± 46.6	766	767
$0.35 < \alpha \leq 0.45$	56.7 ± 2.36	± 47.2	80.7 ± 3.48	± 68.2	398	384
$0 \leq \alpha \leq 0.35$	41.3 ± 1.65	± 27.9	118.9 ± 6.56	± 104.8	285	255
$0 \leq \alpha \leq 1$	78.2 ± 1.36	± 75.9	57.0 ± 0.95	± 53.9	3119	3230

Table 2.3: Mean transition times and number of events extracted from cells expressing Tsr-I214K.

Bias	$\langle \tau_{\mathbf{up}} \rangle$ **(s)**	**± std**	$\langle \tau_{\mathbf{down}} \rangle$ **(s)**	**± std**	$N_{\mathbf{up}}$	$N_{\mathbf{down}}$
$0.65 < \alpha \leq 1$	4.28 ± 0.10	± 3.16	6.09 ± 0.12	± 3.49	970	837
$0.55 < \alpha \leq 0.65$	4.31 ± 0.12	± 3.21	6.07 ± 0.15	± 3.57	660	572
$0.45 < \alpha \leq 0.55$	4.18 ± 0.12	± 3.02	5.89 ± 0.14	± 3.54	681	604
$0.35 < \alpha \leq 0.45$	4.36 ± 0.17	± 3.16	6.18 ± 0.20	± 3.60	362	320
$0 \leq \alpha \leq 0.35$	4.49 ± 0.20	± 3.24	6.35 ± 0.22	± 3.32	262	235
$0 \leq \alpha \leq 1$	4.29 ± 0.06	± 3.15	6.07 ± 0.07	± 3.52	2935	2568

Table 2.4: Mean residence times and number of events extracted from cells expressing Tar [QEEE].

Bias	$\langle \Delta t_{up} \rangle$ **(s)**	**± std**	$\langle \Delta t_{down} \rangle$ **(s)**	**± std**	N_{up}	N_{down}
$0.65 < \alpha \leq 1$	79.4 ± 2.87	± 70.6	28.2 ± 0.58	± 14.8	607	647
$0.55 < \alpha \leq 0.65$	56.5 ± 2.15	± 41.5	37.4 ± 1.22	± 23.7	373	379
$0.45 < \alpha \leq 0.55$	44.7 ± 1.66	± 30.7	45.3 ± 1.68	± 31.1	343	341
$0.35 < \alpha \leq 0.45$	39.0 ± 2.06	± 29.6	58.0 ± 3.56	± 50.1	207	198
$0 \leq \alpha \leq 0.35$	32.0 ± 1.33	± 18.0	86.0 ± 5.94	± 77.0	183	168
$0 \leq \alpha \leq 1$	57.5 ± 3.03	± 52.7	42.6 ± 1.95	± 39.3	1713	1733

Table 2.5: Mean transition times and number of events extracted from cells expressing Tar [QEEE].

Bias	$\langle \tau_{up} \rangle$ **(s)**	**± std**	$\langle \tau_{down} \rangle$ **(s)**	**± std**	N_{up}	N_{down}
$0.65 < \alpha \leq 1$	4.70 ± 0.14	± 3.22	5.73 ± 0.15	± 3.33	556	501
$0.55 < \alpha \leq 0.65$	5.13 ± 0.18	± 3.39	6.00 ± 0.21	± 3.42	346	271
$0.45 < \alpha \leq 0.55$	4.71 ± 0.20	± 3.50	6.39 ± 0.20	± 3.18	301	260
$0.35 < \alpha \leq 0.45$	4.81 ± 0.27	± 3.53	6.26 ± 0.28	± 3.35	176	140
$0 \leq \alpha \leq 0.35$	4.56 ± 0.24	± 3.09	6.61 ± 0.31	± 3.49	171	130
$0 \leq \alpha \leq 1$	4.79 ± 0.08	± 3.34	6.06 ± 0.09	± 3.35	1550	1302

Table 2.6: Fit parameters of mean residence times per cell as a function of energy bias ΔG.

	slope γ_{down}	**slope** γ_{up}	**crossover point** $\tau_{up} = \tau_{down}$	N
Tar [QEEE]	−0.44	0.45	47.0 ± 1 s	204
Tsr-I214K	−0.39	0.45	65.5 ± 1 s	549

Table 2.7: Mean residence times and number of events extracted from numerical simulations using a conformational spread model with a lattice size of 20 × 20 spins and coupling energy $J = 0.475\, k_B T$.

External Field	**Bias**	$\langle \Delta t_{up} \times \omega \rangle$	**± std**	$\langle \Delta t_{down} \times \omega \rangle$	**± std**	N_{up}	N_{down}
H = −0.006	$\alpha \approx 0.79$	4790 ± 381.43	± 4110	1250 ± 76.81	± 840	116	121
H = −0.002	$\alpha \approx 0.63$	2820 ± 172.44	± 2220	1680 ± 95.29	± 1240	166	168
H = 0	$\alpha \approx 0.51$	2190 ± 128.34	± 1600	2130 ± 149.60	± 1870	155	156
H = 0.002	$\alpha \approx 0.44$	1930 ± 97.63	± 1280	2440 ± 155.67	± 2040	172	171
H = 0.006	$\alpha \approx 0.23$	1370 ± 82.68	± 920	4480 ± 359.98	± 3890	123	117
		2185 ± 90.52	± 1597	2132 ± 87.50	± 1868	732	733

Table 2.8: Mean transition times and number of events extracted from numerical simulations using a conformational spread model with a lattice size of 20 × 20 spins and coupling energy $J = 0.475\, k_B T$.

External Field	**Bias**	$\langle \tau_{up} \times \omega \rangle$	**± std**	$\langle \tau_{down} \times \omega \rangle$	**± std**	N_{up}	N_{down}
H = −0.006	$\alpha \approx 0.79$	179.76 ± 10.35	± 111.51	169.54 ± 11.05	± 118.01	116	114
H = −0.002	$\alpha \approx 0.63$	169.18 ± 8.83	± 113.11	166.95 ± 9.16	± 115.50	164	159
H = 0	$\alpha \approx 0.51$	166.57 ± 8.95	± 106.98	156.20 ± 9.24	± 113.49	143	151
H = 0.002	$\alpha \approx 0.44$	184.13 ± 9.74	± 124.39	155.91 ± 7.38	± 95.05	163	166
H = 0.006	$\alpha \approx 0.23$	154.32 ± 8.79	± 91.73	159.81 ± 10.54	± 113.00	109	115
		171.59 ± 8.79	± 111.49	161.30 ± 10.54	± 110.41	695	705

Table 2.9: Mean residence times and number of events extracted from numerical simulations using a conformational spread model with a lattice size of 12 × 12 spins and coupling energy $J = 0.5\,k_B T$.

External Field	**Bias**	$\langle \Delta t_{up} \times \omega \rangle$	**± std**	$\langle \Delta t_{down} \times \omega \rangle$	**± std**	N_{up}	N_{down}
H = −0.02	$\alpha \approx 0.85$	2230 ± 96.18	± 2120	390 ± 11.34	± 250	486	491
H = −0.006	$\alpha \approx 0.66$	1040 ± 45.69	± 930	520 ± 21.05	± 430	412	410
H = 0	$\alpha \approx 0.53$	800 ± 31.53	± 650	700 ± 31.20	± 640	419	420
H = 0.006	$\alpha \approx 0.40$	610 ± 24.81	± 510	920 ± 38.20	± 780	416	415
H = 0.02	$\alpha \approx 0.22$	520 ± 27.07	± 640	1810 ± 69.06	± 1610	551	546
		904 ± 27.60	± 1318	1045 ± 22.34	± 1067	2284	2282

Table 2.10: Mean transition times and number of events extracted from numerical simulations using a conformational spread model with a lattice size of 12 × 12 spins and coupling energy $J = 0.5\,k_B T$.

External Field	**Bias**	$\langle \tau_{up} \times \omega \rangle$	**± std**	$\langle \tau_{down} \times \omega \rangle$	**± std**	N_{up}	N_{down}
H = −0.02	$\alpha \approx 0.85$	56.05 ± 1.89	± 40.04	57.59 ± 1.97	± 41.06	450	434
H = −0.006	$\alpha \approx 0.66$	58.07 ± 1.94	± 38.02	60.16 ± 2.11	± 41.10	385	380
H = 0	$\alpha \approx 0.53$	59.27 ± 2.17	± 43.31	54.42 ± 1.87	± 37.14	398	394
H = 0.006	$\alpha \approx 0.40$	58.84 ± 1.98	± 38.48	57.51 ± 2.14	± 41.90	378	382
H = 0.02	$\alpha \approx 0.22$	60.04 ± 1.99	± 44.15	54.77 ± 1.60	± 36.41	492	516
		58.46 ± 0.89	± 41.03	56.76 ± 0.86	± 39.43	2103	2106

Table 2.11: Fit parameters of exponential fits to residence times extracted from cells expressing Tsr-I214K. Exponential fit of the form $\alpha e^{\beta x}$.

Bias	Δt_{up}	Δt_{down}
$0.65 < \alpha \leq 1$	α = 0.0083 β = -0.0088	α = 0.0460 β = -0.0329
$0.55 < \alpha \leq 0.65$	α = 0.0177 β = -0.0166	α = 0.0289 β = -0.0227
$0.45 < \alpha \leq 0.55$	α = 0.0249 β = -0.0221	α = 0.0216 β = -0.0185
$0.35 < \alpha \leq 0.45$	α = 0.0310 β = -0.0273	α = 0.0139 β = -0.0122
$0 \leq \alpha \leq 0.35$	α = 0.0423 β = -0.0318	α = 0.0073 β = -0.0065

Table 2.12: Fit parameters of exponential fits to residence times extracted from cells expressing Tar [QEEE]. Exponential fit of the form $\alpha e^{\beta x}$.

Bias	Δt_{up}	Δt_{down}
$0.65 < \alpha \leq 1$	α = 0.0154 β = -0.0150	α = 0.0862 β = -0.0504
$0.55 < \alpha \leq 0.65$	α = 0.0231 β = -0.0199	α = 0.0480 β = -0.0342
$0.45 < \alpha \leq 0.55$	α = 0.0360 β = -0.0284	α = 0.0317 β = -0.0243
$0.35 < \alpha \leq 0.45$	α = 0.0556 β = -0.0403	α = 0.0227 β = -0.0194
$0 \leq \alpha \leq 0.35$	α = 0.0746 β = -0.0473	α = 0.0143 β = -0.0142

Table 2.13: Fit parameters of exponential fits to residence times extracted from numerical simulations using a conformational spread model with a lattice size of 20 × 20 spins and coupling energy of J = 0.475 $k_B T$. Exponential fit of the form $\alpha e^{\beta x}$.

Bias	Δt_{up}	Δt_{down}
H = -0.006	α = 0.2280 β = -0.2339	α = 3.3210 β = -1.5900
H = -0.002	α = 0.5589 β = -0.4987	α = 1.4930 β = -1.0050
H = 0	α = 0.7966 β = -0.6830	α = 1.3090 β = -0.9488
H = 0.002	α = 0.8822 β = -0.6558	α = 0.6276 β = -0.5173
H = 0.006	α = 1.0670 β = -0.9160	α = 0.1771 β = -0.0278

Table 2.14: Fit parameters of exponential fits to residence times extracted from numerical simulations using a conformational spread model with a lattice size of 12 × 12 spins and coupling energy of J = 0.5 $k_B T$. Exponential fit of the form $\alpha e^{\beta x}$.

Bias	Δt_{up}	Δt_{down}
H = -0.02	α = 0.5876 β = -0.5844	α = 3.3820 β = -3.4340
H = -0.006	α = 1.4200 β = -1.2040	α = 2.4260 β = -2.3460
H = 0	α = 2.1750 β = -1.6820	α = 2.0490 β = -1.7660
H = 0.006	α = 3.3800 β = -2.3630	α = 1.0920 β = -1.0250
H = 0.02	α = 4.1970 β = -3.2720	α = 0.8545 β = -0.8116

Table 2.15: Parameters that describe the scaling of the timescale ratio with lattice size and critical energy (Eq. 2.20). Each parameter is determined individually from the scaling behavior of residence and transition times (Fig. 2.13). For the scaling relation of the phase diagram (Fig. 2.12), the finite scaling relation was fitted to the iso lines corresponding to Tar, where each fit parameter was allowed to vary according to the fit uncertainty of the individual fits.

Parameter	**From fitting (Fig. 2.13)**	**Used in iso-line fit (Fig. 2.12)**	**Literature**
z	2.2	2.1	2.2 ± 0.1 [81]
b	1.725 ± 0.032	1.75	
c_1	0.294 ± 0.366		
$c_2 = c_0$	1.608 ± 0.466	1.18	
$c_t = e^{c_1}$	1.4 ± 0.5		
c_τ	1 (assumed, not fit)		
$c_R = c_t / c_\tau$	1.03± 0.23	0.8	

3

GROWTH-DEPENDENT SENSORY BET-HEDGING ENHANCES NAVIGATION

Isogenic populations of bacterial cells exhibit substantial cell-to-cell variation in sensory perception and motile behavior. However, the origins of this diversity and its governing mechanisms remain unclear. Here, we quantify the distribution of sensory and behavioral phenotypes, as well as the abundance of key proteins in the Escherichia coli chemotaxis network during growth in various environments. Combining mathematical modeling with single-cell experiments, we pinpoint the origin of sensory diversity to just one cellular random variable: the expression-level ratio of the two major chemoreceptors Tar and Tsr. Calibrated by expression noise measurements of these two proteins, an MWC-type allosteric model accurately predicts chemosensory diversity in every tested environment. At the behavior level, we demonstrate experimentally how diversity in sensing phenotypes benefits navigation in uncertain environments by enhancing readiness to multiple sensory cues. We identify growth rate as a key environment-dependent physiological variable associated with gene expression changes governing not only the mean but also the variance of sensory phenotypes. By contrast, diversity in tumble bias, a key behavior-level phenotype, remained constant across environments. These results reveal a bet-hedging strategy specific to the sensory module of bacterial chemotaxis: attenuated diversity in sensing nutrients currently being consumed enables focused exploitation, while increased sensory diversity towards those not presently utilized enhances exploration for new growth opportunities.

3.1 INTRODUCTION

The survival of an organism depends upon its capacity to adeptly perceive and respond to environmental cues, particularly those associated with vital resources such as nutrients. Sensing and responding rapidly to environmental cues is particularly important in organisms like bacteria, which inhabit diverse ecosystems characterized by rapid and unpredictable changes, such as the mammalian gut [28]. When bacteria are confronted with the exhaustion of a particular nutrient source, they must promptly detect and exploit alternative sources of nutrients to ensure their survival. A strategy to cope with such unpredictability is to establish a population of bacteria with diverse sensing phenotypes. This diversification, often termed "bet-hedging," allows bacterial populations to respond to a range of sensory cues by maintaining subpopulations not adapted to the present environment but prepared for potential future environments [25] [144] [145] [146] [147] [148].

Previous work established that the enteric bacterium *Escherichia coli* can rapidly modify how it hedges its sensory bets without changes in gene expression, through a diversity-tuning mechanism based on covalent modification of allosterically interacting chemoreceptors [29, 30]. However, that posttranslational mechanism works by effectively filtering the underlying diversity in protein counts, which can itself vary on a slower timescale due to stochastic gene expression. Here, we demonstrate that *E. coli* populations do indeed modulate stochasticc gene expression in an environment-dependent manner to implement a bet hedging strategy that modulates diversity in their sensing phenotypes while keeping diversity in their motility phenotypes unchanged.

Escherichia coli achieves motility through a run-and-tumble random walk [11]. To bias this random walk towards attractant and away from repellent, *E. coli* makes use of its chemotaxis pathway, one of the best characterized models of biological signaling. *E. coli* cells detect chemical and physical signals through arrays of transmembrane receptors composed of five different types of chemoreceptors. The two primary receptors, Tar (which mainly senses the amino acid aspartate) and Tsr (which mainly senses the amino acid serine), make up 90% of the total chemoreceptor population when *E. coli* cells are grown in rich media. The other three chemoreceptors—Tap, Trg, and Aer—are present at substantially lower copy numbers [149]. The receptors modulate the activity of the kinase CheA, which phosphorylates the response regulator CheY, producing CheY-P. Binding of attractant molecules to chemoreceptors reduces the activity of CheA, leading to a decrease in the intracellular level of CheY-P due to the activity of the phosphatase CheZ. CheY-P interacts with the flagellar motor, reducing the bacterium's tendency to tumble. Consequently, attractant binding increases the duration of the bacterium's runs, biasing the random walk in the desired direction.

We characterized the diversity of *E. coli*'s sensory and motility phenotypes, as well as the expression of its two major chemoreceptors, Tar and Tsr, under various growth conditions. Specifically, by combining the single-cell FRET microscopy method recently developed in our lab [150] with a microfluidic device that allows tracking hundreds of swimming trajectories simultaneously (Chapter 5) and fluorescent fusions of Tar and Tsr, we quantified sensory and behavioral diversity alongside gene expression noise in isogenic bacteria under nutrient-rich and nutrient-poor environments. Our findings reveal that changes in nutrient composition and cell density alter not only the average sensory phenotype but also the degree of cell-to-cell variability in sensory responses. In contrast, motility phenotypes ——specifically the tumble bias and run speed, which together define the run-and-tumble random walk in the absence of a chemical gradient —— remain constant across all tested environments.

By combining experiments and mathematical analysis of a multi-species allosteric (MWC) model [151, 152], we demonstrate that the standing level of sensory diversity can be explained by changes in just one cellular random variable goverend by stochastic gene expression: the Tar/Tsr receptor protein ratio. By generating populations of cells with increased diversity in sensory phenotypes, we show that a high level of standing diversity confers a discernible advantage for

chemotactic navigation under behavioral contexts where populations are challenged with different chemoattractants as environmental sensory cues. This advantage arises from the rapid filtering for the best-performing phenotypes by the collectively migrating chemotactic population wave, and occurs independently of gene expression changes —– a novel population-level adaptation mechanism we recently predicted and verified experimentally (Chapter 5) [153].

Finally, by utilizing custom microfluidic chemostats amenable to single-cell fluorescence microscopy (variants of the "mother machine" [154]), we found that the chemical composition of the growth environment, rather than growth duration, dictates the distribution of the Tar/Tsr ratio through a growth rate-dependent gene expression mechanism. This gene-expression-based diversity adaptation mechanism operates on a timescale of hours, acting in parallel with the faster, non-genetic collective migration adaptation mechanism that occurs within minutes, and the posttranslational diversity tuning mechanism which operates on the sensory adaptation timescale of ~ 10 seconds.

3.2 RESULTS

3.2.1 SINGLE-CELL FRET REVEALS SUBSTANTIAL DIVERSITY IN LIGAND SENSITIVITY ACROSS AN ISOGENIC POPULATION OF CELLS

To probe the degree of cell-to-cell variation in ligand sensing within a genetically identical population, we performed dose-response measurements by stimulating adaptation-deficient (CheRB-) *E. coli* cells with pulses of the attract amino acid L-serine that binds the major chemoreceptor Tsr, while monitoring the output of the signaling pathway in single cells using an *in vivo* CheYZ FRET sensor [150] for the activity of the kinase CheA (Figure 3.1a). *E. coli* has a sensory adaptation system consisting of the enzymes CheR and CheB that modulate the sensitivity of the chemoreceptors via covalent modifications that maintain the kinase output of the pathway to a constant steady-state level. To decouple diversity in ligand sensitivity from diversity in receptor modification induced by the two adaptation enzymes, we deleted the genes encoding CheR and CheB. We performed dose-response measurements (see methods) with cells grown as batch culture in nutrient-rich (TB) medium containing all 20 amino acids until mid-exponential phase, corresponding to an optical density (OD) of 0.45. The resulting dose-response data were fitted with a sigmoidal Hill function of the form $\frac{1}{1+\left(\frac{[L]}{K_{1/2}}\right)^H}$, where $\frac{1}{K_{1/2}}$, represents ligand sensitivity and H the cooperativity between receptors. This analysis revealed that single-cell dose-response curves can differ substantially from the population-average curve (Figure 3.1b). Extracting the $K_{1/2}$ parameter from these single-cell curves, which corresponds to the ligand concentration necessary to reduce the kinase activity by 50%, revealed a substantial degree of diversity, with the $K_{1/2}$ values of individual cells spanning approximately an order of magnitude (Figure 3.1b), consistent with our previous findings [29, 30, 150] .

3.2.2 SENSITIVITY DISTRIBUTIONS SHIFT AS A FUNCTION OF CELL DENSITY IN RICH MEDIA, BUT NOT IN MINIMAL MEDIA

Considering that *E. coli* can be found in a variety of nutrient-diverse ecological niches, we wondered how chemosensory diversity is influenced by the growth environment. We cultured isogenic populations of cells in the same nutrient-rich batch culture and suspended growth by harvesting at four different cell densities, ranging from OD = 0.30 to OD = 0.80, where cells experience different nutrient concentrations [155]. Dose-response experiments using serine pulses revealed that the distribution of the inverse ligand sensitivity, $K_{1/2}$, shifts towards higher values with increasing cell density (Figure 3.1c). Notably, the diversity in $K_{1/2}$, measured as the coefficient of variation (CV, defined as standard deviation divided by the mean), increases considerably with cell density,

ranging from CV = 0.20 at OD = 0.30 to CV = 0.45 at OD = 0.80.

We then examined how diversity varies as a function of cell density in an environment devoid of chemotactic cues. Cells were grown in minimal media without amino acids, using glycerol as a carbon source, which does not elicit a chemotactic response [7]. Compared to cells grown in rich media, these cells exhibited reduced sensitivity (higher $K_{1/2}$) in their responses to serine (Figure 3.1d). Notably, in minimal media, the distribution of $K_{1/2}$ remained independent of cell density, in contrast to the density-dependent shifts observed in rich media. Furthermore, the coefficient of variation of $K_{1/2}$ remained very high (CV ~ 0.50) across all cell densities in minimal media.

Finally, we wondered how the sensitivity towards the other major *E. coli* chemoattractant, L-aspartate, which binds the chemoreceptor Tar, is modulated by the growth environment. We performed experiments identical to those described above, substituting aspartate for serine. Interestingly, in rich media, we observed the opposite trend compared to serine: cells exhibited higher sensitivity towards aspartate (lower $K_{1/2}$) at higher cell densities (Figure 3.1e). However, as with serine, the distribution of aspartate $K_{1/2}$ was independent of cell density in minimal media (Figure 3.1f). We found that the coefficient of variation of aspartate $K_{1/2}$ was also notably high, ranging from CV = 0.91 at OD = 0.30 to CV = 0.34 at OD = 0.80. In minimal media, the CV of aspartate $K_{1/2}$ remained very high (CV ~ 0.80) across all cell densities.

In summary, these results reveal an inverse scaling of serine and aspartate sensitivity with cell density in rich media: as cell density increases, sensitivity to aspartate increases (lower $K_{1/2}$), whereas sensitivity to serine decreases (higher $K_{1/2}$) (Figure 3.1g). In contrast, in minimal media, the sensitivities to both attractants are typically lower than in rich media and remain invariant with respect to cell density (Figure 3.1h).

3.2.3 TAR/TSR RATIO DISTRIBUTION SHIFT AS A FUNCTION OF CELL DENSITY IN RICH MEDIA, BUT NOT IN MINIMAL MEDIA

Next, we sought to identify the source of this modulation of chemotactic diversity. Previous studies have shown that stochastic gene expression can lead to significant variability in protein levels among isogenic cells, with one study suggesting that proteins in *E. coli* have a baseline variation of 30% in their expression level [156]. Of the dozen or so protein species in the chemotaxis network of *E. coli*, we focused our attention on two, the aspartate receptor Tar and the serine receptor Tsr, since prior studies have demonstrated that the relative ratio of these receptors significantly impact chemotactic behavior, influencing factors such as preference for methyl-aspartate or serine [143] [157], the switch between cryophilic and thermophilic preference [158] [142], and the switch between base-seeking and acid-seeking behavior [159].

To quantify cell-to-cell variability in the Tar/Tsr ratio, we engineered functional fluorescent fusions of the *tar* and *tsr* genes at their native chromosomal loci, fusing *tar* to mCherry and *tsr* to a monomeric form of YFP (Figure 3.2a) and quantified their single-cell expression levels by fluorescence microscopy (see methods). Using the same parent strain of *E. coli*, MG1655, and identical growth conditions as in our FRET experiments, we measured Tar/Tsr ratio diversity under the same conditions in which we assessed chemotactic diversity. When grown in nutrient-rich media to mid-exponential phase (OD = 0.45), cells exhibited substantial cell-to-cell variation in the Tar/Tsr ratio (Figure 3.2b), with a CV of 0.35. This value is comparable to, though slightly lower than, the Tar/Tsr ratio CV reported by a study that used flow cytometry measurements in a different *E. coli* strain, RP437, which exhibited a CV of 0.45 at OD = 0.51 [158]. The Tar/Tsr ratio CV predicted for the same RP437 strain using single-cell FRET data was 0.5 at OD = 0.45 [150]. These differences are likely attributable to expression differences across *E. coli* strains, which are known to be often substantial even among close relatatives [149].

Next, we assessed how the Tar/Tsr ratio evolves as a function of cell density. Using a plate reader, we continuously monitored Tar and Tsr expression and the OD of the cell culture. Cells

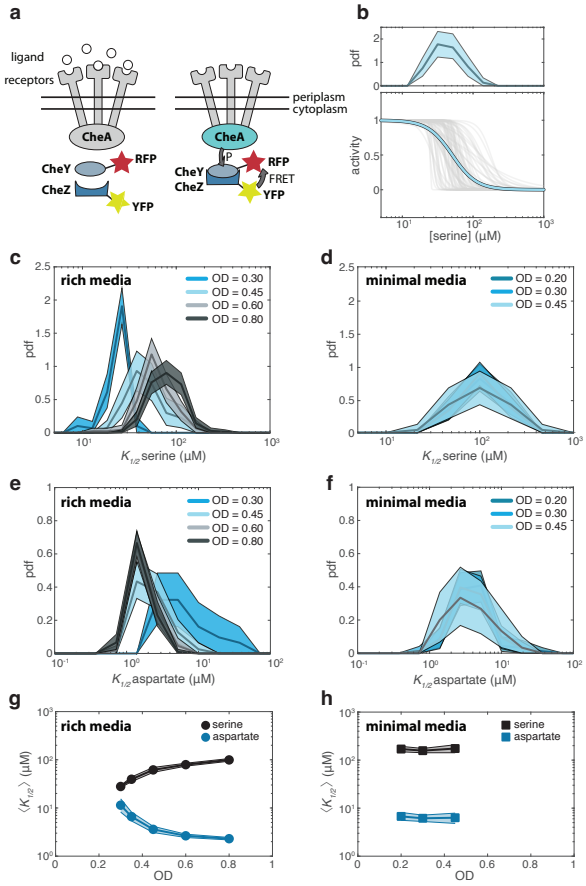

Figure 3.1: Single-cell FRET reveals extensive environment-dependent diversity in ligand sensitivity across an isogenic bacterial population. **(a)** Schematic of the *in vivo* FRET assay. The kinase CheA phosphorylates the response regulator CheY producing CheY-P in the absence of ligand binding to receptors. CheZ dephosphorylates CheY. The FRET signal between fluorescently labeled CheZ and CheY is proportional to the CheA activity. **(b)** (Bottom) single-cell (gray) and population-averaged (blue) Hill function fits to L-serine dose-response data obtained from a single experiment using adaptation-deficient cells grown to OD = 0.45 in rich media. (Top) Histogram of the inverse of ligand sensitivity values, $K_{1/2}$, extracted from the single-cell dose response curves shown above. **(c)** Histograms of L-serine $K_{1/2}$ values obtained from single-cell dose-response curves for cells grown to different ODs in rich media. Each distribution represents data from a single experiment. Shaded areas indicate 95% confidence intervals obtained via bootstrap resampling of the data. **(d)**Same as (c), but for cells grown in minimal media **(e)** Histograms of L-aspartate $K_{1/2}$ values obtained from single-cell dose-response curves for cells grown to different ODs in rich media. Each distribution represents data from a single experiment. Shaded areas indicate 95% confidence intervals obtained via bootstrap resampling. Figure legend and color scheme are consistent with panel (c). **(f)** As in (e), but for cells grown in minimal media. Figure legend and color scheme are consistent with panel (d). **(g)** Scaling of mean L-serine and L-aspartate $K_{1/2}$ as a function of OD for cells grown in rich media. Shaded areas indicate 95% confidence intervals obtained via bootstrap resampling. **(h)** Same as (g), but for cells grown in minimal media.

initially exhibited a low Tar/Tsr ratio, which increased as cell density rose, consistent with previous findings (Figure 3.2c) [143] [158] [160]. Notably, single-cell fluorescence microscopy revealed that the CV of the Tar/Tsr ratio decreased with increasing cell density, ranging from a CV of 0.43 at OD = 0.30 to a CV of 0.23 at OD = 0.80 (Figure 3.2d), consistent with modeling predictions of a previous study [150]. This trend mirrors that of the aspartate $K_{1/2}$, whose CV decreases with increasing cell density, and contrasts with the trends observed for serine $K_{1/2}$, whose CV increases with cell density. The increase in the Tar/Tsr ratio at higher optical densities was primarily driven by increased Tar expression, while Tsr levels only increased marginally (Figure 3.3). We also observed a strong correlation between Tar and Tsr expression at all optical densities (Figure 3.2b, inset and Figure 3.4), which is expected since the genes encoding these receptors—though located in separate operons—are regulated by a common transcriptional regulator, FliA, along with all other chemotaxis genes [158] [161]. Their expression is also likely influenced by global cellular factors that affect the expression of the whole proteome, such as ribosome and polymerase availability [21] [162].

To further investigate how the receptor ratio evolves in different environments, we repeated our plate reader assay in minimal media. In minimal media, the Tar/Tsr ratio remained mostly constant as the cell density increased (Figure 3.2e) and the distribution of Tar/Tsr ratios was identical across all sampled optical densities (Figure 3.2f). This observation aligns with the invariant $K_{1/2}$ distributions observed as a function of OD in minimal media (Figures 3.1d and 3.1f). The average Tar/Tsr ratio in minimal media was skewed towards higher Tar levels (Tar/Tsr ~ 3.3; figure 3.2e), similar to the Tar/Tsr ratio measured at high optical densities in rich media (Tar/Tsr = 3.25 at OD ~ 1.6; figure 3.2c). Additionally, the CV of the Tar/Tsr ratio was lower in minimal media compared to rich media, with a CV of approximately 0.31, across all optical densities. For both rich and minimal media, the standard deviation in Tar and Tsr protein copy numbers increased with increasing mean copy numbers, a result consistent with a previous study that looked at the expression of 1018 proteins in *E. coli* using YFP fusions [156].

Our findings suggest that the shift toward a higher Tar fraction at elevated optical densities in rich media (Figure 3.2c) is the primary driver of increased aspartate sensitivity under these conditions (Figure 3.1g). Although the total Tsr expression increased only marginally, the sharp decrease in serine sensitivity at higher cell densities (Figure 3.1g) is likely a consequence of chemoreceptor cluster organization. Tar and Tsr are known to form mixed clusters within the cell membrane [163]; thus, as Tar expression rises with cell density, newly synthesized Tar receptors dilute pre-existing clusters composed primarily of Tsr molecules. This dilution effect reduces overall serine sensitivity despite the marginal increase in Tsr expression levels.

3.2.4 DIVERSITY IN THE TAR/TSR RATIO IS SUFFICIENT TO QUANTITATIVELY PREDICT CHEMOSENSORY DIVERSITY

To quantitatively compare the measured diversity of $K_{1/2}$ to the measured diversity in the Tar/Tsr ratio, we turned to theoretical modeling. We employed a mixed-species Monod-Wyman-Changeux (MWC) model [151], which has been successful in fitting a number of *in vivo E. coli* chemotaxis single-cell FRET data [29] [30] [150] [152]. Using this model, we generated a serine dose-response curve for each cell, using as input their measured Tar/Tsr ratio. Then, we extracted the single-cell $K_{1/2}$ from each dose-response curve using the same hill function we used to fit experimental data. When comparing the CV of $K_{1/2}$ obtained from our FRET data to the CV of $K_{1/2}$ predicted through the MWC model from our receptor ratio data, we found excellent quantitative agreement across all experimental conditions (Figure 3.5a). This result alone indicates that a significant portion, if not all, of the observed sensory diversity in the chemotaxis system of *E. coli* can be attributed to the stochastic gene expression of its major chemoreceptors, Tar and Tsr.

To further establish direct causality between receptor expression diversity and $K_{1/2}$ diversity, we generated a population of cells with artificially high levels of receptor ratio variability. To achieve

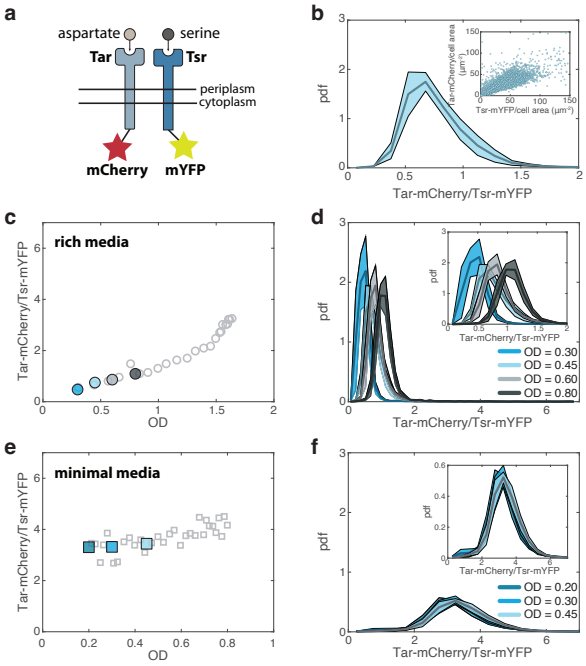

Figure 3.2: Fluorescent fusions of major chemoreceptors reveal extensive environment-dependent diversity in chemoreceptor composition across an isogenic bacterial population. **(a)** Schematic of the receptor protein quantification assay. The chemoreceptor Tar, which binds the amino acid L-aspartate, is fused at its native chromosomal locus to the fluorophore mCherry. The chemoreceptor Tsr, which binds the amino acid L-serine, is fused at its native chromosomal locus to the fluorophore mYFP. **(b)** Histogram of the Tar/Tsr chemoreceptor ratio measured with fluorescence microscopy for cells grown to OD = 0.45 in rich media, growth conditions identical to those used in figure 3.1b. The solid line represents the mean of four independent biological replicates, while shaded areas indicate the standard error of the mean across replicates. Inset: Correlation between Tar-mCherry and Tsr-mYFP expression levels. Each point represents a single cell, derived from four independent biological replicates. Tar and Tsr expression levels are strongly correlated (R^2 = 0.70). **(c)** Relationship between the Tar/Tsr chemoreceptor ratio and OD for cells grown in rich media. Gray hollow points represent the mean of 40 technical replicates measured using a plate reader. Colored points represent the mean Tar/Tsr ratio measured via fluorescence microscopy from four independent biological replicates for each OD. **(d)** Histograms of the Tar/Tsr chemoreceptor ratio measured via fluorescence microscopy for cells grown to different ODs in rich media. Solid lines represent the mean of four independent biological replicates, while shaded areas indicate the standard error of the mean across replicates. The color scheme is consistent with panel c. Inset: magnified version of the same plot. **(e)** Same as panel c, but for cells grown in minimal media. Colored points represent the mean Tar/Tsr ratio from three independent biological replicates for each OD. **(f)** Same as panel d, but for cells grown in minimal media. Solid lines represent the mean of three independent biological replicates, while shaded areas indicate the standard error of the mean across replicates. Inset: magnified version of the same plot.

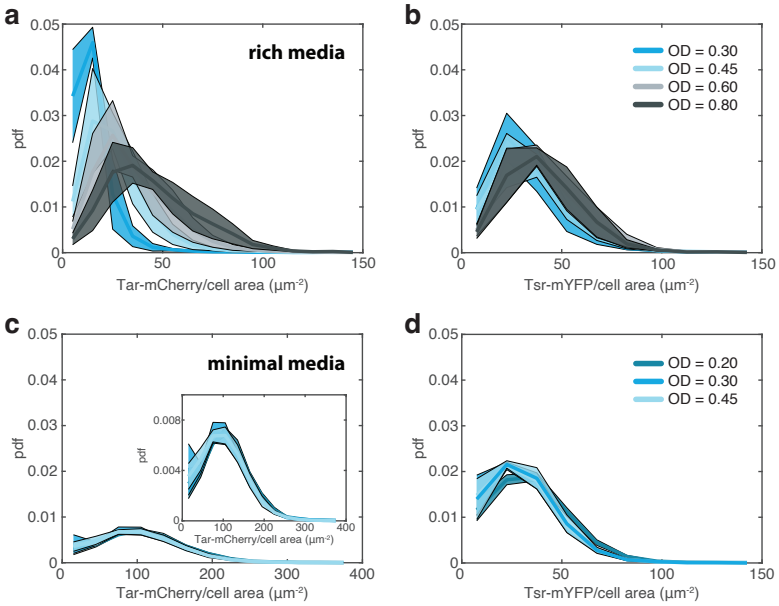

Figure 3.3: Tar and Tsr chemoreceptor expression under different growth conditions. **(a)** Histograms of Tar-mCherry expression measured with fluorescence microscopy for cells grown to different optical densities (ODs) in rich media. Solid lines represent the mean of four independent biological replicates, with shaded areas indicating the standard error of the mean. The Figure legend and color scheme match panel b. **(b)** Same as panel a, but for Tsr-mYFP. **(c)** Histograms of Tar-mCherry expression for cells grown to different ODs in minimal media. Solid lines represent the mean of three independent biological replicates, with shaded areas indicating the standard error of the mean. The Figure legend and color scheme match panel d. Inset: magnified version of the plot. **(d)** Same as panel c, but for Tsr-mYFP.

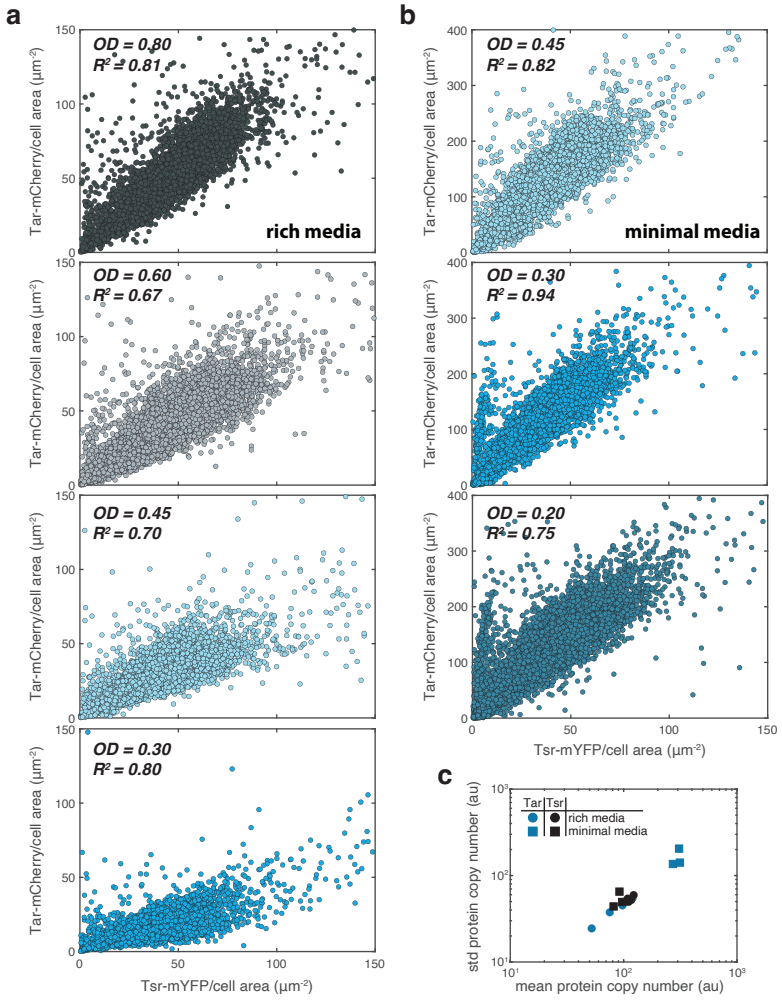

Figure 3.4: Tar and Tsr chemoreceptor expression is corelated under all growth conditions. **(a)** Correlation between Tar-mCherry and Tsr-mYFP expression for cells grown to different optical densities (ODs) in rich media, measured using fluorescence microscopy. Each point represents a single cell, derived from four independent biological replicates. **(b)** Similar to panel a, but for cells grown in minimal media, with points obtained from three independent biological replicates. **(c)** Scaling of the mean and standard deviation of protein copy numbers (in arbitrary units) for Tar and Tsr across all conditions.

that, we cloned the same Tar-mCherry fusion we engineered on the chromosome of *E. coli* into an inducible vector under the control of a leaky Lac promoter. By transforming the receptor-labeled strain with this vector and tuning its induction level in conjunction with tuning the harvesting OD of the strain (which affects receptor ratio variability in rich media; Figure 3.2d), we were able to generate a population of cells with approximately the same mean Tar/Tsr ratio as wild-type cells harvested at OD = 0.80 in rich media, but with an approximately two-fold greater Tar/Tsr ratio CV (Figure 3.5b). We then transformed a strain amenable to FRET experiments with a vector carrying the wild-type Tar receptor under the control of the same leaky Lac promoter. This generated a population of cells with approximately the same mean $K_{1/2}$ as wild-type cells harvested at OD = 0.80 in rich media, but with an approximately three-fold higher $K_{1/2}$ CV (Figure 3.5c). Importantly, MWC modeling again revealed excellent quantitative agreement between measured $K_{1/2}$ CV and $K_{1/2}$ CV predicted by the model calibrated by receptor-ratio measurements (Figure 3.5c, inset), thus demonstrating direct causality between receptor expression diversity and diversity in ligand sensitivity.

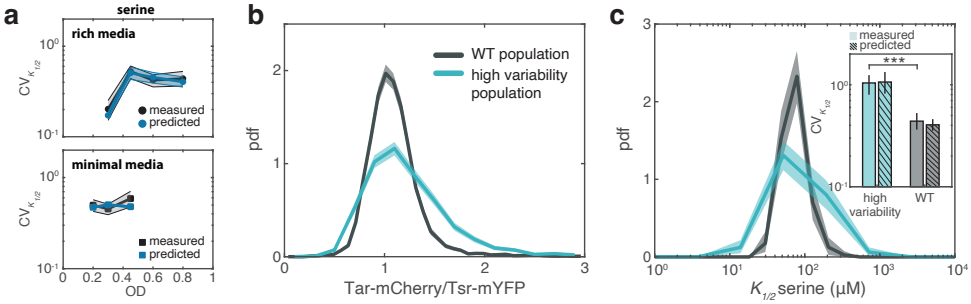

Figure 3.5: Prediction of chemosensory diversity from Tar/Tsr ratio diversity, and establishing causality. **(a)** (Top) Black points represent the measured coefficient of variation (CV) of the inverse of ligand sensitivity, $K_{1/2}$, as a function of OD in rich media, obtained from the single-cell dose-response experiments in Figure 3.1c. Blue points represent the predicted CV of $K_{1/2}$ as a function of OD in rich media, derived through the mixed-species MWC model using single-cell receptor ratio data from Figure 3.2d as an input. Shaded areas indicate 95% confidence intervals obtained through bootstrap resampling. (Bottom) Same as the top panel, but for cells grown in minimal media. The CV was either measured from the single-cell dose-response experiments in Figure 3.1d (black points) or predicted from the mixed-species MWC model using single-cell receptor ratio data from Figure 3.2f as input (blue points). **(b)** Histograms of the Tar/Tsr chemoreceptor ratio measured via fluorescence microscopy for wild-type cells (WT population; replotted OD = 0.80 data from Figure 3.2d) and for a population with artificially increased Tar/Tsr ratio variability (high variability population). Solid lines represent the histograms of all Tar/Tsr ratios from four independent biological replicates (WT population) or a single experiment (high variability population). Shaded areas indicate 95% confidence intervals obtained through bootstrap resampling. **(c)** Histograms of L-serine $K_{1/2}$ values obtained from single-cell dose-response curves for wild-type cells (WT population; replotted OD = 0.80 data from figure 3.1c) or cells with artificially increased Tar/Tsr ratio variability (high variability population). Solid lines represent the histograms from a single experiment, with shaded areas indicating 95% confidence intervals obtained through bootstrap resampling. Inset: Measured CV of $K_{1/2}$ for WT and high variability populations (solid-colored bars), along with predicted CV of $K_{1/2}$ obtained from the mixed-species MWC model using the receptor ratio distributions in Figure 3.5c as input (dashed-colored bars). Error bars indicate 95% confidence intervals obtained through bootstrap resampling. The means are statistically significant different, as determined by a two-sample t-test (p = 2.9x10-12).

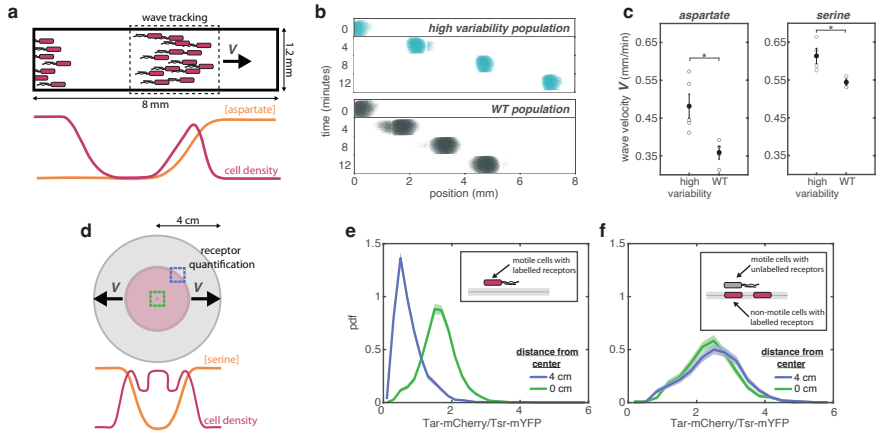

Figure 3.6: Sensory diversity enhances the chemotactic migration of isogenic populations across environments through phenotypic filtering **(a)** Schematic of the bacterial speed competition assay. Cells introduced at the entrance of a microfluidic channel form a band that migrates through a self-generated gradient of L-aspartate, established by bacterial consumption. **(b)** Segmented images of bacterial bands formed by a high variability population (top) and a wild-type (WT) population (bottom). Images are from two separate experiments, aligned at time t = 0 for comparison. Refer to Figures 3.5b and 3.5c for the Tar/Tsr ratio and $K_{1/2}$ distributions of these two populations, respectively. **(c)** Wave velocities of cells migrating up a 100μM L-aspartate gradient (left) or a 100μM L-serine gradient (right). Hollow points represent independent biological replicates, while solid points indicate the mean values across all replicates. Error bars represent standard error of the mean. Means are statistically significant different, as determined by a two-sample t-test with p = 0.0159 for aspartate waves and p = 0.0385 for the serine waves. **(d)** Schematic of the swim plate assay. Cells on rich media swim plates form a high-density band that migrates up a self-generated L-serine gradient. **(e)**) Histograms of the Tar/Tsr chemoreceptor ratio, measured via fluorescence microscopy for motile cells collected from the edge (blue) or center (green) of the expanding colony. **(f)** Same as panel e, but for non-motile cells acting as a biosensor for gene expression collected at the edge (blue) or center (green) of the colony. A motile but unlabeled strain was used to establish the chemical gradient experienced by the biosensor cells. Solid lines represent the histograms of all Tar/Tsr ratios from a single experiment. Shaded areas indicate 95% confidence intervals obtained through bootstrap resampling.

3.2.5 CHEMOSENSORY DIVERSITY BOOSTS COLLECTIVE NAVIGATION IN CONTRASTING ENVIRONMENTS VIA PHENOTYPIC FILTERING

Does increased chemotactic diversity confer a behavioral advantage? To address this question, we devised a bacterial wave speed competition experiment. To this end, we utilized motile versions of the wild-type and high-variability populations described in Figure 3.5, each expressing cytosolic YFP to facilitate wave tracking. To decouple sensing from growth, we suspended the cells in a medium that arrests growth, effectively keeping their receptor ratio constant throughout the experiment (see methods). We introduced the two populations in separate microfluidic swim channels [164] filled with either 100 μm L-aspartate or 100 μm L-serine (Figure 3.6a). The cells rapidly formed chemotactic waves by creating a gradient of ligand through consumption and directed movement (Figure 3.6b) [164] [165] [166]. Comparison of the wave velocities of wild-type and high-variability populations revealed a substantial advantage of the high-variability population in both aspartate and serine gradients (Figures 3.6c and 3.15). This advantage was not due to differences in individual motility traits, as both populations exhibited identical tumble bias and run speed distributions (Figure 3.16). These findings demonstrate a clear evolutionary advantage of increased sensory diversity, potentially enabling more diverse populations to colonize new territories faster, thus improving their overall chance of survival in different environments.

To explore the exact mechanism by which high-variability populations climb a ligand gradient faster, we employed the classical chemotaxis assay on soft agar swim plates [167] using motile cells with labeled Tar and Tsr receptors (Figure 3.6d). On a soft agar swim plate containing nutrient-rich media, *E. coli* cells form a colony with multiple bands of high cell density, the first of which consumes serine [167]. We collected cells from the serine-consuming band and measured their receptor ratios using fluorescence microscopy. At the same time, we measured the receptor ratios of cells in the center of the colony, near the inoculation point. We observed a striking difference between these two populations: cells from the serine-consuming band had a receptor ratio biased towards higher Tsr and lower Tar, compared to those from the center of the colony (Figure 3.6e), demonstrating the existence of a receptor ratio sorting mechanism. This finding aligns with our previous theoretical prediction of such sorting mechanism [153] and its experimental demonstration on Tsr selection on swim plates containing a single amino acid (Chapter 5).

This sorting mechanism is non-genetic, as demonstrated in an experiment using a non-motile strain with labeled Tar and Tsr receptors acting as a biosensor for gene expression. We spread the biosensor strain uniformly across the agar matrix and used its unlabeled wild-type parent strain to establish chemoattractant gradients on the plate. By measuring the receptor ratio of the non-motile strain, we confirmed that there are no changes in the expression of the Tar and Tsr receptors at the center and edge of the colony (Figure 3.6e), consistent with our previous findings for Tsr expression (Chapter 5).

During collective migration, this non-genetic sorting mechanism likely enriches the migrating band with cells best suited for climbing attractant gradients: cells with a low Tar/Tsr ratio are selected for in serine gradients, while cells with a high Tar/Tsr ratio are selected for in aspartate. gradients. The high-variability population contains cells with both higher and lower Tar/Tsr ratios than the wild-type population. As a result, the sorting mechanism can adapt the phenotypic composition of the migrating band further in the case of the high-variability population, resulting in better chemotactic performance. Since the sorting mechanism is non-genetic, it enables rapid phenotypic filtering even is the absence of growth, as it is the case in our bacterial wave speed competition experiment.

3.2.6 GROWTH ENVIRONMENT, AND NOT GROWTH TIME, DICTATES THE TAR/TSR RATIO DISTRIBUTION

We then sought to understand the cause of the observed shift in the Tar/Tsr ratio as a function of cell density in rich media. To test whether the total growth time determines the receptor ratio, we diluted a saturated bacterial culture into fresh rich media at three different final concentrations (Figure 3.7a). We then harvested all cultures at the same optical density (OD = 0.45). As expected, increasing the dilution factor by two-fold extended the total growth time by one division cycle (Figure 3.7b, inset). However, the resulting receptor ratio distributions were identical across all conditions (Figure 3.7b), demonstrating that growth time has no effect on receptor expression. This result is consistent with a previous study that determined the mean receptor ratio at different growth times using quantitative immunoblotting [143].

To explore whether the chemical environment determines the Tar/Tsr ratio instead, we employed a custom microfluidic chemostat amenable to single-cell microscopy (a "mother machine" [154], see methods). Within the microfluidic chemostat, the growth medium is constantly replenished, and excess cells are washed away, maintaining a constant environment and steady-state growth conditions. We grew cells in rich media to the two extremes of the cell densities examined earlier (OD = 0.30 and OD = 0.80) and measured their receptor ratios. In parallel, we collected the supernatant from both cultures. We then exposed cells growing inside the microfluidic chemostat to the collected supernatant and, after a few hours of growth in each supernatant, we determined their receptor ratios (Figure 3.7c). Strikingly, we found excellent quantitative agreement between the receptor ratio distributions of the harvested cells and those of cells growing at steady state in the corresponding supernatant (Figure 3.7d). We also found that growth rate decreases at higher ODs (Figure 3.7d, inset)

Taken together, these results demonstrate that the receptor ratio of *E. coli* does not follow a predetermined developmental trajectory, nor does it employ a timer-based mechanism that resets upon entry into a new environment. Instead, cells sense changes in their environment and dynamically adjust their receptor ratio—and, by extension, their chemotactic behavior—accordingly.

3.2.7 REGULATION OF CHEMORECEPTOR EXPRESSION AS A FUNCTION OF GROWTH RATE

Next, we investigated the molecular mechanism underlying the environment-dependent regulation of the Tar/Tsr ratio. As we showed earlier, the growth rate of cells at early ODs is substantially faster than cells at high ODs (Figure 3.7d, inset). Therefore, we wondered whether the Tar/Tsr ratio regulation is mediated by growth rate. Indeed, in rich media, growth rate decreases as a function of cell density, slowing as the culture approaches saturation (Figure 3.8a, inset). In minimal media, however, growth rate remains approximately constant during exponential phase but can be modulated by supplementing the medium with different carbon sources. To examine how growth rate influences receptor expression, we measured protein expression from the *tar* promoter at different growth rates in rich and minimal media using plate reader assays (see methods). We found a steep decrease in tar expression as the growth rate increased across all environments (Figure 3.8a), consistent with previous studies [168]. Interestingly, expression from the *tsr* promoter remained constant regardless of growth rate (Figure 3.8a).

Subsequently, we estimated the mean intracellular concentrations of Tar and Tsr by normalizing bulk expression levels (Figure 3.8a) to cell volume at different growth rates (Figure 3.8b, inset). The biomass density of *E. coli* is constant with respect to its growth rate [169], therefore the ratio of bulk protein expression level to cell volume is an accurate proxy of intracellular protein concentration. The inferred chemoreceptor concentrations closely matched those obtained via single-cell fluorescence microscopy (Figures 3.3 and 3.8b). We observed a sharp decline in Tar concentration as

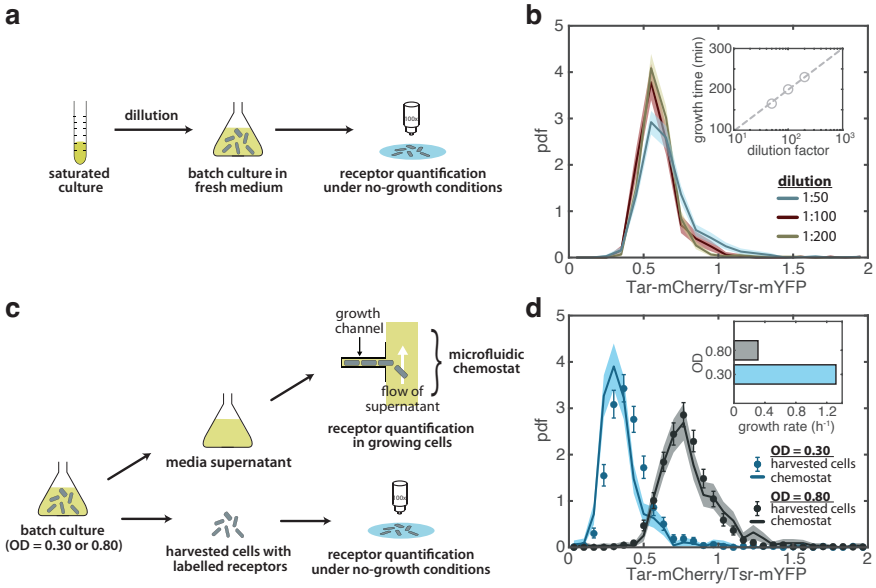

Figure 3.7: Growth environment, rather than growth time, determines Tar/Tsr ratio through growth rate-dependent chemoreceptor expression. **(a)** Schematic of the experimental protocol to assess the effect of growth time on the chemoreceptor ratio distributions. Cells from the same saturated culture were diluted to three different concentrations in fresh rich media and all cultures were harvested at the same optical density (OD = 0.45). **(b)** Histograms of the Tar/Tsr chemoreceptor ratio, measured via fluorescence microscopy, for the three different dilutions in a single experiment. The receptor ratio distribution is independent of the dilution factor. Error bars indicate 95% confidence intervals obtained through bootstrap resampling. Inset: Growth time as a function of dilution. **(c)** Schematic of experimental protocol to assess the effect of the growth environment on chemoreceptor ratio distributions. Cells were grown in rich media to OD = 0.30 and OD = 0.80, after which they were separated from their supernatant. The Tar/Tsr chemoreceptor ratio was measured via fluorescence microscopy in both the harvested cells and in cells growing inside a microfluidic chemostat at steady state, where they were exposed to the collected supernatant. **(d)**Histograms of the Tar/Tsr chemoreceptor ratio for harvested cells (solid lines) and for cells growing inside the chemostat while exposed to supernatant (points). Solid lines and points represent the histograms of all measured Tar/Tsr ratios from a single experiment. Shaded areas and error bars indicate 95% confidence intervals obtained through bootstrap resampling. Inset: growth rate of the cells in the batch culture at OD = 0.30 and OD = 0.80, assessed using a plate reader. Bar plots are the means of 40 technical replicates.

growth rate increased across all environments, while Tsr concentration only decreased marginally.

Taken together, these results suggest that growth rate is the primary — if not sole — determinant of the chemoreceptor ratio. Differences in nutrient availability across growth conditions (e.g., varying cell densities in rich media or different carbon sources in minimal media) modulate growth rate, which in turn regulates chemoreceptor concentrations. This regulation ultimately translates non-linearly into ligand sensitivities (Figure 3.8c and 3.10). The non-linear mapping between receptor ratio and $K_{1/2}$ when switching from rich to minimal media (Figure 3.9) likely arises from differences in receptor cluster organization rather than cluster protein stoichiometry. Cryo-electron tomography data have shown that cells grown in minimal media form tighter receptor clusters compared to cells grown in rich media, despite the similar overall cluster sizes [170]. However, the receptor-to-CheA and receptor-to-CheW stoichiometry is conserved across these two conditions [149] [170], likely because the mocha operon (which includes *cheW* and *cheA*) and meche operon (which includes *tar*) are both regulated by FliA [171].

3.2.8 LEVERAGING GENE-EXPRESSION NOISE AS A SENSORY BET-HEDGING MECHANISM

We found that the degree of sensory diversity, characterized by the CV of $K_{1/2}$, varies as a function of growth rate (Figure 3.8d). Interestingly, the trends for aspartate and serine are opposite in cells grown in rich media: at fast growth rates, cells exhibit lower chemotactic diversity toward serine and higher diversity toward aspartate. This pattern reverses at slow growth rates, where diversity is higher for serine and lower for aspartate. In contrast, in minimal media, diversity remains consistently high for both serine and aspartate, regardless of growth rate. Previous studies have shown that *E. coli* consumes serine at low cell densities (fast growth) and switches to aspartate at higher cell densities (slow growth) when grown in rich media [172] [173] [174]. Our findings align well with a bet-hedging strategy in which bacterial populations maximize their chances of detecting the nutrient that is not currently being utilized, by enhancing sensory diversity, and focus their attention, by reducing sensory diversity, towards the nutrient that is currently being consumed. In line with this strategy, $K_{1/2}$ reaches its lowest value (corresponding to the highest sensitivity) when cells are actively consuming the corresponding ligand (Figure 3.1g). This anticipatory mechanism primes cells to detect alternative nutrient sources once the current one is depleted. Consistent with this idea, the inversion in sensory diversity occurs around OD = 0.50, which is the cell density at which *E. coli* will start swimming away from serine and towards methyl-aspartate (the non-metabolizable analogue of aspartate) [143]. Finally, in environments of greater uncertainty—such as minimal media, where neither serine nor aspartate is present—cells maintain uniformly high chemotactic diversity, ensuring readiness to detect both amino acids when they become available.

Next, we wondered whether there is a similar bet-hedging mechanism at the level of motile behavior. We quantified the two key parameters that define the random walk of bacteria in absence of chemical gradients: tumble bias and run speed. These parameters have been shown to vary greatly within isogenic populations of *E. coli* cells [175]. We tracked the swimming behavior of motile, wild-type cells—the parent strain used for our FRET-based sensory diversity measurements— using a microfluidic device that allows tracking hundreds of cells simultaneously via phase-contrast microscopy (see Chapter 5). As expected, we found a high degree of diversity in run speed (CV ~ 0.25) and even greater diversity in tumble bias (CV ~ 1). Surprisingly, however, neither the diversity in run speed nor in tumble bias changed as a function of growth rate (Figure 3.8e). Similarly, only a weak dependence was observed between their mean values and growth rate (Figure 3.10). The latter observation is consistent with our recent findings in a different *E. coli* strain, RP437, where we measured mean tumble bias as a function of optical density (Chapter 5). However, it contradicts earlier reports that described a non-monotonic relationship between mean run speed and optical density [176], or a steady increase in mean run speed with optical density [177]. These discrepancies are

likely due to the deferent strains used in those studies, specifically RP437 and HE206, respectively.

A possible explanation for the constancy of both the mean and the coefficient of variation in run speeds across different growth rates lies in the primary determinants of run speed, flagellar number and flagellar length [174]. These parameters appear to remain constant over the growth rate range examined here [178], likely due to the stable expression of FliA (σ28), the sigma factor that regulates the expression of flagellar filament and motor genes, irrespective of growth rate [178]. Tumble bias, on the other hand, is controlled by the expression ratio of the chemotaxis proteins CheY, CheZ, CheR, and CheB [179] [180] [171]. The genes encoding these four proteins are located on the same operon as tar (the meche operon), producing a polycistronic mRNA molecule. This effectively provides strong translational coupling between these four proteins and ensures that while the absolute copy numbers of these proteins may vary with growth rate —– similar to how Tar copy numbers change (Figure 3.8b)—– their relative ratios remain conserved [180] [171]. Furthermore, since the sigma factor FliA also controls the expression of both the meche and *tsr* operons, this explains the co-variation we observed between Tar and Tsr (Figure 3.2b, inset and Figure 3.3).

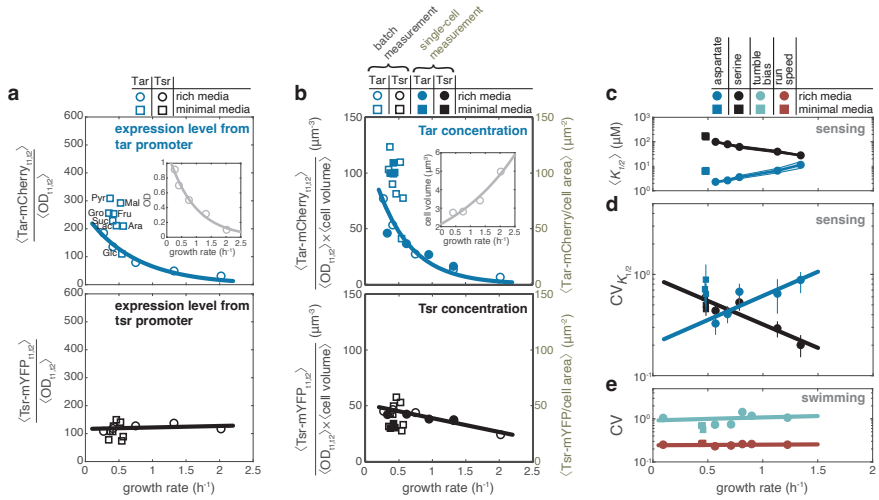

Figure 3.8: Bacteria regulate their sensory diversity based on growth rate. **(a)** (Top) Expression level of *tar* promoter reporter in cells growing in rich and minimal media. Circles represent expression level as a function of growth rate in rich media at different optical densities. Squares represent expression levels in minimal media with different carbon sources. Expression level is defined as the mean fluorescence between two time points during growth (t_1 and t_2), normalized by the mean biomass at the same time points. Carbon sources used to supplement minimal media are indicated: Gro: 0.5% v/v glycerol, Pyr: 20 mM pyruvate, Fru: 20 mM fructose, Suc: 15 mM succinate, Lac: 20 mM lactose, Ara: 20 mM arabinose, Mal: 20 mM Maltose, and Glc: 0.4% v/v glycose. For all minimal media experiments, expression levels were extracted between OD 0.2 and 0.8, during which growth rate remained approximately constant. Inset: growth rate as a function of OD. Points represent growth rates extracted at the same culture phases as expression levels. (Bottom) Same as top panel, but for the *tsr* promoter reporter. Points represent the means of 8 technical replicates for each carbon source in minimal media or 40 technical replicates for each OD in rich media. Solid lines are fits to the data. Growth rate, OD, and batch fluorescence levels were assessed in the same batch cultures using a plate reader. **(b)** (Top) Concentration of Tar proteins as a function of growth rate. Protein concentration in batch cultures (hollow points) is defined as the mean fluorescence divided by the mean biomass and normalized by cell volume. Protein concentration is also measured at the single-cell level via fluorescence microscopy (filled points). Filled points represent the means of the Tar concentration distributions shown in Figure 3.3, and filled squares indicate Tar concentrations in minimal media supplemented with 0.5% v/v glycerol as a carbon source for three different ODs. (Inset) Cell volume as a function of growth rate in rich media. The cell volume scaling deviating from an exponential fit below a growth rate of $\sim 0.7\ h^{-1}$ is consistent with previous observations in *E. coli* MG1655 [181]. (Bottom) Same as the top panel, but for Tsr concentration. Filled points represent the means of the Tsr concentration distributions shown in Figure 3.3. Hollow points are the means of 8 technical replicates for each carbon source in minimal media or 40 technical replicates for each OD in rich media. Solid lines are fits to the data. Growth rate, OD, and batch fluorescence levels were assessed in the same batch cultures using a plate reader. Cell volume was derived from cell area measurements using phase-contrast microscopy for cells harvested at different ODs. **(c)** Scaling of mean L-serine (black) and L-aspartate (blue) $K_{1/2}$ as a function of growth rate for cells grown in rich and minimal media. Shaded areas indicate 95% confidence intervals of the mean $K_{1/2}$ obtained via bootstrap resampling. **(d)** Coefficient of variation (CV) of L-serine (black) and L-aspartate (blue) $K_{1/2}$ as a function of growth rate. Error bars indicate 95% confidence intervals of the CV obtained via bootstrap resampling. **(e)** CV of tumble bias (green) and run speed (brown) as a function of growth rate. Error bars indicate 95% confidence intervals of the CV obtained via bootstrap resampling and are typically on the order of the data point size.

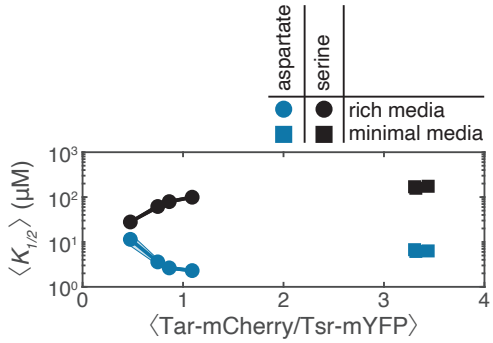

Figure 3.9: Scaling of L-serine and L-aspartate $K_{1/2}$ as a function of receptor ratio. Scaling of mean L-serine (black) and L-aspartate (blue) $K_{1/2}$ as a function of mean receptor ratio for cells grown in rich and minimal media. $K_{1/2}$ and receptor ratio were determined in separate experiments with cells grown under the same conditions. Shaded areas indicate 95% confidence intervals of the mean $K_{1/2}$ obtained via bootstrap resampling.

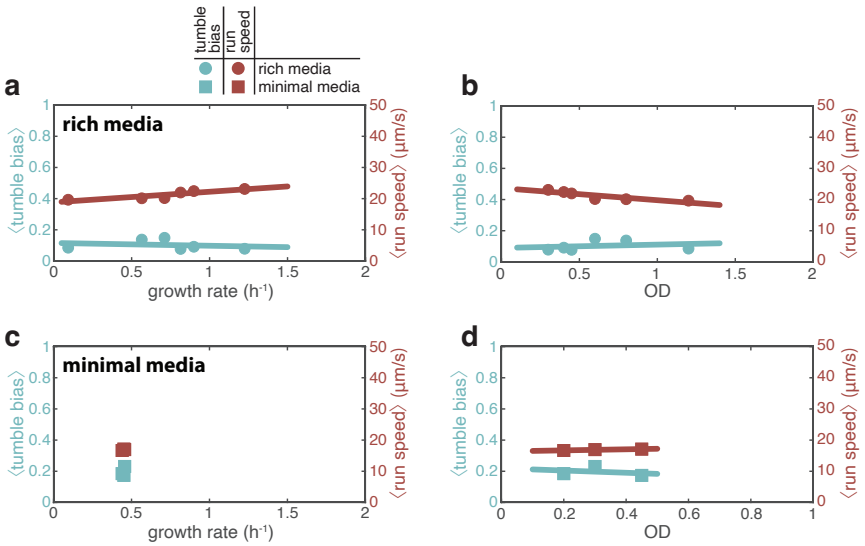

Figure 3.10: Mean tumble bias and run speed as a function of growth rate and OD. **(a)** Mean tumble bias and run speed of WT MG1655 as a function of growth rate for cells grown in rich media. Data from a single experiment. Lines are linear fits to the data. **(b)** Same data as panel (a) but plotted against the optical density of the culture. **(c)** Mean tumble bias and run speed of WT MG1655 as a function of growth rate for cells grown in minimal media. Data from a single experiment. **(d)** Same data as panel (c) but plotted against the optical density of the culture. Lines are linear fits to the data.

3.3 DISCUSSION

Half a century ago, Spudich and Koshland first demonstrated that isogenic *E. coli* populations exhibit substantial behavioral diversity [182]. Here, we systematically characterize this diversity in both sensory perception, measured as variation in sensitivity to serine and aspartate, and motility, quantified by differences in the run-and-tumble random walk. We establish a direct quantitative link between sensory diversity and its origin: stochastic fluctuations in the ratio of the chemoreceptors Tar and Tsr due to gene expression noise. Furthermore, we demonstrate that diversity in ligand sensitivity and its primary determinant, Tar/Tsr expression ratio diversity, depend on the growth environment, whereas diversity in motile behavior remains constant across environments. The environment-dependent modulation of sensory diversity appears to stem from the dependence of *tar* and *tsr* promoter activities on growth rate. Consequently, cells modulate both their mean ligand sensitivity and sensory diversity as an inherent outcome of their growth rate, without requiring dedicated regulatory pathways that couple sensing to gene expression. This regulation is only possible because *tar* and *tsr* are located on separate operons — if *tsr* were co-transcribed with *tar*, as are the cheRBYZ chemotaxis genes, such growth rate-dependent tuning would not be feasible.

Can *E. coli* exploit this intrinsic diversity? Many biological networks actively suppress variability, including the chemotaxis adaptation module [150]. However, we demonstrate that *E. coli* leverages—rather than suppresses—diversity in chemoreceptor expression, and by extension, diversity in its sensitivity to attractants, to enhance navigation. The hypothesis that *E. coli* exploits sensory diversity to enhance chemotactic navigation was previously tested in agent-based simulations [30], but experimental verification was lacking until now. Furthermore, previous experiments in a microfluidic maze containing attractant demonstrated that *E. coli* exhibits a high degree of sensory performance diversity, but lacked a mechanistic explanation of the origins of this diversity [31].

Here, we showed experimentally that in a chemoattractant gradient, the bacterial wave rapidly selects for the best-performing phenotypes — cells with the optimal Tar/Tsr ratio for the chemoattractant being pursued — leading to faster migration. Moreover, we demonstrated that this non-genetic diversity adaptation operates alongside a slower, growth rate-mediated tuning of the chemoreceptor ratio, enabling cells to increase sensory diversity (but not diversity in their random walk in the absence of a chemical gradient) toward the nutrient they are likely to consume next. This bet-hedging strategy ensures that in rapidly fluctuating environments, such as the mammalian gut, a subset of the population is always pre-adapted, priming it to detect and exploit emerging nutrient sources as they become available.

3.4 METHODS

3.4.1 STRAINS AND PLASMIDS

E. coli strain MG1655 ΔFliC::FLP, a generous gift from Victor Sourjik, was used as a background for all FRET and receptor quantification experiments. For FRET experiments, we conducted an in-frame deletion of the CheRBYZ genes. Subsequently, the gene expressing a glass-adhesive mutant of FliC [150] was cloned at the native FliC locus using homologous recombination, resulting in strain TSS2191. The FRET acceptor-donor pair, consisting of CheY-mRFP1 and CheZ-mYFP (A206K variant), was expressed in tandem from a pTrc99A plasmid under IPTG induction (pSJAB106, [150]). To determine the optimal levels of IPTG induction, we compared the motility of strain TSS2114/pSJAB106 to that of that of WT strain TSS2096 carrying an empty FRET plasmid (pTrc99A) on soft agar swim plates (Figure 3.11).

For receptor quantification experiments, *tsr* was translationally fused with mYFP (A206K variant), and *tar* was translationally fused with mCherry, at their respective native chromosomal loci using the same MG1655 ΔFliC::FLP parent strain as in FRET experiments. The cheRB genes were deleted in-frame (yielding strain TSS2155), ensuring comparable Tar receptor expression to that of

the strain used for FRET (TSS2191). Since the cheR and cheB genes are located in the same operon as the *tar* gene, factors such as the primary transcript mRNA length can affect the protein copy numbers of Tar.

For FRET experiments involving receptor overexpression, we constructed a high variability strain by transforming TSS2191 with a pTrc99A plasmid expressing wild-type Tar under IPTG induction (pSJAB21). The same FRET acceptor-donor pair used in all other FRET experiments was cloned into a pRZ30 plasmid under NaSal induction (pSJAB196). To quantify receptor overexpression, strain TSS2155 was transformed with a pTrc99A plasmid expressing a Tar-mCherry fusion under IPTG induction (pMV13). Since pSJAB21 and pMV13 are based on the same plasmid backbone, pTrc99A, and are induced at the same level, wild-type Tar and Tar-mCherry are expected to exhibit uniform expression levels.

For swimming competition experiments, wild-type MG1655, a generous gift from Victor Sourjik, was transformed with the same IPTG-inducible pTrc99A plasmid expressing wild-type Tar as in FRET experiments (pSJAB21) to generate a high-variability strain. To maintain uniform growth conditions, the strain used as a wild type for swimming was transformed with an empty pTrc99A plasmid. Both high-variability and WT strains were transformed with a NaSal-inducible pRR31 plasmid expressing cytosolic EYFP to assist with wave tracking (pVS118, gift from Victor Sourjik).

For receptor ratio quantification on swim plates, an adaptation-proficient (CheRB+) version of TSS2155, TSS2144, was utilized, as adaptation is necessary for ascending gradients of attractants. We modulated the motility of TSS2144 by transforming the strain with an arabinose-inducible pBAD33 plasmid expressing WT FliC (pC100B-12, gift from Howard Berg). To determine the optimal levels of arabinose induction, we compared the motility of strain TSS2144/pC100B-12 to that of that of WT strain TSS2096 carrying an empty pBAD33 plasmid and ΔFliC strain TSS2097 carrying pC100B-12 on rich media soft agar swim plates (Figure 3.12). The same strain, TSS2155, without the plasmid expressing WT FliC, was used as a non-motile sensor for gene expression.

Finally, wild-type MG1655 was also used to determine tumble bias and run speed at different growth rates in rich and minimal media.

For an overview of all the strains used in this Chapter, refer to Table 3.1.

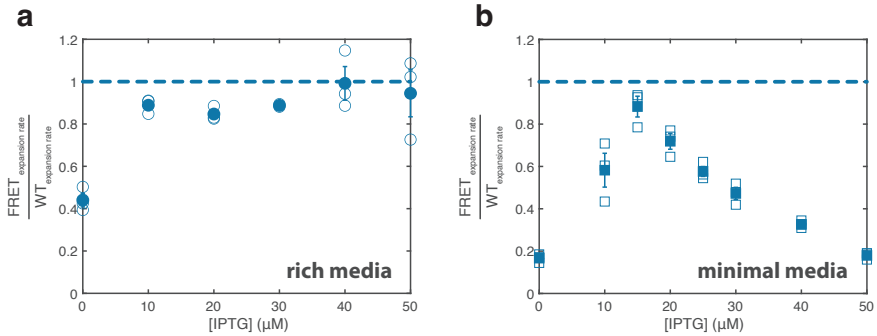

Figure 3.11: Expansion rate of FRET strain colony as a function of FRET pair induction level. **(a)** Cells expressing CheY and CheZ protein fusions (TSS2114/pSJAB106), used for FRET experiments, yield chemotactic phenotypes with expansion rates nearly identical to WT cells (TSS2096/pTrc99A) when inoculated on rich media soft agar swim plates and induced with 40 or 50 μM IPTG. Hollow symbols represent technical replicates (three for each inducer concentration), while filled symbols represent the mean values of the three replicates. Error bars indicate the standard error of the mean and are typically the size of the graph points. **(b)** Similar to panel a, but for minimal media soft agar swim plates. When induced with 15 μM IPTG, the FRET strain yields an expansion rate nearly identical to that of WT cells.

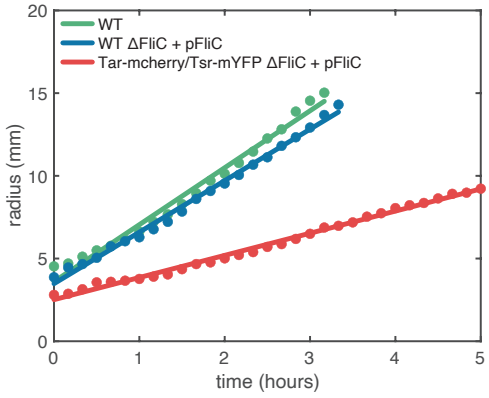

Figure 3.12: Colony expansion of receptor-labeled strain as a function of time. Tar and Tsr protein fusions, used in receptor quantification experiments, produce chemotactic phenotypes when inoculated on rich media soft agar swim plates. Lines represent linear fits to the data points to determine the expansion rates. The expansion rates for the different strains are as follows: 3.23 ± 0.22 mm/hour (WT), 3.10 ± 0.20 mm/hour (WT ΔFliC + pFliC), and 1.28 ± 0.06 mm/hour (Tar-mCherry/Tsr-YFP ΔFliC + pFliC). The abbreviation pFliC denotes pBAD33-based plasmid pC100B-12 expressing WT FliC. WT carries empty pBAD33 (TSS2096/pBAD33), WT ΔFliC + pFliC is strain TSS2097/pC100B-12, and Tar-mCherry/Tsr-YFP ΔFliC + pFliC is strain TSS2144/ pC100B-12. Averages and standard errors of the mean are derived from two technical replicates.

3.4.2 GROWTH CONDITIONS

For experiments conducted in rich media, cells were retrieved from a -80°C glycerol-based stock and inoculated in 2 ml tryptone broth (TB; 1% bactotryptone, 0.5% NaCl, adjusted to pH 7.0) supplemented with 100 μg/mL ampicillin and 34 μg/mL chloramphenicol to maintain plasmids when necessary. The cultures were then incubated overnight at 30°C and 400 RPM until saturation. Subsequently, cells from the saturated overnight culture were diluted 1:50 (except for figure 3.7b, where the initial dilution was varied) in 10 ml of TB and supplemented with 100 μg/mL ampicillin and 34 μg/mL chloramphenicol, along with appropriate inducer concentrations to induce plasmids (refer to Table 3.2). For swimming competition experiments in serine gradients cells were grown 1:50 in 20 ml TB, to achieve higher cell counts within the bacterial wave. For supernatant experiments, cells were grown 1:50 in 50 ml TB, to collect a large volume of supernatant. All cultures were grown at 33.5°C with shaking at 250 RPM. Optical density (OD) was measured at 600 nm using a spectrophotometer (Genesys 10vis, Thermo Fisher Scientific), with a permitted error of ±0.01 for all reported OD values.

For experiments conducted in minimal media, cells were retrieved from the same -80°C glycerol-based stock and inoculated in 2 ml H1 minimal salts medium (MMH1; 50 mM KPO4, 0.5 mM MgSO4, 7.6 mM (NH4)2SO4, 1.25 μM Fe2(SO4)3, adjusted to pH 7.0) supplemented with 0.5% v/v glycerol, 0.01% w/v thiamine hydrochloride, and 100 μg/mL ampicillin when necessary to maintain plasmids. Cultures were then incubated for approximately 2 days at 30°C and 400 RPM until saturation. Subsequently, cells from the saturated culture were diluted at least 1:200 in 10 ml of MMH1 supplemented with the same supplements indicated before and appropriate inducer concentrations to induce plasmids (refer to Table 3.2). Cultures were grown overnight at 33.5 °C with shaking at 250 RPM. As in the experiments conducted in rich media, OD was measured at 600 nm, with a permitted error of ±0.01 for all reported OD values.

For receptor promoter experiments in minimal media, cells were incubated overnight in TB, as described above, and then they were washed with 2 ml MMH1 without glycerol or thiamine

Table 3.1: Strains used in this Chapter.

Background Strain	**Background Strain Source**	**Background Strain Genotype**	**Plasmid 1**	**Plasmid 2**
TSS1735	[183]	MG1655 6TetO 6LacO ΔLac	pOB2	-
TSS2096	V. Sourjik	WT MG1655	-	-
TSS2096	V. Sourjik	WT MG1655	pTrc99A	-
TSS2096	V. Sourjik	WT MG1655	pBAD33	-
TSS2096	V. Sourjik	WT MG1655	pSJAB21	pVS118
TSS2096	V. Sourjik	WT MG1655	pTrc99A	pVS118
TSS2097	V. Sourjik	MG1655 ΔFliC	-	-
TSS2097	V. Sourjik	MG1655 ΔFliC	pC100B-12	-
TSS2114	This study	MG1655 ΔCheYZ	pSJAB106	-
TSS2191	This study	MG1655 FliC* ΔCheRBYZ	pSJAB106	-
TSS2191	This study	MG1655 FliC* ΔCheRBYZ	pSJAB21	pSJAB196
TSS2144	This study	MG1655 ΔFliC::FLP Tar-mCherry Tsr-YFP	-	-
TSS2144	This study	MG1655 ΔFliC::FLP Tar-mCherry Tsr-YFP	pC100B-12	-
TSS2155	This study	MG1655 ΔFliC::FLP Tar-mCherry Tsr-YFP ΔcheRB	-	-
TSS2155	This study	MG1655 ΔFliC::FLP Tar-mCherry Tsr-YFP ΔCheRB	pMV13	-

hydrochloride three times. Cells were then inoculated in fresh MMH1 supplemented with the indicated carbon source.

Table 3.2: Plasmids used in this study.

Plasmid	Source	Product	System	Induction	Resistance
pSJAB21	This study	WT Tar	pTrc99A	30 μM IPTG	amp
pMV13	This study	Tar-mCherry	pTrc99A	30 μM IPTG	amp
pSJAB106	[150]	CheY-mRFP1 CheZ-mYFP	pTrc99A	50 μM IPTG (rich media) 15 μM IPTG (minimal media)	amp
pSJAB196	This study	CheY-mRFP1 CheZ-mYFP	pRZ30	8.5 μM NaSal	cam
pVS118	V. Sourjik	EYFP	pRR31	10 μM NaSal (aspartate waves) 20 μM NaSal (serine waves)	cam
pC100B-12	H. Berg	WT FliC	pBAD33	0.01% Arabinose	cam
pOB2	[183]	LacI-mCherry TetR-EYFP	pBAD24	no induction (relied on promoter leakiness)	amp

Table 3.3: Parameters used to fit the mixed-species MWC model

Parameter	Value	Reference
C	0.314	[152]
ϵ_0	0.826	[152]
ϵ_A	1.23	[152]
ϵ_s	1.54	[152]
$\tilde{K}$	30 μM	-
$N_{\text{total}} = N_A + N_s$	32 (rich media) 100 (minimal media)	-

3.4.3 SINGLE-CELL FRET MICROSCOPY

Single-cell FRET microscopy was performed essentially as described in Chapter 2. Briefly, cells (strain TSS2191/pSJAB106 for WT experiments or TSS2191/pSJAB21/pSJAB196 for high variability experiments) were collected by centrifugation (5 min at 5,000 RPM) and washed twice in 10mL motility media (MotM; 10 mM KPO4, 0.1 mM EDTA, 1 μM L-methionine, and 10 mM lactic acid, adjusted to pH 7.0). Following this, cells were resuspended in MotM and incubated at room temperature (approximately 22°C) for 90 minutes prior to imaging, to allow for further fluorophore maturation. In each experiment, cells immobilized on a glass coverslip were placed in a flow cell under continuous flow of MotM (400 μL/min) regulated by a syringe pump (PHD 2000, Harvard

Apparatus). MotM solutions were utilized to incrementally add and remove varying concentrations of the attractants L-serine or L-aspartate (Sigma-Aldrich), with each concentration sustained for approximately 80 seconds.

Imaging was conducted using an inverted microscope (Eclipse Ti-E, Nikon) equipped with an oil-immersion 100x 1.45 NA phase-contrast objective lens (Nikon). Illumination occurred every 2 seconds using a 500 nm LED (pE-4000, CoolLED) with a pulse duration of 20 milliseconds for experiments with serine stimuli or a broad-spectrum LED (SOLA SE, Lumencor) with a pulse duration of 50 milliseconds for experiments with aspartate stimuli. For experiments with serine stimuli, epifluorescent light was split into two channels via a 2-camera image splitter (TwinCam, Cairn Research) equipped with a 580 nm dichroic mirror (Semrock) and two emission filters (520 nm and 593 nm, Semrock), each feeding into identical sCMOS cameras (ORCA-Flash 4.0 V2, Hamamatsu), capturing donor (YFP) and acceptor (RFP) channels separately. For experiments with aspartate stimuli, epifluorescent light was split into two channels via a single camera image splitter (OptoSplit II, Cairn Research) equipped with a 580 nm dichroic mirror (Semrock) and two emission filters (542 nm and 641 nm, Semrock), each projecting side-by-side into a single sCMOS camera (ORCA-Flash 4.0 V2, Hamamatsu), capturing donor (YFP) and acceptor (RFP) channels simultaneously.

FRET images were binned by a factor of 4x4 pixels to maximize their signal-to-noise ratio. All experiments were conducted at room temperature (approximately 22°C). FRET dose-response experiments were highly reproducible (Figure 3.13). Control experiments verified negligible growth throughout the entire duration of the experiment (Figure 3.17).

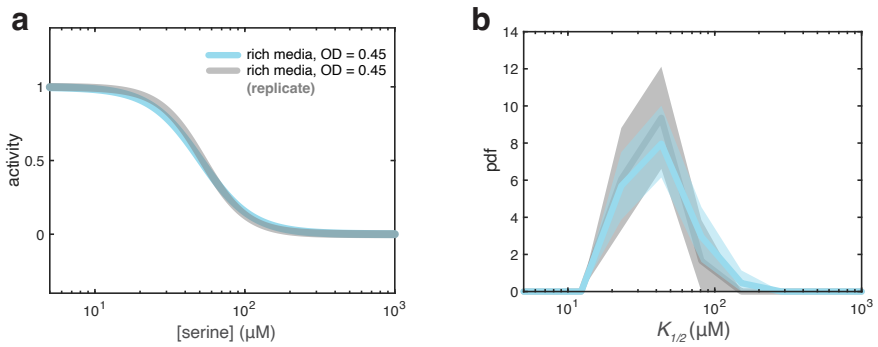

Figure 3.13: Reproducibility of FRET dose-response experiment. **(a)** Hill function fits to the population-averaged L-serine dose-response data for cells grown to OD = 0.45 in rich media. The blue dose-response curve is replotted from Figure 3.1b. The gray dose-response curve represents a biological replicate performed on a different day with different ligand dillutionsdilutions and is identical to the original dose-response curve. **(b)** Histograms of $k_{1/2}$ values obtained from single-cell dose-response curves for cells grown to OD = 0.45 in rich media. The blue distribution is replotted from Figure 3.1b, and the gray distribution is extracted from single-cell dose-response curves from the same biological replicate as in panel a, showing identical of $k_{1/2}$ distributions. Shaded areas represent 95% confidence intervals obtained through bootstrap resampling of the data.

3.4.4 FRET IMAGE ANALYSIS

Image analysis was conducted using custom MATLAB scripts. Initially, to compensate for any movement of the flow cell, all images were registered based on the first image of the experiment by employing a rigid transformation. Subsequently, alignment of donor and acceptor channels was achieved through an affine transformation. Following alignment, cell segmentation was performed on the donor (YFP) channel (given its typically higher brightness compared to the acceptor channel), utilizing a modified Otsu algorithm. After segmentation, a rectangular region of interest (ROI) of

constant area was defined for each cell. The average YFP and RFP intensities over the ROI were then extracted as a function of time. To mitigate the drift in fluorescence intensities primarily attributed to fluorophore bleaching, the FRET ratio of each cell (defined as RFP/YFP) was fitted with a double exponential function. Subsequently, the FRET ratio was divided by the double exponential and normalized between one (unstimulated steady-state activity) and zero (activity upon addition of a saturating dose of the attractant serine or aspartate), which corresponds to the kinases CheA in the cell being fully active and fully inactive, respectively. Therefore, the kinase activity of each cell is given by:

$$\alpha(t) = \frac{FRET(t) - FRET_{\text{saturating}}}{FRET_{\text{steady-state}} - FRET_{\text{saturating}}} \tag{3.1}$$

3.4.5 MWC MODEL

To obtain a distribution of $K_{1/2}$ parameters from the receptor expression data, we employed the mixed-species MWC model as described in [152]. The expression for the normalized response to L-serine is:

$$a = \frac{\epsilon_0 \epsilon_s^{N_s} \epsilon_A^{N_A} \left(1 + C\frac{[L]}{\tilde{K}}\right)^{N_s}}{\left(1 + \frac{[L]}{\tilde{K}}\right)^{N_s} + \epsilon_0 \epsilon_s^{N_s} \epsilon_A^{N_A} \left(1 + C\frac{[L]}{\tilde{K}}\right)^{N_s}} \tag{3.2}$$

where ϵ_A, ϵ_s, and ϵ_0 are the L-serine binding energies to Tar, Tsr, and to the three minor receptors, respectively. The number of Tsr receptors is denoted by N_s, while the number of Tar receptors is denoted by N_A. The vector $[L]$ represents the concentrations of L-serine and C and $\tilde{K}$ describe the ligand dissociation constant for the active state of the receptor, as:

$$K_A = \frac{\tilde{K}}{C} \tag{3.3}$$

All variables apart from parameters N_s and N_A were kept constant for all cells and are given in Table 3.3. The L-serine concentration vector $[L]$ was defined as a logarithmically spaced vector between 0.1 and 10,000. To transform the measured Tar/Tsr ratio to the MWC receptor count N_s and N_A, we used:

$$N_s = \frac{N_{\text{total}}}{\frac{\text{Tar}}{\text{Tsr}} + 1} \tag{3.4}$$

$$N_A = N_{\text{total}} - N_s \tag{3.5}$$

The normalized expression for the response to L-serine yielded a sigmoidal function between 0 and 1 for all measured receptor ratios in rich media. For minimal media experiments, a fraction of cells with extreme receptor ratios did not produce a response between 0 and 1. These data points were excluded from $K_{1/2}$ extraction. It is likely that these cells correspond to the fraction of non-motile cells, which is known to be larger for cells grown in minimal media compared to cells grown in rich media [177]. Finally, to extract $K_{1/2}$ from the MWC normalized response to L-serine we used a Hill function of the form:

$$a = \frac{1}{1 + \left(\frac{[L]}{K_{1/2}}\right)^H} \tag{3.6}$$

where $K_{1/2}$ and H are the fit parameters. The same Hill function was used to fit experimental dose-response data.

3.4.6 COLONY EXPANSION RATE QUANTIFICATION

To calibrate the FRET pair (pSJAB106) and WT FLiC plasmid expression (pC100B-12), we assessed the expansion rate of bacterial colonies carrying the plasmid of interest (strain TSS2114/pSJAB106 or TSS2097/pC100B-12) alongside WT colonies (strain TSS2096) carrying an empty version of the same plasmid (Figures 3.11 and 3.12). Cells grown in rich media were collected at OD = 0.45 and cells grown in minimal media were collected at OD = 0.30 and diluted to OD = 0.01 using fresh media. Then, 10 μL of cell culture was inoculated in the center of semi-solid agar plates. Liquid media and agar plates were supplemented with appropriate antibiotics and inducers, refer to Table 3.2. All colony expansion rate experiments were conducted at 33.5°C and 100% humidity. For each experiment, six swim plates were imaged simultaneously using a custom-built motorized turret. Images of each plate were taken every 10 minutes using a Canon DSLR camera. To extract the expansion rate, the diameter of the expanding colony was determined as a function of time by fitting an ellipse with an eccentricity <0.2 using the MATLAB regionprops function on every image, after subtracting the first image of each plate (taken before the colony had formed).

3.4.7 CHEMORECEPTOR COPY NUMBER QUANTIFICATION

The quantification of Tar and Tsr chemoreceptor copy numbers was conducted using both a plate reader assay and single-cell fluorescence microscopy. For growth and chemoreceptor copy number measurements in the plate reader (Victor X3 2030 Multilabel reader, PerkinElmer), cells (strain TSS2155) were diluted from an overnight saturated culture into fresh media (dilution ratios 1:50 for TB and 1:200 for MMH1) and 200μL of cell culture was aliquoted into each well of a 96-well plate (96-well Clear Flat Bottom TC-treated Microplate, Corning). Cultures were grown at 33.5 °C with double orbital shaking with a shaking amplitude of 2 mm until they reached saturation. Fluorescence (YFP and mCherry) and optical density (OD600) were measured every 15 minutes. The autofluorescence of the non-fluorescent parent strain of TSS2155, TSS2097, grown in the same well plate, was subtracted from all fluorescent measurements. The OD units of the plate reader were calibrated against the OD units of the spectrophotometer used to measure the OD of the batch cultures for single-cell fluorescence microscopy experiments (Genesys 10vis, Thermo Fisher Scientific) by constructing a calibration curve through serial dilution of a saturated culture. The receptor ratio units measured with the plate reader were calibrated against mean receptor ratios obtained from fluorescence microscopy for the same optical densities.

For single-cell quantification of chemoreceptor copy numbers, cells (strain TSS2155 for WT experiments or TSS2155/pMV13 for high variability experiments) were harvested from batch TB or MMH1 culture at the appropriate OD by centrifugation (5 min at 5,000 RPM). The cells were then washed twice in 10mL minimal motility media (minimal MotM; 10 mM KPO4 and 0.1mM EDTA, adjusted to pH 7.0). After washing, cells were diluted in minimal motility media, allowed to mature, and plated on agarose pads (1.5% agarose in minimal MotM). The pads were left to dry for 10 minutes before immediate imaging.

Imaging was performed using an inverted microscope (Eclipse Ti-E, Nikon) equipped with an oil-immersion 100x 1.45 NA phase-contrast objective lens (Nikon). YFP and mCherry fluorescence was excited using an LED system (pE-4000, CoolLED), and emissions were captured sequentially using a multi-band filter (Semrock) and directed into two identical sCMOS cameras (ORCA-Flash 4.0 V2, Hamamatsu) via a 2-camera image splitter (TwinCam, Cairn) equipped with a 580 nm dichroic mirror (Semrock). Approximately 20 fields of view, totaling around 1000 cells, were typically imaged per experiment. Measurements took place at room temperature (approximately 22°C). A control experiment revealed that nearly zero growth took place during the total duration of the experiment (Figure 3.17b).

To ensure accurate determination of the Tar/Tsr ratio, excitation pulse durations and intensities for YFP and mCherry were calibrated using a two-color fluorescent repressor-operator system

(FROS) standard [183]. This FROS strain (strain TSS1735/pOB2) contained six mCherry- and YFP-repressor fusions on its chromosome. By using a 100 ms 500 nm LED excitation pulse for mYFP and a 200 ms 580 nm LED excitation pulse for mCherry (both at maximum intensity), nearly identical emission intensities for mCherry and YFP were achieved, effectively equating the measured mCherry/YFP fluorescent intensity ratio to the true Tar/Tsr receptor abundance ratio (Figure 3.14). To avoid movement of the chromosome due to diffusion during the measurement, cells were chemically fixed by incubating them for 10 min at room temperature in a 4% paraformaldehyde solution (Sigma-Aldrich).

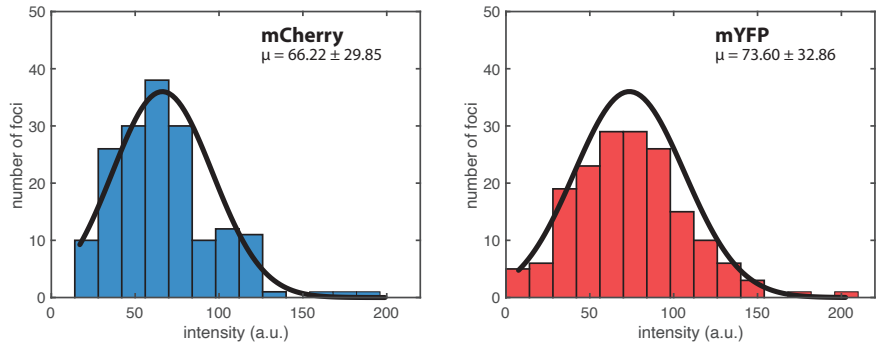

Figure 3.14: Equating the Tar-mCherry/Tsr-mYFP fluorescence intensity ratio to Tar/Tsr receptor abundance ratio. A chemically fixed FROS strain containing six mCherry- and mYFP-repressor fusions on its chromosome was imaged using the same settings and optical path as used in receptor-labeled experiments. The mean measured mCherry/YFP fluorescence intensity ratio (μ denotes mean value ± standard deviation) was close to unity, indicating that the Tar-mCherry/Tsr-mYFP fluorescence intensity ratio effectively reflects the Tar/Tsr receptor abundance ratio.

3.4.8 CHEMORECEPTOR IMAGE ANALYSIS

In each field of view, a set of images comprising one phase-contrast, one YFP, and one mCherry channel image was obtained. Alignment of images from the two cameras was performed using a custom MATLAB script through an affine transformation. Subsequently, cell segmentation was conducted on the phase-contrast channel utilizing a modified Otsu algorithm. We used the phase-contrast channel to segment the cells instead of one of the two fluorescent channels to ensure that cells with low fluorescence (and hence low receptor expression) are included in the analysis. Following segmentation, background subtraction was applied to each image, and a rectangular ROI of the same area is defined for each cell. The average mCherry and YFP fluorescent intensities over the ROI are extracted for every cell. When indicated, average fluorescent intensities are normalized by cell area, determined by fitting an ellipse on the detected cells in the phase-contrast channel

3.4.9 FABRICATION OF MICROFLUIDIC CHEMOSTATS

Microfluidic chemostats, commonly referred to as "mother machines," were fabricated using the silicone polymer polydimethylsiloxane (PDMS). The master mold for the PDMS device is a silicon wafer on which features are imprinted on a layer of SU-8, an epoxy-based negative photoresist [184]. Features are imprinted using UV light exposure through two separate photomasks. The first layer of the device comprises an array of shallow and narrow growth channels measuring 25 μm in length and 0.96 μm in height. To allow the tight confinement of cells of different widths and hence accommodate growth at different growth rates, the width of the growth channels varies

within the range of 0.7 μm to 1.2 μm, with a step size of 0.1 μm. The edges of the channels were smoothed to reduce optical aberrations during phase-contrast imaging [185]. The second layer of the device features a deeper and wider feeding channel with low fluidic resistance, enabling rapid liquid exchange. The feeding channel measures 12 mm in length, 100 μm in width, and 32.5 μm in height. The designs for the two different layers were created using CAD software (klayout) and transferred onto two separate quartz photomasks (Photronics). Fabrication of the silicon master mold was conducted at AMOLF's cleanroom facilities. Following fabrication, a hydrophobic coat of chlorotrimethylsilane (Sigma-Aldrich) was applied via vapor deposition.

To cast PDMS devices, the master mold was coated with a layer of degassed 10:1 PDMS:curing agent mixture (Sylgard 184, Dow Corning) and cured at 80°C for 1 hour. After cooling the wafer to room temperature, individual devices were cut and separated from the wafer, and inlets and outlets for each feeding channel were created using a 0.75-mm biopsy punch (World Precision Instruments). To remove any residual uncured PDMS, devices were immersed in a pentane bath for 2 hours and then in an acetone bath twice for 2 hours each. The PDMS devices were then allowed to dry at room temperature overnight. To facilitate bonding, the PDMS devices were cleaned with transparent adhesive tape (Magic Tape, Scotch) and treated, along with glass-bottom dishes (GWST-5040, WillCo Wells), in a plasma cleaner (PDC-002, Harrick Plasma). Following a 60-second exposure to ambient air plasma under a 300 mTorr vacuum, the devices were laminated onto the glass-bottom dishes and baked on an 80°C hot plate for 5 minutes to establish a covalent bond. In order to passivate the PDMS surface and prevent cell attachment, the devices were incubated with a 10 mg/ml BSA solution for 45 minutes at 37°C to allow the BSA solution to be drawn into the growth channels via evaporation through the gas-permeable PDMS. The devices were then immediately used for experiments.

3.4.10 SUPERNATANT EXPERIMENTS

For supernatant experiments, cells (TSS2155) grown in rich media were collected at OD = 0.30 and OD = 0.80 by centrifugation (5 min at 5,000 RPM) and washed twice in 10mL minimal MotM. The supernatant of those cultures was filtered using a 0.22 μm syringe filter and stored at 3°C until the experiment. The washed cells were imaged following the same protocol as for all receptor-labeled cells, with the exception that imaging took place at 33.5°C, so the measured receptor ratios are directly comparable to those of growing cells in the microfluidic chemostat.

Simultaneously, 10μL of the original OD = 0.30 culture was injected into a microfluidic chemostat through its inlet. The inlet and outlet of the chemostat were then sealed with adhesive tape (Magic Tape, Scotch) to prevent flow and the entire device was centrifuged for 20 minutes at 800 RPM, orienting the growth channels parallel to the centrifugal force axis to force cells into the growth channels. Following centrifugation, the device was incubated for 2 hours at 33.5°C, to allow for additional cells to enter the growth channels via diffusion. Subsequently, the collected supernatants were placed inside sterile glass reservoirs pressurized to 130 kPa using nitrogen. These reservoirs were then connected through separate tubes to a distribution valve (M Switch, Fluigent), which in turn was connected to the microfluidic device through a tube plugged into its inlet. The distribution valve input, and hence the growth environment of the cells, was controlled through a custom MATLAB script.

To extract the receptor ratio of the growing cells, the microfluidic device was imaged using the same microscopy setup and imaging settings we employed for all receptor-labeled cell experiments. However, imaging occurred at 33.5°C, instead of room temperature, to facilitate cell growth. To extract the morphology of the cells and to determine a segmentation mask, phase-contrast images were acquired from a single field of view every minute. Furthermore, at 20-minute intervals, corresponding to the maximum division rate observed in our experiment, one mCherry and one YFP image were acquired to quantify receptor expression.

3.4.11 IMAGE ANALYSIS OF MICROFLUIDIC CHEMOSTAT EXPERIMENTS

To accurately segment bacteria cells growing in the microfluidic chemostat, we trained a machine learning model to predict the outline of each cell. We used a convolutional neural network (CNN) based on the U-Net architecture [186] [187] to transform the original microscopy images into maps of cell outlines using custom Python scripts. To train the network, we simultaneously acquired fluorescent images, using the bright CheY-mRFP1 fusion, and phase-contrast images of growing cells. Subsequently, we manually created binary masks of all cell outlines in 500 CheY-mRFP1 512x512 pixel images and augmented this dataset using geometric transformations such as scaling, translation, and rotation. This augmented dataset was then utilized to train the CNN.

Following the training phase, we applied the CNN to transform 2000 CheY-mRFP1 frames, distinct from the original training dataset, without any post-processing of the images. The CNN generated unique 512x512 pixel output matrices for each image, with high scores corresponding to cell outlines while cell bodies and the background contained nearly zero scores. We then re-trained the CNN using the phase-contrast images and the binary masks created by the CNN based on CheY-mRFP1 images as inputs. Additionally, we augmented these datasets further using geometric transformations. Through this training method, we increased our training dataset by a factor of 4, while manually segmenting only CheY-mRFP1 images, which are substantially easier to segment compared to phase-contrast images due to the brightness of the fluorescent fusion protein and the near-zero background fluorescence.

The primary advantage of using phase-contrast images for cell segmentation is the elimination of the need for an additional fluorescent protein and imaging channel, as well as the avoidance of phototoxicity associated with fluorescent imaging. Visual inspection of the transformed images revealed consistent cell masks produced by the CNN, irrespective of whether the original image was obtained through fluorescence or phase-contrast microscopy.

Subsequently, the CNN output binary matrices underwent further processing by thresholding using a modified Otsu algorithm and removing small clusters of unconnected pixels, effectively setting only the pixels corresponding to cell outlines to unity and every other pixel to zero. Then, alignment of images from the two cameras was performed using a custom MATLAB script employing an affine transformation. All images were then registered based on the first image of the experiment using a rigid transformation to correct for movement of the microfluidic device. Fiducial markers in the form of growth channel numbering were incorporated into the device to assist with image registration. Finally, individual growth channels were cropped out by summing the fluorescence of both channels and detecting peaks in the fluorescence intensity profile.

For cell segmentation, we employed the MATLAB regionprops function, which detects cells in the CNN-transformed images as elliptical objects. For each cell, we determined its minor and major axes, along with the x- and y-coordinates of its centroid. The centroid was then tracked across all frames, under the assumption that interframe movement could not exceed a threshold defined as one quarter of the shortest cell length in any given image. Movement was considered only along the long axis of the growth channel, as the cells were constrained along their width, thereby minimizing tracking to a one-dimensional problem. Divisions were identified by abrupt changes in cell length (the major axis of the fitted ellipse), coupled with an increase in cell count. Conversely, a reduction in cell count, alongside the disappearance of centroids near the origin of the growth channel, indicated cells exiting towards the feeding channel. Subsequently, the minor and major axes of the fitted ellipses were utilized to define rectangular segmentation masks, facilitating the extraction of fluorescent intensity for each cell across all frames. Areas devoid of cells were used to extract the background intensity of each frame.

3.4.12 FABRICATION OF MICROFLUIDIC DEVICES FOR SWIMMING COMPETITION EXPERIMENTS

For swimming competition experiments, we utilized a microfluidic device comprising a long linear channel with dimensions of 1.2 mm x 2 cm x 100 μm (width, length, height). These devices were fabricated following the procedure outlined in [164]. To establish a cost-effective method of producing devices without the necessity for silicon wafer masters, we manufactured epoxy molds utilizing the silicon wafer-molded PDMS devices as masters [188]. The devices were submerged in a degassed mixture of epoxy and hardener (epoxacast 690, Smooth-On) in a 10:3 ratio, and the mixture was allowed to solidify at room temperature for 2 days. Similar to silicon wafers, a hydrophobic coat of chlorotrimethylsilane was applied via vapor deposition.

To cast PDMS devices, the master mold was coated with a layer of degassed 10:1 PDMS:curing agent mixture (Sylgard 184, Dow Corning) and cured at room temperature for 2 days due to the low glass transition temperature of the epoxy mold. Individual devices were then cut and separated from the wafer, and a 0.75-mm outlet and a 2-mm cell reservoir were created on either side of the linear channel using biopsy punches (World Precision Instruments). Subsequently, the devices underwent cleaning with transparent adhesive tape (Magic Tape, Scotch), followed by rinsing sequentially with isopropanol, methanol, and Millipore-filtered water. After drying the devices using nitrogen, they were treated, alongside glass-bottom dishes (GWST-5040, WillCo Wells), in a plasma cleaner (PDC-002, Harrick Plasma). Following a 60-second exposure to ambient air plasma under a 300 mTorr vacuum, the devices were laminated onto the glass-bottom dishes and baked on an 80°C hot plate for 5 minutes to establish a covalent bond. Then, after cooling the devices to room temperature, they were immediately utilized for experiments.

3.4.13 SWIMMING COMPETITION EXPERIMENTS

For swimming competition experiments, cells (TSS2096/pTrc99A/pVS118 for WT experiments or TSS2096/ pSJAB21/pVS118 for high-variability experiments) grown in rich media were collected at the appropriate OD by centrifugation (5 min at 5,000 RPM) and washed twice in 10mL MotM. Cells were then concentrated to OD = 1.0 for aspartate wave experiments or OD = 2.0 for serine wave experiments. In parallel, the microfluidic linear channel devices were filled with either 100μM L-aspartate or 100μM L-serine (Sigma-Aldrich) in MotM supplemented with 0.05% w/v polyvinylpyrrolidone-40 (Sigma-Aldrich) from the 0.75-mm outlet. Subsequently, excess liquid was removed from the 2-mm cell reservoir and 5μL cell suspension was loaded gently into the reservoir. The outlet was sealed with adhesive tape (Magic Tape, Scotch) to prevent flow due to differences in hydrostatic pressure across the device.

Migrating waves in swimming competition experiments were imaged immediately after cell loading using an inverted microscope (Eclipse Ti-E, Nikon) equipped with an environmental chamber (Okolab) set to a temperature of 33.5°C and 80% humidity. YFP images of the bacterial wave were captured through a 10x 0.30 NA objective lens (Nikon). The field of view was illuminated with a 500 nm LED (pE-4000, CoolLED) set to maximum intensity, with an exposure time of 100 ms. Images were recorded by a sCMOS camera (ORCA-Flash 4.0 V2, Hamamatsu). To track the bacterial wave, the microscope stage (MicroStage, Mad City Labs) was programmed using a custom MATLAB script to translocate every 10 seconds by one frame width (1.33 mm). Six consecutive images were taken for each sweep, and full sweeps occurred every 60 seconds until the wave had traversed all six consecutive fields of view. A control experiment revealed that nearly zero growth took place during the total duration of the experiment (Figure 3.17c and 3.17d).

For wave speed analysis, raw YFP images were stitched into single images for each sweep using custom MATLAB scripts. The initial stitched image, which lacked cells, was subtracted from subsequent images to eliminate imaging artifacts. Images were then segmented using a modified Otsu algorithm, filtering out objects smaller than 100 pixels. Subsequently, image intensities were

normalized between one and zero, and a Gaussian function was fitted to the intensity profile along the long axis of the channel (Figure 3.15). The wave position was determined by identifying the peak of each Gaussian, and velocity was calculated by extracting the distance between successive peaks and dividing it by the time between sweeps (60 seconds).

3.4.14 CHEMORECEPTOR COPY NUMBER QUANTIFICATION ON SWIM PLATES

Experiments with swim plates were performed similarly to what we reported on Chapter 5.

Briefly, to quantify the chemoreceptor copy number of cells forming colonies on swim plates, cells (strain TSS2144/pC100B-12) grown in rich media were collected at OD = 0.45 and diluted to OD = 0.01 using fresh media. Then, 10 μL of cell culture was inoculated in the center of semi-solid agar plates. The agar plates were made using rich media, as described above, supplemented with 0.26% bacteriological agar (Avantor). Liquid media and agar plates were supplemented with appropriate antibiotics and inducers, refer to Table 3.2. The plates were incubated at a temperature of 33.5°C and 100% humidity until the colonies reached the edge of the plate. Cells from the center and the edge of the migrating colony were collected using pipette tips and diluted into minimal MotM for subsequent fluorescent imaging. To quantify chemoreceptor numbers, we followed the same fluorescent imaging protocol as for receptor-labeled cells grown in liquid cultures.

For experiments involving non-motile cells used as biosensors for gene expression, cells (strain TSS2144) grown in rich media were collected at OD = 0.45 and mixed with fresh rich media supplemented with 0.26% bacteriological agar to achieve a final OD = 0.01. Swim plates were allowed to solidify at room temperature for 2-3 hours, following which 10 μL of OD = 0.01 motile cell culture (strain TSS2096) was inoculated in the center of the semi-solid agar plates. The motile population of cells shapes the gradient of the plate, ensuring that the non-motile biosensor strain encounters the same local environment as motile cells. Once the migrating cell colony reached the edge of the plate, cells from the center and the edge of the colony were collected using pipette tips and diluted into minimal MotM for subsequent fluorescent imaging.

3.4.15 FABRICATION OF MICROFLUIDIC DEVICES FOR SINGLE CELL SWIM TRACKING

To track the run-and-tumble motion of single cells, we utilized a microfluidic device comprising a long linear channel with dimensions of 0.5 mm x 3 cm x 60 μm (width, length, height). These devices were fabricated following the procedure outlined in Chapter 5. Briefly, the master mold was coated with a layer of degassed 10:1 PDMS:curing agent mixture (Sylgard 184, Dow Corning) and cured at 80°C for 12 hours. After cooling the wafer to room temperature, individual devices were cut and separated from the wafer, and a 0.75-mm outlet and a 0.75-mm inlet were created on either side of the linear channel using biopsy punches (World Precision Instruments). Subsequently, the devices underwent cleaning with transparent adhesive tape (Magic Tape, Scotch), followed by rinsing sequentially with isopropanol, methanol, and Millipore-filtered water. A 22 mm x 50 mm glass coverslip was rinsed sequentially with acetone, isopropanol, methanol, and Millipore-filtered water. After drying the devices and the coverslips using nitrogen, they were treated in a plasma cleaner (PDC-32G, Harrick Plasma). Following a 60-second exposure to ambient air plasma under a 300 mTorr vacuum, the devices were laminated onto the glass coverslips and baked on an 80°C hot plate for 5 minutes to establish a covalent bond. Then, after cooling the devices to room temperature, they were immediately utilized for experiments.

3.4.16 SWIM TRACKING EXPERIMENTS

For swim tracking experiments, WT cells (strain TSS2096) grown in rich or minimal media were collected at the appropriate OD by centrifugation (5 min at 5,000 RPM) and washed twice in 10mL

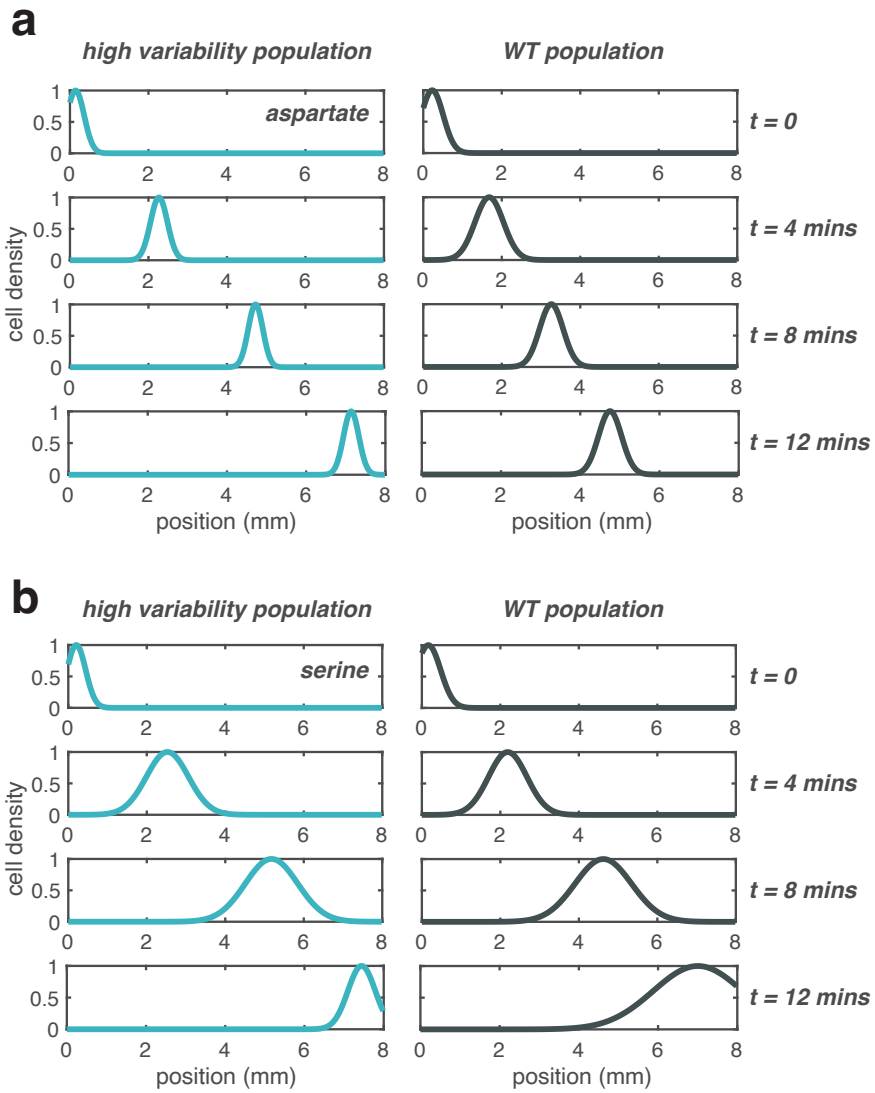

Figure 3.15: Wave position extraction. **(a)** Wave position of the high variability (left) and wild-type (WT) population (right) in a gradient of 100 μM L-aspartate. Cell density is extracted from the segmented wave images shown on figure 3.6b. Curves represent Gaussian function fits to the images. **(b)** Similar to panel a, but for cells in a gradient of 100 μM L-serine.

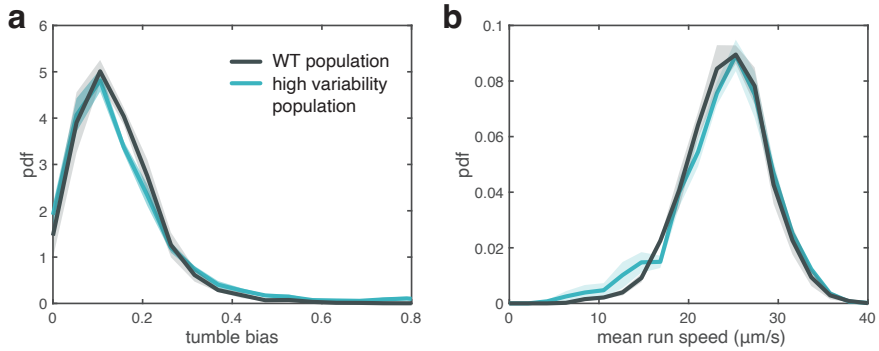

Figure 3.16: Tumble bias and run speed distributions are identical for the WT and high variability populations. **(a)** Tumble bias distribution of the high variability and wild-type populations in the absence of a chemical gradient are identical. Solid lines represent the mean of four independent biological replicates, with shaded areas indicating the standard error of the mean. **(b)** Same as panel a, but for the mean run speed of the high variability and wild-type populations.

MotM supplemented with 0.05% w/v polyvinylpyrrolidone-40 (Sigma-Aldrich). Cells were then diluted to an OD of 0.001. Subsequently, 10 μL of the mixture was introduced into the device from the inlet and excess liquid was removed from the outlet. Both the outlet and the inlet were then sealed with adhesive tape (Magic Tape, Scotch) to prevent flow due to differences in hydrostatic pressure across the device.

Swimming cells were imaged immediately after cell loading using an inverted microscope (Eclipse Ti-E, Nikon) equipped with a custom environmental chamber set to a temperature of 30°C and 50% humidity for experiments in Figure 3.8e and 3.10 or 33.5°C and 80% humidity for experiments in Figure 3.16, to match the environmental conditions of swimming competition experiments. Phase-contrast images of swimming bacteria were captured through a 4x 0.13 NA phase objective lens (Nikon). Images were recorded by a sCMOS camera (ORCA-Flash 4.0 V2, Hamamatsu) at 20 frames per second.

To detect and track cells and extract their tumble bias and run speed, a custom MATLAB script was used as described in [189]. Trajectories shorter than 10 seconds were excluded for further analysis. In a typical experiment, 4 fields of view where imaged for 200 seconds each, containing a total of at least 1000 cell trajectories.

3.4.17 GROWTH RATE MEASUREMENTS

To assess the growth rate of the FRET (TSS2191/pSJAB106) and WT (TSS2097) strains, we employed a microplate reader (Epoch 2 microplate reader, BioTek). Overnight cultures in rich media were diluted 1:50 into fresh media and overnight cultures in minimal media were diluted 1:200 into fresh media. For the FRET strain, the appropriate antibiotic and inducer concentrations were added to the media (refer to Table 3.2). Subsequently, 200 μL of diluted cells were aliquoted into each well of a 96-well plate (Costar 3595, Corning) and loaded into the plate reader. The plates were incubated at 33°C while continuously shaking in a double orbital pattern (1 mm radius, 807 cpm). The OD of each well was measured every 10 minutes for 12 hours for rich media and every 20 minutes for 24 hours for minimal media. The growth rates measured in the plate reader were within 10% of those obtained by sampling the shaking batch culture used for microscopy experiments.

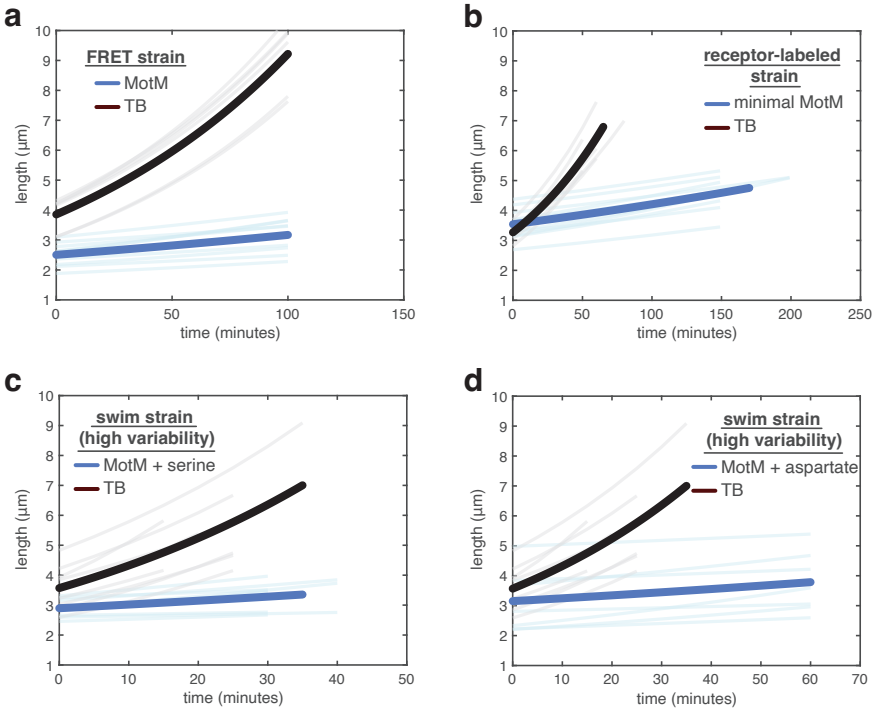

Figure 3.17: Growth rate of the strains used in this study is negligible during experiments. **(a)** Cell elongation of the FRET strain (TSS2191/pSJAB106) as a function of time. Blue line represents the mean elongation rate of the stain in motility media (MotM), the buffer used for FRET experiments, while the black line represents the mean elongation rate of the same strain in TB, the rich media used to grow the strain. **(b)** Similar to panel a, but for the strain used in receptor-quantification experiments (TSS2155) in its measurement buffer, minimal motility media (minimal MotM). **(c)** Similar to panel a, but for the high variability strain used in swimming competition experiments (TSS2096/pTrc99A/pVS118) in MotM with 100 μM L-serine added. **(d)** Same as in panel c, but with 100 μM L-aspartate added to MotM.

3.4.18 GROWTH RATE AND CELL VOLUME QUANTIFICATION

The quantification of *tar* and *tsr* promoter activities as a function of growth rate was conducted using a plate reader assay, as described above. The growth rate of the bacteria is expressed as doublings per hour and is calculated as:

$$\text{growth rate} = \frac{\log_{10}(\text{OD}_{t_2}) - \log_{10}(\text{OD}_{t_1})}{(t_2 - t_1)\log_{10}(2)} \tag{3.7}$$

To extract cell volume from the two-dimensional phase-contrast images, we assume that cells are cylinders flanked by hemispherical caps. For a cell of width w_{cell} and length L_{cell}, the total volume of the two hemispherical caps is given by:

$$V_{\text{sphere}} = \frac{4}{3}\pi r^3 = \frac{1}{6}\pi w_{\text{cell}}^3 \tag{3.8}$$

While the volume of the cylindrical segment of the cell is given by:

$$V_{\text{cylinder}} = \pi r^2 L = \pi\left(\frac{w_{\text{cell}}}{2}\right)^2 (L_{\text{cell}} - w_{\text{cell}}) = \frac{1}{4}\pi w_{\text{cell}}^2 (L_{\text{cell}} - w_{\text{cell}}) \tag{3.9}$$

And the total cell volume is given by:

$$V_{\text{cell}} = V_{\text{sphere}} + V_{\text{cylinder}} = \frac{1}{6}\pi w_{\text{cell}}^3 + \frac{1}{4}\pi w_{\text{cell}}^2 (L_{\text{cell}} - w_{\text{cell}}) \tag{3.10}$$

4

DYNAMICS OF SENSORY DIVERSITY WITHIN AND ACROSS GENERATIONS

Even in constant environments, isogenic bacterial cell populations demonstrate remarkable levels of sensory diversity. While we have shown that this diversity originates from stochastic gene expression, it remains unclear how sensory phenotypes change during the cell's division cycle. Additionally, how sensory preferences are transmitted across generations is poorly understood. In this Chapter, utilising the bacterium E. coli as a model system, we demonstrate that the average sensory phenotype of individual cells remains stable throughout their lifetime. This is because its primary determinant — the ratio of the two major chemoreceptors (Tar/Tsr) — remains constant throughout the cell cycle, exhibiting robustness against protein concentration fluctuations associated with cell growth. However, we observe a decrease in the diversity of sensory phenotypes as the cell cycle progresses, driven by a reduction in Tar/Tsr ratio diversity. Furthermore, we identify an asymmetry in the inheritance of the Tar/Tsr ratio between daughter cells, directly influencing the heritability of sensory preferences. We identify receptor protein clustering and the asymmetric partitioning of these clusters during cell division as the primary mechanisms driving this asymmetry. These findings highlight the contributions of cell-cycle-related temporal variations to the standing sensory diversity, while also providing new quantitative insights regarding epigenetic transmission and persistence of sensory phenotypes across generations.

4.1 INTRODUCTION

Phenotypic diversity in bacterial populations, despite their clonal nature and limited genetic diversity, is a well-recognized phenomenon [175] [150] [29] [190] [26]. In particular, chemotaxis—bacteria's movement in response to chemical stimuli—benefits significantly from non-genetic diversity. This diversity enables cell populations to adopt a variety of sensing phenotypes, allowing them to adapt to fluctuating environmental conditions, as we demonstrate in Chapter 3 of this thesis. Although the diversity in chemotaxis and sensing has been extensively characterized in bacterial cells with a fixed proteome, the dynamic changes in sensing phenotypes as cells grow remain poorly understood.

The *Escherichia coli* chemotaxis pathway [11], an entirely protein-based signaling network, serves as a robust experimental model for studying sensing mechanisms independent of gene expression and growth. However, this characteristic has limited studies of behavioral diversity to non-growing cells, providing only a snapshot of cell-to-cell variability due to stochastic gene expression [175] [150] [29] [30]. This approach neglects key cellular parameters, such as the cell cycle phase. Consequently, research on the temporal variability of the *E. coli* chemotaxis pathway under no-growth conditions primarily captures noise from stochastic protein-protein interactions, failing to account for how slow temporal variations related to cell growth impact behavior. As cells grow, new proteins in the chemotaxis pathway must be synthesized to counterbalance dilution, potentially altering sensing behavior significantly. Moreover, the stochastic partitioning of chemotaxis pathway proteins among daughter cells during division contributes to cell-to-cell variability in sensing [191] [192]. This aspect is particularly important in bacterial chemotaxis where chemoreceptor proteins are organized in large molecular assemblies, the chemoreceptor clusters. How these clusters are partitioned upon division and how this partitioning affects sensory preference has never been studied before.

The *E. coli* chemotaxis pathway is one of the most well-characterized models of biological signaling. It detects chemical and physical signals through arrays composed of five distinct types of chemoreceptors. The two primary receptors, Tar (sensing aspartate) and Tsr (sensing serine), make up 90% of the total chemoreceptor population when *E. coli* is grown in rich media. *E. coli* achieves motility through a run-and-tumble mechanism: active kinase CheA phosphorylates the response regulator CheY, producing CheY-P. Attractant molecules binding to chemoreceptors decrease CheA activity, reducing CheY-P levels and decreasing the bacterium's tendency to tumble, thereby enhancing its directed movement.

One significant challenge in studying behavior in growing cells is the need for precise environmental control while minimally perturbing the cells. To address this, we designed a custom microfluidic chemostat, known as a "mother machine" [154], which is amenable to high-throughput single-cell fluorescent and phase-contrast microscopy. By combining this microfluidic device with an in vivo FRET sensor for the activity of the kinase CheA, we measured several signaling parameters in single cells, such as ligand sensitivity and pre-stimulus activity of the chemotaxis pathway, while monitoring cell-cycle phases and positions in the lineage tree using phase-contrast microscopy and a machine learning-based image segmentation approach. Since bacterial cultures are asynchronous, i.e., different cells in a population are at a different cell-cycle phase, it is necessary to follow a cell from its birth to its division in order to extract its cell-cycle phase.

Additionally, using chromosomal fluorescent fusions of Tar and Tsr, we tracked the copy numbers of these key chemotaxis proteins in growing cells.

These tools enabled us to study how cell-cycle-related temporal variations influence sensing behavior in individual bacteria and how sensory preferences are transmitted across generations in isogenic populations. Our approach provides new insights into the mechanisms governing sensory diversity and inheritance in bacterial populations.

4.2 RESULTS

4.2.1 SENSITIVITY TO LIGAND IS ON AVERAGE ROBUST AGAINST CELL-CYCLE PHASE VARIATION

To probe ligand sensitivity as a function of the cell-cycle phase, we developed a custom microfluidic chemostat that enables thousands of cells to undergo steady-state growth. The device features an array of narrow and shallow growth channels where cells are confined perpendicular to a large main feeding channel with low fluidic resistance, ensuring continuous and rapid flow of growth medium (Figure 4.1a). This design allows rapid stimulus delivery, necessary for dose-response measurements, while maintaining steady-state conditions by ensuring consistent nutrient supply and waste removal—critical for observing cellular behavior under a constant environment.

We performed dose-response measurements by stimulating adaptation-deficient (CheRB-) cells with pulses of the attractant α-methylaspartate (MeAsp). MeAsp, a non-metabolizable analogue of the amino acid aspartate, was chosen because it elicits a chemotactic response without affecting cellular growth [193], allowing us to measure chemotactic responses without interference from metabolic effects. Cells were grown in minimal media supplemented with glycerol as the sole carbon source, which is not a chemoattractant and thus does not influence the chemotactic response to MeAsp [7]. Minimal media solutions were used to incrementally add and remove varying concentrations of MeAsp, ensuring that cell growth was not disrupted during the dose-response measurement. The total duration of each dose-response measurement was limited to 15 minutes, which is a small fraction of the cell division time in that medium, determined to be over 2 hours. To mitigate phototoxicity, FRET measurements were limited to 150 frames every 2.5 hours. Importantly, cell growth resumed normally post-FRET assessment (Figure 4.1b, left panels), affirming that cells were minimally perturbed by the fluorescent measurement.

We monitored the output of the signaling pathway via fluorescent microscopy in single cells using an *in vivo* CheYZ FRET sensor for the activity of the kinase CheA, while simultaneously tracking the cell-cycle phase by observing cell elongation and division events using phase-contrast microscopy and machine-learning-based cell segmentation (*Methods*). We define $\phi = 0$ as the cell-cycle phase at birth and $\phi = 1$ as the cell-cycle phase immediately before the cell divides again. The cell-cycle phase during the FRET measurement was therefore defined as: $\phi_{\text{FRET}} = \frac{t_{\text{FRET}} - t_B}{t_D - t_B}$ where t_{FRET} is the midpoint of the FRET experiment, t_B the birth time, and t_D the division time. The time interval between birth and division is well approximated by a single exponential function (Figure 4.1b, left panels). The resulting dose-response data for each cell were fitted with a sigmoidal Hill function of the form $\frac{1}{1+\left(\frac{[L]}{K_{1/2}}\right)^H}$ where $K_{1/2}$ represents ligand sensitivity and H the cooperativity between receptors (Figure 4.1b, right panels).

Although single-cell dose-response curves varied significantly, owing to the high cell-to-cell variability in $K_{1/2}$ and H, the average dose-response curves for cells binned according to their cell-cycle phase were identical (Figure 4.1c). This indicates that sensing is, on average, robust against variations in cell-cycle phase and thus remains constant throughout the cell's lifetime. Extracting the $K_{1/2}$ and H parameters from those dose-response curves reaffirmed that they remain constant regardless the cell-cycle phase (Figure 4.1d). Further supporting this observation, a scatter plot of single-cell $K_{1/2}$ values as a function of cell-cycle phase ϕ can be fitted with a flat line, indicating no correlation between $K_{1/2}$ and ϕ (Figure 4.1e).

To verify that sensing is truly constant as a function of cell-cycle phase and not an artifact of under-sampling the dose-response curve, we conducted an experiment with more densely sampled dose-response curve, were we increased the number of datapoints from 7 to 11. To avoid excessive cell growth during the dose-response measurement, we stimulated cells, on average, with only one concentration of MeAsp per cell cycle. The dose-response curves, constructed from the average

response of multiple cells within the same cell-cycle phase bin, were again identical for all phase bins (Figure 4.6).

Interestingly, we found that the diversity of $K_{1/2}$, measured as the coefficient of variation (CV, defined as standard deviation divided by the mean), decreases as the cell cycle progresses, even though the mean $K_{1/2}$, remains constant (Figure 4.1f), indicating that populations comprised of cells early in their cell cycle are more diverse.

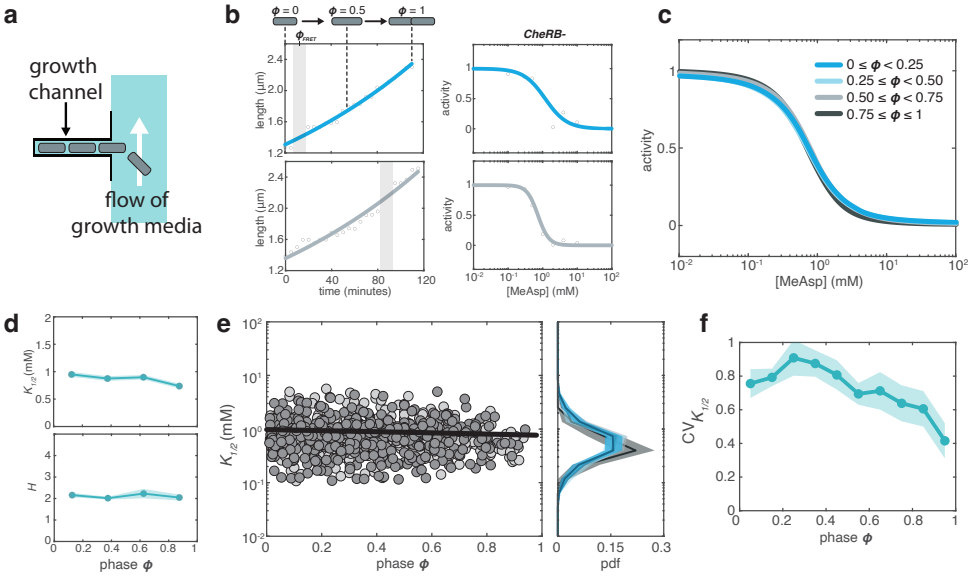

Figure 4.1: Average ligand sensitivity remains robust to cell-cycle phase variation in adaptation-deficient cells. **(a)** Schematic of microfluidic chemostat. Cells are confined within growth channels, where they undergo steady-state growth. Growth media and ligand stimuli for dose-response measurements are delivered through diffusion inside the growth channels via the feeding channel. **(b)** (Left) Cell length as a function of time for two representative cells. The interval between birth and division is fitted by a single exponential function. Shaded area represents the time interval of the FRET measurement. (Right) Hill function fits to MeAsp dose-response data from the same two cells. Line color of the exponential and Hill fits corresponds to the cell-cycle phase bin of the cells. The color scheme matches panel (c). **(c)** Population-averaged Hill function fits to MeAsp dose-response data obtained for cells belonging to four distinct cell-cycle phase bins. Data from two independent experiments. **(d)** Scaling of average $K_{1/2}$ (top) and H (bottom) across four cell-cycle phase bins, with data from two independent experiments. Shaded areas indicate the standard error of the mean. **(e)** Single-cell $K_{1/2}$ values as a function of cell-cycle phase ϕ. Solid line is a linear fit to the data. Data from two independent experiments indicated by different shades of gray. (Right margin) Histograms of $K_{1/2}$ values from single-cell dose-response curves for four cell-cycle phase bins. The color scheme matches panel (c). Shaded areas represent 95% confidence intervals obtained through bootstrap resampling. **(f)** Scaling of coefficient of variation (CV) of the inverse of ligand sensitivity, $K_{1/2}$, as a function of cell cycle phase ϕ. Each bin represents 10% of the total cell cycle, with points centered in each interval. Shaded areas indicate 95% confidence intervals obtained through bootstrap resampling.

4.2.2 PRE-STIMULUS ACTIVITY OF THE CHEMOTAXIS PATHWAY IS ON AVERAGE ROBUST AGAINST CELL-CYCLE PHASE VARIATION

Next, we investigated how the steady-state kinase activity of the chemotaxis system changes throughout the cell cycle. This kinase activity is crucial for bacterial behavior, as it controls flagellar motor

rotation. We used the same microfluidic system and wild-type, adaptation-proficient (CheRB+) cells growing in minimal media to determine the steady-state kinase activity via FRET measurement. To calibrate the FRET levels, we applied a saturating step of a mixture of MeAsp and L-serine to determine the FRET level corresponding to zero kinase activity (activity = 0). We then determined the FRET level for fully active kinases (activity = 1) after removing the saturating stimulus following adaptation (Figure 4.2a). The steady-state activity a_0 of each cell was defined as the time-averaged activity before ligand addition.

We monitored cell elongation and division events (Figure 4.2a) and determined the cell cycle phase ϕ associated with each a_0. Plotting steady-state activity a_0 against cell cycle phase ϕ revealed no correlation, indicating that steady-state kinase activity is robust against variations in the cell cycle phase. The steady-state activity a_0 varied strongly between cells, with a coefficient of variation (CV) of 0.23, identical to the value observed for cells measured under non-growth conditions [150].

Interestingly, when cells were binned according to their cell cycle phase, the CV of the steady-state activity a_0, unlike the CV of the inverse of ligand sensitivity, $K_{1/2}$, remained mostly constant across all cell cycle phase bins (Figure 4.2c). This suggests that both the steady-state activity and variability in the steady-state activity are constant throughout the cell cycle.

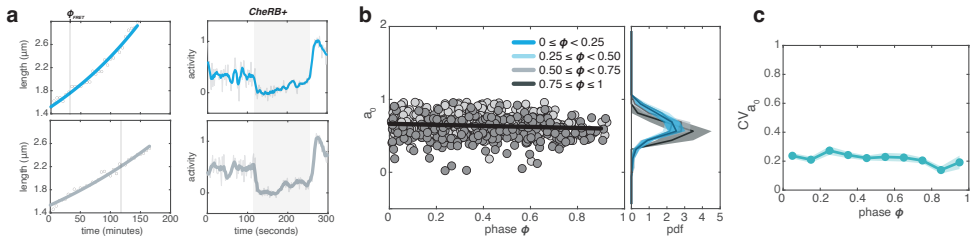

Figure 4.2: Average pre-stimulus activity remains robust to cell-cycle phase variation in adaptation-proficient cells. **(a)** (Left) Cell length as a function of time for two representative cells. The interval between birth and division is fitted by a single exponential function. Shaded area represents the time interval of the FRET measurement. (Right) Normalized kinase activity of the same two cells. Shaded area represents stimulation with a mixture of 1mM MeAsp and 1mM L-serine. Gray lines represent unfiltered data and superimposed colored lines represent the same data filtered with a 10s moving average filter. Line color of the exponential and Hill fits corresponds to the cell-cycle phase bin of the cells. The color scheme matches panel **b**. **(b)** Single-cell a_0 values as a function of cell-cycle phase ϕ. Solid line is a linear fit to the data. Data from two independent experiments indicated by different shades of gray. (Right margin) Histograms of a_0 values for four cell-cycle phase bins. Shaded areas represent 95% confidence intervals obtained through bootstrap resampling. **(c)** Scaling of coefficient of variation (CV) of the pre-stimulus activity, a_0, as a function of cell cycle phase ϕ. Each bin represents 10% of the total cell cycle, with points centered in each interval. Shaded areas indicate 95% confidence intervals obtained through bootstrap resampling.

4.2.3 RATIO OF THE TWO MAJOR CHEMORECEPTORS, TAR/TSR, IS CONSTANT AS A FUNCTION OF CELL-CYCLE PHASE

Next, we sought to understand how cells maintain a constant $K_{1/2}$, robust against protein copy number fluctuations resulting from the synthesis of new proteins in the chemotaxis pathway and dilution due to cell growth. In Chapter 3, We have shown that the primary determinant of $K_{1/2}$ is the ratio of the two major chemoreceptors, the aspartate receptor Tar and the serine receptor Tsr. To investigate how the Tar/Tsr ratio evolves as a function of cell cycle phase, we used fusions of the tar and tsr genes at their native chromosomal loci, where tar is fussed to mCherry and tsr to a monomeric form of YFP (mYFP). Using the same microfluidic and microscopy system employed for the FRET experiments, we were able to periodically measure the Tar and Tsr protein copy

numbers and the associated cell cycle phase ϕ of thousands of growing cells. Receptor protein copy numbers were measured every 20 minutes in minimal media to minimize phototoxicity and photobleaching, which could result in underestimating the number of receptors, while the cell cycle was measured every 5 minutes with phase-contrast microscopy that delivers very small amounts of light power and thus perturbs the cells minimally [194]. Importantly, the growth rate of cells inside the mother machine was identical to that of cells growing in a batch culture (Figure 4.10a and 4.10b), highlighting the minimal perturbance of cells in the mother machine under our experimental conditions.

A confounding factor when measuring fast dynamic events, such as gene expression, is the maturation time of the fluorophores. The fluorophore maturation time affects the accuracy of measured protein levels, as the non-fully matured fluorophore fraction does not fluoresce with its maximum intensity. To address this, we estimated the maturation profiles of the two fluorophores using an exponential function and retrieved the original gene expression dynamics from the measured fluorescence by performing deconvolution in the frequency domain. To assess the exact time required for mCherry and mYFP to reach 50% of their full intensity, we exposed cells growing at steady state in the mother machine to the non-lytic translational inhibitor antibiotic chloramphenicol. The subsequent measured increase in fluorescence was therefore due to fluorophore maturation and not fluorophore production (Figure 4.7) [195].

When plotting the deconvolved Tar/Tsr ratio, we found that it remains constant as a function of cell cycle phase ϕ for both adaptation-deficient (CheRB-) and adaptation-proficient (CheRB+) cells grown in minimal media (Figures 4.3a and 4.3c, respectively). Similarly, CheRB+ cells grown in rich media also exhibited a constant Tar/Tsr ratio as a function of ϕ (Figure 4.8). We found that the CV of these ratios decreases as the cell cycle progresses (Figures 4.3b and 4.3d), consistent with theoretical predictions [191].

We observe the same trends—namely, a constant Tar/Tsr ratio and a decreasing coefficient of variation (CV) of the ratio—when using cell length as a proxy for cell-cycle phase in an experiment where cellular growth was suspended, allowing cells to mature before imaging (Figure 4.9). As a result, fluorescence deconvolution was not required. This confirms that our observations are not artifacts of the fluorescence deconvolution process.

These results suggest that the trend we observed in the $K_{1/2}$ –cell cycle phase relationship—constant mean but decreasing CV—can be fully explained by the evolution of the Tar/Tsr ratio as a function of the cell cycle phase. On the other hand, the magnitude of pre-stimulus kinase activity a_0 likely depends on the ratio of the adaptation enzymes CheR/CheB, rather than the Tar/Tsr receptor ratio. Furthermore, the CheB phosphorylation feedback has been shown to attenuate cell-to-cell variability [150]. This provides a sufficient explanation for why the CV of a_0 remains constant as a function of ϕ, while the CV of the Tar/Tsr ratio decreases as a function of ϕ in CheRB+ cells.

Lastly, we explored the origin of this decrease of Tar/Tsr diversity as the cell-cycle progresses. Receptor proteins tend to form clusters that primarily localize at the cell poles [196] [197], hence, when the cell divides, each daughter cell inherits a single receptor protein cluster, leading to biased partitioning of the receptor proteins. Mutants of the scaffolding protein CheW, such as the CheW-X3 mutant [198], form signaling complexes that are dispersed across the cell membrane instead of clustering at the cell poles. This can be observed by comparing the cell intensity profile in the inset of Figure 4.3f to the profiles in the insets of Figures 4.3b and 4.3d. The deconvolved Tar/Tsr ratio remained constant as a function of cell cycle phase ϕ in CheW-X3 cells (figure 4.3e), while the CV of the ratio only decreased marginally as a function of the cell cycle phase (figure 4.3f) and was lower in magnitude than the Tar/Tsr ratio CV of cell with wild-type CheW (figure 4.3d). These results suggest that the biased partitioning of receptor clusters upon cell division drives the observed high Tar/Tsr ratio diversity in cells early in their cell-cycle phase.

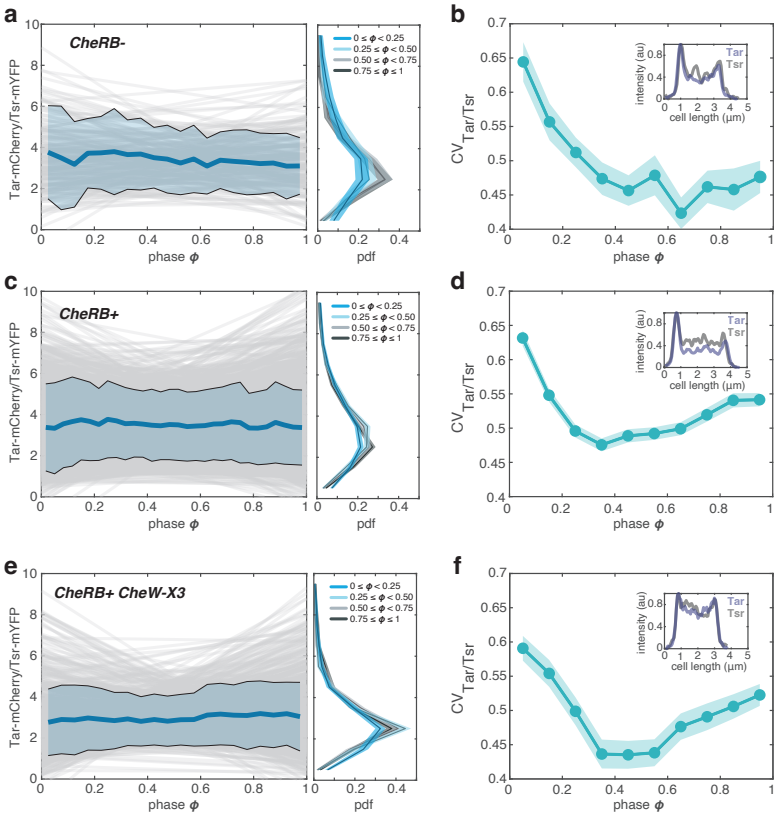

Figure 4.3: Major chemoreceptor ratio, Tar/Tsr, is constant as a function of cell-cycle phase in adaptation-deficient and adaptation-proficient cells. **(a)** Chemoreceptor Tar/Tsr ratio as a function of cell-cycle phase ϕ in adaptation-deficient (CheRB$^-$) cells. Gray lines represent polynomial fits to single-cell receptor copy number measurements deconvolved for fluorophore maturation. Blue line is a polynomial fit to the average of all measurements. Shaded area represents the standard deviation of the mean. (Right margin) Histograms of Tar/Tsr ratio distributions for four cell-cycle phase bins. Shaded areas represent 95% confidence intervals obtained through bootstrap resampling. Cells from a single experiment. **(b)** Scaling of coefficient of variation (CV) of the Tar/Tsr ratios as a function of cell cycle phase ϕ. Each bin represents 6.66% of the total cell cycle, with points centered in each interval. Shaded areas indicate 95% confidence intervals obtained through bootstrap resampling. (Inset) Tar-mCherry and Tsr-mYFP fluorescence intensity along the long axis of a representative cell. **(c)** As in (a), but for adaptation-proficient (CheRB$^+$) cells. Cells from two independent experiments. **(d)** As in (b), but for adaptation-proficient (CheRB$^+$) cells. **(e)** As in (c), but for cells defective in cluster formation (CheW-X3 mutation). Cells from a single experiment. **(f)** As in (d), but for cells defective in cluster formation (CheW-X3 mutation).

4.2.4 SLOW RELAXATION OF THE TAR/TSR RATIO UPON GROWTH ENVIRONMENT SHIFT DEMONSTRATES THE EXISTENCE OF AN EPIGENETIC ENVIRONMENTAL MEMORY

Next, we investigated how the Tar/Tsr receptor ratio evolves across generations in cells wild-type for chemotaxis. We monitored the receptor ratio, after deconvolving the maturation timescale, in the cell located at the end of the growth channel, known as the "old-pole mother cell" [154], which typically remains confined in the growth channel for the entire experiment. This cell retains its old pole through successive divisions, incrementing its generation number with each division.

Our findings indicate that in minimal media, the receptor ratio remains constant across generations (Figure 4.4a). Similarly, in rich media, the receptor ratio stabilizes after a brief relaxation period (Figure 4.4b). The initial high receptor ratio is due to transferring the cells from a shaking culture, where they had partially depleted the amino acids, to the chemostat culture, where they experience a stable environment. As we demonstrated in Chapter 3, the receptor ratio is influenced by cell density in rich media but remains constant in minimal media.

We also explored how rapidly a sensing phenotype can adapt to a new environment. We measured the Tar/Tsr ratio of cells initially growing in minimal media and then switched to rich media after approximately two generations. The receptor ratio gradually adjusted to the level typically observed in rich media (Figure 4.4c), taking about eight generations to fully relax. This slow relaxation establishes the existence of an epigenetic memory of the environment that is inherited from mother to daughter cells and lasts for about eight generations.

This epigenetic memory highlights the importance of maintaining high chemotactic diversity to respond rapidly to environmental changes. In the measured Tar/Tsr ratio distributions, the tail of the receptor ratio distribution in minimal media partially overlaps with that of rich media (figure 4.4d), meaning that a subset of cells in minimal media already has the optimal receptor ratio needed to thrive in rich media. In a scenario where the entire population in minimal media has low Tar/Tsr ratio diversity, the entire population would require multiple generations, corresponding to many hours of growth, to adapt to the new environment. To demonstrate that effect, we simulated a population of cells with a Tar/Tsr distribution following a normal distribution with a mean value equal to the experimentally determined mean Tar/Tsr ratio in minimal media but with a standard deviation identical to that of the Tar/Tsr ratio in rich media (figure 4.4e). Then, we assessed the overlap of the high diversity distribution (experimentally determined Tar/Tsr ratio distribution in minimal media) and the low diversity distribution (simulated distribution) with the Tar/Tsr ratio distribution in rich media. The percent overlap of the two distributions is a measure of "population readiness" to the new environment upon abrupt environment shifts (figure 4.4f). Cells in the measured high diversity population had a non-zero population readiness already from the first generation after the environment shifted. In contrast, cells in the simulated low diversity population required multiple generations until their readiness reached non-zero values, demonstrating the need of high chemotactic diversity for *E. coli* to survive in rapidly changing environments, such as the mammalian gut.

4.2.5 NON-GENETIC INHERITANCE OF SENSORY PREFERENCE

Finally, we aimed to understand how sensory phenotypes and sensory preferences are inherited among mother and daughter cells. As previously discussed, in WT cells, chemoreceptors form clusters often localized at the cell's poles (figure 4.5a, top panel). Mutations in the scaffolding protein CheW, such as the CheW-X3 mutation, cause the receptor clusters to disperse along the cell membrane (figure 4.5a, bottom panel). Due to the polar localization of receptor clusters in WT cells, each time the mother cell, which remains confined at the dead-end of its growth channel, divides, one daughter cell inherits the old-pole cluster ("old daughter"), while the other daughter

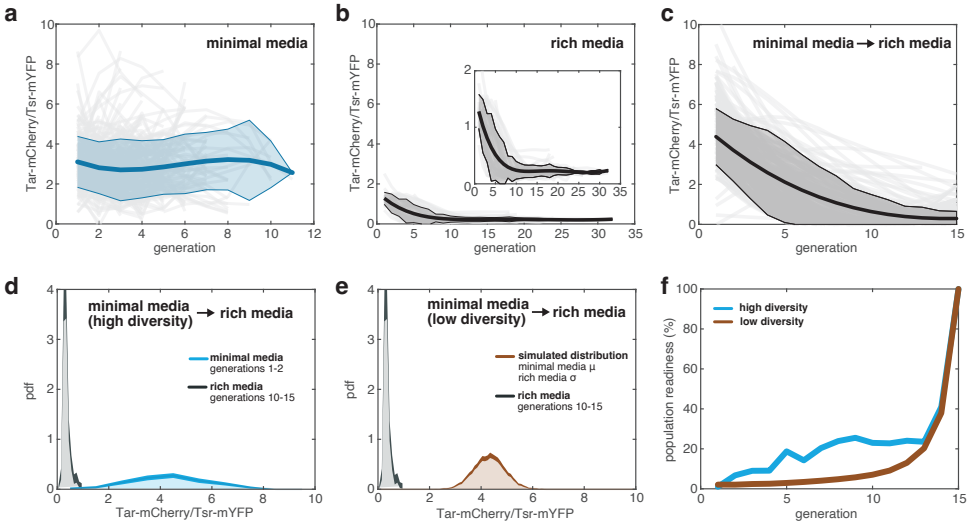

Figure 4.4: Slow relaxation of the Tar/Tsr ratio upon growth environment shift demonstrates the existence of an epigenetic environmental memory. **(a)** Chemoreceptor Tar/Tsr ratio as a function of generation number in adaptation-proficient (CheRB$^+$) cells. Gray lines represent polynomial fits to single-lineage receptor copy number measurements deconvolved for fluorophore maturation. Blue line is a polynomial fit to the average of all measurements. Shaded area represents the standard deviation of the mean. Data from a single experiment. **(b)** As in (a), but for cells grown in rich media. **(Inset)** Magnified version of the same plot. **(c)** As in (a), but the environment is shifted from minimal to rich media after approximately two generations. **(d)** Histograms of Tar/Tsr ratio distributions of the cells in panel (c). Darker shaded areas represent 95% confidence intervals obtained through bootstrap resampling. **(e)** Histogram of a simulated low diversity Tar/Tsr ratio distribution (red curve) with a mean value μ equal to that of the blue curve in panel (d) and a standard deviation σ equal to that of the black curve in panel (d). Rich media distribution is replotted from panel (d). **(f)** Population readiness to environment shifts, determined as the percent overlap of the low (panel (e)) and high (panel (d)) diversity distributions to the rich media distribution at generation 15. The simulated low diversity distribution retains the same standard deviation for all generations, but its mean is shifted every generation by a constant step size until it reaches the mean value of the rich media distribution at generation 15.

cell inherits the new-pole cluster ("young daughter"), as shown schematically in figure 4.5b. We compared the receptor ratio of adaptation-proficient WT cells grown in rich media.

We compared the receptor ratio of adaptation-proficient WT cells grown in rich media and found a positive correlation between mother cells and their progeny (Figure 4.5c). Similarly, when comparing the receptor ratio of adaptation-proficient CheW-X3 mutant cells grown in rich media, we also found a positive correlation between mother cells and their progeny (Figure 4.5d). Similar correlation was also found for Tar and Tsr separately ((Figure 4.11)).

To assess the degree of phenotypic similarity between mother and daughter cells, we calculated the Pearson correlation coefficient ρ between all mother-daughter pairs [199]. We found that, for WT cells grown in both rich and minimal media, the mother cell has a higher degree of similarity with its old daughter cell compared to its young daughter cell (Figure 4.5e). This asymmetry between old and young daughter cells is largely alleviated in the CheW-X3 mutant in both rich and minimal media.

Taken together, these results suggest that receptor protein clustering at the cell poles and the asymmetric partitioning of these clusters during cell division is the primary mechanism driving the asymmetry in the heritability of the Tar/Tsr ratio between daughter cells.

Interestingly, this non-genetic phenotypic inheritance directly affects the inheritance of sensory preference and chemotactic behavior: the inverse of ligand sensitivity, $K_{1/2}$, and pre-stimulus activity, a_0, of mother are more strongly correlated with their old daughter cells compared to their young daughter cells (Figure 4.5f).

In conclusion, our findings demonstrate that the polar clustering of receptor proteins and their asymmetric inheritance during cell division play crucial roles in the heritability of sensory phenotypes and sensory preferences. The differential inheritance patterns between mother and daughter cells, particularly between old and young daughters, highlight the importance of cellular architecture in non-genetic phenotypic inheritance

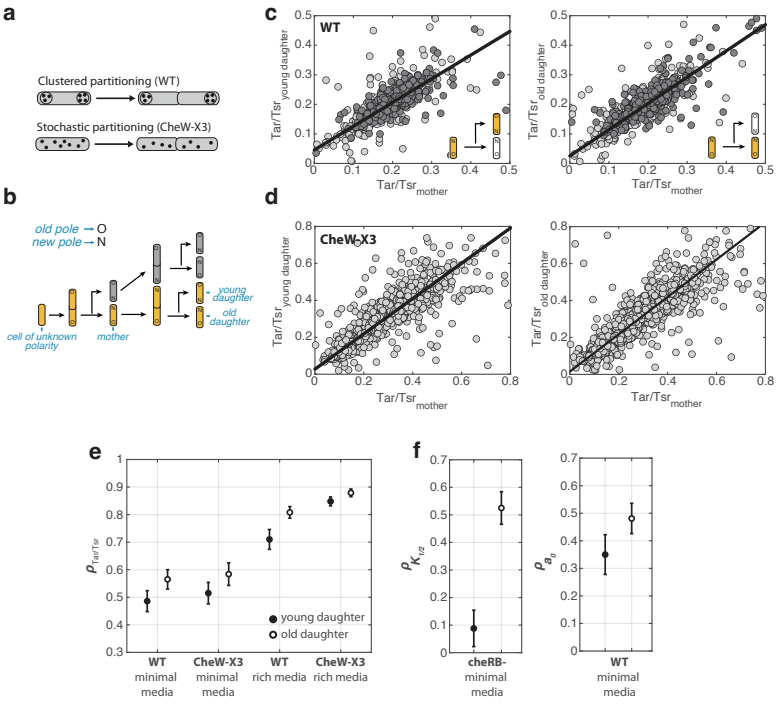

Figure 4.5: Asymmetric inheritance of Tar/Tsr ratio and sensory preference. **(a)** Schematic diagram of protein localization and inheritance. Clustered proteins (top), such as the chemoreceptor clusters, are partitioned in a biased manner during cell division. On the other hand, when clustering is disrupted (bottom), such as in cells carrying the CheW-X3 mutation, proteins are partitioned in a stochastic manner. **(b)** Schematic diagram of pole inheritance. When a mother cell divides, its young daughter cell inherits the newer cell pole (and hence the newer receptor cluster), while its old daughter cell inherits the old pole and cluster. **(c)** Scatter plot of Tar/Tsr ratio in mother-young daughter (left) and mother-old daughter (right) pairs for WT adaptation-proficient cells grown in rich media. Data from two independent experiments indicated by different shades of gray. **(d)** As in (c), but for CheW-X3 adaptation-proficient cells grown in rich media. Data from a single experiment. **(e)** Pearson correlation coefficients of Tar/Tsr ratio for WT and CheW-X3 cells grown in either rich or minimal media. Quantities are derived from two independent experiments for WT cells and a single experiment for CheW-X3 cells. Error bars represent 95% confidence intervals and standard error of the mean obtained through bootstrap resampling. **(f)** Pearson correlation coefficients of $K_{1/2}$ (left) and a_0 (right) for adaptation-deficient (CheRB-0 and WT cells, respectively). Both quantities are derived from two independent experiments. Error bars represent standard error of the mean and 95% confidence intervals obtained through bootstrap resampling.

4.3 DISCUSSION

Our study aimed to understand how sensory phenotypes change during an organism's lifetime and how those phenotypes are transmitted across generations. Bacteria serve as an excellent system to study these questions since they reproduce clonally and are genetically uniform. Through advancements in microfluidic technology, automated microscopy, and machine-learning-based image analysis, we measured both the sensory phenotypes of growing cells and their molecular determinants, specifically the copy numbers of sensory proteins, for the first time.

Utilizing the *E. coli* chemotaxis pathway as a model, we observed that the sensory phenotype, represented by the inverse of ligand sensitivity, $K_{1/2}$, primarily determined by the ratio of the two major chemoreceptors, Tar and Tsr, remains stable throughout the cell cycle. This stability persists despite fluctuations in protein concentration due to cell growth, suggesting a robust mechanism that maintains sensory function regardless of cell-cycle phase.

Interestingly, while the mean $K_{1/2}$ remains constant, the diversity of $K_{1/2}$ decreases as the cell cycle progresses. This reduction in variability indicates that cells early in their cell cycle exhibit greater sensory diversity, which gradually diminishes as they approach division. This trend is corroborated by our observation that the Tar/Tsr ratio diversity also decreases over the cell cycle. Such a trend can act as a bet-hedging strategy: newly born cells, which need resources to grow, exhibit diverse sensing phenotypes, allowing them to more efficiently detect and exploit new nutrient sources.

Furthermore, we observed that the pre-stimulus activity of the cell, a_0, is also robust against cell-cycle variations. This finding complements the observation that the steady-state FRET level does not correlate with cell length, a proxy for cell-cycle phase [29], and aligns with classic observations from nearly 50 years ago that the tumbling bias after stimulus recovery does not correlate with cell length [182].

Our discovery of an epigenetic environmental memory, wherein the Tar/Tsr ratio adjusts slowly to new growth conditions, highlights the adaptive advantage conferred by maintaining a diverse sensory phenotype population. This diversity ensures that some cells are pre-adapted to potential environmental shifts, facilitating the survival of the population as a whole in rapidly fluctuating environments.

Finally, a key finding of our study is the identification of receptor clustering at the cell poles and its asymmetric partitioning during cell division as critical determinants of sensory phenotype inheritance. In wild-type cells, receptor clusters localize at the poles, resulting in one daughter cell inheriting the old-pole cluster and the other the new-pole cluster. This asymmetrical inheritance leads to a higher degree of similarity in the Tar/Tsr ratio between mother cells and their old daughter cells compared to their young daughter cells. Such asymmetry is largely mitigated in CheW-X3 mutants, which lack polar receptor clustering, underscoring the importance of spatial protein organization in sensory inheritance. This non-genetic phenotypic inheritance has implications for the inheritance of sensory preferences. We demonstrated that the sensory phenotype, characterized by ligand sensitivity and pre-stimulus activity, is more strongly correlated between mother cells and their old daughter cells than between mother cells and their young daughter cells. The inheritance of pre-stimulus activity between mother and daughter cells complements the recent observation that behavioral states in swimming cells are inherited [199].

Taken together, our results suggest that *E. coli* has evolved to ensure that its sensing capabilities and unstimulated behavior are robust against slow fluctuations associated with the progression of its cell cycle. Furthermore, our findings highlight the importance of phenotypic diversity to counteract the slow epigenetic environmental memory and the importance of spatial organization in the inheritance of phenotypes.

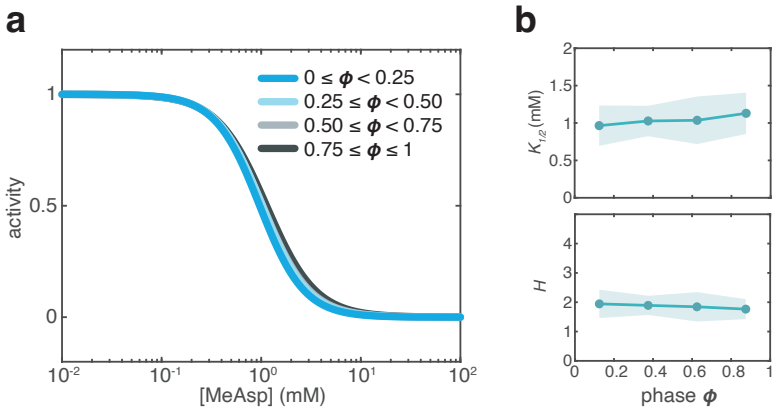

Figure 4.6: Average ligand sensitivity remains robust to cell-cycle phase variation in adaptation-deficient cells when cells are stimulated on average once per cell cycle. **(a)** Population-averaged Hill function fits to MeAsp dose-response data obtained from cells belonging to four distinct cell-cycle phase bins. Data were collected by stimulating cells, on average, once during their cell cycle. A total of 11 MeAsp stimuli were delivered throughout the experiment, each administered every 2 hours, which approximately corresponds to the duration of a single cell cycle under our experimental conditions. The dose-response curve was constructed by binning all cells that belonged to the same cell-cycle phase bin and experienced the same stimulus. While this method does not provide single-cell dose-response data (as presented in Figure 4.1), it minimally perturbs the cells and allows for better sampling of the dose-response curve (11 points here vs. 7 points in Figure 4.1). Even with this approach, no discernible differences in the dose-response curves were observed among cells at different cell-cycle phase bins. **(b)** Scaling of average $K_{1/2}$ (top) and H (bottom) across the four cell-cycle phase bins. Shaded areas indicate fitting error.

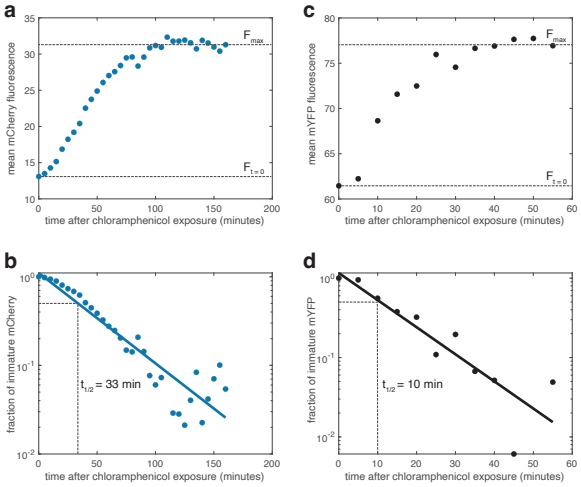

Figure 4.7: Assessment of maturation time of mCherry and mYFP. **(a)** Cells expressing the Tar-mCherry and Tsr-mYFP fusion proteins are exposed to the non-lytic translational inhibitor antibiotic chloramphenicol in the mother machine at time $t = 0$. In the absence of translation, the subsequent increase in mCherry fluorescence is solely due to fluorophore maturation. Here, $F_{t=0}$ denotes the fluorescence at the moment of antibiotic exposure, and $F_{\max}$ represents the maximum fluorescence. The trajectory shown is the average fluorescence of 5 cells. **(b)** To determine the fraction of immature mCherry proteins, we transform the mean mCherry fluorescence into the fraction of immature proteins using the following formula [195]: $1 - \frac{F(t)-F_{t=0}}{F_{\infty}-F_{t=0}}$. From this analysis, the maturation half-time for mCherry (time to reach 50% maturation) is determined to be 33 minutes. **(c)** Same as (a), but for mYFP. **(d)** Same as (b), but for mYFP. Analysis shows that the maturation half-time for mYFP is 10 minutes.

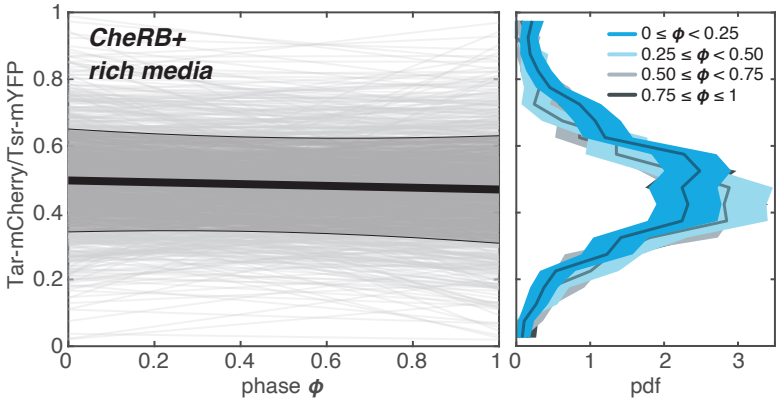

Figure 4.8: Major chemoreceptor ratio, Tar/Tsr, is constant as a function of cell-cycle phase in adaptation-proficient cells grown in rich media. **(a)** Chemoreceptor Tar/Tsr ratio as a function of cell-cycle phase ϕ in adaptation-proficient (CheRB$^+$) cells. Gray lines represent polynomial fits to single-cell receptor copy number measurements deconvolved for fluorophore maturation. Blue line is a polynomial fit to the average of all measurements. Shaded area represents the standard deviation of the mean. (Right margin) Histograms of Tar/Tsr ratio distributions for four cell-cycle phase bins. Shaded areas represent 95% confidence intervals obtained through bootstrap resampling. Cells from a single experiment.

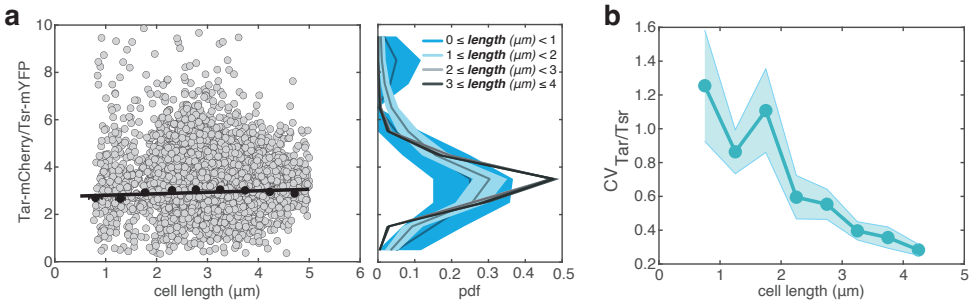

Figure 4.9: Major Chemoreceptor Ratio, Tar/Tsr, remains constant as a function of cell length in adaptation-deficient cells grown in minimal media **(a)** The chemoreceptor Tar/Tsr ratio is plotted as a function of cell length in adaptation-deficient (CheRB$^-$) cells grown in minimal media to an optical density (OD) of 0.45. The cell genotype and growth media composition are identical to those used in Figure 4.3a. Growth was suspended by placing the cells in minimal motility media (see Chapter 3 for details). No deconvolution for fluorophore maturation was performed since cell were allowed to mature at room temperature before imaging. Gray points represent individual cells from a single experiment. The black line represents a linear fit to the binned data (black points). On the right margin, histograms show the distributions of the Tar/Tsr ratio for four cell-cycle phase bins. Shaded areas represent 95% confidence intervals obtained through bootstrap resampling. **(b)** Scaling of the coefficient of variation (CV) of the Tar/Tsr ratio as a function of cell length. Shaded areas indicate 95% confidence intervals obtained through bootstrap resampling.

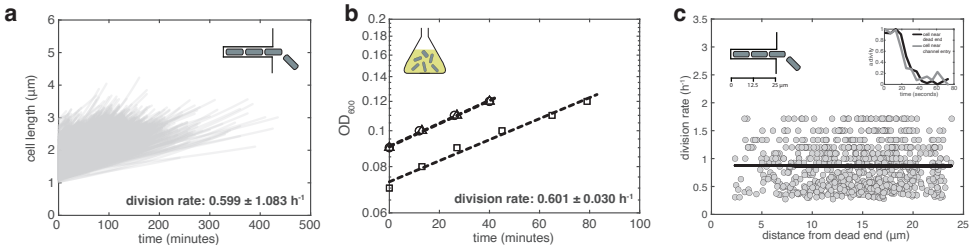

Figure 4.10: Growth rate is identical in the mother machine and batch cultures, and independent of cell position within growth channels. **(a)** Cell length of adaptation-proficient, receptor-labeled cells growing in the mother machine as a function of time. Gray lines represent exponential fits to single-cell data. The growth rate is derived from the same experiment as shown in Figure 4.3c. On average, the division rate is identical to that of the same genotype growing in batch culture (panel b) and is expressed as the mean ± standard deviation across all cells. **(b)** Optical density of adaptation-proficient, receptor-labeled cells as a function of time growing in minimal media batch culture in early exponential phase. The growth rate was measured by sampling the batch culture at regular intervals. Different symbols represent data from three biological replicates, while dashed lines indicate exponential fits to the data. The division rate is reported as the mean ± standard deviation of the three replicates. **(c)** Division rate of adaptation-proficient, receptor-labeled cells as a function of their position within the growth channel in the mother machine. Gray points represent the growth rates of individual cells. Unlike panels (a) and (b), this analysis examines cells growing in rich media rather than minimal media. This distinction is made because the growth rate of fast-growing cells is expected to be more sensitive to potential delays in nutrient diffusion or upstream consumption within the growth channels compared to cells grown in minimal media. However, the data indicate that the growth rate remains independent of cell position within the growth channel. The growth rate data are from the same experiment presented in Figure 4.8. Inset: The response time delay to a saturating concentration of MeAsp is below 6 seconds (the acquisition interval in this experiment) between a cell located near the dead-end of the channel and a cell near the entrance of the same channel. This highlights that diffusion is rapid within the growth channels of the mother machine. Nutrient consumption is not a factor here, as MeAsp is not metabolizable by *E. coli*. FRET data are from the experiment presented in Figure 4.1.

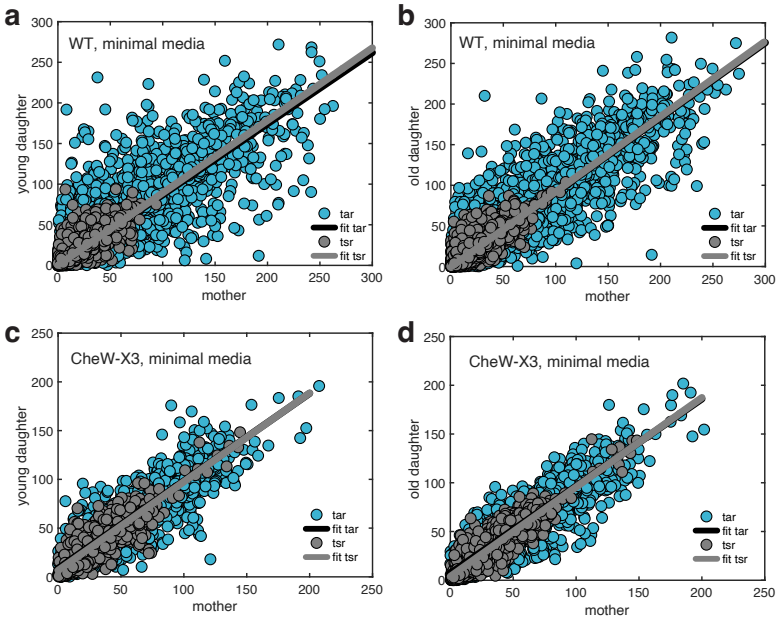

Figure 4.11: Tar and Tsr inheritance in WT and CheW-X3 cells growing in minimal media. Tar and Tsr are inherited in a similar fashion between the young daughter and mother cells **(a)** or the old daughter and mother cells **(b)** of WT (adaptation-proficient cells), and between the young daughter and mother cells **(c)** or the old daughter and mother cells **(d)** of WT CheW-X3 cells. Lines are linear fits to the single-cell data and are identical for Tar and Tsr in all cases.

4.4 METHODS

4.4.1 STRAINS AND PLASMIDS

E. coli strain MG1655 ΔFliC::FLP, a generous gift from Victor Sourjik, was used as a background for all FRET and receptor quantification strains.

For FRET experiments, we conducted an in-frame deletion of the cheYZ genes, resulting in strain TSS2104 and an in-frame deletion of the cheRBYZ genes, resulting in strain TSS2105. The FRET acceptor-donor pair, consisting of CheY-mRFP1 and CheZ-mYFP (A206K variant), was expressed in tandem from an IPTG induced, pTrc99A plasmid (pSJAB106, [150]).

For receptor quantification experiments, starting with the same MG1655 ΔFliC::FLP parent strain used in FRET experiments, tsr was translationally fused with mYFP (A206K variant), and tar was translationally fused with mCherry, at their respective native chromosomal loci, yielding strain TSS2144. Additionally, we produced a variant where the cheRB genes were deleted in-frame (yielding strain TSS2155), and a variant where the CheW-X3 mutation was introduced (yielding strain TSS2263).

4.4.2 GROWTH CONDITIONS

For experiments conducted in minimal media, cells were retrieved from a -80°C glycerol-based stock and inoculated in 2 ml H1 minimal salts medium (MMH1; 50 mM KPO4, 0.5 mM MgSO4, 7.6 mM (NH4)2SO4, 1.25 μM Fe2(SO4)3, adjusted to pH 7.0) supplemented with 0.5% v/v glycerol, 0.01% w/v thiamine hydrochloride, and 100 μg/mL ampicillin when necessary to maintain the FRET plasmid. Cultures were then incubated for approximately 24 hours at 33.5°C and 250 RPM until saturation. Subsequently, cells from the saturated culture were diluted at least 1:200 in 10 ml of MMH1 supplemented with the same supplements indicated above and 100 μg/mL ampicillin and 15 μM IPTG when necessary to maintain and induce the FRET plasmid. Cultures were grown overnight at 33.5°C with shaking at 250 RPM until mid-exponential phase.

For experiments conducted in rich media, cells were retrieved from the same -80°C glycerol-based stock and inoculated in 2 ml tryptone broth (TB; 1% bactotryptone, 0.5% NaCl, adjusted to pH 7.0). The cultures were then incubated overnight at 33.5°C and 250 RPM until saturation. Subsequently, cells from the saturated overnight culture were diluted 1:50 in 10 ml of TB and grown at 33.5°C and 250 RPM until mid-exponential phase.

4.4.3 MICROFLUIDIC CHEMOSTAT DESIGN AND FABRICATION

Custom microfluidic chemostats, commonly known as "mother machines [154]," were fabricated using the silicone polymer PDMS as we described in Chapter 3. Briefly, the master mold for the PDMS device was created on a silicon wafer with features imprinted on a layer of SU-8, an epoxy-based negative photoresist [184]. The features were defined using UV light exposure through two separate photomasks.

The first layer of the device consisted of an array of shallow and narrow growth channels, each measuring 25 μm in length and 0.96 μm in height. To accommodate cells of varying sizes due to different growth rates in minimal and rich media, the growth channels had widths ranging from 0.7 μm to 1.2 μm, with increments of 0.1 μm. This variation ensured the tight confinement of cells regardless of their size. The edges of these channels were smoothed to minimize optical aberrations during phase-contrast imaging [185]. The second layer of the device featured a deeper and wider feeding channel with low fluidic resistance, essential for rapid liquid exchange during stimulus-response measurements. This feeding channel measured 12 mm in length, 100 μm in width, and 32.5 μm in height. The designs for both layers were created using CAD software (klayout) and transferred onto two separate quartz photomasks (Photronics). The silicon master mold was fabricated at AMOLF's cleanroom facilities. After fabrication, a hydrophobic coating of

chlorotrimethylsilane (Sigma-Aldrich) was applied via vapor deposition to the master mold.

To cast the PDMS devices, the master mold was coated with a degassed 10:1 PDMS:curing agent mixture (Sylgard 184, Dow Corning) and cured at 80°C for 1 hour. Once cooled to room temperature, individual devices were cut from the wafer, and inlets and outlets for each feeding channel were created using a 0.75-mm biopsy punch (World Precision Instruments). The device was designed to be axially symmetric, allowing the inlet and outlet of each feeding channel to be swapped. In each experiment, the opening closer to the imaged cells was used as the inlet to minimize liquid exchange time. To remove any residual uncured PDMS, the devices were immersed in a pentane bath for 2 hours, followed by two 2-hour acetone baths. The PDMS devices were then dried at room temperature overnight.

For bonding, the PDMS devices were cleaned with transparent adhesive tape (Magic Tape, Scotch) and treated, along with glass-bottom dishes (GWST-5040, WillCo Wells), in a plasma cleaner (PDC-002, Harrick Plasma). A 60-second exposure to ambient air plasma under a 300 mTorr vacuum facilitated the lamination of the PDMS devices onto the glass-bottom dishes. These laminated devices were then baked on an 80°C hot plate for 5 minutes to establish a covalent bond. To prevent cell attachment, the PDMS surface was passivated by incubating the devices with a 10 mg/ml BSA solution for 45 minutes at 37°C, allowing the BSA solution to be drawn into the growth channels via evaporation through the gas-permeable PDMS. The devices were then immediately used for experiments.

4.4.4 FRET AND RECEPTOR RATIO MEASUREMENTS IN GROWING CELLS

Experiments were conducted similarly to what is described in Chapter 3. Briefly, cells were collected by centrifugation (5 min at 5,000 RPM) and concentrated tenfold in their growth media. Then, 10 μL of this concentrated culture was injected into a microfluidic chemostat through its inlet. The inlet and outlet of the chemostat were sealed with adhesive tape (Magic Tape, Scotch) to prevent flow, and the entire device was centrifuged for 20 minutes at 800 RPM, with the growth channels oriented parallel to the centrifugal force to force cells into the growth channels. Following centrifugation, the device was incubated for 2-5 hours at 33.5°C to allow additional cells to enter the growth channels via diffusion. Next, the growth media were placed inside glass reservoirs pressurized to 130 kPa using nitrogen. For stimulus-response experiments, ligands were placed inside 15 mL Falcon tubes and pressurized to 150 kPa alongside the growth media reservoirs to enable rapid liquid exchange. These reservoirs were then connected through separate tubes to a distribution valve (M Switch, Fluigent), which in turn was connected to the microfluidic device via a tube plugged into the inlet. The distribution valve input was controlled through a custom MATLAB script.

Imaging was performed using an inverted microscope (Eclipse Ti-E, Nikon) equipped with an oil-immersion 100x 1.45 NA phase-contrast objective lens (Nikon) and an automated stage (MicroStage, Mad City Labs). The microscope was set to a temperature of 33.5°C and 80% humidity within an environmental chamber (Okolab) for all experiments.

For FRET experiments, illumination occurred every 7 seconds for CheRB- cells or 2 seconds for CheRB+ cells using a 500 nm LED (pE-4000, CoolLED) with a pulse duration of 20 milliseconds. Epifluorescent light was split into two channels via a 2-camera image splitter (TwinCam, Cairn Research) equipped with a 580 nm dichroic mirror (Semrock) and two emission filters (520 nm and 593 nm, Semrock), capturing donor (YFP) and acceptor (RFP) channels separately. To mitigate the drift in fluorescence intensities due to fluorophore bleaching, the FRET ratio of each cell (defined as RFP/YFP) was fitted with an exponential function. Subsequently, the FRET ratio was divided by the exponential and normalized between one and zero, as desribed in the main text.

For receptor quantification experiments, mYFP and mCherry fluorescence were excited using an LED system (pE-4000, CoolLED). A 100 ms 500 nm LED excitation pulse was used for mYFP and a 200 ms 580 nm LED excitation pulse for mCherry, both at maximum intensity. Emissions

were captured sequentially using a multi-band filter (Semrock) and directed into two identical sCMOS cameras (ORCA-Flash4.0 V2, Hamamatsu) via a 2-camera image splitter (TwinCam, Cairn) equipped with a 580 nm dichroic mirror (Semrock). Imaging occurred every 20 minutes to minimize phototoxicity and photobleaching, except for experiments determining the receptor ratio as a function of the cell cycle phase in rich media, where images were acquired every 5 minutes. To ensure accurate determination of the Tar/Tsr ratio, excitation pulse durations and intensities for mYFP and mCherry were calibrated using a two-color fluorescent repressor-operator system (FROS) standard as described in Chapter 3.

Phase-contrast images were acquired in all experiments every minute for growth in rich media or every 5 minutes for growth in minimal media to extract cell morphology and cell-cycle phase and to determine a segmentation mask. For FRET experiments, a single field of view (FOV) was imaged, while for receptor-ratio experiments, 6 sequential (but non-overlapping, to avoid over-excitation) FOVs were imaged.

4.4.5 FRET AND RECEPTOR RATIO IMAGE ANALYSIS

Image analysis was performed as described in Chapter 3. Briefly, to accurately segment bacteria cells growing in the microfluidic chemostat, we trained a convolutional neural network (CNN) based on the U-Net architecture [186] [187] to predict the outline of each cell. Using custom Python scripts, we transformed the original microscopy images into maps of cell outlines. For training, we simultaneously acquired fluorescent images of cells expressing the bright CheY-mRFP1 fusion and phase-contrast images. We then manually created binary masks for cell outlines in 500 CheY-mRFP1 512x512 pixel images and augmented this dataset using geometric transformations such as scaling, translation, and rotation. This augmented dataset was used to train the CNN.

After the training phase, we applied the CNN to transform 2000 CheY-mRFP1 frames, distinct from the training dataset, without any post-processing. The CNN generated 512x512 pixel output matrices for each image, with high scores corresponding to cell outlines, while cell bodies and the background had nearly zero scores. We then re-trained the CNN using phase-contrast images and the binary masks generated by the CNN from CheY-mRFP1 images as inputs, further augmenting these datasets with geometric transformations. This method increased our training dataset fourfold, while only manually segmenting CheY-mRFP1 images, which are easier to segment than phase-contrast images due to the brightness of the fluorescent fusion protein and near-zero background fluorescence.

The main advantage of using phase-contrast images for cell segmentation is the elimination of the need for an additional fluorescent protein and imaging channel, as well as avoiding phototoxicity associated with fluorescent imaging. Visual inspection of the transformed images revealed consistent cell masks produced by the CNN, regardless of whether the original image was obtained through fluorescence or phase-contrast microscopy.

The CNN output binary matrices were further processed by thresholding using a modified Otsu algorithm and removing small clusters of unconnected pixels, setting only the pixels corresponding to cell outlines to unity and all other pixels to zero. Image alignment from the two cameras was performed using a custom MATLAB script employing an affine transformation. All images were registered based on the first image of the experiment using a rigid transformation to correct for movement of the microfluidic device. Fiducial markers in the form of growth channel numbering were incorporated into the device to assist with image registration. Finally, individual growth channels were cropped by summing the fluorescence of both channels and detecting peaks in the fluorescence intensity profile.

For cell segmentation, we used the MATLAB regionprops function, which detects cells in the CNN-transformed images as elliptical objects. For each cell, we determined its minor and major axes, along with the x- and y-coordinates of its centroid. The centroid was tracked across all frames,

assuming that interframe movement could not exceed a threshold defined as one quarter of the shortest cell length in any given image. Movement was considered only along the long axis of the growth channel, minimizing the tracking problem to a one-dimensional problem. Cell divisions were identified by abrupt changes in cell length (the major axis of the fitted ellipse), coupled with an increase in cell count. Conversely, a reduction in cell count, along with the disappearance of centroids near the origin of the growth channel, indicated cells exiting towards the feeding channel. Finally, the minor and major axes of the fitted ellipses were used to define rectangular segmentation masks, facilitating the extraction of fluorescent intensity for each cell across all frames. Areas devoid of cells were used to extract the background intensity of each frame.

4.4.6 FLUOROPHORE MATURATION CORRECTION

To accurately measure gene expression dynamics using fluorophore-tagged genes, it is necessary to account for the fluorophore maturation time, which can distort the observed dynamics. We employed a deconvolution approach to separate the true gene expression signal from the maturation effects. The maturation kinetics were modeled as an exponential function:

$$m(t) = 1 - e^{-\lambda t} \tag{4.1}$$

where λ is the maturation constant of the fluorophore. The maturation time t_m is related to λ by $t_m = \frac{1}{\lambda}$. We determined experimentally the time $t_{1/2}$ for the fluorophores to reach 50% maturation to be 33 minutes for mCherry and 10 minutes for mYFP (Figure 4.7), which is identical to values reported in the literature for the same fluorophores [195]. By setting $m(t) = 0.5$, we then obtain:

$$\lambda = \frac{\ln(2)}{t_{1/2}} \tag{4.2}$$

The observed fluorescence $F(t)$ signal was treated as the convolution of the maturation function $m(t)$ with the actual gene expression dynamics $g(t)$:

$$F(t) = (g * m)(t) = \int_0^t g(\tau)\, m(t-\tau)\, d\tau \tag{4.3}$$

which then becomes:

$$F(t) = \int_0^t g(\tau) \left(1 - e^{-\lambda(t-\tau)}\right) d\tau \tag{4.4}$$

By transforming both the observed signal and the maturation function into the frequency domain using a Fourier transform of the form:

$$\hat{F}(f) = \hat{g}(f) \cdot \hat{m}(f) \tag{4.5}$$

which is equivalent to:

$$\hat{g}(f) = \frac{\hat{F}(f)}{\hat{m}(f)} \tag{4.6}$$

We were able to divide the transformed signals and apply the inverse Fourier transform to retrieve the deconvolved gene expression rate $g(t)$.

One assumption of this model is that the total fraction of fluorophores is immature at the start of the cell cycle. This is true for newly synthesized fluorophores, but does not account for the fluorophore fraction inherited from the mother cell upon cell division. To account for that, we track the lineage of each cell and identify their mother cell. Then, we follow the same deconvolution

process for the mother cell and assume that half of the total matured fluorophore fraction is inherited to each daughter cell at division. Therefore, the total gene expression product is given by:

$$g_{\text{total}}(t) = g_{\text{daughter}}(t) + \frac{1}{2} g_{\text{mother}}(t = t_{\text{division}}) \tag{4.7}$$

This method allows for an accurate assessment of gene expression by mitigating the confounding effects of fluorophore maturation.

5

NON-GENETIC ADAPTATION BY COLLECTIVE MIGRATION

Cell populations must adjust their phenotypic composition to adapt to changing environments. One adaptation strategy is to maintain distinct phenotypic subsets within the population and to modulate their relative abundances via gene regulation. Another strategy involves genetic mutations, which can be augmented by stress-response pathways. Here, we studied how a migrating bacterial population regulates its phenotypic distribution to traverse diverse environments. We generated isogenic Escherichia coli populations with varying distributions of swimming behaviors and observed their phenotype distributions during migration in liquid and porous environments. We found that the migrating populations became enriched with high-performing swimming phenotypes in each environment, allowing the populations to adapt without requiring mutations or gene regulation. This adaptation is dynamic and rapid, reversing in a few doubling times when migration ceases. By measuring the chemoreceptor abundance distributions during migration towards different attractants, we demonstrated that adaptation acts on multiple chemotaxis-related traits simultaneously. These measurements are consistent with a general mechanism in which adaptation results from a balance between cell growth generating diversity and collective migration eliminating under-performing phenotypes. Thus, collective migration enables cell populations with continuous, multi-dimensional phenotypes to flexibly and rapidly adapt their phenotypic composition to diverse environmental conditions.

5.1 INTRODUCTION

Cell populations use various mechanisms to adapt their phenotypic distribution to new environments. One approach is to acquire mutations, such as in bacterial efflux pumps [200] [201] or the binding sites of EGFR [202] in cancer cells, to evade stressors. These processes typically occur over tens of generations [203] [204] [205]. Another common approach is to regulate gene expression or switching between discrete phenotypic states [206] [207]. A classic example of phenotypic switching is persister formation, where bacteria [26] [206] [208] or cancer cells [209] transition between antibiotic-resistant and chemotherapy-tolerant states [210] [211].

Here, we examined whether and how a migrating bacterial population regulates its phenotypic composition according to the environments it encounters. Groups of *Escherichia coli* cells collectively migrate by consuming attractant cues in their environment and chasing the traveling gradient that they create [165] [212]. Individual cells with the same genotype exhibit varying tumble biases (TB) (Figure 5.1a), chemoreceptor abundances (Figure 5.1b), and other chemotaxis-relevant phenotypes, leading to differences in the speeds at which they climb the attractant gradients [175]. These cells can travel together by spatially organizing within the migrating group such that their gradient-climbing abilities match the local steepness of the attractant gradient [165] (Figure 5.1c). However, this spatial sorting mechanism is imperfect: cells at the back, or the low performers, slowly fall behind the migrating population because the attractant concentration falls below the detection limit of their receptors [165]. To maintain migration, the lost cells must be replaced through cell divisions [153] [213].

A recent theoretical model proposed that a dynamic balance between loss of low-performing phenotypes due to migration and production of new phenotypes by growth might be sufficient to adapt the population's composition to new environments [153]. These two processes would balance out such that the traveling population becomes enriched with "fitter" phenotypes—those with higher chemotactic performance—increasing its expansion speed [165] [153]. Since the demands of migration are different in different environments, which phenotypes are enriched should depend on the environment the population traverses [153] (Figure 5.1d). This proposed mechanism does not require environment-dependent mutations or gene regulation. However, this model has never been experimentally tested.

Here, we experimentally demonstrate this novel adaptation mechanism. By measuring the distribution of swimming behaviors and chemoreceptor abundances during migration in distinct environments, we observed that migrating *E. coli* populations tune their own distributions of chemotactic behaviors, without relying on gene regulation or mutations. Adaptation relies on the balance between the differential loss of low-performing phenotypes and the generation of diversity by growth during migration in each environment. The relaxation from the adapted distribution to the standing batch distribution occurs in approximately two generations. More broadly, migration and other collective behaviors when combined with growth may generally provide rapid and flexible ways for diverse populations to adapt to changing conditions.

5.2 RESULTS

5.2.1 COLLECTIVE MIGRATION TUNES THE POPULATION'S DISTRIBUTION OF SWIMMING PHENOTYPES

First, we investigated whether the TB distribution of an *E. coli* population can be adapted during collective migration with growth. Given that some swimming phenotypes are better at navigating than others [165] [175] we expected the TB distribution of a population, regardless of its starting point, to enrich for higher performing TBs during collective migration. To test this hypothesis, we compared the TB distributions of populations grown to exponential phase in batch cultures to those

of populations migrating at constant speed on agarose swim plates containing excess nutrients. Excess nutrients ensure that cells in the migrating front are experiencing exponential growth [214] [177].

Populations with different batch TB distributions were generated by controlling the expression levels of the phosphatase CheZ using an inducible promoter in cells lacking the endogenous cheZ gene, as previously described [165] [215] (Methods). Growing this strain with a high concentration (16 ng/mL) or low concentration (2 ng/mL) of the inducer anhydrotetracycline (aTc) resulted in a population with low average TB or high average TB, respectively (Figure 5.7). The TB distribution of wild-type (WT) *E. coli* falls between these two extremes (Figure 5.1a).

To propagate migrating waves of growing bacteria, we utilized the classic swim plate assay, in which cells migrate through a fibrous mesh of 0.14% w/v semisolid agarose supplemented with excess nutrients [212] [167]. We inoculated *E. coli* populations with different batch TB distributions at the center of agarose swim plates, let them migrate for 15 hours, collected cells at the edge of the expanding colonies ("wave"), and measured their TB distributions by transferring the cells to a liquid buffer and tracking single cells under a microscope. In parallel, we grew these same populations with identical inducer concentrations in shaking flasks ("batch") until exponential growth phase and measured their TB distributions (Figure 5.2a). The inducer aTc degrades over time; therefore, we aged aTc before adding it to the batch culture growth medium to mimic the conditions in the migrating wave (Figure 5.2; Methods). The same experiments were performed with WT cells in the absence of aTc. By comparing the TB distributions of populations that had migrated on the plates with those propagated in batch culture, we quantified the effect of collective migration on the populations' TB distributions.

We found that the TB distribution of the high-TB population (batch mean TB = 0.31 ± 0.01, uncertainties throughout are the standard errors of the mean across biological replicates) shifted toward lower TBs (final mean TB = 0.23 ± 0.03) during migration on plates (Figure 5.2e, 5.1h). Conversely, the TB distribution of the low-TB population (batch mean TB = 0.10 ± 0.01) shifted to higher TBs (final mean TB = 0.18 ± 0.01) after migration on the plates (Figure 5.2c, 5.2f). In both cases, the populations became enriched for cells with intermediate TBs of ~ 0.2, close to the mean TB of wild-type populations grown in batch culture (mean TB = 0.22 ± 0.03) (Figure 5.9). Consistent with these observations, the TB distribution of the migrating WT population (final mean TB = 0.22 ± 0.01) was similar to its batch culture distribution (Figure 5.2d, 5.2g). All changes in the mean TB during migration were statistically significant, as measured by two-sided t-test, except that of the WT population. Samples harvested 1 cm behind the migrating populations were marginally enriched for the low-performing TBs, though the effect was not significant, possibly because growth also occurred between the moment when these cells fell behind and when they were harvested (Figure 5.10).

To quantify how these shifts in phenotype composition affected migration speed, we measured the expansion radius of the migrating waves of the three populations on agarose swim plates over time and calculated the steady-state expansion speed using the slope of the linear part of the expansion radius profile (Methods; Figure 5.2b and Figure 5.11). Early time points in migration could not be measured because the ring was not clearly visible. We found that the CheZ mutants reached their steady state speeds much later than the WT, possibly due to the scarcity of high-performing phenotypes in the batch culture distributions. However, once the CheZ mutants reached steady state, their migration speeds were close to that of the WT, illustrating the effectiveness of the adaptation mechanism. In particular, the WT population (mean steady-state expansion speed 0.174 ± 0.007 mm/min) and the high-TB population (0.170 ± 0.02 mm/min) expanded the fastest (difference in speed was not statistically significant). The low-TB population was slower (0.150 ± 0.02 mm/min; significant to $P < 0.005$), possibly due to the presence of very low-TB cells in the adapted population (Figure 5.9). The growth rates of WT, low-TB, and high-TB populations were

similar (Figure 5.12), therefore differences in the steady state expansion speeds were solely due to differences in chemotactic performance. Thus, migrating populations become enriched with high-performing phenotypes, increasing migration speed. In this environment, cells with TB close to 0.22 appear to perform best, which coincides with the average TB of the WT population in batch culture (Figure 5.9).

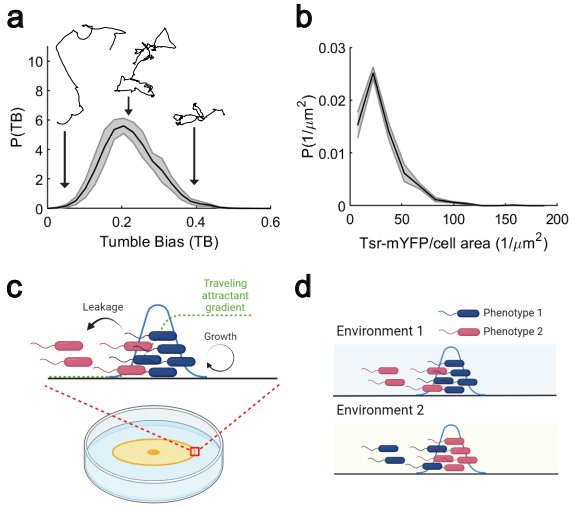

Figure 5.1: Isogenic populations of bacteria exhibit diversity in behavioral and sensory phenotypes while performing collective migration. **(a)** In an isogenic population of *E. coli*, there is diversity in swimming behaviors, which can be quantified, for example, by measuring tumble bias in *E. coli* RP437 ($N_{\text{rep}} = 3$, $N_{\text{cells}} = 9,417$). **(b)** There is also diversity in sensory ability, which correlates with variations in *Tsr* levels (as measured in *E. coli* MG1655, $N_{\text{rep}} = 3$, $N_{\text{cells}} = 1,695$). **(c)** Under nutrient-replete conditions, cells consume attractants and collectively migrate using the resulting traveling attractant gradients [177]. During this process, cells spatially organize based on their ability to climb the traveling gradients [165]. Cells with higher chemotactic performances lead at the front, while cells with lower chemotactic performances travel at the back and eventually fall behind the migrating group. In such nutrient-replete conditions, cells continue to divide and generate diversity by replenishing phenotypes. **(d)** Theory predicts [153] that the balance between environment-dependent cell loss and growth enables the migrating isogenic population to dynamically tune its phenotypic composition to the environments it traverses.

5.2.2 TUNING OF SWIMMING PHENOTYPE DISTRIBUTIONS IS NON-GENETIC AND OCCURS WITHOUT CHANGES IN CHEYZ EXPRESSION

What mechanism enables a migrating bacterial population to tune its TB distribution? Our recent theory predicts that the tuning of phenotypic distributions is a dynamic, non-genetic process mediated by the loss of low-performing chemotaxis phenotypes [165] and production of new phenotypes through growth [153] [176] [199]. However, during our swim plate assays, cells in the migrating populations could potentially acquire mutations that permanently altered their swimming behaviors [203] [204] [205]. If TB tuning was non-genetic, then we expected that the TB distributions of cells in the migrating waves would revert to their standing TB distributions when grown in batch culture.

To distinguish between these possibilities, we isolated cells from the edge of the low- and high-TB migrating colonies on agarose swim plates, inoculated them into batch cultures with aTc, and

measured their TB distributions after growth (Figure 5.3a). The TB distributions of the migrating populations relaxed to their standing TB distributions after re-growth in batch culture, suggesting that the cells in the migrating population did not acquire mutations that permanently altered their swimming behaviors (Figure 5.3b, 5.3c).

Even without mutations, the observed shifts in TB distribution during migration could have been due to changes in gene expression. Chemotaxis is regulated during *E. coli* growth, leading to changes in a population's TB distribution at different growth phases [176]. We verified that, in our conditions, TB and tumble frequency (TF) did not vary during steady, exponential growth phase (see Figure 5.13 and discussion therein). Still, if cells experienced different growth conditions as they migrated, expression of the response regulator CheY and its phosphatase CheZ could be affected, thus changing TB [165] [175]. Given that there was excess nutrient on the plates, we expected that bacteria would remain in exponential phase for the duration of the experiment, and therefore that cheY and cheZ regulation would be constant throughout the plate as the population migrates. We measured the protein expression levels of CheY and CheZ by fusing them to fluorescent proteins (RFP and YFP, respectively) at their native chromosomal loci in a non-motile strain. This non-motile strain acted as a biosensor for detecting *in vivo* changes in cheYZ expression. We spread these cells uniformly on agarose swim plates, initiated migrating waves of motile, unlabeled WT cells at the center of the plates, and then picked cells from both the center and the edge of the migrating colonies (Methods). Fluorescent microscopy measurements (Methods) revealed no significant differences in CheY and CheZ levels between cells sampled from the center vs. the edge (Figure 5.14). This indicated that the expression of cheY and cheZ remains constant across the entire plate even as the wave migrates. We confirmed that migrating populations did not experience catabolite repression [216] [217] during the period of our measurements since catabolite repression effects only appeared at much longer times (Figure 5.15).

Together, these observations indicated that the adaptation of TB distributions was highly unlikely to be mediated by mutations or gene regulation.

5.2.3 TUNING OF SWIMMING PHENOTYPE DISTRIBUTIONS ADAPTS THE POPULATION TO THE PHYSICAL ENVIRONMENT

We have demonstrated that migrating cell populations non-genetically tune their own phenotypic composition, enriching the population for high-performing chemotaxis phenotypes. Since the performance of chemotaxis phenotypes varies in different environments [153], we expected that the TB distribution during migration would depend on the environment that the population traversed. Whereas cells need to tumble to escape traps in semisolid agarose [153] [167] [218], past work has shown that cells with low TB climb chemical gradients faster in liquid [175] [219]. This suggests that the highest-performing phenotype in liquid has a lower TB than that in semisolid agarose, and thus migrating populations would enrich for lower TBs in liquid than in agarose.

To test this, we measured the TB distributions of migrating populations after traveling through a liquid environment (Figure 5.4a). We again generated populations of *E. coli* with low and high average TBs and propagated migrating waves with these populations, as well as the wild-type, in capillary tubes filled with liquid media for 9 hours. aTc was pre-aged so that the total aging time at the end of the capillary experiments was the same as in our agarose swim plate experiments. We then isolated cells from the migrating populations and measured their TB distributions after migration.

The WT population's TB distribution (batch mean TB = 0.22 ± 0.03) shifted to lower TB (final mean TB = 0.18 ± 0.01) during collective migration in liquid (Figure 5.4d, 5.4g). Low-TB cells were enriched up to a factor of 10, whereas high-TB cells were filtered out. When the population with high TB (batch mean TB = 0.31 ± 0.01) traveled through capillary tubes, its TB distribution shifted lower than it did when traveling on agarose swim plates (final mean TB = 0.16 ± 0.01) (Figure 5.4e).

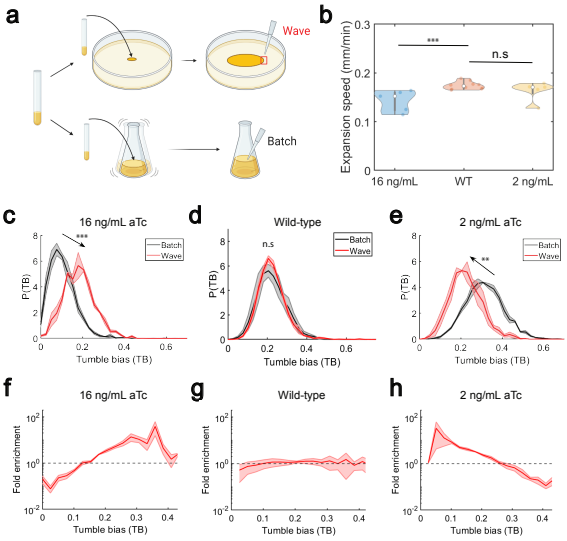

Figure 5.2: Migration in agarose swim plate tunes TB distribution of the population. **(a)** Experimental design: a swim plate and shaking flask containing the same amount of inducer are inoculated with the same initial population. TB distributions are measured and compared between batch and the migrating ring ("wave") after spending the same amount of time in either condition. **(b)** Expansion speeds of RP437 wild-type (mean expansion speed 0.174 ± 0.007 mm/min; uncertainties throughout the paper are the standard errors of the mean across replicates; here, $N_{\text{rep}} = 12$), $\Delta cheZ$ (pTet-CheZ) induced with 2 ng/mL aTc (mean 0.170 ± 0.02 mm/min; $N_{\text{rep}} = 6$), and 16 ng/mL (mean 0.150 ± 0.02 mm/min; $N_{\text{rep}} = 6$) populations on agarose swim plates. The expansion radius over time was measured laterally and in one direction from the center to the edge of the migrating colony. Two-sided t-tests were performed throughout the text to determine significance of the difference between pairs of means (throughout, *** = $P < 0.0005$, ** = $P < 0.005$, * = $P < 0.05$, and n.s. = not significant). **(c)** Populations with low initial mean TB (mean TB = 0.10 ± 0.01; $N_{\text{rep}} = 3$, $N_{\text{cells}} = 21,891$) shift toward a higher mean TB after migration on the plates (0.18 ± 0.01; $N_{\text{rep}} = 3$, $N_{\text{cells}} = 5,103$). The shaded area on the TB distribution represents the standard error of the mean probability in each TB bin. Significance here and throughout the Figures refers to change in the mean of the distribution. **(d)** There was minimal or no shift in wild-type population's TB distribution during collective migration on the plates (0.22 ± 0.01; $N_{\text{rep}} = 3$, $N_{\text{cells}} = 15,774$ cells) compared to batch culture (0.22 ± 0.03; $N_{\text{rep}} = 3$, $N_{\text{cells}} = 9,417$). **(e)** On the other hand, populations with high initial mean TB (0.31 ± 0.01; $N_{\text{rep}} = 3$, $N_{\text{cells}} = 26,254$) shifted toward a lower mean TB after migration (0.23 ± 0.03; $N_{\text{rep}} = 3$, $N_{\text{cells}} = 6,951$). **(f)** When low-TB populations migrated on the plates, fold enrichment of cells with high TB was observed, while cells with low TB were filtered out ($N_{\text{rep}} = 3$). The shaded area on the fold-enrichment throughout represents the standard errors of the mean enrichment values within each TB bin. **(g)** No enrichment or filtering of TB was observed in wild-type populations ($N_{\text{rep}} = 3$). **(h)** When high-TB populations migrated on the plates, enrichment of cells with low TB was observed, while cells with high TB were filtered out ($N_{\text{rep}} = 3$).

The enrichment of low-TB cells and filtering out of high-TB cells were much stronger in the capillary tubes (Figure 5.4h) compared to the agarose swim plates (Figure 5.2h). The TB distributions of the low-TB population (batch mean TB = 0.10 ± 0.01) shifted to a slightly higher mean TB when traveling through capillary tubes (final mean TB = 0.15 ± 0.03), but the shift was not statistically significant (Figure 5.4c). In this case, the enrichment of high-TB cells and filtering out of low-TB cells was weaker in the capillary tubes (Figure 5.4f) compared to agarose swim plates (Figure 5.2f).

As in agarose, the position of migrating waves in capillary tubes increased linearly after they had propagated a few centimeters, indicating that their expansion speeds had reached steady state at the time we measured TB (Figure 5.16). Adaptation enabled the CheZ mutants and WT population to reach similar steady state migration speeds. The low-TB population had the fastest expansion speed (mean expansion speed 0.396 ± 0.003 mm/min). Its TB distribution shifted the least during migration in capillary tubes, suggesting that its standing TB distribution was better adapted for migration in liquid than the WT and high-TB populations (Methods; Figure 5.4b). The expansion speed of the WT population was statistically indistinguishable from this (0.386 ± 0.01 mm/min). Finally, the high-TB population expanded slower than the other two populations (0.353 ± 0.001 mm/min).

Together, these results established that shifts in TB distribution during collective migration of *E. coli* enriched for phenotypes with highest chemotaxis performance in the environment being traversed.

We also tested whether environment-dependent adaptation of TB distributions by collective migration occurred in other wild-type *E. coli* strains, including: 1) HE205, a NCM3722 derivative from the Cremer and Hwa labs [177], 2) AW405, a K-12 strain originated from the Berg lab [167], 3) MG1655, a common K-12 lab strain [220], and 4) TW09231, or Escherichia sp. TW09231, a wild isolate from Lake Michigan [221]. In all cases, migration in liquid resulted in populations enriched with lower TB cells than when migrating in agarose (Figure 5.17), consistent with adaptation by collective migration. These results demonstrate environment-dependent tuning of TB distributions across a wide range of both lab *E. coli* strains and a wild isolate, highlighting the universality of this adaptation mechanism.

5.2.4 ADAPTED TB DISTRIBUTION RAPIDLY RELAXES BACK TO BATCH DISTRIBUTION

How quickly do the adapted phenotypic distributions of a migrating population revert to the original batch distribution?To quantify this, *E. coli* populations were isolated from capillary tube assays and reinoculated into batch cultures. TB distributions were measured every 15-30 minutes throughout the growth period (Figure 5.5a). We fitted the mean TB values over time to an exponential model to determine the characteristic timescale on which the mean TB returns to the level observed in batch culture (Methods). For wild-type RP437, it took about 2 doubling times for the TB distributions to return to those observed in batch cultures (Figure 5.5b). The relaxation time scale of the mean was τ=65.2±1.6 min and the doubling time was 68.8±1.5 min. The result was similar for an *E. coli* strain with slower growth rate, HE205. Its TB distribution also relaxed within approximately 2 doubling times (Figure 5.5c). The relaxation time scale of the mean was τ=106.1±6.3 min and the doubling time was 92.3±3.4 min. These results demonstrate that adaptation by collective migration is rapidly reversible, requiring only a few generations of growth.

5.2.5 COLLECTIVE MIGRATION TUNES THE POPULATION'S DISTRIBUTION OF SENSING PHENOTYPES TO ADAPT TO THE CHEMICAL ENVIRONMENT

Numerous phenotypic traits, in addition to tumble bias, affect a bacterium's chemotactic performance. One such trait is the cell's sensing capability, which correlates with the abundances of its

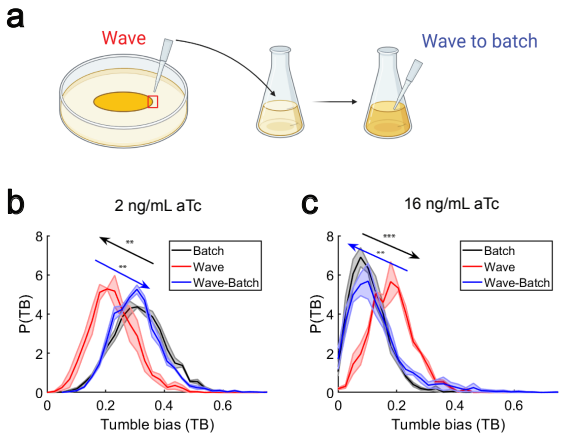

Figure 5.3: Tuning of TB by collective migration is reversible. **(a)** To determine whether the tuning of TB becomes fixed or remains adaptable, we isolated cells from the edge of the migrating colonies ("wave"), grew the cells in liquid batch culture until exponential phase, and measured the TB distributions after growth ("wave-batch"). **(b)** Black and red are the TB distributions of populations with high initial TB before and after migrating on agarose swim plates (data replotted from Figure 5.2e). Blue: TB distribution of cells that migrated (red) after regrowth in batch culture (mean TB = 0.30 ± 0.01; $N_{\text{rep}} = 3, N_{\text{cells}} = 15,774$). The TB distributions of the populations that migrated on agarose swim plates, after growing in flasks, shifted back to the original batch culture's distributions. **(c)** Similar to (b), the TB distributions of populations with low initial TB, after growing in flask (blue; 0.13 ± 0.02; $N_{\text{rep}} = 3, N_{\text{cells}} = 20,403$), shifted back to the TB distributions observed in batch culture (black and red distributions are replotted from Figure 5.2c). The mean values of "batch" and "wave-batch" TB distributions in both cases are not significantly different.

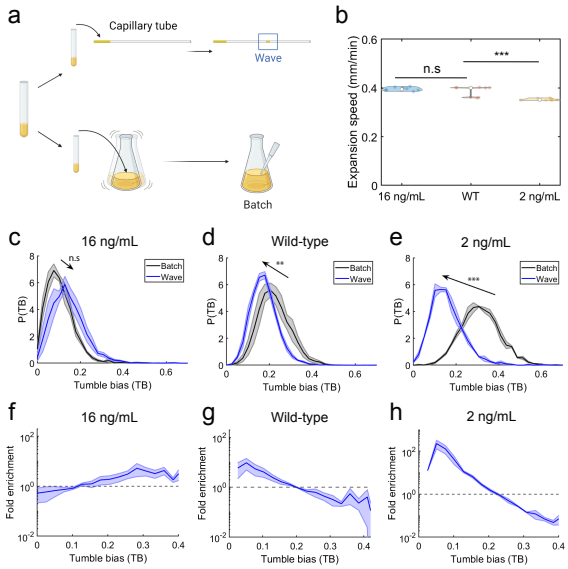

Figure 5.4: Tuning of TB distribution is different in liquid environment. **(a)** Experimental design: a capillary tube and shaking flask containing the same amount of inducer are inoculated with the same initial population. TB distributions are measured and compared between batch and the migrating cells ("wave"). **(b)** Expansion speeds of RP437 wild-type (mean 0.386 ± 0.01 mm/min; $N_{\text{rep}} = 9$), ΔcheZ (pTet-CheZ) induced with 2 ng/mL aTc (mean 0.353 ± 0.001 mm/min; $N_{\text{rep}} = 9$), and 16 ng/mL aTc (0.396 ± 0.003 mm/min; $N_{\text{rep}} = 9$) populations in capillary tubes. **(c)** In liquid, populations with low initial mean TB (mean TB = 0.10 ± 0.01; $N_{\text{rep}} = 3$, $N_{\text{cells}} = 21,891$) shift toward a higher mean TB (0.15 ± 0.03; $N_{\text{rep}} = 3$, $N_{\text{cells}} = 20,403$), but which is slightly lower than the mean TB in agarose swim plates (0.18 ± 0.01, as in Figure 5.2c). **(d)** Unlike in agarose swim plates, wild-type population's TB distribution (0.22 ± 0.03; $N_{\text{rep}} = 3$, $N_{\text{cells}} = 9,417$) shifted toward a lower mean TB during collective migration in capillary tubes (0.18 ± 0.01; $N_{\text{rep}} = 3$, $N_{\text{cells}} = 16,768$). **(e)** Populations with high initial mean TB (0.31 ± 0.01; $N_{\text{rep}} = 3$, $N_{\text{cells}} = 26,254$) shifted toward a lower mean TB (0.16 ± 0.01; $N_{\text{rep}} = 3$, $N_{\text{cells}} = 13,434$). The mean TB value is lower than what was observed during migration on agarose swim plates (0.23 ± 0.03, as in Figure 5.2d). **(f)** For the migration of low-TB populations, the fold enrichment is smaller than in agarose swim plates ($N_{\text{rep}} = 3$). **(g)** Wild-type populations migrating in capillary tubes were enriched for low-TB cells ($N_{\text{rep}} = 3$), unlike what we observed when they migrated on agarose. **(h)** For high-TB populations, fold enrichment was stronger in capillary tubes compared to migration in agarose swim plates ($N_{\text{rep}} = 3$). More low-TB cells are enriched during migration in capillary tubes than on agarose plates.

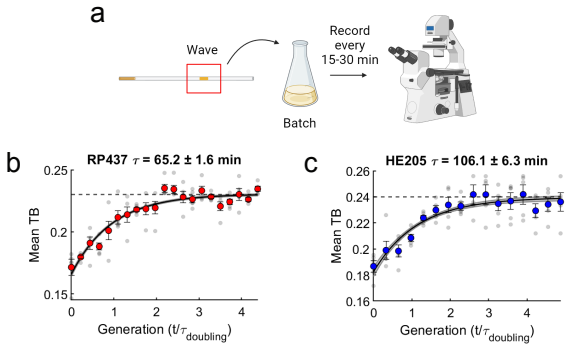

Figure 5.5: Adapted TB distribution relaxes back to the standing batch distributions within a few generations. **(a)** Experimental design: *E. coli* RP437 and HE205 populations were inoculated in capillary assays and allowed to migrate for 9 hours. Migrating populations were isolated and grown in batch cultures. TB measurements were taken from the batch culture over the course of growth every 15 minutes (RP437) or 30 minutes (HE205). **(b)** In approximately 2 generations (growth rate = 0.604 ± 0.01 hour^{-1}; τ_{doubling} = 68.8 ± 1.5 minutes; errors are the standard errors of the mean growth rates and doubling times; $N_{\text{rep}} = 3$), the mean TB of migrating populations returns back to the mean TB of populations observed in batch culture (the mean TB of the batch culture is represented as a horizontal dashed line). The gray dots represent the mean TB of individual biological replicates. The red dots represent the means across replicates (calculated from more than 30,844 trajectories for each time point; $N_{\text{rep}} = 5$), and the error bars indicate the standard errors of the mean. The means and standard errors across replicates were fitted with an exponential model, and a characteristic relaxation timescale τ and its error were determined using maximum likelihood estimation (see Methods). The black line represents the model fit, and the shaded area represents the standard deviation of the model. τ for RP437 is 62.5 ± 1.6 minutes—the error is the standard deviation of the estimated τ. **(c)** Same as (b), but for HE205. The blue dots represent the means across replicates (calculated from more than 5,920 trajectories for each time point; $N_{\text{rep}} = 5$). It takes approximately 2 generations (growth rate = 0.45 ± 0.01 hour^{-1}; τ_{doubling} = 92.3 ± 3.4 minutes; $N_{\text{rep}} = 3$) for the TB distributions to relax back to the batch culture. τ for HE205 is 106.1 ± 6.3 minutes.

chemoreceptors [222] [150]. *E. coli* express five chemoreceptor species, of which ~90% are either Tar, which binds preferentially to L-aspartate, or Tsr, which binds preferentially to L-serine [160] [172] [149]. Notably, Tsr is expressed separately from the chemotaxis operon—which includes, among other genes, Tar, CheY, and CheZ [2]—allowing its abundance to vary independently of other chemotaxis genes affecting chemotaxis performance. Therefore, we predicted that Tsr could be enriched in a migrating wave that chases its cognate ligand L-serine.

We measured the Tsr protein expression levels in populations of *E. coli* migrating on agarose swim plates with 100 μM L-aspartate or 100 μM L-serine as attractants, and no other amino acids (Figure 5.6a). As a carbon source, we used glycerol because it is not an attractant [212]. To measure single-cell Tsr levels, we fused *tsr* on its native locus with mYFP (Methods). We used MG1655 as the parent strain here because, unlike RP437 [2] [223], it is not restricted by auxotrophic limitation and can grow in minimal media in the absence of amino acids. The expansion speed of the population was faster in serine (0.88 ± 0.05 mm/hr) than in aspartate (0.52 ± 0.1 mm/hr) (Figure 5.6b), consistent with previous reports [177].

We compared the average mYFP fluorescence in single cells picked from the edge of the migrating colonies versus those grown in batch cultures supplemented with the same concentration of either L-aspartate or L-serine (Methods). When aspartate was the chemoattractant, distributions of Tsr levels within the migrating populations on swim plates were similar to those grown in batch cultures, with the mean Tsr level statistically indistinguishable from batch culture (Figure 5.6c; mean intensities $\langle \text{Tsr} \rangle_{\text{batch}} = 23.7 \pm 0.4\ \mu\text{m}^{-2}$ and $\langle \text{Tsr} \rangle_{\text{wave}} = 27.2 \pm 3.8\ \mu\text{m}^{-2}$). We observed a slight enrichment of intermediate Tsr levels (Figure 5.6d), possibly because of the assistance Tsr provides to the adaptation of Tar (CheR and CheB can methylate and demethylate neighboring Tar receptors when bound to the pentapeptide of Tsr) [224] [225].

In contrast, collective migration led to strong enrichment for cells with high levels of Tsr when the population chased serine (Figure 5.6e, 5.6f; $\langle \text{Tsr} \rangle_{\text{batch}} = 29.6 \pm 2.9\ \mu\text{m}^{-2}$ and $\langle \text{Tsr} \rangle_{\text{wave}} = 53.6 \pm 6.5\ \mu\text{m}^{-2}$). While the distribution of Tsr changed significantly depending on the attractant the population was chasing (see Figure 5.18 for a direct comparison), the distributions of TB were similar across attractants, with only a mild adjustment in serine (Figure 5.19), suggesting that adaptation of these two traits is nearly independent.

To confirm that the shift in the distribution of Tsr levels was not due to gene regulation, we employed an analogous strategy to the one described above for CheY and CheZ (Figure 5.13a), here using a non-motile strain expressing fluorescently-labelled Tsr from its native locus (Figure 5.20a). There were no differences in the Tsr levels between non-motile cells harvested at the migrating edge and at the center of the plate, suggesting that *tsr* gene expression changes negligibly during collective migration (Figure 5.20b, 5.20c). Tsr levels were not regulated by serine or aspartate consumption (when these amino acids were present in batch cultures at the same concentrations as in the swim plates) (Figure 5.21), nor were TB distributions (Figure 5.22). This further indicated that the receptor enrichment that we measured after migration on swim plates was not caused by altered gene expression or metabolic effects due to the presence of amino acids.

Taken together, these observations demonstrated that adaptation by collective migration generalizes to sensory phenotypes: migrating populations non-genetically adapted their distributions of receptor abundances, depending on the attractants they were chasing. Thus, collective migration combined with growth can enrich for multiple, continuous phenotypic traits and non-genetically adapt migrating populations to diverse environmental conditions.

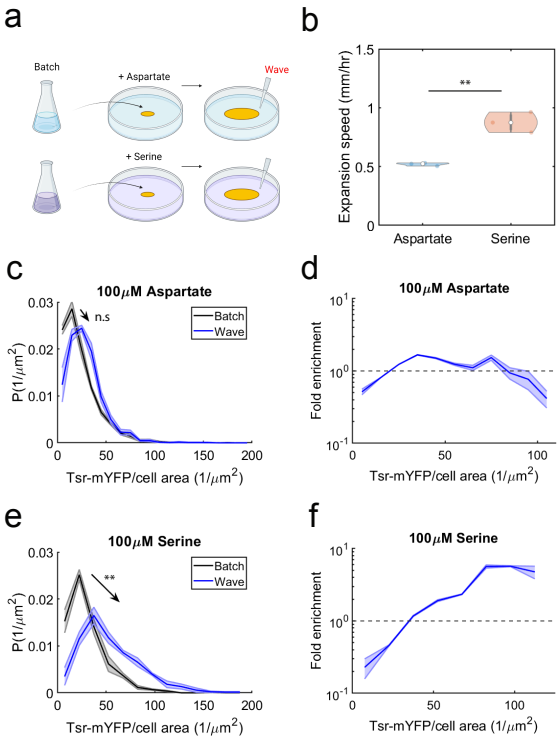

Figure 5.6: Collective migration tunes the chemoreceptor levels depending on the attractants. **(a)** Experimental design: *E. coli* MG1655 wild-type with YFP-labelled Tsr was inoculated on swim plates supplemented with 100 μM aspartate or 100 μM serine. The fluorescence of single cells was measured in populations at the edge of the migrating colonies ("wave") and in populations growing in batch culture. The single-cell fluorescence divided by the cell area is used as a proxy for receptor concentration. **(b)** The expansion speeds of the migrating populations in agarose swim plates supplemented with 100 μM aspartate (0.52 ± 0.1 mm/hr; $N_{\text{rep}} = 3$) or 100 μM serine (0.88 ± 0.05 mm/hr; $N_{\text{rep}} = 3$). **(c)** Black is the distribution of Tsr levels of populations grown in batch culture with added aspartate (mean Tsr intensity = 23.7 ± 0.4 μm^{-2}; $N_{\text{rep}} = 3, N_{\text{cells}} = 2,076$), and blue is the distribution of Tsr levels of the migrating populations that chased aspartate (27.2 ± 3.8 μm^{-2}; $N_{\text{rep}} = 3, N_{\text{cells}} = 1,617$). Shaded areas on the Tsr intensity distributions are the standard errors of the mean probabilities in each bin of intensity value. **(d)** When chasing aspartate, the distributions of Tsr levels in migrating populations remained close to that in batch cultures, with only a weak fold increase in cells with intermediate Tsr levels and a weak fold decrease in cells with high Tsr levels. The shaded area on the fold-enrichment throughout is the standard error of the mean enrichment values within each bin of Tsr intensity value. **(e)** Black is the distribution of Tsr levels of populations grown in batch culture with added serine (29.6 ± 2.9 μm^{-2}; $N_{\text{rep}} = 3, N_{\text{cells}} = 1,695$), and blue is the distribution of Tsr levels of the migrating populations that chased serine (53.6 ± 6.5 μm^{-2}; $N_{\text{rep}} = 3, N_{\text{cells}} = 675$). **(f)** During collective migration on swim plates supplemented with serine, there was a strong enrichment of cells with higher Tsr levels, while cells with lower Tsr levels were filtered out.

5.3 DISCUSSION

Here, we investigated how a population of cells adapts its distribution of phenotypes to migrate effectively in multiple environments. We discovered that migrating populations of *E. coli* can tune their distributions of swimming behaviors and sensing capabilities based on the physical and chemical properties of their environment. This tuning occurs dynamically and is explained by a model in which loss of low-performing chemotaxis phenotypes from a migrating front [165] balances the production of new phenotypes by growth [153] [199]. This mechanism, which we demonstrated in multiple *E. coli* strains, can act on pre-existing variability in gene expression but does not require de novo changes in gene expression or mutations. By rapidly and reversibly enriching for fitter individuals based on the demands of the current environment, this mechanism increases the population's expansion speed across a wide variety of potential environments.

We examined two phenotypes that impact chemotaxis performance: tumble bias and receptor abundance. In liquid, low tumble bias cells are known to climb a fixed gradient faster [175]. Consistent with this, wild-type RP437 populations enriched for low-TB cells when migrating in liquid. When migrating on agarose, however, the TB distribution did not change from the standing batch distribution. Furthermore, both CheZ-inducible populations, with high or low initial mean TB, shifted toward the standing batch distribution of the wild-type RP437 (Figure 5.8). This suggests that the standing batch TB distribution of wild-type RP437 is already adapted for navigation in agar/agarose. Indeed, RP437 is a standard laboratory strain that has been used to study motility for decades [223] [226] and was originally selected for motility on agar swim plates. In all the strains we tested, the tumble bias distribution when migrating in liquid was enriched for lower TB cells than when migrating on agarose (Figure 5.5a, 5.5b, and Figure 5.15). This is consistent with previous findings that tumbling slows migration in liquid [175] [219], but that tumbles are needed to escape traps in porous environments [167] [227] [228]. More broadly, we expect that any phenotypic trait that contributes to chemotaxis performance can be enriched during collective migration. For example, standing variation in FliC expression can lead to variation in swimming speed [174], and migrating fronts have been shown to be enriched with cells with higher FliC expression [214]. This observation could be due to adaptation by collective migration, possibly in tandem with gene regulation. Finally, it is always possible for one of the countless strains of bacteria in nature to encounter an environment in which its phenotype composition is poorly adapted. In these cases, we expect non-genetic adaptation to have large effects on its traveling phenotype distribution.

We also found that the adapted TB distributions relaxed back to the batch culture distribution in about two generations, indicating some degree of nongenetic inheritance. This is consistent with a previous study which showed that swimming traits of individual *E. coli* cells are partially and nongenetically inherited across multiple generations [199]. While non-genetic inheritance of chemotactic traits [199], and other traits like antibiotic resistance [229], sporulation [230], iron metabolism [231] were studied previously, the molecular mechanism of how these traits are inherited remains to be explored further. Indeed, non-genetic inheritance of chemotactic traits may involve partitioning of chemoreceptors, flagellar components, and other regulatory elements from the mother to daughter cells during cell division.

Recent research emphasizes the crucial role of emergent spatial structures during collective migration in enhancing genetic diversity within bacterial communities [232]. In traditional well-mixed environments, resource competition leads to the extinction of species with lower relative growth fitness [233]. However, during collective migration, species with lower relative growth fitness can coexist by competing for spatial territories rather than resources [203] [232], and avoid extinction by colonizing specific habitats within the migrating colony. Furthermore, recent experiments demonstrate the evolution of mutants with different navigation capabilities from isogenic migrating populations [203], suggesting that the emergent spatial organization of phenotypes could contribute to genetic diversity [165] [177] [166] [234]. Together with our observation that environ-

ment determines the specific distribution of phenotypes that is enriched, these results suggest that relative spatial arrangements of phenotypes within migrating groups may play an important role in eco-evolutionary dynamics.

Collective migration is not exclusive to bacteria; it also occurs in eukaryotic systems where cells consume or degrade attractants to form and chase self-generated gradients, a mechanism observed in various contexts including cancer and development [235] [236]. Some examples are the migration of lateral line of zebrafish embryos [237], neural crest cells in *Xenopus laevis* [238], and melanoma cells [239]. The tuning of phenotypic distributions during collective migration only requires that some cells, due to their specific traits, are more adept at navigating than others, therefore creating a "leader-follower" structure. Thus, adaptation by collective migration may be a general strategy for cell populations to colonize diverse environments effectively.

Our work demonstrates a new mechanism for population-level adaptation in biology. Adaptation mechanisms such as stochastic switching [207] [26] [240] and regulating gene expression are fast (~1 generation) but are limited to the adaptation of a few phenotypic traits and often require dedicated pathways to implement. Adaptation by genetic mutations avoids these limitations but is slow (~10 generations) [203] [204] [205]. In contrast, standing variation in numerous phenotypic traits among individual cells is ubiquitous. Our findings demonstrate that when collective behaviors create selection pressures which shape that variation, cell populations can reversibly adapt multiple traits with a level of speed and flexibility that is difficult to achieve via classical mechanisms.

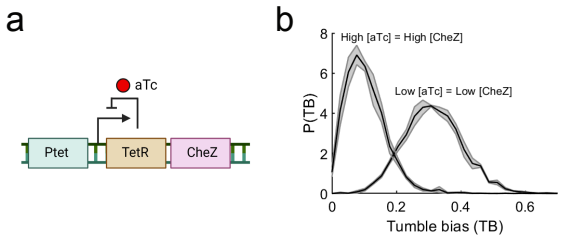

Figure 5.7: A genetic construct that tunes TB distribution of a population. **(a)** To tune tumble bias distributions, we utilized an *E. coli* RP437 Δ*cheZ* strain that carries an aTc-inducible cassette of *cheZ* that is integrated in the chromosome at the *attB* site (RP437 Δ*cheZ pTet-cheZ*). **(b)** *E. coli* populations with different initial TB distributions were generated by inducing RP437 Δ*cheZ pTet-cheZ* strain with different aTc concentrations. High aTc concentration (16 ng/mL) formed low mean TB populations (mean TB = 0.10 ± 0.01; N_{rep} = 3, N_{cells} = 21,891), and low aTc concentration (2 ng/mL) formed high mean TB populations (mean TB = 0.31 ± 0.01; N_{rep} = 3, N_{cells} = 26,254).

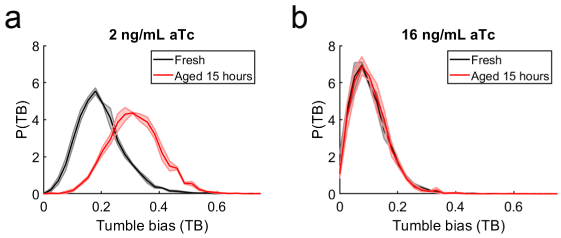

Figure 5.8: The inducer aTc degrades over time. Tumble bias distribution of RP437 Δ*cheZ pTet-cheZ* grown in batch culture supplemented media with 2 ng/mL (mean TB = 0.2 ± 0.01; $N_{rep} = 3$, $N_{cells} = 42{,}301$), **(a)** and 16 ng/mL (mean TB = 0.10 ± 0.01; $N_{rep} = 3$, $N_{cells} = 21{,}093$), **(b)** of fresh aTc or aTc that was aged for 15 hours (replotted from Figure 5.1b). 15 hours was how long we waited until we isolated the edge of the migrating colony. Except for 16 ng/mL aTc, the distributions of tumble biases increased in mean values if the strain was grown in aged aTc, suggesting that aTc degrades in the growth media over time.

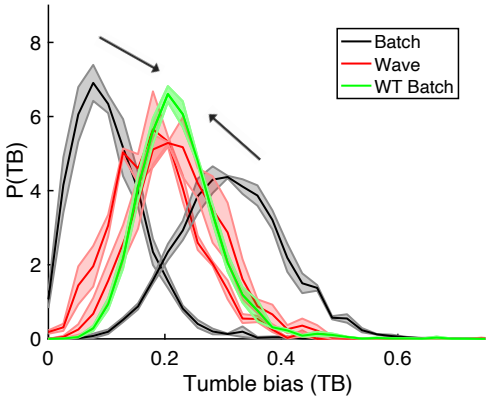

Figure 5.9: Migration in agarose swim plate tunes the population's TB distribution toward the TB distribution of wild-type population. The black curves are the TB distributions of low- and high-TB populations grown in batch culture, and the red curves are the TB distributions of those populations after migration on agarose swim plates, as shown in Figure 5.2c and 5.2e. The green curve is the TB distribution of wild-type *E. coli* RP437 grown in batch culture (mean TB = 0.22 ± 0.03; $N_{rep} = 3$, $N_{cells} = 9{,}417$).

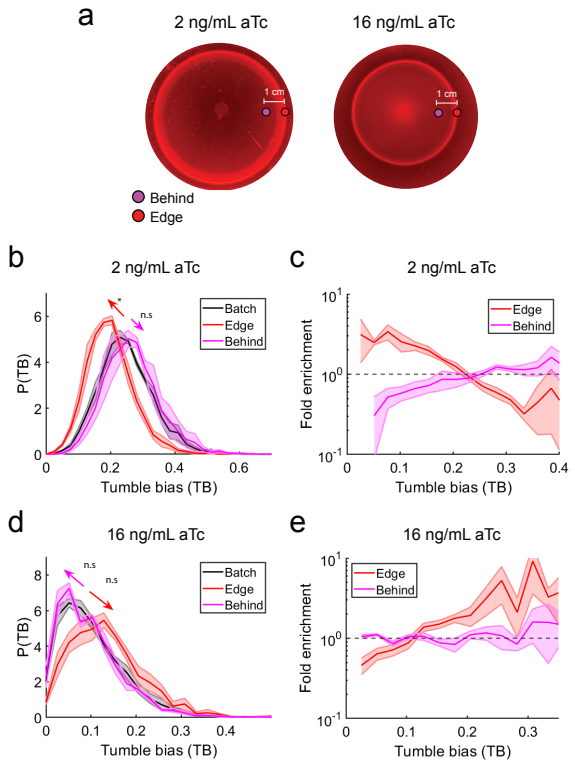

Figure 5.10: TB distributions of cell populations that fall behind during collective migration. **(a)** Experimental design: Low-TB and high-TB *E. coli* HE205 Δ*cheZ* (*pTet-CheZ*) populations ("batch") was inoculated on swim plates supplemented with 100 μM aspartate and appropriate inducer concentrations. After 16 hours of growth and migration on swim plates, the TB distributions of populations picked at the edge (red) and middle (located ~1 cm behind the edge, magenta) were measured. **(b)** Populations with higher initial mean TB (0.25 ± 0.01; $N_{rep} = 3$, $N_{cells} = 5,164$) shift toward a lower mean TB after migration on the plates (0.20 ± 0.01; $N_{rep} = 3$, $N_{cells} = 6,307$), similar to our observation in *E. coli* RP437 (see Figure 5.2e). The TB distributions of populations at the "middle" (mean TB = 0.26 ± 0.02; $N_{rep} = 3$, $N_{cells} = 5,602$) were similar to the TB distributions observed in batch cultures, and the TB distributions of populations at the "center" have the highest mean TB. **(c)** Cells with low TBs were enriched, while cells with high TBs were filtered at the edge of the migrating colonies. Cells with low TBs were depleted behind the wave ($N_{rep} = 3$). **(d)** Same as (b) but with populations with lower initial mean TB. The TB distributions of populations with lower mean TB (0.10 ± 0.01; $N_{rep} = 3$, $N_{cells} = 2,090$) shifted to a higher mean TB value (0.13 ± 0.01; $N_{rep} = 3$, $N_{cells} = 3,151$) during migration on the swim plates. The population that fell behind exhibited similar TB distributions to the batch cultures (0.10 ± 0.01; $N_{rep} = 3$, $N_{cells} = 2,625$). Shaded area is the standard errors of the probability density values at each TBs ($N_{rep} = 3$, $N_{cells} > 1000$ for each TB distributions). **(e)** Cells with higher TBs were enriched, while cells with very low TBs were filtered out at the edge of the migrating colonies. No enrichment was observed behind the migrating edge ($N_{rep} = 3$).

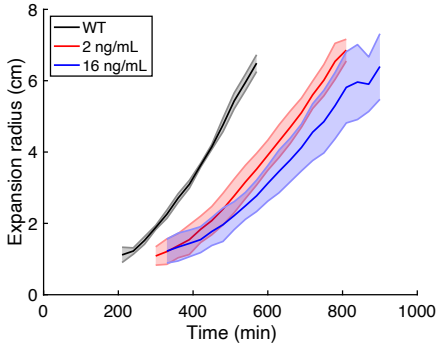

Figure 5.11: Expansion dynamics of migrating *E. coli* RP437 populations on swim plates. Expansion radius of wild-type *E. coli* RP437 and the CheZ-inducible population (induced with 2 ng/mL and 16 ng/mL aTc) over time. Shaded area is the standard error of the mean expansion radius. The curves start at when the expansion ring became visible on the swim plate assays ($N_{rep} = 6$ for the 2 ng/mL and 16 ng/mL curves; $N_{rep} = 12$ for the WT curve).

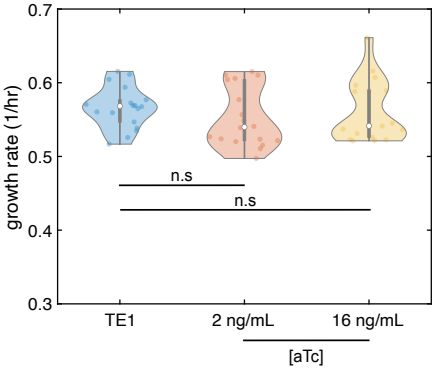

Figure 5.12: The growth rates of RP437 wild-type and Δ$cheZ$ (pTet-CheZ) populations are identical. Growth rates of RP437 wild-type (mean 0.5663 ± 0.03 1/hr, throughout, uncertainty is the standard deviation of the means across replicates, $N_{rep} = 3$), Δ$cheZ$ (pTet-CheZ) induced with 2 ng/mL aTc (mean 0.5526 ± 0.04 1/hr, $N_{rep} = 3$), and 16 ng/mL aTc (mean 0.5608 ± 0.04 1/hr, $N_{rep} = 3$) populations. The differences in growth rates cannot explain the differences in the expansion speeds of WT and Δ$cheZ$ (pTet-CheZ) populations in agarose swim plates and capillary tube assays.

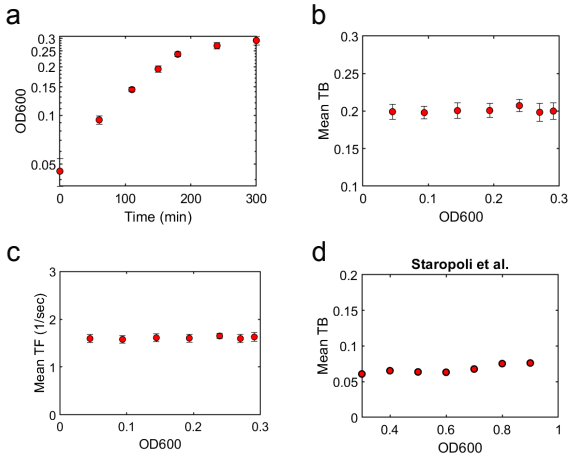

Figure 5.13: Mean TB and TF do not change across various optical densities during steady exponential growth phase in batch cultures. **a)** Growth curve of *E. coli* RP437 during steady exponential growth into saturation. To eliminate the effect of the recovery from stationary growth phase on motility, overnight cultures were diluted into fresh media by a factor of 100 and grown to early exponential growth phase (OD600 = 0.1). The cultures were diluted again into fresh media to OD600 = 0.05. OD600, mean tumble bias (TB) and tumble frequency (TF) were then measured at different timepoints of growth until early stationary growth phase. **b,c)** Mean TB and TF did not vary across different OD600 during steady exponential phase growth. Red points are the mean and error bars are the standard errors of the means (N_{rep} = 5, each mean TB was calculated from at least 17,719 trajectories). A previous study by Staropoli *et al.*[176] observed that TF and tumble duration (TD) varied with OD600. However, in that study, motility was measured after diluting cells from stationary phase into fresh media. This could affect tumble measurements, as motility is low during the recovery from stationary to exponential phase [177]. **d)** Still, calculating TB = TF/(TF+1/TD) from Staropoli et al.'s data shows that TB is invariant with respect to OD600 in their conditions.

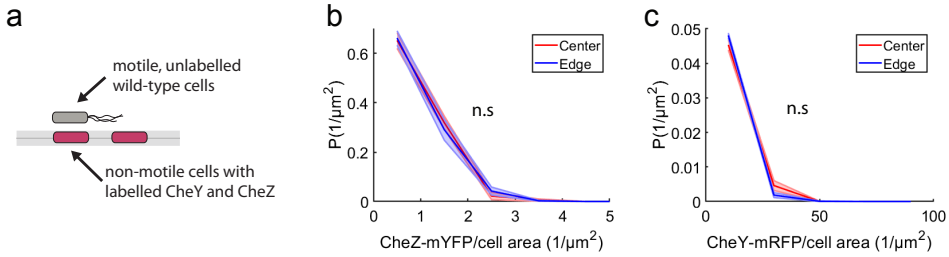

Figure 5.14: The shift in TB distribution is not due to changes in the CheY and CheZ expressions. **(a)** Motile RP437 wild-type bacteria migrated in agarose swim plates that were filled homogeneously with non-motile *E. coli* RP437 cells with labelled CheY or CheZ (CheY-mRFP or CheZ-mYFP respectively). Fluorescent signal of CheY or CheZ of the biosensor were measured at the center versus the edge of the migrating colonies. **(b)** Distribution of CheZ-mYFP over a single cell's area at the center (mean CheZ intensity = 0.96 ± 0.02 μm^{-2}; N_{rep} = 3, N_{cells} = 739) and the edge (mean CheZ intensity = 6.3 ± 4.6 μm^{-2}; N_{rep} = 3, N_{cells} = 1,076) of the colony. **(c)** Distribution of CheY-mRFP over a single cell's area at the center (mean CheY intensity = 0.95 ± 0.19 μm^{-2}; N_{rep} = 3, N_{cells} = 739) and the edge (mean CheY intensity = 11.3 ± 1.4 μm^{-2}; N_{rep} = 3, N_{cells} = 1,076) of the colony. The distributions at the center and edge of the migrating colonies are similar, suggesting that the shift in TB distributions observed after migration on agarose swim plates is not due to changes in gene expression of CheY and CheZ. Shaded area is the standard error of the mean probabilities within each bin of CheZ or CheY intensity values.

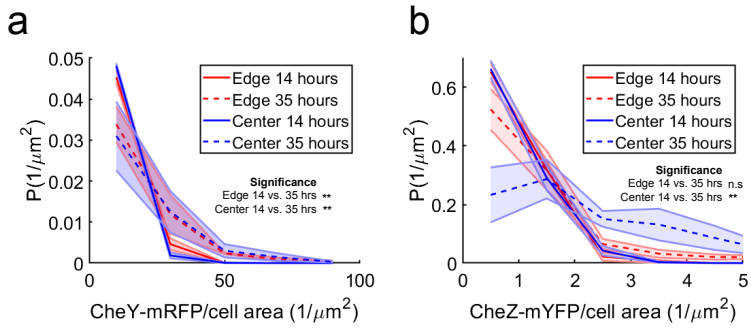

Figure 5.15: Cells experience catabolite repression after prolonged migration. Using the same experimental setup (shown in Figure 5.13), the CheY and CheZ expressions were measured at the center versus the edge of the migrating colonies at 14 hours and 35 hours. After 35 hours of migration, populations at the edge and center exhibit higher CheY **(a)** and CheZ **(b)** expression. The CheY expression of populations isolated at the center (mean CheY intensity = 22.3 ± 10.2 μm^{-2}; N_{rep} = 3, N_{cells} = 1,090) and edge (18.5 ± 2.72 μm^{-2}; N_{rep} = 3, N_{cells} = 1,993) are not significantly different. The CheZ expression of populations picked at the center (mean CheZ intensity = 2.67 ± 0.65 μm^{-2}; N_{rep} = 3, N_{cells} = 1,090) is significantly higher than the CheZ expression of populations picked at the edge (1.43 ± 0.08 μm^{-2}; N_{rep} = 3, N_{cells} = 1,993). Shaded area is the standard errors of the probability density values of CheY and CheZ expressions (N_{rep} = 3, N_{cells} > 600 for each distribution). Two-sided T-tests were performed to determine significance of the difference between pairs of means of CheY and CheZ expression.

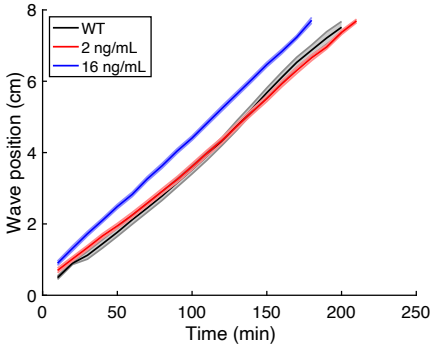

Figure 5.16: Expansion dynamics of migrating *E. coli* RP437 populations in capillary tubes. Wave positions of wild-type *E. coli* RP437 and the CheZ-inducible population (induced with 2 ng/mL and 16 ng/mL aTc) migrating across capillary tubes over time. Shaded area is the standard error of the mean expansion position. The curves start at when wave became visible in the capillary tubes (N_{rep} = 9 for all conditions).

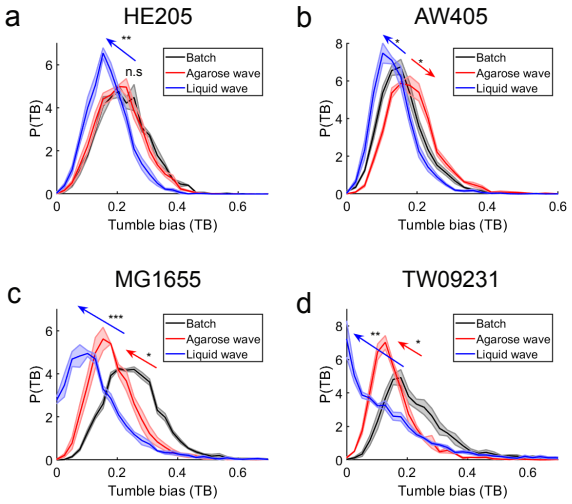

Figure 5.17: Environment-dependent tuning of TB distributions across *E. coli* strains. TB distributions of *E. coli* HE205, AW405, MG1655, and TW09231 (*Escherichia sp.* TW09231) were measured during collective migration in agarose swim plates, capillary tube assays, and during growth in batch cultures. **(a)** The mean TB values of HE205 during migration in agarose swim plates (mean TB = 0.21 ± 0.01; $N_{rep} = 3$, $N_{cells} = 3,134$) were the same as the mean TB values observed in batch cultures (0.22 ± 0.005; $N_{rep} = 3$, $N_{cells} = 5,164$). On the other hand, the mean TB values were lowered during migration in capillary tube assays (0.17 ± 0.01; $N_{rep} = 3$, $N_{cells} = 2,164$). **(b)** The mean TB values of AW405 during migration in agarose swim plates (0.19 ± 0.004; $N_{rep} = 3$, $N_{cells} = 4,634$) were higher than the mean TB values observed in batch cultures (0.16 ± 0.003; $N_{rep} = 3$, $N_{cells} = 3,038$). The mean TB values were lowered during migration in capillary tube assays (0.14 ± 0.01; $N_{rep} = 3$, $N_{cells} = 5,300$). **(c)** The mean TB values of MG1655 during migration in agarose swim plates (0.19 ± 0.01; $N_{rep} = 3$, $N_{cells} = 5,164$) were significantly higher than the mean TB values observed in batch cultures (0.26 ± 0.004; $N_{rep} = 3$, $N_{cells} = 5,916$). The mean TB values were lowered during migration in capillary tube assays (0.16 ± 0.01; $N_{rep} = 3$, $N_{cells} = 3,164$). **(d)** The mean TB values of TW09231 during migration in agarose swim plates (0.16 ± 0.01; $N_{rep} = 3$, $N_{cells} = 4,781$) were significantly higher than the mean TB values observed in batch cultures (0.23 ± 0.02; $N_{rep} = 4$, $N_{cells} = 3,497$). The mean TB values were lowered during migration in capillary tube assays (0.14 ± 0.01; $N_{rep} = 4$, $N_{cells} = 5,140$).

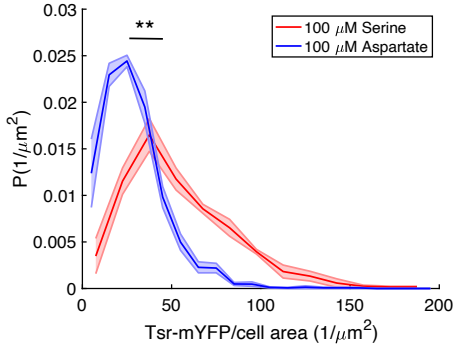

Figure 5.18: Direct comparison of the Tsr distributions during collective migration in serine and aspartate. The distributions of Tsr levels in populations of *E. coli* MG1655 wild-type with YFP-labelled Tsr when chasing 100 μM aspartate (mean Tsr intensity = 27.2 ± 3.8 μm^{-2}; $N_{rep} = 3$, $N_{cells} = 1,617$) or 100 μM serine (53.6 ± 6.5 μm^{-2}; $N_{rep} = 3$, $N_{cells} = 675$) on swim plates. Shaded area is the standard errors of the probability density values of Tsr expressions ($N_{rep} = 3$, the distributions are the same as in Figure 5.6b and 5.6d. Two-sided T-tests were performed to determine significance of the difference between pairs of means of Tsr intensities.

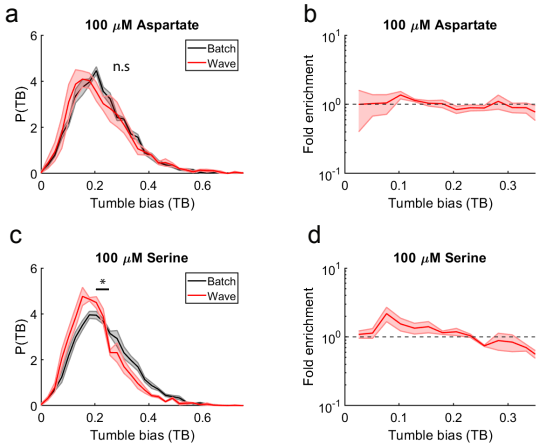

Figure 5.19: Tuning of TB distributions when the migrating populations are chasing aspartate and serine. Motile *E. coli* MG1655 cells expressing Tsr-YFP was grown in agarose swim plates supplemented with 100 μM aspartate (**a,b**) or 100 μM serine (**c,d**). The TB distributions of populations isolated from the edge of the migrating colonies were measured and compared to the TB distributions observed in batch cultures, which were also supplemented with aspartate or serine. There was no significant difference between the mean TB of populations grown in batch cultures (mean TB = 0.23 ± 0.004; $N_{rep} = 3$, $N_{cells} = 9,321$) and the mean TB of populations migrated in swim plates supplemented with aspartate (0.22 ± 0.02; $N_{rep} = 3$, $N_{cells} = 4,361$). On the other hand, the mean TB of populations migrated in swim plates supplemented with serine (0.21 ± 0.01; $N_{rep} = 3$, $N_{cells} = 3,686$) exhibited a slightly, but significantly lower mean TB value compared to the mean TB value observed in batch cultures (0.25 ± 0.01; $N_{rep} = 3$, $N_{cells} = 7,888$). **(b,d)** Fold-enrichment of TB during collective migration on swim plates. Migrating on swim plates supplemented with serine mildly, but statistically significantly enriches for lower TBs. Shaded area is the standard errors of the probability density values at each TB. Two-sided T-tests were performed to determine significance of the difference between pairs of means.

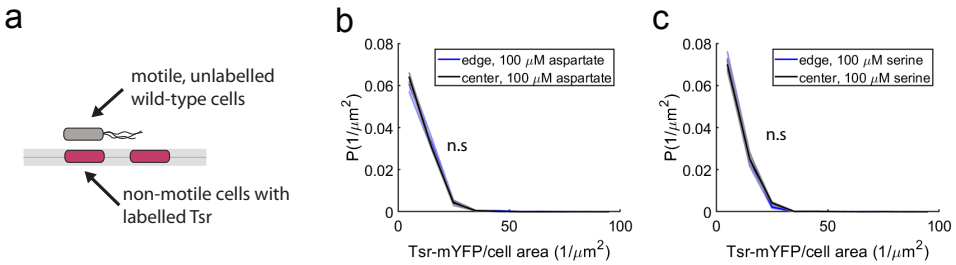

Figure 5.20: The shift in Tsr levels during collective migration is not due to *tsr* regulation. **(a)** Motile MG1655 wild-type bacteria migrated in agarose swim plates (supplemented with 100 μM Aspartate) that were filled homogeneously with non-motile *E. coli* MG1655 cells expressing Tsr-YFP from the native locus, effectively acting as a biosensor for the regulation of gene expression by the passage of the migrating wave. Fluorescent signals, a proxy for *tsr* expression of the biosensor strain, were measured at the center versus the edge of the migrating colonies. **(b)** Distribution of Tsr levels at the center (mean Tsr intensity = $8.8 \pm 0.5\ \mu m^{-2}$; $N_{rep} = 3$, $N_{cells} = 2,285$) and the edge (mean Tsr intensity = $9.4 \pm 1.0\ \mu m^{-2}$; $N_{rep} = 3$, $N_{cells} = 2,390$) of the colony on plates supplemented with aspartate were identical, indicating that there was no regulation of *tsr* expression upon passage of the migrating wave. **(c)** Center (mean Tsr intensity = $7.8 \pm 0.6\ \mu m^{-2}$; $N_{rep} = 3$, $N_{cells} = 1,911$) and edge (mean Tsr intensity = $7.9 \pm 1.0\ \mu m^{-2}$; $N_{rep} = 3$, $N_{cells} = 2,696$) same as (b), but on plates supplemented with Serine. Shaded area is the standard error of the mean probabilities within each bin of Tsr intensity values. Two-sided T-tests were performed to determine significance of the difference between pairs of means.

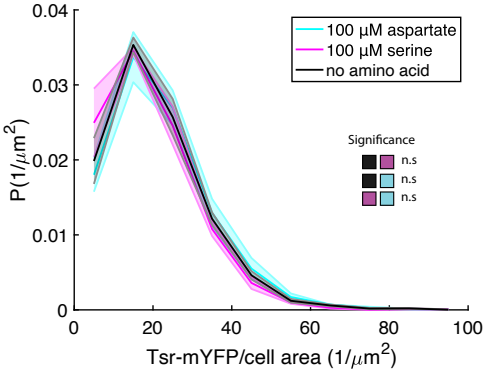

Figure 5.21: Expression of *tsr* is not regulated by serine or aspartate consumption during growth. Fluorescence of the biosensor *E. coli* MG1655 cells expressing Tsr-YFP from the native locus grown in batch culture with minimal media H1 supplemented either with no amino acids or with 100 μM serine or 100 μM aspartate were measured. Distribution of Tsr levels of cells when grown in serine (mean Tsr intensity = $18.7 \pm 2.1\ \mu m^{-2}$; $N_{rep} = 3$, $N_{cells} = 1,695$) in aspartate (mean Tsr intensity = $21.2 \pm 2.5\ \mu m^{-2}$; $N_{rep} = 3$, $N_{cells} = 3,442$), and with no amino acid added (mean Tsr intensity = $20.3 \pm 1.7\ \mu m^{-2}$; $N_{rep} = 3$, $N_{cells} = 2,908$). The distributions of Tsr levels are identical across conditions, suggesting that *tsr* expression is not regulated by aspartate or serine consumption. Shaded area is the standard error of the mean probabilities within each bin of Tsr intensity values. Two-sided T-tests were performed to determine significance of the difference between pairs of means.

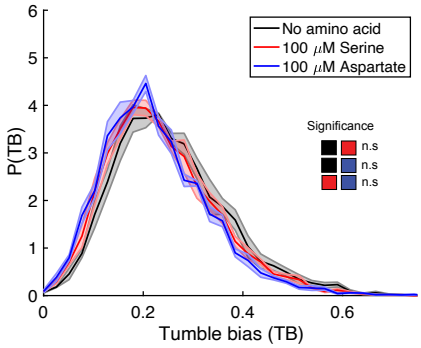

Figure 5.22: The presence of an attractant does not affect TB distributions. The TB distributions of motile *E. coli* MG1655 cells expressing Tsr-YFP were measured after growth in batch cultures supplemented with no amino acids (mean TB = 0.25 ± 0.01; $N_{rep} = 3$, $N_{cells} = 6,111$), 100 μM aspartate (0.23 ± 0.01; $N_{rep} = 5$, $N_{cells} = 9,321$), or 100 μM serine (0.25 ± 0.01; $N_{rep} = 5$, $N_{cells} = 7,888$). Addition of aspartate or serine did not significantly change the TB distributions of the populations. Shaded area is the standard errors of the probability density values at each TB bins. Two-sided T-tests were performed to determine significance of the difference between pairs of means.

5

5.4 METHODS

5.4.1 STRAINS, MEDIA, AND GROWTH CONDITIONS

Most experiments were performed with *E. coli* K12 RP437 and MG1655 derivatives. Other strains used in this study are *E. coli* HE205, AW405, and wild-isolate TW09231 (*Escherichia* sp. TW09231). To tune tumble bias distributions, we utilized *E. coli* RP437 ΔcheZ and HE205 ΔcheZ strains that carry an aTc-inducible cassette of *cheZ* that is integrated in the chromosome at the *attB* site (RP437 ΔcheZ pTet-*cheZ* and HE205 ΔcheZ pTet-*cheZ*). To measure single-cell *Tsr* receptor abundances, we utilized an *E. coli* MG1655 ΔfliC:FLP mutant (gift from Victor Sourjik) that has *tsr* translationally fused with monomeric YFP (A206K) on its native chromosomal locus (MG1655 ΔfliC:FLP, *tsr*-mYFP). To modulate motility in the previous strain, we transformed an arabinose-inducible plasmid expressing WT *FliC* (pBad-*fliC*, gift from Howard Berg) into MG1655 ΔfliC:FLP, *tsr*-mYFP and induced it with 0.005% w/v arabinose. RP437 ΔfliC with *CheY* and *CheZ* translationally fused with mRFP and mYFP, respectively, on their native chromosomal loci (RP437 ΔfliC *cheY*-mRFP and *cheZ*-mYFP) was used as a biosensor to measure expression of the *cheY* and *cheZ* genes in the swim plate assays. MG1655 ΔfliC:FLP, *tar*-mCherry, *tsr*-mYFP was used as a biosensor to measure expression of the *tsr* gene. To insert genes on the native loci of the *E. coli* chromosome, we employed the phage λ Red recombination system.

RP437-derived strains were stored as -80°C freezer DMSO-based stocks, and MG1655-derived strains were stored as glycerol-based stocks at the same temperature. M9 buffer supplemented with casamino acids, glycerol, and $MgSO_4$ (1x M9 salts, 0.4% v/v glycerol, 0.1% v/v casamino acids, 1mM $MgSO_4$; pH 7.0) were used to grow RP437-derived strains, AW405, and TW09231. H1 minimal salts medium (MMH1: 50 mM KPO_4, 0.5 mM $MgSO_4$, 7.6 mM $(NH_4)_2SO_4$, 1.25 μM $Fe_2(SO_4)_3$; pH 7.0) supplemented with 0.5% v/v glycerol and 0.01% w/v thiamine hydrochloride was used to grow MG1655-derived strains. MOPS glycerol media (8.37 g/L MOPS adjusted to pH 7.0 with KOH, 0.712 g/L tricine adjusted to pH 7.0 with KOH, 0.00278 g/L $FeSO_4 \cdot 7H_2O$, 0.0481 g/L K_2SO_4, 0.0000555 g/L $CaCl_2$, 0.106 g/L $MgCl_2 \cdot 6H_2O$, 2.91 g/L NaCl, 0.0230 g/L K_2PO_4, 2 mM NH_4Cl, and 4 mL/L glycerol) were used to grow HE205-derived strains. To grow overnight cultures, small inoculants

from the freezer stocks were added into test tubes containing 2 mL of media (with appropriate concentrations of inducers and antibiotics) in a shaking incubator at 30°C rotating at 250 RPM. To grow day cultures for cell tracking experiments, RP437-derived strain overnight cultures were diluted by 100-fold and re-grown in 5 mL of the appropriate media until exponential phase (OD_{600} = 0.20). For receptor quantification experiments, MG1655-derived strains were diluted 200-fold and re-grown in 10 mL of the appropriate media until exponential phase (OD_{600} = 0.30). For cell tracking experiments, chemotaxis buffer (1x M9 buffer, 0.4% v/v glycerol, 0.010 mM methionine, 0.1 mM EDTA, and 0.1% v/v PVP-40) was used to wash and dilute cells. For receptor quantification experiments, minimal chemotaxis buffer (10 mM KPO_4 and 0.1mM EDTA; pH 7.0) was used to wash and dilute cells. For the TB measurements in batch cultures, RP437 ΔcheZ pTet-*cheZ* were grown in media supplemented with aTc that was aged for 15 hours.

5.4.2 GROWTH RATES MEASUREMENTS

Growth measurements were done using a microplate reader (BioTek Epoch 2 microplate spectrophotometer). Overnight cultures were diluted by 100-fold into fresh media supplemented with appropriate inducer concentrations. 200 μL of diluted cells were aliquoted into each well of polystyrene 96-well plates (Falcon 96-wells REF 353072), and the plates were loaded into the plate reader. The plates were incubated at 30°C while continuously shaking linearly at 567 cpm. The OD600 of each well was measured every 7 minutes for 36 hours. To extract the growth rates of each sample, the slopes of the linear region (at the mid-exponential growth phases) of the natural log of OD600 versus time (hours) curves were calculated.

5.4.3 FORMATION OF PROPAGATING WAVES AND EXPANSION SPEED MEASUREMENTS USING SWIM PLATE AND CAPILLARY TUBE ASSAYS

For the swim plate assay, 3 μL of cells in exponential phase were inoculated at the center of semi-solid agarose plates for RP437-derived strains or 10 μL of cells in exponential phase for MG1655-derived strains. For RP437-derived strains, the semi-solid agarose plates were made using M9-based media, as described above, supplemented with 0.14% agarose (American Bioanalytical Agarose GPG/LE) and appropriate concentrations of aTc. Similarly, for MG1655-derived strains, the semi-solid agarose plates were made using H1 minimal media, as described above, supplemented with 0.14% agarose. The plates were incubated at 30°C for 15 hours (RP437-derived strains) or at 33.5°C for 48 hours (MG1655-derived strains). The edges of the migrating colonies were picked using pipette tips and diluted into chemotaxis buffer (for RP437-derived strains) or minimal chemotaxis buffer (for MG1655-derived strains) for subsequent tracking and imaging analyses. To measure the expansion speeds of bacterial populations in swim plates, images were taken with a Canon DS126291 camera every 30 minutes. The diameters of the expansion rings as a function of time and expansion speeds were extracted from the images using a customized MATLAB code.

For the capillary tube assay, overnight cultures were inoculated 100-fold into 5 mL of media with appropriate inducers and grown at 30°C until OD600 = 0.2. Cells were concentrated to an OD600 = 6. A 12-inch capillary tube was filled with growth media (M9 glycerol with casamino acids, MgSO4, and PVP-40) and 6-hours aged aTc, and one side of the tube was plugged by stabbing the tube into a plate filled with solidified agar (1.5% agar in distilled water). The concentrated cell mixture was filled on the other side of the tube using a 1 mL syringe, and another agar plug was added into that side. Both sides of the tube were then plugged with clay. The tubes are incubated horizontally at 30°C for 9 hours. To isolate the wave, a 3-cm section of the tube that contained the wave was fractionated, and the mixture inside the 3-cm section was diluted into chemotaxis buffer for subsequent tracking analysis. To measure the expansion speeds of bacterial populations in capillary tubes, images were taken with a Canon DS126291 camera every 10 minutes. Positions

of the populations as a function of time and expansion speeds were extracted from images using ImageJ.

5.4.4 MICROFLUIDIC DEVICE PREPARATION

To track single cell swimming behavior, we utilized a rectangular channel microfluidic device (0.5 mm wide, 30 mm long, and 60 μm deep). The device was constructed from PDMS with standard lithography methods. To cast the device, a pre-prepared mold was coated with a 5-mm thick layer of degassed 10:1 PDMS-to-curing agent mixture (Sylgard 184, Dow Chemical). The mold was then baked at 70°C for 12 hours. Devices were cut out of the mold, and a hole was punched using a 20-gauge blunt-tip needle on each side of the channel. The device was rinsed with isopropanol, methanol, and water. A 22 mm x 50 mm glass coverslip was rinsed with acetone, isopropanol, methanol, and water. The coverslip and device were then treated inside a plasma cleaner for 1 minute and bonded together. The bonded device was heated at 80°C for 15 minutes and cooled to room temperature before cells were injected inside.

5.4.5 TRACKING SINGLE CELLS AND TUMBLE DETECTION

Washed cells were diluted with chemotaxis buffer to an OD600 = 0.0005. The diluted mixture was injected inside the microfluidic device using a 1 mL syringe. To prevent evaporation, holes on both sides of the microfluidic device were taped. The device was placed on an inverted microscope (Nikon Eclipse Ti-U) equipped with a custom environmental chamber (50% humidity and 30°C). A custom MATLAB script was used to record 3-minute phase contrast videos at 4X magnification and 20 frames-per-second. Data from video recordings were stored as .bin files.

A customized MATLAB code was used to detect tumble and extract tumble bias of single cells, as previously described [189]. Only trajectories longer than 10 seconds were considered for analysis. Each tumble bias distribution was generated using 4 3-minute videos that contained ~1000 total trajectories.

5.4.6 MEASURING THE TIME SCALES OF RELAXATION OF TB DISTRIBUTION TO THE STANDING BATCH DISTRIBUTION

E. coli RP437 or HE205 were grown to early-exponential phases and allowed to migrate in capillary assays for 9 hours, as mentioned above. The sections of the capillary tubes containing the migrating bacterial populations were fractioned, and the cells were added into 1 mL of growth media.

For every 15- or 30-minute interval during growth in the batch cultures, the TB distributions of the populations were measured. The mean of TB distributions normalized by the trajectory lengths was determined for each time point.

The equation to model the relaxation of mean TB is:

$$TB(t) = TB_{\text{batch}} - (TB_{\text{batch}} - TB_0)e^{-t/\tau} \tag{5.1}$$

where $TB(t)$ is the mean TB over time, TB_{batch} is the mean TB of the batch culture, TB_0 is the mean TB during collective migration in the capillary tubes, and τ is the relaxation timescale.

To estimate τ, we fitted the means of the mean TBs across replicates and the standard error of the means across replicates to the equation using maximum likelihood estimation. To estimate the error of τ, we sampled the posterior distribution using Markov Chain Monte Carlo simulation to obtain 100 simulated parameter values and calculate the standard deviation of those values.

5.4.7 PROTEIN EXPRESSION MEASUREMENTS IN SWIM PLATES

Non-motile MG1655-derived cells expressing labeled Tsr or non-motile RP437-derived cells expressing labeled CheY and CheZ used as biosensors for gene expression were grown as described

above. Subsequently, cells were mixed with the appropriate media and 0.14% liquified agarose to a final OD600 = 0.01. Swim plates were left to solidify at room temperature for 2-3 hours, and afterward, 10 / muL of OD600 = 0.01 motile WT MG1655 (labeled Tsr experiments) or motile WT RP437 (labeled CheY and CheZ experiments) cells were inoculated in the center of the plate. The motile population of cells shapes the gradient of the plate and ensures that the non-motile biosensor strain experiences the same local environment as motile cells. After a colony of migrating cells has formed, cells from the center and the edge of the colony are picked and diluted into minimal chemotaxis buffer for subsequent imaging.

5.4.8 SINGLE-CELL PROTEIN COPY NUMBER QUANTIFICATION USING FLUORESCENT MICROSCOPY

Washed cells were diluted 10-fold and plated on agarose pads (1.5% agarose in minimal chemotaxis buffer). The cell suspension was left to dry for 10 minutes, and cells were immediately imaged afterward. Imaging was performed using an inverted microscope (Nikon Eclipse Ti-E) equipped with an oil immersion 100x phase-contrast objective lens. To measure the fluorescence intensity of the strain expressing cheY-mRFP and cheZ-mYFP, fluorescent proteins were excited using a light-emitting diode illumination system (pE-4000, CoolLED). The RFP and YFP channels were imaged consecutively using a multi-band filter (Semrock), and the fluorescence emissions were led into a 2-camera image splitter (TwinCam, Cairn), leading to two identical sCMOS cameras (ORCA-Flash4.0 V2, Hamamatsu). The same setup was used to measure the fluorescence intensity of the strain expressing Tsr-mYFP. In a typical experiment, 20 fields of view, containing approximately 1000 cells in total, are imaged.

5.4.9 FLUORESCENT IMAGE ANALYSIS FOR PROTEIN COPY NUMBER QUANTIFICATION

For each field of view, one phase contrast, one YFP, and one RFP channel images were acquired. Using a custom MATLAB script, images from the two cameras were aligned using an affine transformation, and cells were segmented on the phase-contrast channel using a modified Otsu algorithm. Then, the image background was subtracted from each image, and the fluorescent intensity of every cell was extracted. Finally, the area of each cell was calculated by fitting an ellipsoid. The fluorescent intensity of each cell was divided by the cell area as a measure of protein concentration.

5.4.10 REPRODUCIBILITY AND STATISTICAL ANALYSIS

All experiments reported in this Chapter were repeated at least 3 times. All measurement values of TB, expansion speeds, growth rates, protein levels were reported as the average of the means of the distributions across biological replicates. Uncertainties in these average values were reported as the standard deviation of the means of the distributions. To construct the TB distributions, TB values were sorted into bins, and the probability density were normalized by dividing the trajectory time within each bin by the total trajectory time. To represent the variations in TB distributions, the standard error of the mean TBs within each bin was calculated. Similarly, with the Tsr intensity distribution, single-cell Tsr intensities were sorted into bins, and the probability density in each bin was calculated. The variations in Tsr intensity distributions are represented as the standard error of the mean intensities within each bin. To construct the fold-enrichment curve, the probability density values of each TB or Tsr intensity bins observed in the distributions during collective migration were divided by the values observed in batch cultures. Variations in fold-enrichments are represented as the standard error of the mean fold-enrichment values within each bin. To determine statistical significance between TB and protein level distributions, two-sided t-test was performed on the mean values. Similarly, two-sided t-test was performed to determine significance of growth

rates and expansion speeds between experiments (throughout, *** = P<0.0005, ** = P<0.005, * = P<0.05, and n.s. = not significant).

6

SUMMARY

In this thesis, we employ a diverse set of experimental tools to study the *Escherichia coli* chemotaxis network—a paradigmatic model for signal transduction. Our work centers on two fundamental questions: (1) How can a simple protein network give rise to the complex behavior of critical tuning? (2) How does this same network generate behavioral diversity within clonal populations, how does this diversity evolve during an organism's lifetime, and how do individual bacteria exploit this diversity to adapt to different environments?

In **chapter 2**, we utilize single-cell Förster Resonance Energy Transfer (FRET) microscopy to measure two-state switching fluctuations in *E. coli* chemosensory arrays. Our numerical simulations indicate that these arrays operate near the second-order phase transition of the Ising model. We demonstrate that this critical tuning optimizes the trade-off between response amplitude and speed, underscoring a fundamental design principle in biological signaling networks.

chapter 3 focuses on sensory diversity and its significance in bacterial navigation. Using FRET microscopy, we show that *E. coli* populations exhibit a broad range of ligand sensitivities, regulated by the cell's growth rate. Using fluorescent fusions of key chemotaxis proteins and mathematical modeling, we show that this diversity arises from variability in Tar/Tsr chemoreceptor ratios due to gene expression noise. Furthermore, by tracking collective cell migration, we show that this heterogeneity enhances bacterial expansion rates across diverse environments, supporting a bet-hedging survival strategy in which subpopulations are preadapted to various potential future conditions.

chapter 4, we examine how sensory diversity is maintained and transmitted across generations using a microfluidic chemostat and machine learning-based imaged analysis techniques. Our findings indicate that individual *E. coli* cells maintain stable sensory phenotypes despite fluctuations in their cell cycle. However, environmental shifts induce gradual adaptation of receptor distributions, revealing a form of epigenetic memory. This suggests that non-genetic inheritance of sensory traits contributes to bacterial adaptation in dynamic environments.

Finally, **chapter 5** explores how *E. coli* populations collectively adjust their swimming phenotypes in response to environmental cues. By tracking the swimming behavior of single cells, we demonstrate that bacterial migration reshapes the distribution of motility traits within a population without genetic modifications. This dynamic adaptation allows for the rapid optimization of collective migration in response to fluctuating physical landscapes, unveiling a novel mechanism of non-genetic adaptation.

BIBLIOGRAPHY

REFERENCES

[1] F. Wöhler. Ueber künstliche Bildung des Harnstoffs. *Annalen der Physik*, 88(2):253–256, January 1828.

[2] Frederick R. Blattner, Guy Plunkett, Craig A. Bloch, Nicole T. Perna, Valerie Burland, Monica Riley, Julio Collado-Vides, Jeremy D. Glasner, Christopher K. Rode, George F. Mayhew, Jason Gregor, Nelson Wayne Davis, Heather A. Kirkpatrick, Michael A. Goeden, Debra J. Rose, Bob Mau, and Ying Shao. The Complete Genome Sequence of *Escherichia coli* K-12. *Science*, 277(5331):1453–1462, September 1997.

[3] Frederick C. Neidhardt, editor. *Escherichia coli and salmonella: cellular and molecular biology*. ASM Press, Washington, 1996.

[4] Howard C. Berg. Motile Behavior of Bacteria. *Physics Today*, 53(1):24–29, January 2000.

[5] Ron Milo and Rob Phillips. *Cell biology by the numbers*. Garland Science, Taylor & Francis Group, New York, NY, 2016.

[6] E M Purcell. Life at low Reynolds number. *American Journal of Physics*, 45(1), 1976.

[7] Julius Adler, Gerald L. Hazelbauer, and M. M. Dahl. Chemotaxis Toward Sugars in *Escherichia coli*. *Journal of Bacteriology*, 115(3):824–847, September 1973.

[8] Julius Adler. Chemoreceptors in Bacteria. *Science*, 166, 1969.

[9] Howard C. Berg. How to Track Bacteria. *Review of Scientific Instruments*, 42(6):868–871, June 1971.

[10] Howard C. Berg and Douglas A. Brown. Chemotaxis in Escherichia coli analysed by Three-dimensional Tracking. *Nature*, 239(5374):500–504, October 1972.

[11] John S. Parkinson, Gerald L. Hazelbauer, and Joseph J. Falke. Signaling and sensory adaptation in Escherichia coli chemoreceptors: 2015 update. *Trends in Microbiology*, 23(5):257–266, May 2015.

[12] Howard C. Berg. *Random walks in biology*. Princeton University Press, Princeton, N.J, expanded ed edition, 1993.

[13] Herbert B. Callen. *Thermodynamics and an introduction to thermostatistics*. Wiley, New York, 2nd ed edition, 1985.

[14] Thomas Andrews. XVIII. *The Bakerian Lecture* .—On the continuity of the gaseous and liquid states of matter. *Philosophical Transactions of the Royal Society of London*, 159:575–590, December 1869.

[15] Thierry Mora and William Bialek. Are Biological Systems Poised at Criticality? *Journal of Statistical Physics*, 144(2):268–302, July 2011.

[16] Thierry Mora, Aleksandra M. Walczak, William Bialek, and Curtis G. Callan. Maximum entropy models for antibody diversity. *Proceedings of the National Academy of Sciences*, 107(12):5405–5410, March 2010.

[17] Sarah L. Veatch, Pietro Cicuta, Prabuddha Sengupta, Aurelia Honerkamp-Smith, David Holowka, and Barbara Baird. Critical Fluctuations in Plasma Membrane Vesicles. *ACS Chemical Biology*, 3(5):287–293, May 2008.

[18] Joseph W. Larkin, Xiaoling Zhai, Kaito Kikuchi, Samuel E. Redford, Arthur Prindle, Jintao Liu, Sacha Greenfield, Aleksandra M. Walczak, Jordi Garcia-Ojalvo, Andrew Mugler, and Gürol M. Süel. Signal Percolation within a Bacterial Community. *Cell Systems*, 7(2):137–145.e3, August 2018.

[19] Janina Hesse and Thilo Gross. Self-organized criticality as a fundamental property of neural systems. *Frontiers in Systems Neuroscience*, 8, September 2014.

[20] Andrea Cavagna, Alessio Cimarelli, Irene Giardina, Giorgio Parisi, Raffaele Santagati, Fabio Stefanini, and Massimiliano Viale. Scale-free correlations in starling flocks. *Proceedings of the National Academy of Sciences*, 107(26):11865–11870, June 2010.

[21] Michael B. Elowitz, Arnold J. Levine, Eric D. Siggia, and Peter S. Swain. Stochastic Gene Expression in a Single Cell. *Science*, 297(5584):1183–1186, August 2002.

[22] Arjun Raj and Alexander Van Oudenaarden. Nature, Nurture, or Chance: Stochastic Gene Expression and Its Consequences. *Cell*, 135(2):216–226, October 2008.

[23] Aaron Novick and Milton Weiner. Enzyme induction as an all-or-none phenomenon. *Proceedings of the National Academy of Sciences*, 43(7):553–566, July 1957.

[24] Tom Philippi and Jon Seger. Hedging one's evolutionary bets, revisited. *Trends in Ecology & Evolution*, 4(2):41–44, February 1989.

[25] Martin Ackermann. A functional perspective on phenotypic heterogeneity in microorganisms. *Nature Reviews Microbiology*, 13(8):497–508, August 2015.

[26] Nathalie Q. Balaban, Jack Merrin, Remy Chait, Lukasz Kowalik, and Stanislas Leibler. Bacterial Persistence as a Phenotypic Switch. *Science*, 305(5690):1622–1625, September 2004.

[27] Simon V. Avery. Microbial cell individuality and the underlying sources of heterogeneity. *Nature Reviews Microbiology*, 4(8):577–587, August 2006.

[28] Johannes M. Keegstra, Francesco Carrara, and Roman Stocker. The ecological roles of bacterial chemotaxis. *Nature Reviews Microbiology*, 20(8):491–504, August 2022.

[29] K. Kamino, J. M. Keegstra, J. Long, T. Emonet, and T. S. Shimizu. Adaptive tuning of cell sensory diversity without changes in gene expression. *Science Advances*, 6(46):eabc1087, November 2020.

[30] Jeremy Philippe Moore, Keita Kamino, Rafaela Kottou, Thomas S. Shimizu, and Thierry Emonet. Signal integration and adaptive sensory diversity tuning in Escherichia coli chemotaxis. *Cell Systems*, 15(7):628–638.e8, July 2024.

[31] M. Mehdi Salek, Francesco Carrara, Vicente Fernandez, Jeffrey S. Guasto, and Roman Stocker. Bacterial chemotaxis in a microfluidic T-maze reveals strong phenotypic heterogeneity in chemotactic sensitivity. *Nature Communications*, 10(1):1877, April 2019.

[32] Yongdae Shin and Clifford P Brangwynne. Liquid phase condensation in cell physiology and disease. *Science*, 357(6357):4382, 2017.

[33] Salman F Banani, Hyun O Lee, Anthony A Hyman, and Michael K Rosen. Biomolecular condensates: organizers of cellular biochemistry. *Nature reviews Molecular cell biology*, 18(5):285–298, 2017.

[34] Hao Wu. Higher-order assemblies in a new paradigm of signal transduction. *Cell*, 153(2):287–292, 2013.

[35] Hao Wu and Monika Fuxreiter. The structure and dynamics of higher-order assemblies: amyloids, signalosomes, and granules. *Cell*, 165(5):1055–1066, 2016.

[36] Elgin Korkmazhan, Peter Tompa, and Alexander R Dunn. The role of ordered cooperative assembly in biomolecular condensates. *Nature Reviews Molecular Cell Biology*, 22(10):647–648, 2021.

[37] Xiaolei Su, Jonathon A Ditlev, Enfu Hui, Wenmin Xing, Sudeep Banjade, Julia Okrut, David S King, Jack Taunton, Michael K Rosen, and Ronald D Vale. Phase separation of signaling molecules promotes t cell receptor signal transduction. *Science*, 352(6285):595–599, 2016.

[38] William YC Huang, Steven Alvarez, Yasushi Kondo, Young Kwang Lee, Jean K Chung, Hiu Yue Monatrice Lam, Kabir H Biswas, John Kuriyan, and Jay T Groves. A molecular assembly phase transition and kinetic proofreading modulate ras activation by sos. *Science*, 363(6431):1098–1103, 2019.

[39] Adam Klosin, Florian Oltsch, Tyler Harmon, Alf Honigmann, Frank Jülicher, Anthony A Hyman, and Christoph Zechner. Phase separation provides a mechanism to reduce noise in cells. *Science*, 367(6476):464–468, 2020.

[40] D Bray and T Duke. Conformational spread: The propagation of allosteric states in large multiprotein complexes. *Annu. Rev. Biophys. Biomol. Struct.*, 33:53–73, 2004.

[41] Rodolfo Ciuffa, Trond Lamark, Abul K Tarafder, Audrey Guesdon, Sofia Rybina, Wim JH Hagen, Terje Johansen, and Carsten Sachse. The selective autophagy receptor p62 forms a flexible filamentous helical scaffold. *Cell reports*, 11(5):748–758, 2015.

[42] Xin Cai, Jueqi Chen, Hui Xu, Siqi Liu, Qiu-Xing Jiang, Randal Halfmann, and Zhijian J Chen. Prion-like polymerization underlies signal transduction in antiviral immune defense and inflammasome activation. *Cell*, 156(6):1207–1222, 2014.

[43] Jianbin Ruan, Shiyu Xia, Xing Liu, Judy Lieberman, and Hao Wu. Cryo-em structure of the gasdermin a3 membrane pore. *Nature*, 557(7703):62–67, 2018.

[44] Yunjie Chang, Kai Zhang, Brittany L Carroll, Xiaowei Zhao, Nyles W Charon, Steven J Norris, Md A Motaleb, Chunhao Li, and Jun Liu. Molecular mechanism for rotational switching of the bacterial flagellar motor. *Nature structural & molecular biology*, 27(11):1041–1047, 2020.

[45] A Briegel, D.R. Ortega, E.I Tocheva, K. Wuichet, Z. Li, S. Chen, A Mueller, C.V. Iancu, G.E. Murphy, M. J Dobro, I.B. Zuhlin, and G.J. Jensen. Universal architecture of bacterial chemoreceptor arrays. *PNAS*, 106:17181–86, 2009.

[46] Chang-Cheng Yin, Leon G D'Cruz, and F Anthony Lai. Ryanodine receptor arrays: not just a pretty pattern? *Trends in cell biology*, 18(4):149–156, 2008.

[47] Éva S Vanamee and Denise L Faustman. Structural principles of tumor necrosis factor superfamily signaling. *Science Signaling*, 11(511):eaao4910, 2018.

[48] Liqiang Pan, Tian-Min Fu, Wenbin Zhao, Linlin Zhao, Wen Chen, Chixiao Qiu, Wenhui Liu, Zhijun Liu, Alessandro Piai, Qingshan Fu, Shuqing Chen, Hao Wu, and James J. Chou. Higher-order clustering of the transmembrane anchor of dr5 drives signaling. *Cell*, 176(6):1477–1489.e14, 2019.

[49] V Sourjik and HC Berg. Receptor sensitivity in bacterial chemotaxis. *PNAS*, 99(1):123–127, 2002.

[50] Shuangyu Bi and Victor Sourjik. Stimulus sensing and signal processing in bacterial chemotaxis. *Current Opinion in Microbiology*, 45:22–29, October 2018.

[51] Peijun Zhang, Cezar M Khursigara, Lisa M Hartnell, and Sriram Subramaniam. Direct visualization of escherichia coli chemotaxis receptor arrays using cryo-electron microscopy. *Proceedings of the National Academy of Sciences*, 104(10):3777–3781, 2007.

[52] A Briegel, X Li, AM Bilwes, KT Hughes, GJ Jensen, and BR Crane. Bacterial chemoreceptor arrays are hexagonally packed trimers of receptor dimers networked by rings of kinase and coupling proteins. *PNAS*, 109:3767, 2012.

[53] Jun Liu, Bo Hu, Dustin R Morado, Sneha Jani, Michael D Manson, and William Margolin. Molecular architecture of chemoreceptor arrays revealed by cryoelectron tomography of escherichia coli minicells. *Proceedings of the National Academy of Sciences*, 109(23):E1481–E1488, 2012.

[54] J. M. Keegstra, K. Kamino, F. Anquez, M.D. Lazova, T. Emonet, and T. S. Shimizu. Phenotypic diversity and temporal variability in a bacterial signaling network revealed by single-cell fret. *eLife*, 6:e27455, 2017.

[55] R Colin, C Rosazza, A Vaknin, and C Sourjik. Multiple sources of slow activity fluctuations in a bacterial chemosensory network. *eLife*, 6:e26796, 2017.

[56] Derek Greenfield, Ann L McEvoy, Hari Shroff, Gavin E Crooks, Ned S Wingreen, Eric Betzig, and Jan Liphardt. Self-organization of the escherichia coli chemotaxis network imaged with super-resolution light microscopy. *PLoS biology*, 7(6):e1000137, 2009.

[57] Moriah Koler, Eliran Peretz, Chetan Aditya, Thomas S Shimizu, and Ady Vaknin. Long-term positioning and polar preference of chemoreceptor clusters in e. coli. *Nature communications*, 9(1):1–10, 2018.

[58] E Korobkova, T Emonet, J. M. Vilar, TS Shimizu, and P Cluzel. From molecular noise to behavioural variability in a single bacterium. *Nature*, 428(6982):574–578, 2004.

[59] Nuris Figueroa-Morales, Rodrigo Soto, Gaspard Junot, Thierry Darnige, Carine Douarche, Vincent A Martinez, Anke Lindner, and Éric Clément. 3d spatial exploration by e. coli echoes motor temporal variability. *Physical Review X*, 10(2):021004, 2020.

[60] Haiyan Huo, Rui He, Rongjing Zhang, and Junhua Yuan. Swimming escherichia coli cells explore the environment by lévy walk. *Applied and environmental microbiology*, 87(6):e02429–20, 2021.

[61] Y Tu and G Grinstein. How white noise generates power-law switching in bacterial flagellar motors. *Phys. Rev. Lett.*, 94:208101, 2005.

[62] T. Emonet and P. Cluzel. Relationship between cellular response and behavioral variability in bacterial chemotaxis. *PNAS*, 105(9):3304–3309, March 2008.

[63] D Clausznitzer and RG Endres. Noise characteristics of the escherichia coli rotary motor. *BMC Systems Biology*, 5:151, 2011.

[64] M. Li and G. L. Hazelbauer. Cellular stoichiometry of the components of the chemotaxis signaling complex. *J. Bacteriol.*, 186(12):3687–3694, June 2004.

[65] TS Shimizu, Y Tu, and HC Berg. A modular gradient-sensing network for chemotaxis in Escherichia coli revealed by responses to time-varying stimuli. *Mol. Sys. Biol.*, 6, June 2010.

[66] S Kitanovic, P. Ames, and J.S. Parkinson. Mutational analysis of the control cable that mediates transmembrane signaling in the escherichia coli serine chemoreceptor. *J Bacteriol*, 193(19):5062–5072, 2011.

[67] Rob Phillips. The molecular switch. In *The Molecular Switch*. Princeton University Press, 2020.

[68] Victor Sourjik and Howard C. Berg. Localization of components of the chemotaxis machinery of *Escherichia coli* using fluorescent protein fusions. *Molecular Microbiology*, 37(4):740–751, August 2000.

[69] Brian J Cantwell, Roger R Draheim, Richard B Weart, Cameran Nguyen, Richard C Stewart, and Michael D Manson. Chez phosphatase localizes to chemoreceptor patches via chea-short. *Journal of Bacteriology*, 185(7):2354–2361, 2003.

[70] H Tajima, K Imada, M Sakuma, F Hattori, T Nara, K Noaki, M Homma, and I Kawagishi. Ligand specificity determined by differentially arranged common ligand-binding residues in bacterial amino acid chemoreceptors tsr and tar. *J Biol Chem*, 286:42200–42210, 2011.

[71] C Wolff and J S Parkinson. Aspartate taxis mutants of the Escherichia coli tar chemoreceptor. *Journal of Bacteriology*, 170(10):4509–4515, October 1988.

[72] Shuangyu Bi, Manika Kargeti, Remy Colin, Niklas Farke, Hannes Link, and Victor Sourjik. Dynamic fluctuations in a bacterial metabolic network. *Nature Communications*, 14(1):2173, April 2023.

[73] Hendrik Anthony Kramers. Brownian motion in a field of force and the diffusion model of chemical reactions. *Physica*, 7(4):284–304, 1940.

[74] TAJ Duke and D Bray. Heightened sensitivity of a lattice of membrane receptors. *PNAS*, 96:10104–8, 1999.

[75] BA Mello, LB Shaw, and Y Tu. Effects of receptor interaction in bacterial chemotaxis. *Biophys. J.*, 87:1578–95, 2004.

[76] ML Skoge, RG Endres, and NS Wingreen. Receptor-Receptor coupling in bacterial chemotaxis: Evidence for strongly coupled clusters. *Biophys. J.*, 90(12):4317–4326, June 2006.

[77] F Bai, RW Branch, DV Nicolau, T Pilizota, BC Steel, PK Maini, and RM Berry. Conformational spread as a mechanism for cooperativity in the bacterial flagellar switch. *Science*, 327:685–9, 2010.

[78] Fangbin Wang, Hui Shi, Rui He, Renjie Wang, Rongjing Zhang, and Junhua Yuan. Non-equilibrium effect in the allosteric regulation of the bacterial flagellar switch. *Nature Physics*, 13(7):710–714, July 2017.

[79] M E Fisher and M N Barber. Scaling theory for finite-size effects in the critical region. *Phys. Rev. Lett.*, 28:1516–1519, Jun 1972.

[80] H. Takano. Finite-Size Scaling Approach to the Kinetic Ising Model. *Progress of Theoretical Physics*, 68(2):493–507, August 1982.

[81] S. Miyashita and H. Takano. Dynamical Nature of the Phase Transition of the Two-Dimensional Kinetic Ising Model. *Progress of Theoretical Physics*, 73(5):1122–1140, May 1985.

[82] Arthur E Ferdinand and Michael E Fisher. Bounded and inhomogeneous ising models. i. specific-heat anomaly of a finite lattice. *Physical Review*, 185(2):832, 1969.

[83] D. P. Landau. Finite-size behavior of the Ising square lattice. *Physical Review B*, 13(7):2997–3011, April 1976.

[84] C Keith Cassidy, Benjamin A Himes, Dapeng Sun, Jun Ma, Gongpu Zhao, John S Parkinson, Phillip J Stansfeld, Zaida Luthey-Schulten, and Peijun Zhang. Structure and dynamics of the e. coli chemotaxis core signaling complex by cryo-electron tomography and molecular simulations. *Communications biology*, 3(1):1–10, 2020.

[85] M Li and G.L. Hazelbauer. Core unit of chemotaxis signaling complexes. *PNAS*, 108:9390–5, 2011.

[86] GE Piñas, V Frank, A Vaknin, and JS Parkinson. The source of high signal cooperativity in bacterial chemosensory arrays. *PNAS*, 113(12):3335–3340, 2016.

[87] R. G. Smock and L. M. Gierasch. Sending Signals Dynamically. *Science*, 324(5924):198–203, April 2009.

[88] JR Lewandowski, ME Halse, M Blackledge, and L Emsley. Direct observation of hierarchical protein dynamics. *Science*, 348(6234):587–581, May 2015.

[89] Yonathan Goldtzvik, Mauro Lorenzo Mugnai, and D. Thirumalai. Dynamics of Allosteric Transitions in Dynein. *Structure*, 26(12):1664–1677.e5, December 2018.

[90] David D. Boehr, Dan McElheny, H. Jane Dyson, and Peter E. Wright. Millisecond timescale fluctuations in dihydrofolate reductase are exquisitely sensitive to the bound ligands. *PNAS*, 107(4):1373–1378, January 2010.

[91] Sebastian Buchenberg, Florian Sittel, and Gerhard Stock. Time-resolved observation of protein allosteric communication. *PNAS*, 114(33):E6804–E6811, August 2017.

[92] M Skoge, Y Meir, and NS Wingreen. Dynamics of cooperativity in chemical sensing among cell-surface receptors. *Phys. Rev. Lett.*, 107:178101, 2011.

[93] Matthijs Meijers, Sosuke Ito, and Pieter Rein ten Wolde. Behavior of information flow near criticality. *Phys. Rev. E*, 103:L010102, Jan 2021.

[94] JE Segall, SM Block, and HC Berg. Temporal comparisons in bacterial chemotaxis. *PNAS*, pages 8987–8991, 1986.

[95] Damon A Clark and Lars C Grant. The bacterial chemotactic response reflects a compromise between transient and steady-state behavior. *Proceedings of the National Academy of Sciences*, 102(26):9150–9155, 2005.

[96] Yann S Dufour, Xiongfei Fu, Luis Hernandez-Nunez, and Thierry Emonet. Limits of feedback control in bacterial chemotaxis. *PLoS computational biology*, 10(6):e1003694, 2014.

[97] Ralph E Steuer. Multiple criteria optimization. *Theory, computation and applications*, 1986.

[98] JE Segall, MD Manson, and HC Berg. Signal processing times in bacterial chemotaxis. *Nature*, 296:855–7, 1982.

[99] V Sourjik and HC Berg. Binding of the Escherichia coli response regulator CheY to its target measured in vivo by fluorescence resonance energy transfer. *PNAS*, 99(20):12669–12674, 2002.

[100] V Sourjik and HC Berg. Functional interactions between receptors in bacterial chemotaxis. *Nature*, 428(6981):437–441, 2004.

[101] MD Levin, TS Shimizu, and D Bray. Binding and diffusion of cher molecules within a cluster of membrane receptors. *Biophys. J.*, 82:1809–17, 2002.

[102] TS Shimizu, SV Aksenov, and D Bray. A spatially extended stochastic model of the bacterial chemotaxis signalling pathway. *J. Mol. Biol.*, 329(2):291–309, 2003.

[103] Antonio Carlos Costa, Gautam Sridhar, Claire Wyart, and Massimo Vergassola. Fluctuating landscapes and heavy tails in animal behavior. *PRX Life*, 2(2):023001, 2024.

[104] KM Taute, S Gude, SJ Tans, and TS Shimizu. High-throughput 3d tracking of bacteria on a standard phase contrast microscope. *Nat. Comm.*, 6, 2015.

[105] Germán E Piñas, Michael D DeSantis, C Keith Cassidy, and John S Parkinson. Hexameric rings of the scaffolding protein chew enhance response sensitivity and cooperativity in escherichia coli chemoreceptor arrays. *Science Signaling*, 15(718):eabj1737, 2022.

[106] Thierry Mora, Aleksandra M Walczak, William Bialek, and Curtis G Callan Jr. Maximum entropy models for antibody diversity. *Proceedings of the National Academy of Sciences*, 107(12):5405–5410, 2010.

[107] Sarah L Veatch, Pietro Cicuta, Prabuddha Sengupta, Aurelia Honerkamp-Smith, David Holowka, and Barbara Baird. Critical fluctuations in plasma membrane vesicles. *ACS chemical biology*, 3(5):287–293, 2008.

[108] Janina Hesse and Thilo Gross. Self-organized criticality as a fundamental property of neural systems. *Frontiers in Systems Neuroscience*, 8, September 2014.

[109] Arnold J. T. M. Mathijssen, Joshua Culver, M. Saad Bhamla, and Manu Prakash. Collective intercellular communication through ultra-fast hydrodynamic trigger waves. *Nature*, 571(7766):560–564, July 2019.

[110] Andrea Cavagna, Alessio Cimarelli, Irene Giardina, Giorgio Parisi, Raffaele Santagati, Fabio Stefanini, and Massimiliano Viale. Scale-free correlations in starling flocks. *Proceedings of the National Academy of Sciences*, 107(26):11865–11870, 2010.

[111] Thierry Mora and William Bialek. Are Biological Systems Poised at Criticality? *Journal of Statistical Physics*, 144(2):268–302, July 2011.

[112] Mikhail N. Levit, Yi Liu, and Jeffry B. Stock. Mechanism of CheA Protein Kinase Activation in Receptor Signaling Complexes. *Biochemistry*, 38(20):6651–6658, May 1999.

[113] David Hathcock, Qiwei Yu, Bernardo A Mello, Divya N Amin, Gerald L Hazelbauer, and Yuhai Tu. A nonequilibrium allosteric model for receptor-kinase complexes: The role of energy dissipation in chemotaxis signaling. *Proceedings of the National Academy of Sciences*, 120(42):e2303115120, 2023.

[114] David Hathcock, Qiwei Yu, and Yuhai Tu. Time-reversal symmetry breaking in the chemosensory array: asymmetric switching and dissipation-enhanced sensing. *arXiv preprint arXiv:2312.17424*, 2023.

[115] Ariel J. Ben-Sasson, Joseph L. Watson, William Sheffler, Matthew Camp Johnson, Alice Bittleston, Logeshwaran Somasundaram, Justin Decarreau, Fang Jiao, Jiajun Chen, Ioanna Mela, Andrew A. Drabek, Sanchez M. Jarrett, Stephen C. Blacklow, Clemens F. Kaminski, Greg L. Hura, James J. De Yoreo, Justin M. Kollman, Hannele Ruohola-Baker, Emmanuel Derivery, and David Baker. Design of biologically active binary protein 2d materials. *Nature*, 589(7842):468–473, 2021.

[116] J S Parkinson. Complementation analysis and deletion mapping of Escherichia coli mutants defective in chemotaxis. *Journal of Bacteriology*, 135(1):45–53, July 1978.

[117] P Ames, CA Studdert, RH Reiser, and JS Parkinson. Collaborative signaling by mixed chemoreceptor teams in escherichia coli. *PNAS*, 99:7060–65, 2002.

[118] D. R. Ortega, C. Yang, P. Ames, J. Baudry, J. S. Parkinson, and I. B. Zhulin. A phenylalanine rotameric switch for signal-state control in bacterial chemoreceptors. *Nature Communications*, 4:1–8, 2013.

[119] O Oleksiuk, V Jakovljevic, N Vladimirov, R Carvalho, E Paster, WS Ryu, Y Meir, NS Wingreen, M Kollmann, and V Sourjik. Thermal robustness of signaling in bacterial chemotaxis. *Cell*, 145(2):312–321, 2011.

[120] P Thévanas, UE Ruttimann, and M Unser. A pyramid approach to subpixel registration based on intensity," ieee transactions on image processing. *IEEE Transactions on Image Processing*, 7:27–41, 1998.

[121] LP Coelho. Mahotas: Open source software for scriptable computer vision. *Journal of Open Research Software*, 1:e3, 2013.

[122] S Schulmeister, M Ruttorf, S Thiem, D Kentner, D Lebiedz, and V Sourjik. Protein exchange dynamics at chemoreceptor clusters in Escherichia coli. *PNAS*, 105(17):6403–6408, April 2008.

[123] A Vaknin and HC Berg. Single Cell FRET imaging of phosphatase activity in the escherichia coli chemotaxis system. *PNAS*, 101(49):170272–7, 2004.

[124] Alfred B Bortz, Malvin H Kalos, and Joel L Lebowitz. A new algorithm for monte carlo simulation of ising spin systems. *Journal of Computational Physics*, 17(1):10–18, 1975.

[125] J.S. Parkinson, G.L. Hazelbauer, and J.J. Falke. Signaling and sensory adaptation in escherichia coli chemoreceptors: 2015 update. *Trends in Microbiology*, 23(5):257–266, 2015.

[126] TC Terwilliger, JY Wang, and DE Koshland. Kinetics of receptor modification. *Journal of Biol Chemistry*, 261:10814–20, 1986.

[127] Simon A Simms, Ann M Stock, and Jeffry B Stock. Purification and Characterization of the S-Adenosy1methionine:Glutamyl Methyltransferase That Modifies Membrane Chemoreceptor Proteins in Bacteria. *The Journal of Biological Chemistry*, 262(18):8537–8543, 1987.

[128] Daniel V. Schroeder. *Introduction to Thermal Physics*. Addison Wesley Longman, 2000.

[129] XS Han and JS Parkinson. An unorthodox sensory adaptation site in the e. coli serine chemoreceptor. *Journal of Bacteriology*, 196:641–649, 2014.

[130] E. Ising. Beitrag zur theorie des ferromagnetismus. *Z. Physik*, 31:253, 1925.

[131] Jean-Pierre Changeux. 50 years of allosteric interactions: the twists and turns of the models. *Nature Reviews Molecular Cell Biology*, 14(12):819–829, December 2013.

[132] Lars Onsager. Crystal Statistics. I. A Two-Dimensional Model with an Order-Disorder Transition. *Physical Review*, 65(3-4):117–149, February 1944.

[133] Leo P Kadanoff. Scaling laws for ising models near t c. *Physics Physique Fizika*, 2(6):263, 1966.

[134] John Cardy. *Finite-size scaling*. Elsevier, 1988.

[135] A Papoulis. *Probability, Random Variables, and Stochastic Processes*. McGraw-Hill, New York, 2nd edition, 1984.

[136] K. Binder and D. P. Landau. Finite-size scaling at first-order phase transitions. *Physical Review B*, 30(3):1477–1485, August 1984.

[137] T. A. Duke, N. Le Novère, and D. Bray. Conformational spread in a ring of proteins: a stochastic approach to allostery. *J. Mol. Biol.*, 308:541–53, 2001.

[138] BA Mello and Y Tu. An allosteric model for heterogeneous receptor complexes: Understanding bacterial chemotaxis responses to multiple stimuli. *PNAS*, 102(48):17354–17359, 2005.

[139] JE Keymer, RG Endres, M Skoge, Y Meir, and NS Wingreen. Chemosensing in Escherichia coli: Two regimes of two-state receptors. *PNAS*, 103(6):1786–1791, February 2006.

[140] Michael E Fisher. The theory of equilibrium critical phenomena. *Reports on progress in physics*, 30(2):615, 1967.

[141] D Greenfield, AL McEvoy, H. Shroff, GE Crooks, NS Wingreen, E Betzig, and J Liphardt. Self-organization of the escherichia coli chemotaxis network imaged with super-resolution light microscopy. *PLoS Biology*, 7, 2009.

[142] H Salman and A Libchaber. A concentration-dependent switch in the bacterial response to temperature. *Nature Cell Biology*, 9(9):1098–1100, 2007.

[143] Yevgeniy Kalinin, Silke Neumann, Victor Sourjik, and Mingming Wu. Responses of *Escherichia coli* Bacteria to Two Opposing Chemoattractant Gradients Depend on the Chemoreceptor Ratio. *Journal of Bacteriology*, 192(7):1796–1800, April 2010.

[144] BingKan Xue, Pablo Sartori, and Stanislas Leibler. Environment-to-phenotype mapping and adaptation strategies in varying environments. *Proceedings of the National Academy of Sciences*, 116(28):13847–13855, July 2019.

[145] Jeffrey N. Carey, Erin L. Mettert, Manuela Roggiani, Kevin S. Myers, Patricia J. Kiley, and Mark Goulian. Regulated Stochasticity in a Bacterial Signaling Network Permits Tolerance to a Rapid Environmental Change. *Cell*, 173(1):196–207.e14, March 2018.

[146] Frank Schreiber, Sten Littmann, Gaute Lavik, Stéphane Escrig, Anders Meibom, Marcel M. M. Kuypers, and Martin Ackermann. Phenotypic heterogeneity driven by nutrient limitation promotes growth in fluctuating environments. *Nature Microbiology*, 1(6):16055, May 2016.

[147] Nicholas W Frankel, William Pontius, Yann S Dufour, Junjiajia Long, Luis Hernandez-Nunez, and Thierry Emonet. Adaptability of non-genetic diversity in bacterial chemotaxis. *eLife*, 3:e03526, October 2014.

[148] Adam James Waite, Nicholas W. Frankel, and Thierry Emonet. Behavioral Variability and Phenotypic Diversity in Bacterial Chemotaxis. *Annual Review of Biophysics*, 47(1):595–616, May 2018.

[149] Mingshan Li and Gerald L. Hazelbauer. Cellular Stoichiometry of the Components of the Chemotaxis Signaling Complex. *Journal of Bacteriology*, 186(12):3687–3694, June 2004.

[150] Johannes M Keegstra, Keita Kamino, François Anquez, Milena D Lazova, Thierry Emonet, and Thomas S Shimizu. Phenotypic diversity and temporal variability in a bacterial signaling network revealed by single-cell FRET. *eLife*, 6:e27455, December 2017.

[151] Jacque Monod, Jeffries Wyman, and Jean-Pierre Changeux. On the nature of allosteric transitions: A plausible model. *J. Mol. Biol.*, 12:88–118, 1965.

[152] Bernardo A. Mello and Yuhai Tu. An allosteric model for heterogeneous receptor complexes: Understanding bacterial chemotaxis responses to multiple stimuli. *Proceedings of the National Academy of Sciences*, 102(48):17354–17359, November 2005.

[153] Henry H. Mattingly and Thierry Emonet. Collective behavior and nongenetic inheritance allow bacterial populations to adapt to changing environments. *Proceedings of the National Academy of Sciences*, 119(26):e2117377119, June 2022.

[154] Ping Wang, Lydia Robert, James Pelletier, Wei Lien Dang, Francois Taddei, Andrew Wright, and Suckjoon Jun. Robust Growth of Escherichia coli. *Current Biology*, 20(12):1099–1103, June 2010.

[155] Yiling Yang, Abiola M. Pollard, Carolin Höfler, Gernot Poschet, Markus Wirtz, Rüdiger Hell, and Victor Sourjik. Relation between chemotaxis and consumption of amino acids in bacteria. *Molecular Microbiology*, 96(6):1272–1282, June 2015.

[156] Yuichi Taniguchi, Paul J. Choi, Gene-Wei Li, Huiyi Chen, Mohan Babu, Jeremy Hearn, Andrew Emili, and X. Sunney Xie. Quantifying *E. coli* Proteome and Transcriptome with Single-Molecule Sensitivity in Single Cells. *Science*, 329(5991):533–538, July 2010.

[157] Lusi Li, Xuanqi Zhang, Yanhong Sun, Qi Ouyang, Yuhai Tu, and Chunxiong Luo. Phenotypic Variability Shapes Bacterial Responses to Opposing Gradients. *PRX Life*, 2(1):013001, January 2024.

[158] Anna Yoney and Hanna Salman. Precision and Variability in Bacterial Temperature Sensing. *Biophysical Journal*, 108(10):2427–2436, May 2015.

[159] Yiling Yang and Victor Sourjik. Opposite responses by different chemoreceptors set a tunable preference point in <*span style="font-variant:small-caps;"*>E *scherichia coli* pH taxis. *Molecular Microbiology*, 86(6):1482–1489, December 2012.

[160] Hanna Salman and Albert Libchaber. A concentration-dependent switch in the bacterial response to temperature. *Nature Cell Biology*, 9(9):1098–1100, September 2007.

[161] GS Chilcott and KT Hughes. Coupling of flagellar gene expression to flagellar assembly in salmonella enterica serovar typhimurium and escherichia coli. *Microbiol Mol Biol Rev*, 64:694–708, 2000.

[162] Rohan Balakrishnan, Matteo Mori, Igor Segota, Zhongge Zhang, Ruedi Aebersold, Christina Ludwig, and Terence Hwa. Principles of gene regulation quantitatively connect DNA to RNA and proteins in bacteria. *Science*, 378(6624):eabk2066, December 2022.

[163] Peter Ames, Claudia A. Studdert, Rebecca H. Reiser, and John S. Parkinson. Collaborative signaling by mixed chemoreceptor teams in *Escherichia coli*. *Proceedings of the National Academy of Sciences*, 99(10):7060–7065, May 2002.

[164] Trung V. Phan, Henry H. Mattingly, Lam Vo, Jonathan S. Marvin, Loren L. Looger, and Thierry Emonet. Direct measurement of dynamic attractant gradients reveals breakdown of the Patlak–Keller–Segel chemotaxis model. *Proceedings of the National Academy of Sciences*, 121(3):e2309251121, January 2024.

[165] X. Fu, S. Kato, J. Long, H. H. Mattingly, C. He, D. C. Vural, S. W. Zucker, and T. Emonet. Spatial self-organization resolves conflicts between individuality and collective migration. *Nature Communications*, 9(1):2177, June 2018.

[166] Yang Bai, Caiyun He, Pan Chu, Junjiajia Long, Xuefei Li, and Xiongfei Fu. Spatial modulation of individual behaviors enables an ordered structure of diverse phenotypes during bacterial group migration. *eLife*, 10:e67316, November 2021.

[167] A J Wolfe and H C Berg. Migration of bacteria in semisolid agar. *Proceedings of the National Academy of Sciences*, 86(18):6973–6977, September 1989.

[168] Bin Ni, Remy Colin, Hannes Link, Robert G. Endres, and Victor Sourjik. Growth-rate dependent resource investment in bacterial motile behavior quantitatively follows potential benefit of chemotaxis. *Proceedings of the National Academy of Sciences*, 117(1):595–601, January 2020.

[169] C L Woldringh, J S Binnerts, and A Mans. Variation in Escherichia coli buoyant density measured in Percoll gradients. *Journal of Bacteriology*, 148(1):58–63, October 1981.

[170] Cezar M Khursigara, Ganhui Lan, Silke Neumann, Xiongwu Wu, Suchie Ravindran, Mario J Borgnia, Victor Sourjik, Jacqueline Milne, Yuhai Tu, and Sriram Subramaniam. Lateral density of receptor arrays in the membrane plane influences sensitivity of the E. coli chemotaxis response. *The EMBO Journal*, 30(9):1719–1729, May 2011.

[171] Markus Kollmann, Linda Løvdok, Kilian Bartholomé, Jens Timmer, and Victor Sourjik. Design principles of a bacterial signalling network. *Nature*, 438(7067):504–507, November 2005.

[172] Yiling Yang, Abiola M. Pollard, Carolin Höfler, Gernot Poschet, Markus Wirtz, Rüdiger Hell, and Victor Sourjik. Relation between chemotaxis and consumption of amino acids in bacteria. *Molecular Microbiology*, 96(6):1272–1282, June 2015.

[173] B M Prüss, J M Nelms, C Park, and A J Wolfe. Mutations in NADH:ubiquinone oxidoreductase of Escherichia coli affect growth on mixed amino acids. *Journal of Bacteriology*, 176(8):2143–2150, April 1994.

[174] Irina Lisevich, Remy Colin, Hao Yuan Yang, Bin Ni, and Victor Sourjik. Physics of swimming and its fitness cost determine strategies of bacterial investment in flagellar motility. *Nature Communications*, 16(1):1731, February 2025.

[175] Adam James Waite, Nicholas W Frankel, Yann S Dufour, Jessica F Johnston, Junjiajia Long, and Thierry Emonet. Non-genetic diversity modulates population performance. *Molecular Systems Biology*, 12(12):895, December 2016.

[176] John F. Staropoli and Uri Alon. Computerized Analysis of Chemotaxis at Different Stages of Bacterial Growth. *Biophysical Journal*, 78(1):513–519, January 2000.

[177] Jonas Cremer, Tomoya Honda, Ying Tang, Jerome Wong-Ng, Massimo Vergassola, and Terence Hwa. Chemotaxis as a navigation strategy to boost range expansion. *Nature*, 575(7784):658–663, November 2019.

[178] Tomoya Honda, Jonas Cremer, Leonardo Mancini, Zhongge Zhang, Teuta Pilizota, and Terence Hwa. Coordination of gene expression with cell size enables *Escherichia coli* to efficiently maintain motility across conditions. *Proceedings of the National Academy of Sciences*, 119(37):e2110342119, September 2022.

[179] Yann S. Dufour, Sébastien Gillet, Nicholas W. Frankel, Douglas B. Weibel, and Thierry Emonet. Direct Correlation between Motile Behavior and Protein Abundance in Single Cells. *PLOS Computational Biology*, 12(9):e1005041, September 2016.

[180] Linda Løvdok, Kajetan Bentele, Nikita Vladimirov, Anette Müller, Ferencz S. Pop, Dirk Lebiedz, Markus Kollmann, and Victor Sourjik. Role of Translational Coupling in Robustness of Bacterial Chemotaxis Pathway. *PLoS Biology*, 7(8):e1000171, August 2009.

[181] Hai Zheng, Yang Bai, Meiling Jiang, Taku A. Tokuyasu, Xiongliang Huang, Fajun Zhong, Yuqian Wu, Xiongfei Fu, Nancy Kleckner, Terence Hwa, and Chenli Liu. General quantitative relations linking cell growth and the cell cycle in Escherichia coli. *Nature Microbiology*, 5(8):995–1001, May 2020.

[182] John L. Spudich and D. E. Koshland. Non-genetic individuality: chance in the single cell. *Nature*, 262(5568):467–471, August 1976.

[183] Jacopo Solari. *Spatial organization of the bacterial cell: in vivo imaging across scales*. PhD thesis, VU Amsterdam, The Netherlands, 2019. OCLC: 1088406919.

[184] Dong Qin, Younan Xia, and George M Whitesides. Soft lithography for micro- and nanoscale patterning. *Nature Protocols*, 5(3):491–502, March 2010.

[185] J. Mark Kim, Mayra Garcia-Alcala, Enrique Balleza, and Philippe Cluzel. Stochastic transcriptional pulses orchestrate flagellar biosynthesis in *Escherichia coli*. *Science Advances*, 6(6):eaax0947, February 2020.

[186] Olaf Ronneberger, Philipp Fischer, and Thomas Brox. U-Net: Convolutional Networks for Biomedical Image Segmentation, May 2015. arXiv:1505.04597 [cs].

[187] Keita Kamino, Nirag Kadakia, Fotios Avgidis, Zhe-Xuan Liu, Kazuhiro Aoki, Thomas S. Shimizu, and Thierry Emonet. Optimal inference of molecular interaction dynamics in FRET microscopy. *Proceedings of the National Academy of Sciences*, 120(15):e2211807120, April 2023.

[188] J. W. Kamande, Y. Wang, and A. M. Taylor. Cloning SU8 silicon masters using epoxy resins to increase feature replicability and production for cell culture devices. *Biomicrofluidics*, 9(3):036502, May 2015.

[189] H. H. Mattingly, K. Kamino, B. B. Machta, and T. Emonet. Escherichia coli chemotaxis is information limited. *Nature Physics*, 17(12):1426–1431, December 2021.

[190] Hédia Maamar, Arjun Raj, and David Dubnau. Noise in Gene Expression Determines Cell Fate in *Bacillus subtilis*. *Science*, 317(5837):526–529, July 2007.

[191] Dann Huh and Johan Paulsson. Non-genetic heterogeneity from stochastic partitioning at cell division. *Nature Genetics*, 43(2):95–100, February 2011.

[192] Dann Huh and Johan Paulsson. Random partitioning of molecules at cell division. *Proceedings of the National Academy of Sciences*, 108(36):15004–15009, September 2011.

[193] Robert Mesibov and Julius Adler. Chemotaxis Toward Amino Acids in *Escherichia coli*. *Journal of Bacteriology*, 112(1):315–326, October 1972.

[194] Urszula Łapińska, Georgina Glover, Pablo Capilla-Lasheras, Andrew J. Young, and Stefano Pagliara. Bacterial ageing in the absence of external stressors. *Philosophical Transactions of the Royal Society B: Biological Sciences*, 374(1786):20180442, November 2019.

[195] Enrique Balleza, J Mark Kim, and Philippe Cluzel. Systematic characterization of maturation time of fluorescent proteins in living cells. *Nature Methods*, 15(1):47–51, January 2018.

[196] Sonja Schulmeister, Michaela Ruttorf, Sebastian Thiem, David Kentner, Dirk Lebiedz, and Victor Sourjik. Protein exchange dynamics at chemoreceptor clusters in *Escherichia coli*. *Proceedings of the National Academy of Sciences*, 105(17):6403–6408, April 2008.

[197] Moriah Koler, Eliran Peretz, Chetan Aditya, Thomas S. Shimizu, and Ady Vaknin. Long-term positioning and polar preference of chemoreceptor clusters in E. coli. *Nature Communications*, 9(1):4444, October 2018.

[198] Germán E. Piñas, Vered Frank, Ady Vaknin, and John S. Parkinson. The source of high signal cooperativity in bacterial chemosensory arrays. *Proceedings of the National Academy of Sciences*, 113(12):3335–3340, March 2016.

[199] Maroš Pleška, David Jordan, Zak Frentz, BingKan Xue, and Stanislas Leibler. Nongenetic individuality, changeability, and inheritance in bacterial behavior. *Proceedings of the National Academy of Sciences*, 118(13):e2023322118, March 2021.

[200] Benjamin K. Chan, Mark Sistrom, John E. Wertz, Kaitlyn E. Kortright, Deepak Narayan, and Paul E. Turner. Phage selection restores antibiotic sensitivity in MDR Pseudomonas aeruginosa. *Scientific Reports*, 6(1):26717, May 2016.

[201] Keith Poole. Outer Membranes and Efflux: The Path to Multidrug Resistance in Gram-Negative Bacteria. *Current Pharmaceutical Biotechnology*, 3(2):77–98, June 2002.

[202] Michael W. Schmitt, Lawrence A. Loeb, and Jesse J. Salk. The influence of subclonal resistance mutations on targeted cancer therapy. *Nature Reviews Clinical Oncology*, 13(6):335–347, June 2016.

[203] Weirong Liu, Jonas Cremer, Dengjin Li, Terence Hwa, and Chenli Liu. An evolutionarily stable strategy to colonize spatially extended habitats. *Nature*, 575(7784):664–668, November 2019.

[204] David T Fraebel, Harry Mickalide, Diane Schnitkey, Jason Merritt, Thomas E Kuhlman, and Seppe Kuehn. Environment determines evolutionary trajectory in a constrained phenotypic space. *eLife*, 6:e24669, March 2017.

[205] Bin Ni, Bhaswar Ghosh, Ferencz S. Paldy, Remy Colin, Thomas Heimerl, and Victor Sourjik. Evolutionary Remodeling of Bacterial Motility Checkpoint Control. *Cell Reports*, 18(4):866–877, January 2017.

[206] Edo Kussell and Stanislas Leibler. Phenotypic Diversity, Population Growth, and Information in Fluctuating Environments. *Science*, 309(5743):2075–2078, September 2005.

[207] Thomas M. Norman, Nathan D. Lord, Johan Paulsson, and Richard Losick. Stochastic Switching of Cell Fate in Microbes. *Annual Review of Microbiology*, 69(1):381–403, October 2015.

[208] Thomas K. Wood, Stephen J. Knabel, and Brian W. Kwan. Bacterial Persister Cell Formation and Dormancy. *Applied and Environmental Microbiology*, 79(23):7116–7121, December 2013.

[209] Yaara Oren, Michael Tsabar, Michael S. Cuoco, Liat Amir-Zilberstein, Heidie F. Cabanos, Jan-Christian Hütter, Bomiao Hu, Pratiksha I. Thakore, Marcin Tabaka, Charles P. Fulco, William Colgan, Brandon M. Cuevas, Sara A. Hurvitz, Dennis J. Slamon, Amy Deik, Kerry A. Pierce, Clary Clish, Aaron N. Hata, Elma Zaganjor, Galit Lahav, Katerina Politi, Joan S. Brugge, and Aviv Regev. Cycling cancer persister cells arise from lineages with distinct programs. *Nature*, 596(7873):576–582, August 2021.

[210] Paul C Bressloff. Stochastic switching in biology: from genotype to phenotype. *Journal of Physics A: Mathematical and Theoretical*, 50(13):133001, March 2017.

[211] Tianhai Tian and Kevin Burrage. Stochastic models for regulatory networks of the genetic toggle switch. *Proceedings of the National Academy of Sciences*, 103(22):8372–8377, May 2006.

[212] Julius Adler. Chemotaxis in Bacteria. *Science*, 153, 1966.

[213] Jerome Wong-Ng, Antonio Celani, and Massimo Vergassola. Exploring the function of bacterial chemotaxis. *Current Opinion in Microbiology*, 45:16–21, October 2018.

[214] Daniel A. Koster, Avraham Mayo, Anat Bren, and Uri Alon. Surface Growth of a Motile Bacterial Population Resembles Growth in a Chemostat. *Journal of Molecular Biology*, 424(3-4):180–191, December 2012.

[215] Hai Zheng, Po-Yi Ho, Meiling Jiang, Bin Tang, Weirong Liu, Dengjin Li, Xuefeng Yu, Nancy E. Kleckner, Ariel Amir, and Chenli Liu. Interrogating the *Escherichia coli* cell cycle by cell dimension perturbations. *Proceedings of the National Academy of Sciences*, 113(52):15000–15005, December 2016.

[216] N.V. Vorobyeva, M.Yu. Sherman, and A.N. Glagolev. Bacterial chemotaxis controls the catabolite repression of flagellar biogenesis. *FEBS Letters*, 143(2):233–236, July 1982.

[217] Matthew Scott and Terence Hwa. Shaping bacterial gene expression by physiological and proteome allocation constraints. *Nature Reviews Microbiology*, 21(5):327–342, May 2023.

[218] Nicholas A. Licata, Bitan Mohari, Clay Fuqua, and Sima Setayeshgar. Diffusion of Bacterial Cells in Porous Media. *Biophysical Journal*, 110(1):247–257, January 2016.

[219] Yann S. Dufour, Xiongfei Fu, Luis Hernandez-Nunez, and Thierry Emonet. Limits of Feedback Control in Bacterial Chemotaxis. *PLoS Computational Biology*, 10(6):e1003694, June 2014.

[220] Clive S. Barker, Birgit M. Prüß, and Philip Matsumura. Increased Motility of *Escherichia coli* by Insertion Sequence Element Integration into the Regulatory Region of the *flhD* Operon. *Journal of Bacteriology*, 186(22):7529–7537, November 2004.

[221] Chengwei Luo, Seth T. Walk, David M. Gordon, Michael Feldgarden, James M. Tiedje, and Konstantinos T. Konstantinidis. Genome sequencing of environmental *Escherichia coli* expands understanding of the ecology and speciation of the model bacterial species. *Proceedings of the National Academy of Sciences*, 108(17):7200–7205, April 2011.

[222] Yuhai Tu, Thomas S. Shimizu, and Howard C. Berg. Modeling the chemotactic response of *Escherichia coli* to time-varying stimuli. *Proceedings of the National Academy of Sciences*, 105(39):14855–14860, September 2008.

[223] JS Parkinson and SE Houts. Isolation and behavior of escherichia coli deletion mutants lacking chemotaxis functions. *J. Bacteriol.*, 151:106–13, 1982.

[224] Robert G. Endres and Ned S. Wingreen. Precise adaptation in bacterial chemotaxis through "assistance neighborhoods". *Proceedings of the National Academy of Sciences*, 103(35):13040–13044, August 2006.

[225] Victor Sourjik. Receptor clustering and signal processing in E. coli chemotaxis. *Trends in Microbiology*, 12(12):569–576, December 2004.

[226] J S Parkinson. cheA, cheB, and cheC genes of Escherichia coli and their role in chemotaxis. *Journal of Bacteriology*, 126(2):758–770, May 1976.

[227] Tapomoy Bhattacharjee and Sujit S. Datta. Bacterial hopping and trapping in porous media. *Nature Communications*, 10(1):2075, May 2019.

[228] Christina Kurzthaler, Suvendu Mandal, Tapomoy Bhattacharjee, Hartmut Löwen, Sujit S. Datta, and Howard A. Stone. A geometric criterion for the optimal spreading of active polymers in porous media. *Nature Communications*, 12(1):7088, December 2021.

[229] Arvi Jõers and Tanel Tenson. Growth resumption from stationary phase reveals memory in Escherichia coli cultures. *Scientific Reports*, 6(1):24055, April 2016.

[230] Jan-Willem Veening, Eric J. Stewart, Thomas W. Berngruber, François Taddei, Oscar P. Kuipers, and Leendert W. Hamoen. Bet-hedging and epigenetic inheritance in bacterial cell development. *Proceedings of the National Academy of Sciences*, 105(11):4393–4398, March 2008.

[231] Souvik Bhattacharyya, Nabin Bhattarai, Dylan M. Pfannenstiel, Brady Wilkins, Abhyudai Singh, and Rasika M. Harshey. A heritable iron memory enables decision-making in *Escherichia coli*. *Proceedings of the National Academy of Sciences*, 120(48):e2309082120, November 2023.

[232] Sebastian Gude, Erçağ Pinçe, Katja M. Taute, Anne-Bart Seinen, Thomas S. Shimizu, and Sander J. Tans. Bacterial coexistence driven by motility and spatial competition. *Nature*, 578(7796):588–592, February 2020.

[233] Joshua E Goldford, Nanxi Lu, Djordje Baji, Alicia Sanchez-Gorostiaga, Daniel Segrè, Pankaj Mehta, and Alvaro Sanchez. Emergent simplicity in microbial community assembly. *Science*, 361:469–474, 2018.

[234] Wenlong Zuo and Yilin Wu. Dynamic motility selection drives population segregation in a bacterial swarm. *Proceedings of the National Academy of Sciences*, 117(9):4693–4700, March 2020.

[235] Gayatri Venkiteswaran, Stephen W. Lewellis, John Wang, Eric Reynolds, Charles Nicholson, and Holger Knaut. Generation and Dynamics of an Endogenous, Self-Generated Signaling Gradient across a Migrating Tissue. *Cell*, 155(3):674–687, October 2013.

[236] Cally Scherber, Alexander J. Aranyosi, Birte Kulemann, Sarah P. Thayer, Mehmet Toner, Othon Iliopoulos, and Daniel Irimia. Epithelial cell guidance by self-generated EGF gradients. *Integrative Biology*, 4(3):259, 2012.

[237] Nicolas B. David, Dora Sapède, Laure Saint-Etienne, Christine Thisse, Bernard Thisse, Christine Dambly-Chaudière, Frédéric M. Rosa, and Alain Ghysen. Molecular basis of cell migration in the fish lateral line: Role of the chemokine receptor CXCR4 and of its ligand, SDF1. *Proceedings of the National Academy of Sciences*, 99(25):16297–16302, December 2002.

[238] Eric Theveneau and Roberto Mayor. Neural crest delamination and migration: From epithelium-to-mesenchyme transition to collective cell migration. *Developmental Biology*, 366(1):34–54, June 2012.

[239] Andrew J. Muinonen-Martin, Olivia Susanto, Qifeng Zhang, Elizabeth Smethurst, William J. Faller, Douwe M. Veltman, Gabriela Kalna, Colin Lindsay, Dorothy C. Bennett, Owen J. Sansom, Robert Herd, Robert Jones, Laura M. Machesky, Michael J. O. Wakelam, David A. Knecht, and Robert H. Insall. Melanoma Cells Break Down LPA to Establish Local Gradients That Drive Chemotactic Dispersal. *PLoS Biology*, 12(10):e1001966, October 2014.

[240] Murat Acar, Jerome T Mettetal, and Alexander Van Oudenaarden. Stochastic switching as a survival strategy in fluctuating environments. *Nature Genetics*, 40(4):471–475, April 2008.

LIST OF PHD PUBLICATIONS

PUBLICATIONS INCLUDED IN THIS THESIS

- J.M. Keegstra*, **F. Avgidis***, Y. Mulla, E. Usher, J.S. Parkinson, T.S. Shimizu. Near-critical tuning of conformational spread revealed by spontaneous switching in an allosteric signalling array (**under revision at Nature Physics**, 2025) (*equal contribution) - Chapter 2
  Author contributions:
  J.M.K. and T.S.S. conceived study; F.A. and J.M.K. performed experiments; J.M.K. and F.A. performed numerical simulations, with code developed by Y.M.; J.M.K., F.A., E.U., J.S.P., and T.S.S. analyzed and interpreted data; J.S.P. provided the chemoreceptor mutants; J.M.K., F.A., and T.S.S. wrote the manuscript with input from J.S.P., Y.M., and E.U.
- **F. Avgidis**, R. Jurgelyte, T. Emonet, T.S. Shimizu. Growth-dependent control of sensory bet-hedging enhances navigation (**in preparation**) - Chapter 3
  Author contributions:
  F.A., T.S.S., and T.E. conceived the study; F.A. performed experiments; R.J. assisted with receptor quantification experiments; F.A. analyzed the data and wrote the manuscript; F.A., R.J., T.S.S., and T.E. edited the manuscript.
- **F. Avgidis**, C. Borrias, T. Emonet, T.S. Shimizu. Dynamics of sensory diversity within and across generations (**in preparation**) - Chapter 4
  Author contributions:
  F.A., T.S.S., and T.E. conceived the study; F.A. performed experiments; C.B. engineered genetic constructs; F.A. analyzed the data and wrote the manuscript; F.A., C.B., T.S.S., and T.E. edited the manuscript.
- L. Vo*, **F. Avgidis***, H.H. Mattingly*, K. Edmonds, I.Burger, R. Balasubramanian, T.S. Shimizu, B.I. Kazmierczak, T. Emonet. Non-genetic adaptation by collective migration (**PNAS 122 8**, 2025) (*equal contribution) - Chapter 5
  Author contributions:
  L.V., F.A., H.H.M., T.S.S., B.I.K., and T.E. designed experiments; L.V., F.A., K.E., I.B., and R.B. performed experiments; L.V. and F.A. analyzed data; and L.V., F.A., H.H.M., T.S.S., B.I.K., and T.E. wrote the manuscript.

PUBLICATIONS NOT INCLUDED IN THIS THESIS

- K. Kamino, N. Kadakia, **F. Avgidis**, Z. Liu, K. Aoki, T.S. Shimizu, T. Emonet. Optimal inference of molecular interaction dynamics in FRET microscopy (**PNAS 120 15**, 2023)

ACKNOWLEDGMENTS

Science is never a solitary endeavor, and I've been fortunate to share this journey with many wonderful people. I would like to express my deepest gratitude here.

First and foremost, Tom, thank you for entrusting a student from a quantum computing lab, with no formal background in biology, to work with living cells. Your scientific curiosity and enthusiasm are truly inspirational. Thierry, thank you for guiding me as both my PhD co-advisor and now postdoc advisor. You've always helped me stay focused on the bigger picture.

Johannes and Keita, I have been privileged to stand on your shoulders. You trained me in the early days, and without your support, this thesis would not exist. Johannes, I admire your scientific rigor and breadth of knowledge. Working with you over the years to complete the switching paper has been a deeply valuable experience. Thank you for traveling to Basel to have dinner with me. Keita, I seem to follow in your footsteps—from Amsterdam to New Haven. I've always appreciated your kindness and diligence. It was great seeing you again in Charleston and working together on the FRET paper. Simone, your genetics work made everything in this thesis possible. Your perseverance is admirable. Charlotte, thank you for your positive spirit and kindness. We learned so much together about genetic engineering. Henry, thank you for hosting me at Flatiron. It was a pleasure working with you on the adaptation paper, and now on the noise paper. Sandy and Victor, thank you for always generously sharing strains, plasmids, and your vast knowledge. A large part of this thesis wouldn't have been possible without you.

Sander, Jeroen, Bela, Pieter Rein, and Kristina—thank you for your valuable feedback throughout my PhD. Pieter Rein, our conversations on chemotaxis and the art of Hieronymus Bosch were always appreciated. Bela, I still can't believe you speak better Greek than I do.

Pieter Rein and Victor, I also want to thank you for serving on my PhD committee, together with Katja, Ariane, Frank, and Alise. I'm deeply grateful that you all took the time to review my thesis on such short notice. It is an honor to have had such an esteemed panel of experts evaluating my work.

I would also like to thank the late Howard Berg. Though we interacted only once and briefly, his book *Random walks in Biology* inspired me to switch fields and pursue biology.

Ercag, thank you for showing me that collective behavior is far more interesting than I initially thought. I miss our talks on biofilms and Greek-Turkish relations. Steffen, I never beat you at chess, but at least I managed a few wins in table football. Thank you for the delightful late-night discussions that turned into Zoom calls. Speaking of late-nights—Dhawal, Chris, Kathi, and Nebojsa—thank you for being around the lab at hours nobody should be working. Dhawal, I'll never forget your airport dash to catch a comedy show with me. Chris, our discussion on the origins of life—aptly held in a swimming pool—was a highlight. Nebojsa, thank you for your practical advice about life in the US and beyond. Kathi, thank you for always being so kind and for sharing the ups and downs of PhD life.

Evan, it's been a pleasure training you. I'm glad I got to pass the baton of single-cell FRET to a child prodigy. You've been a great student and an even better friend. Thanks for being my paranymph. The same goes to you, Brian. Thank you for being my paranymph and my friend since our first year at university. I am glad we both grew out of electrical engineering. Coco, I always admired your intellect and calm demeanor. Thank you for leaving my apartment spotless when I was in Lisbon. I hope you enjoyed going through my books. Thomas, our discussions about life often left me in existential crisis. You and Emma are wonderful people. Antoine, our conversations on artificial intelligence and US politics were always a highlight—Utrecht was fun. Mathijs, your

energy was infectious. The lab felt much quieter after you left. Jacopo, thank you for pioneering the mother machine experiments in the lab and for offering life advice early in my PhD that proved entirely accurate. Loreto, your engineering skills—and cooking—were equally impressive. Thanks to you and Leo for having me for dinner in Den Haag. Malin, Rachael, Max, Marije, Justin, Achille, Simon, and Jaap—it was always fun to hear about your fungal pursuits.

I had the privilege of supervising some excellent students. Elmar, you were the only student I trusted with FRET. Your friendliness and experimental rigor stood out. Chi, you started as my student and nearly finished your PhD before me. I appreciate your kindness, dedication, and—perhaps most of all—the coffee you brought me from Canada. Maybe one day we will finally write a paper together. Ruta, you ignored my advice and didn't skip work to visit a museum—and I'm thankful. You generated an impressive dataset for Chapter 3 of this thesis. Camille, your experimental skills and work ethic spoiled me for future students. Cherin, you're one of the kindest people I've met—you brought warmth to the lab. Thanks for staying positive even when experiments didn't work.

Giulia and Marco, thank you for the career advice in Egmond aan Zee, even if I foolishly didn't follow it. Antony, our conversations—whether about fonts or the futility of life—were always enjoyable. Marko, Hinco, Dimitry, Dion, Iliya, and Brahim—your technical expertise made large parts of this thesis possible. Age, I appreciated our talks about chemotaxis and Dutch healthcare, two famously complicated systems. Thanks to you and Irena for having dinner with me in New York. Max, our chats about science, brutalist architecture, and obscure Dutch payment systems were always a pleasure. Science is lucky you didn't become an architect. Burak, our conversations on biological criticality and Balkan history were always fascinating. Kasper, your breadth of knowledge and grounded demeanor were much appreciated. Luca, I thoroughly enjoyed our talks on the global economy and our photo walks through Amsterdam. Alexander, always a pleasure chatting with you in broken German, Russian, or Greek. Daan, I admired your physics knowledge and singing skills—the latter revealed during our stay in adjacent rooms in Dresden.

Thanks also to my past and present office mates—Parisa, Sima, Theo, Zabreen, Miriam, Pietro, Jeppe, Anne-Sophie, Esmee, and Mohsin, among others—for making the office a productive and friendly place.

Timo, our conversations about food, books, and science were always enjoyable. We may look alike, but we certainly have different opinions on what makes a good model organism. Thanks for having me over for dinner in Utrecht. Vanda, I learned so much from you. Thank you for your energetic attitude and empathy—and for letting me work in the lab when I shouldn't. Marcel, I always enjoyed your dry humor. Sorry again for working in the lab when I shouldn't. Bernard, thank you for gifting me your coffee—it was very much needed. Rutger, I always appreciated your calm demeanor and kindness. Thank you for quoting me in your thesis and inevitably exposing my ignorance. Xuan, your friendly waves always brightened my day.

Marc, Toby, Maike, Jonas, Arthur, and Vassilis—thank you for the timely and much-needed career advice.

To all past and present members of AMOLF—Mareike, Isabelle, Manuel, Kim, Maria, Jack, Yifei, Tzeni, Lukas, Giada, Mario, Marloes, Giorgio, Rene, Pascal, Imme, Simone, Yuval, Federica, Anders, Harmen, Balazs, Vahe, Avishek, Alex, Vashist, Paul, Finn, Ariane, SaFyre, Ananya, Yvonne, Martijn, Florian, Olga, Joleen, Jente, Melle, Lori, Sofija—and many more I am surely forgetting: thank you for making AMOLF such a great place to do science.

To my new scientific family at Yale: Lam, thank you for showing me around New Haven. Working with you on the adaptation paper has been a great learning experience—I look forward to our future projects. Jeremy, I always admired your breadth of knowledge—and recently, your absurd humor too. Almost getting attacked by a pack of stray dogs in Mexico was memorable. Jyot, we always had engaging discussions, whether about the flagellar motor, Indian food, or life in general. Ethan, I enjoyed every conversation about microscopy, languages, and religion. Thank you for choosing

chemotaxis over structural biology. Kiri and Sam—movie nights were always a joy. Kevin, thanks for joining me for so many classical music concerts. Gustavo, I appreciate your dry humor—it's nice to always have company in the lab, no matter how late at night. Diana, it's fascinating how our paths crossed in Geneva, New York, and now New Haven. Thank you and James for the Thanksgiving dinner. I must, however, confess to all the neuroscientists in the group that I find your stray flies mildly annoying—they insist on landing on me. Bacteria are far more disciplined.

Finally, Alexandra, thank you for your constant and unconditional support, and for tolerating my unreasonable working habits. To my friends and family around the world—even if I don't see you as often as I'd like—you remain a central part of my life. To my parents, to whom I dedicate this thesis: thank you for instilling in me your work ethic and passion for biology. We may disagree about nature vs. nurture, but clearly, some combination of the two made me who I am today.

I type these words late at night in the Yale School of Medicine Library, surrounded by sleep-deprived medical students. It feels fitting to close this thesis with a quote from Plato's *Republic*, inscribed above the library entrance, which captures the essence of the PhD journey:

ΛΑΜΠΑΔΙΑ ΕΧΟΝΤΕΣ ΔΙΑΔΩΣΟΥΣΙΝ ΑΛΛΗΛΟΙΣ
Those who have the torch should pass it on to others